Low Temperature Selective Oxidation of Methane using Hydrogen Peroxide and Oxygen

Nishtha Agarwal

A dissertation submitted for the partial fulfilment

for the degree of doctor of philosophy by

Cardiff Catalysis Institute

Cardiff School of Chemistry

Cardiff University

2018

Acknowledgements

First of all, I would like to acknowledge my supervisors Prof Graham J. Hutchings and Dr. David J. Willock for all of the help and guidance they have given me over the course of my PhD program. Thanks to them I have been able to develop the skills required of me to excel at my research, and without their guidance none of this work would be possible. I would also like to express my sincere gratitude to Dr Simon Freakley for getting me started in Cardiff, teaching and training me in the lab and more importantly, for all his support and advice during my thesis. I am also grateful to my mentor Dr M Sankar and Dr Alison Paul for their valuable suggestions and feedback throughout the various stages of my PhD.

I would also like to express my gratitude to Prof Stuart Taylor, Dr Robert Jenkins, Dr Qian He, Dr Robert Armstrong and Dr Nikos Dimitratos for all their discussions and suggestions during the project. I would particularly like to thank Prof Chris Kiely and his group, especially Sultan, for the amazing STEM images along with Dr Dave Morgan for running and interpretation of XPS data.

I greatly acknowledge MaxNet team members, students and postdocs, and staff who have worked alongside me. I would also like to thank the methane team; Chris and Kit and the computational chemistry team for all their support and help during my work.

I would like to thank Cardiff University for financial support as a part of MaxNet Energy Consortium and HPC Wales and ARCCA for providing the computing time required for the computational simulations.

Many thanks to all my friends from India and Cardiff for the support and a great time during my PhD. Also, thanks to Amir, Wafi and Zoe for laughs and dinners in Cardiff. Special thanks to Vikram for putting up with me talking about chemistry and methane and proof reading most of this thesis.

Most importantly, I would like to thank my family from the bottom of my heart for their constant encouragement and support throughout the course of study.

Summary

The selective oxidation of methane, which is the primary component of natural gas, is one of the most important challenges in catalysis. While the search for catalysts capable of converting methane to higher value commodity chemicals and liquid fuels such as methanol has been ongoing for over a century, an industrially viable process has not yet been developed. Currently, large scale upgradation of natural gas proceeds indirectly employing high temperature conversion to syngas which is then processed to synthesise fuels and chemicals. Different catalysts are currently being studied for direct low temperature selective oxidation of methane to liquid oxygenates primarily methanol. One of the systems studied is based on gold-palladium supported nanoparticles using hydrogen peroxide. Though the catalyst was shown to be active, high wastage of hydrogen peroxide was observed along with low productivities. The work in this thesis shows the removal of support can be used to increase the activity and efficiency of the reaction. By tuning the amount of hydrogen peroxide, high productivities and selectivities were observed. Further optimisation of catalyst preparation and methane oxidation were also performed. A theoretical study based on density functional theory into interactions between metal particles, such as gold and palladium and substrates such as oxygen, hydrogen and water was also carried out to identify the active sites and reaction mechanism underway with hydrogen peroxide and these metal particles.

List of Publications

- Aqueous Au-Pd colloids catalyze selective CH_4 oxidation to CH_3OH with O_2 under mild conditions.

  Science 358, no. 6360 (2017): 223-227.

- Hydrocarbon oxidation

  Patent Applied : GB1707621.7

- Selective oxidation of methane to methanol : Accepted

  Book Chapter: Green Oxidation Reactions by Springer Nature

- Mechanistic insights into direct synthesis of hydrogen peroxide using gold and palladium clusters: a theoretical study.

  Under Preparation

Abstract

The research presented in this thesis addresses one of the grand challenges in catalysis; namely the direct selective oxidation of methane under mild conditions. In nature this process is selectively demonstrated by methane monooxygenase with dioxygen at room temperature, no industrially viable process has yet been discovered. Current utilisation of methane is performed using an energy intensive indirect process of producing syngas (CO + H_2) which is then converted to fuels and value added chemicals. Present approaches for direct conversion include high temperature routes which are characterised by poor oxygenate selectivities, and low temperature routes, which are limited due to limited conversion and non-closed catalytic cycles. The system researched upon in this thesis is based on gold and palladium.

Bimetallic gold-palladium supported nanoparticles were previously shown to be active for methane oxidation at 50 °C with hydrogen peroxide as the oxidant. However, they showed a high consumption of hydrogen peroxide with low productivity. In this thesis investigations are carried out to understand the reasons for the low efficiency of catalysts and verify if unsupported bimetallic gold-palladium colloidal catalysts could be a highly efficient and selective catalyst for the target reaction.

Kinetic and time-on-line analysis showed that methyl hydroperoxide was the primary product of the methane oxidation reaction and methanol, formic acid and carbon dioxide were observed consecutively. Further studies were performed to utilise dioxygen as the oxidant. Insertion of molecular oxygen was confirmed using isotope labelling experiments. It was also revealed that the reaction only occurred in the presence of hydrogen

peroxide. Subsequent work focused on low temperature methane oxidation using hydrogen peroxide and oxygen. Further analysis by varying reaction parameters and reactants showed first order dependence on the pressure of methane and concentration of hydrogen peroxide with zero order dependence on oxygen. Activation energy of the reaction system was calculated to be 39 kJ/mol. Further investigations were also carried into the effects of catalyst preparation where it was revealed that polymer stabilisation is essential since unstabilised colloids showed high decomposition of hydrogen without any significant activity.

Finally Density Functional Theory was used to explore the interactions between gold and palladium nanoparticles with oxygen and hydrogen. 38 atom containing clusters were optimised and oxygen adsorption was studied on square (100) and trigonal (111) facets. Transition state theory was utilised to elucidate reaction mechanism and the active species for synthesis of hydroperoxy species where it was shown that the protic solvent such as water plays a very important role. Synthesis of hydroperoxy species is also considered to be an important step in understanding direct synthesis of hydrogen peroxide, which is an important commodity chemical and a green oxidant used for methane oxidation. Work performed in this thesis has implications in fields of methane oxidation, direct synthesis of hydrogen peroxide and in oxidation catalysis in general.

Contents

1 Introduction

In this chapter basic concepts of catalysis are introduced followed by a discussion of the catalytic system and substrate used in this thesis.

1.1 Introduction to Catalysis

Catalysis is arguably one of the most important advancements in the industrial process in the modern history. It is vital to society in many ways since it is used in the production of important chemical commodities [1]. For example, production of ammonia by Haber-Bosch process which is used in manufacture of fertilisers, uses an iron-based catalyst [2]. Thus it can inarguably be said that catalysis is indirectly responsible for world's food production. Other chemical industries like energy processing, manufacture of bulk and fine chemicals also utilise catalysis and it is often estimated that 90% of all commercially produced chemical products involve catalysts at some stage in the process of their manufacture [1]. With catalysis being so central to almost all aspects of life, catalytic research has gained importance in recent years.

Catalysis can be classified as either homogeneous or heterogeneous. Homogeneous catalysis is where the catalyst is in the same phase as the reactant molecule whereas heterogeneous catalysis is the one where catalyst is not in the same phase as the reactants. Here, typically gases or liquids are adsorbed onto the surface of a solid catalyst. This gives a definition of a catalyst as a substance that increases the rate of a chemical reaction without

itself being consumed in the process and without affecting the overall change in standard Gibbs energy of the reaction [3]. The catalyst can enhance the reaction rate by reducing the activation energy barrier by providing a lower energy pathway for the reaction to take place, as shown in figure 1.1a possibly through several intermediates or transition states.

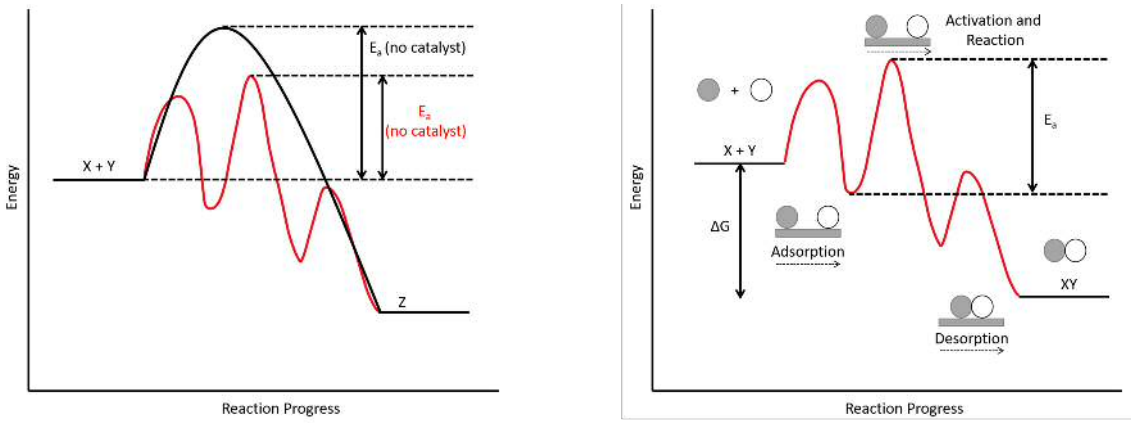

(a) (b)

Figure 1.1: Energy level diagram showing the effect of catalyst for a chemical reaction X + Y to give the product Z where E_a = activation energy and ΔG = change in Gibbs free energy. a) The presence of catalyst shows the lowering of activation energy by providing different reaction pathway. b) Possible elementary steps in a catalysed reaction of X + Y to give Z

As seen from the figure 1.1a, a catalyst does not alter the thermodynamics of a reaction. The overall Gibbs free energy remains same for the catalysed and un-catalysed reactions while only the rate is altered. The catalysed reaction pathway though more energetically favoured, may contain more reaction steps and intermediates than the un-catalysed reaction. Thus dividing the overall catalytic process into a number of elementary steps as shown in figure 1.1b. These steps include adsorption of the reactants either by physisorption or chemisorption, breaking or weakening of bonds to produce and destroy intermediates forming products and finally desorption of the products.

In catalysis, the reaction takes place on the surface of the catalyst. In terms of surface reactions, there are three mechanisms which are presented [4].

- *Langmuir-Hinshelwood mechanism*: The two molecules X and Y both are adsorbed to the surface. While adsorbed to the surface, the X and Y interact and bond, and

then the new molecule Z is desorbed.On the other hand, one molecule can also be adsorbed leading to unimolecular dissociation.

- *Rideal-Eley mechanism*: Of the two molecules X, one of them adsorbs to the surface. The second molecule Y interacts, reacts and binds to X without adsorbing on the surface. The new molecule then desorbs.
- *Precursor mechanism*: Similar to R-E mechanism, one molecule X is adsorbed on the surface. The second molecule Y collides with surface, forming a molecule precursor state. Y then collides with X on the surface, reacting, binding to form the product Z and the new molecule desorbs.

Any surface reaction can be described as following one of these mechanisms or a combination of these. Catalyst provides a surface or active site where the reactants can be brought together for these surface reactions. Thus, the activity of a catalyst scales with the number of active sites. These active sites are usually provided by metals such as gold, platinum, palladium or nickel. To increase the high number of active sites to increase the catalytic activity, these metals are synthesised as nanoparticles usually dispersed on high surface area supports. Small sized nanoparticles usually provide high surface area and increase the number of surface sites present. Choice of support has also been shown to be of importance and is known to affect the activity and selectivity by metal-support interactions [5]. In this thesis, gold and palladium based catalysts are studied for methane oxidation. Following section describes the use and need to upgrade and oxidise methane.

1.2 Methane and Natural Gas

Natural gas is a mixture comprised primarily of gaseous hydrocarbons such as methane, ethane and other higher hydrocarbons in various concentrations. In addition, contaminants like sulphide and nitrogen are also present in the crude mixture. In 2016, natural gas production was estimated to be about 3,613 billion cubic metres and continues to rise annually. It is considered as a versatile fuel and supplies 22% of worldwide energy de-

mand and is expected to grow faster than both oil and coal [6]. It also plays a crucial role as a chemical feedstock for industry, especially for methanol production and has environmental benefits compared to other fossil fuels, by increasing air quality by decreasing greenhouse emissions and volatile organic compound (VOC) [7]. With the recent advancements in the liquefaction and transportation of natural gas, usage as a feedstock has increased drastically over recent years. However, it still remains a widely underutilised feedstock, primarily due to high costs and significant safety concerns associated with it's transportation. About 4% of global production of natural gas is still being flared at the oilfield well-heads because of its inconvenient locations which results in lack of feasible long term options. [8].

Therefore, whilst natural gas is currently used as an energy source, its valorisation to energy-dense liquid derivatives (such as methanol or mid-range hydrocarbons) is highly desirable to increase its utilisation. The composition is primarily methane (up to 0.99 molar fraction), along with higher hydrocarbons such as ethane as shown in table 1.1 [9].

Table 1.1: Typical composition range of natural gas

Compound	Molar fraction
Hydrocarbons	
Methane	0.75 - 0.99
Ethane	0.01 - 0.15
Propane	0.01 - 0.10
n-Butane	0.00 - 0.02
Isobutane	0.00 - 0.01
n-Pentane	0.00 - 0.01
Isopentane	0.00 - 0.01
Hexane	0.00 - 0.01
Heptane plus higher hydrocarbons	0.00 - 0.001
Non-hydrocarbons	
Nitrogen	0.00 - 0.15
Carbon dioxide	0.00 - 0.30
Hydrogen sulfide	0.00 - 0.30
Helium	0.00 - 0.05

Methane is also a significant byproduct of oil refining and chemical processing. Since

methane is one of the main components of natural gas, many approaches are being employed to convert methane to a product (chemical or fuel) that could be easily transported. Since methane has the potential to be a source of carbon for the synthesis of chemical commodities, its transformation is of utmost importance and direct activation of methane has been dubbed as one of the grand challenges for chemists [10].

Current approaches of methane transformation (Figure 1.2) include conversion of methane to methanol or formic acid (either directly or indirectly) via synthesis gas (explained in section 1.3.1), oxidative coupling to higher hydrocarbons and non-oxidative conversion of methane to aromatics such as benzene [11]. Methane to methanol (MTM) process is by far the most attractive among these, since not only is methanol a more energy-dense liquid derivative which aids transportation costs, it is also a highly desirable precursor to a number of commodity chemicals and useful products such as ethylene, dimethyl ether, methyl methacrylate, etc. [12]. In addition, it is also used as a solvent in chemical processing, used itself for production of higher hydrocarbons and gasoline with industrial processes [13, 14] and has also been proposed as a candidate for cleaner and greener fuel [11, 15, 16].

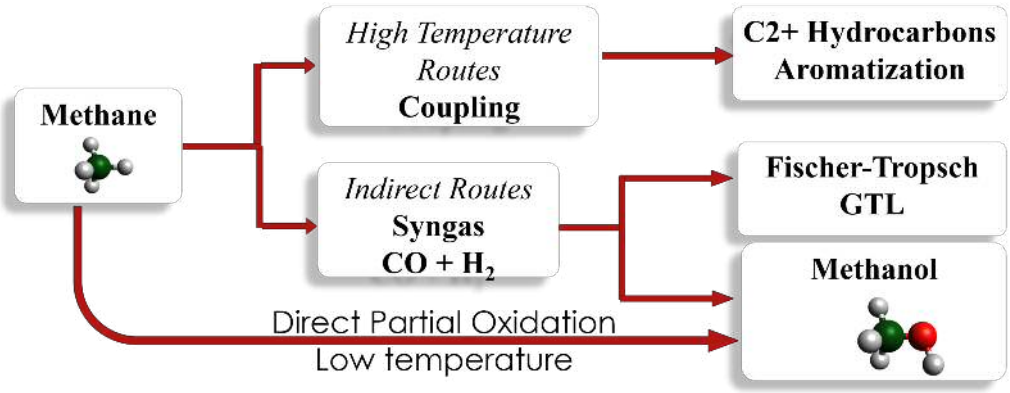

Figure 1.2: Overview of different routes for the valorisation of methane [11].

Thus, while, activation and direct oxidation of methane to methanol is highly desirable, this reaction is highly unfavourable due to spin restrictions of applying triplet O_2 directly

with CH_4 oxidation (equation 1.1).

$$CH_4 + \frac{1}{2}O_2 \rightarrow CH_3OH \tag{1.1}$$

Methane is the least reactive of all hydrocarbons, due to a very high C-H bond strength of 439 kJ/mol [17]. Hence, the oxidation processes are either limited to lower conversion or to lower selectivity with energy-intensive conditions. Deeper oxygenated species (COx) become the major product because the conditions used for methane oxidation also have the undesirable effect of activating the target products, given that C-H bond strength in these species is much lower than methane (373 kJ/mol in the case of methanol [18]). Selective oxidation of methane to value added products requires design of a highly efficient catalytic system and its process development has been an area of research and development for many years [15].

1.3 Routes for Methane Valorisation

As mentioned earlier, there are several approaches that have been used and studied over the years for methane activation and upgrading. This section explores different processes that are being used industrially and academic studies for direct activation and oxidation both at high temperature in the gas phase and low temperature liquid phase methods. Liquid phase activation typically uses mild conditions to increase selectivity but the catalytic cycle is usually not closed in most of these cases.

1.3.1 Industrial Methane Processing

Because of the difficulty of directly oxidising methane, industrial utilisation of methane into useful products is performed at large scale by producing synthesis gas (a mixture of carbon monoxide and hydrogen) which can be further transformed to methanol, or to higher hydrocarbons via Fischer-Tropsch synthesis [16]. Different ratios of CO and H_2

can be achieved based on methane reforming (steam or dry) or partial oxidation reactions. Methane reforming reactions

$$CH_4 + H_2O \rightarrow CO + 3H_2 \tag{1.2}$$

$$CH_4 + CO_2 \rightarrow 2CO + 2H_2 \tag{1.3}$$

are endothermic whereas partial oxidation

$$CH_4 + \frac{1}{2}O_2 \rightarrow CO + 2H_2 \tag{1.4}$$

is slightly exothermic but it requires oxygen which adds the hazards of handling large quantities of undiluted oxygen as well as O_2/CH_4 mixtures. Partial oxidation (equation 1.4) can be seen as a combination of total combustion and reforming which are separated in a process known as auto-thermal reforming [19]. Steam reforming with H_2O (equation 1.2) is a commonly used technique and dry reforming with CO_2 (equation 1.3) is another potential technology but it has not yet reached the efficiency needed to be used industrially. It however continues to be a very attractive option because it utilises two of the major greenhouse gases.

Nickel based catalysts used for methane reforming are operated under energy intensive conditions with high temperatures (850 °C) and moderate pressures (40 bar). This puts limitations on size of reactors due to problems related to heat transfer. The catalyst itself is also prone to deposition of graphitic carbon.

Following the manufacture of synthesis gas (CO + H_2) and some CO_2 which is present due to reforming reactions, methanol synthesis is performed by the following two methods.

$$CO + 2H_2 \rightarrow CH_3OH \tag{1.5}$$

$$CO_2 + 3H_2 \rightarrow CH_3OH + H_2O \tag{1.6}$$

Methanol yield is maximised at temperatures around 250 °C, pressure at 5-10 bar and by adjusting concentrations of CO and CO_2 over Cu-ZnO-Al_2O_3 catalyst with numerous dopants [18]. As a result of process optimisation over decades, high yields and selectivity towards methanol are achieved, but it is clear that this indirect process of methane to methanol process is highly energy intensive due to the very high temperatures and pressures and with high operational costs. Given these disadvantages, direct partial oxidation of methane to methanol at mild conditions is highly desirable and is being researched extensively.

1.4 Methane Oxidation

Conversion of methane to value added products is difficult due to inherent stability and low reactivity of methane. This is further complicated by over-oxidation processes to COx. There is a need to design and develop a catalytic system and process which activates methane and avoids over-oxidation. Due to these difficulties, catalytic conversion of methane to partial oxygenates has been dubbed as the holy-grail of catalysis and has been studied by employing various approaches which are broadly classified into gas phase (usually at high temperatures) and low temperature liquid phase reactions. Despite the difficulties in a highly selective and active process to oxidise methane to methanol at low temperature in an aqueous solution, such a method exists in nature.

1.4.1 Biological Methane Oxidation

Methanotropic micro-organisms have an enzyme called methane monooxygenase (MMO) which catalyses methane oxidation as an initial step in their respiration process (equation 1.7)

$$\mathrm{CH_4 + NADH + H^+ + O_2 \rightarrow CH_3OH + NAD^+ + H_2O} \tag{1.7}$$

The two major forms are membrane-bound particulate (pMMO) and soluble (sMMO), the former being more common. But due to difficulties in isolation and purification, sMMO variations from *Methylococcus capsulates* (Bath) have been well characterised and studied [20]. Studies have also demonstrated the non-specificity of MMO enzyme which efficiently oxidises a wide range of aliphatic and aromatic hydrocarbons, it is also an efficient catalyst for methane to methanol oxidation selectively without forming formic acid or other over-oxidation products [21]. The productivity of sMMO for methane oxidation with molecular oxygen was found to be 5.05 $\text{moles}_{(\text{methanol})}\text{kg}^{-1}_{(\text{protein})}\text{h}^{-1}$.

Primary active sites have been identified as a binuclear iron μ-oxo species as shown in figure 1.3 [22]. These binuclear Fe sites are responsible for the reductive activation of O_2 with an NADH co-factor [22] and during the redox cycle, it is considered that each Fe centre varies between +2 and +4 oxidation states leading to the formation of high-valent ferryl ion ($[FeO]^{2+}$). It is also believed that this provides the driving force towards the hydroxylation of non-activated C-H bond.

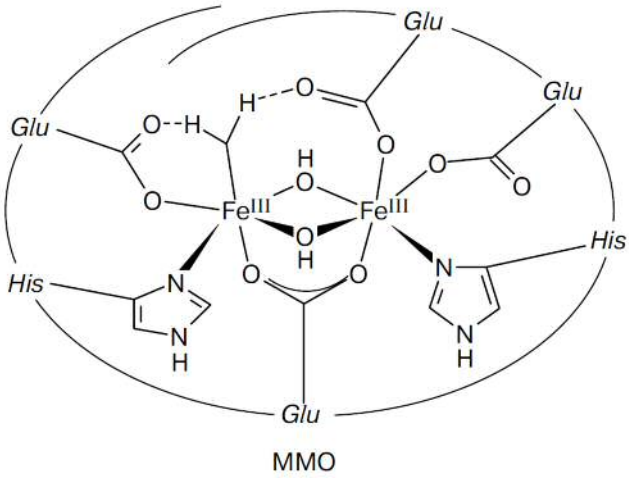

Figure 1.3: Active centre containing a di-iron μ-oxo sites in methane monooxygenase enzyme taken from reference [22].

Methyl monooxygenase enzyme with active sites other than Fe metal have also been recently studied. Although, not completely understood, the active site in pMMO is considered to contain copper as opposed to sMMO [20]. These biological systems are unlikely to be used industrially due to high costs associated with isolation and purification of these

enzymes. Additionally, enzymatic systems are also prone to deactivation with temperature, pressure and concentration fluctuations and hence have a limited working range. But these enzymes have provide insights into development of synthetic catalysts.

1.4.2 Gas Phase Oxidative Routes

Typical gas phase oxidation reactions are carried out with air, molecular oxygen and nitrous oxide as oxidants at high temperatures. High temperature oxidation systems generally involve complex radical pathways which also leads to side coupling products and over-oxidation products limiting selectivity and yield of primary products [23]. By varying reaction parameters and reactor design, moderate selectivity to methanol could be achieved at higher temperatures (450-600 °C) and moderate pressures (30-60 bar) [24]. By tuning the methane partial pressure, radical concentration can be tuned to reduce competition with coupling reactions; but generally, major gas phase oxygenates produced are formaldehyde rather than methanol [25]. O_2 is used as the oxidant in these cases which oxidises the methoxy radical ($CH_3O\cdot$) species before protonation to produce CH_3OH. This leads to over-oxidation to CO_2 leading to lower selectivity.

In order to mimic the methane monooxygenase enzymatic systems (explained in subsection 1.4.1), heterogeneous catalysts were developed based on zeolite systems. Zeolites are microporous, crystalline aluminosilicates which can accommodate a wide variety of cations. They are composed of SiO_4 and AlO_4^- tetrahedra which are connected by bridging oxygen atoms. The extra-framework cations balance the negative charge of the AlO_4^- tetrahedra and are exchangeable which gives rise to a diverse chemistry associated with zeolites [26]. Some example of zeolites used for methane oxidation are MFI type zeolites such as Fe-Cu-ZSM-5, TS-1; chabasite, modernite etc. The composition of zeolites can be manipulated to modify levels of Brønsted acidity with H^+ as the counter-cation and Lewis acidity through dealumination of the zeolite framework. This gives a huge advantage in tuning the activity and selectivity of zeolite based catalyst. Zeolites are arranged into a 3-dimensional system of pores and cavities with dimensions varying from 3 Å- 14 Åand

this pore specificity based on type of zeolite makes them highly shape-selective catalysts tuning substrate and product selectivity [27]. These porous cavities also demonstrate confinement effect changing the contact time between different substrates and catalytic active sites.

Cyclic gas-phase oxidation of CH_4 with metal-exchanged zeolite catalysts with O_2, N_2O, or H_2O has been studied at high temperatures (150-500 °C) to activate the oxidant and desorb the CH_3OH produced. Panov *et al.* showed that methane could be oxidised with Fe-ZSM-5 to methanol using N_2O as an oxidant [28]. N_2O decomposition creates an anion-radical species which is an active species for oxidation of methane. The problem with the system is a lack of a complete catalytic cycle because it needs an additional step to extract the formed methanol typically by steaming or washing the zeolite. Addition of water into feed-stream showed an increase in methanol selectivity from 1.9% to 16% [29, 30]. But the same Fe-ZSM-5 system with molecular O_2 led to total combustion products [31]. Bimetallic Fe and Cu modified ZSM-5 catalyst was also found to be effective for this reaction using H_2O_2 under continuous flow conditions [32]. A methanol selectivity of 92% was observed at 0.5% conversion (0.46% yield). Oxidants like H_2O_2 or N_2O lead to higher conversion compared to O_2. Instead of Fe, Cu containing ZSM-5 and mordernite (MOR) have also been studied inspired by sMMO systems [33]. Recently, an isothermal catalytic cycle was reported to convert methane to methanol over Cu-modernite at 200 °C with molecular O_2 [34]. In this process, the catalyst was first activated with O_2 followed by reaction with methane and methanol was extracted using steam. The active site was then re-activated for further oxidation cycles. A methanol yield of 56.2 μmolg^{-1} was observed after 13 hours of O_2 activation followed by reaction at methane pressure of 37 bar. Instead of a sequential process, continuous production of methanol from methane, oxygen and water was achieved with Cu modified zeolites by tuning the process conditions [35]. In this, case 1.81 μmolh^{-1}g$_{cat}{}^{-1}$ of methanol was obtained with 0.981 bar of CH_4. Catalyst was pre-treated with O_2 at 550 °C for 5 hours. Cu containing modernite zeolites (CuMOR) were also utilised for methane conversion to methanol using water. Sushkevich *et al.* recently reported anaerobic direct oxidation by using water both as a

solvent and an oxidant with a high methanol selectivity of 97% [36]. Water molecules not only acted as a cheap and abundant source of oxygen but also regenerated the active sites. It also facilitated desorption of the product and stabilisation of the reaction intermediates. Figure 1.4 shows the reaction process of partial oxidation of methane using water along with the schematic representation of CuMOR catalyst used.

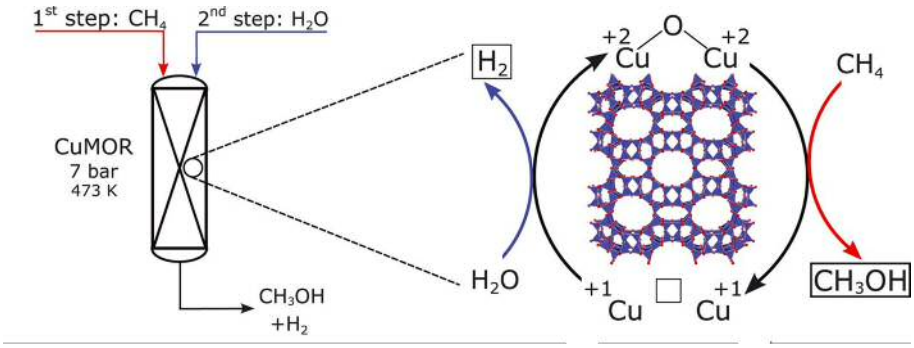

Figure 1.4: Schematic representation of methane oxidation with water using CuMOR taken from ref [36].

The activation of the catalyst was performed at 400 °C which was followed by the reaction with 7 bar of methane and then water at 200 °C. A consistent production of 0.2 mol of CH_3OH was observed per mol of copper. The mechanism involving reduction of dicopper sites of modernite providing two electrons to oxidise methane to methanol was presented. Subsequent reduction of water with concurrent formation of hydrogen returns the two electrons for rejuvenation of the mono(μ-oxo)dicopper active core.

1.4.3 Liquid Phase Oxidation

Gas phase and high temperature processes have limited methanol yield due to lower methanol stability and hence decreased selectivity on higher conversions. Compared to previously discussed gas phase oxidation, liquid phase approaches use milder conditions to avoid over-oxidation of methanol to COx. A lot of catalyst developments in low temperature approaches was inspired by nature.

Electrophilic activation of methane

Earlier methane oxidation approaches were based on work pioneered by Shilov and co-workers on electrophilic activation by oxidation-tolerant complexes [37]. They showed that both methanol (and methyl chloride) can be obtained as shown in equation 1.8 in a Cl^- containing aqueous medium at 120 °C with a Pt catalytic system [37–39] using water as the source of oxygen.

$$\mathrm{R{-}H} + [\mathrm{PtCl_6}]^{2-} \xrightarrow[\mathrm{H_2O/120\,^\circ C}]{\text{cat. } [\mathrm{PtCl_6}]^{2-}} \mathrm{R{-}OH} + \mathrm{R{-}Cl} + \mathrm{PtCl_4}^{2-} + 2\mathrm{HCl} \qquad (1.8)$$

The reaction (Equation 1.8) is catalytic in Pt(II) but requires Pt(IV) in stoichiometric amounts which makes it not feasible on any large scale, but it demonstrated the possibility of catalytic oxidation of methane via activation of C-H bond with late transition metals with the general scheme as shown in figure 1.5.

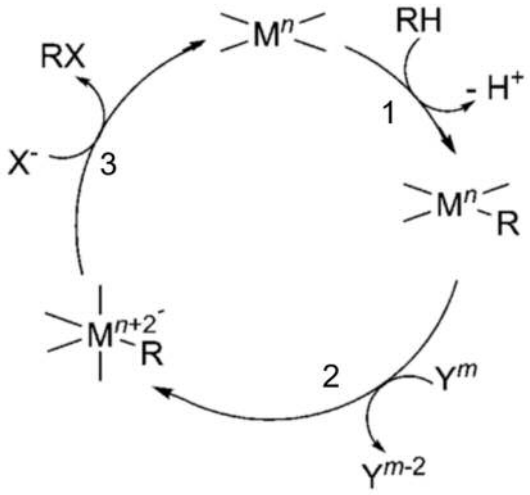

Figure 1.5: Reaction cycle for electrophilic activation of C-H bond as seen in Shilov systems taken from ref [37].

The first step in Shilov type catalytic system is the activation of methane by formation of methyl-Pt complex. Next, $[PtCl_6]^{2-}$ oxidises the complex by electron donation, making it susceptible to nucleophilic attack by water (or chlorine) at C-Pt bond liberating CH_3OH (or CH_3Cl) and HCl [39]. Along with the stoichiometric use of $[PtCl_6]^{2-}$, the catalytic

species are also not very stable in solution due to formation of metallic platinum, since the redox potential for Pt(II)-Pt(0) couple is very close to redox potential for Pt(IV)-Pt(II) couple. Understanding the proposed Shilov mechanism (figure 1.5) was crucial in understanding electrophilic activation of methane and led to development of various liquid phase catalysts. Periana *et al.* later showed that $[PtCl_6]^{2-}$ can be replaced by conc. H_2SO_4 as an oxidant *i.e.* using S in +6 oxidation state as highly oxidising species [40]. A homogeneous Hg(II) based catalyst was also employed. The reaction carried out at 180 °C and produced methyl bisulphate (CH_3OSO_3H) from methane and water and sulphur dioxide from H_2SO_4 [40].

$$CH_4 + 2H_2SO_4 \rightarrow CH_3OSO_3H + SO_2 + 2H_2O \tag{1.9}$$

Though at 50% conversion, 85% selectivity to CH_3OSO_3H was achieved (eqn. 1.9), this product had to be separately hydrolyzed to generate methanol as shown in scheme 1.10 giving a total yield of 43%.

$$CH_3OSO_3H + H_2O \rightarrow CH_3OH + H_2SO_4 \tag{1.10}$$

An advantage of bisulphate moiety is product protection from over-oxidation. Due to electron withdrawing nature of this group, there is a decrease in electron density on the primary carbon making it two orders of magnitude less susceptible to over-oxidation [40]. But as shown in equation 1.11, the process is also limited by re-oxidation of SO_2 which limits it's application industrially.

$$SO_2 + 0.5O_2 + H_2O \rightarrow H_2SO_4 \tag{1.11}$$

As the reaction is not fully efficient, dil H_2SO_4 is steadily produced and a fully closed catalytic cycle is not achieved. This remains a limitation for liquid phase oxidation even if there is site separation between methane oxidation and oxidant regeneration [11]. The overall equation represented in scheme 1.12 shows a partial methane oxidation to

methanol using O_2 but the oxidant used is concentrated H_2SO_4.

$$\text{Net:} CH_4 + 0.5O_2 \rightarrow CH_3OH \tag{1.12}$$

This process was later improved upon by the same researchers who substituted the mercuric catalyst by bipyramidal bis(2,2'-bipirimidine)Pt(II)Cl_2 complex as shown in figure 1.6a [41]. This turned out to be a better system with 90% conversion of methane at a selectivity of 81% to methyl bisulfate and is used as a benchmark to compare catalyst efficiency. Similar to the mechanism proposed by Shilov, the electrophilic Pt(II)-CH_3 intermediate was proposed as shown in figure 1.6b. Similarly thallium, palladium, and the cations of gold were also used to oxidise methane to methanol.

(a) (b)

Figure 1.6: Pt based Periana catalyst a) Structure of the bipyramidal catalyst and b) Pt(II)-CH_3 intermediate where OP is the oxidising ligand, in this case Cl or HSO_4 [41].

Pd(II) was shown to activate methane in similar manner but the yield was limited due to formation of Pd(0) [42, 43]. This was overcome by Kalucki and co-workers by using metallic palladium in fuming sulphuric acid. Fuming sulphuric acid contains free sulphur trioxide which is a stronger oxidant and as a result of which, Pd(0) was oxidised to Pd(II) and was used to activate methane as shown in scheme 1.7 [44]. The metal itself could be recovered and reused for multiple reactions and showed higher activity with higher SO_3 content.

Similarly, Jones *et. al.* used cationic gold as an efficient electrophilic catalyst but even in strong acidic media such as triflic or sulphuric acid, there was irreversible formation of metallic gold after only one cycle, which led to only stoichiometric reaction and a

turnover of < 1% [45]. Au(III) species were found to be essential for the reaction as metallic Au showed no activity. Selenic acid with Se(VI) was used as the oxidising agent since it is more powerful compared to S(VI). It is almost as acidic as sulphuric acid and could stabilise the Au(III) cationic species. The reaction was then catalytic with turnover numbers of up to 30. [45].

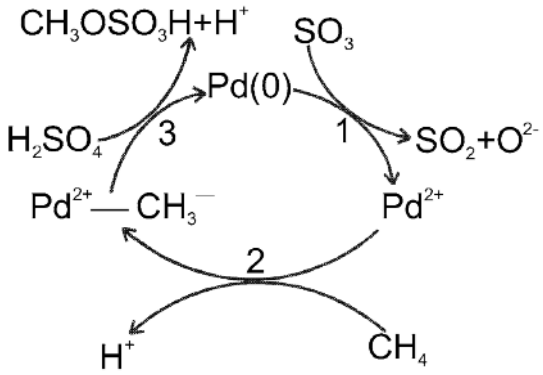

Figure 1.7: Reaction cycle for electrophilic activation of C-H bond as seen in Shilov systems adapted from ref [37].

In addition to concentrated H_2SO_4 and oleum, and stronger acids such as SO_3 and $HSeO_4$, Pd based catalysts along with other transition metals have also been studied in trifluoroacetic acid systems to activate methane. Sen and co-workers showed that peroxytrifluoroacetic acid which was generated from hydrogen peroxide and trifluoroacetic acid anhydride can oxidise methane to methyl trifluoroacetate (CF_3COOCH_3) and this reaction is catalysed by Pd(II) [46]. Park *et al.* reported the oxidation of methane to a mixture of CF_3COOCH_3 and CH_3OOH over a C-supported Pd heterogeneous catalyst in the presence of $Cu(CH_3COO)_2$ additive [47, 48]. In these cases, trifluoroacetic acid acts as the solvent and as a protecting group for methanol and H_2O_2 could also be synthesised *in situ* through the reaction between H_2 and O_2 [47]. Vargaftic *et. al.* also proposed methane activation using Co(III) based catalysts in trifluoroacetic acid at 180 °C which produced methyl trifluoroacetate [49]. The reaction was stoichiometric due to conversion to Co(II). The reaction was rendered catalytic in presence of O_2 which regenerated the catalytic Co(III) species. H_2O_2 is favoured as an oxidant because of its high oxygen content and benign nature of its by-product *i.e.* water, but the low yield and high cost of H_2O_2 limits industrial viability.

Despite the efficacy of the C-H activation approach discussed above and the high methane selectivities observed for methanol derivatives with H_2SO_4 and CF_3COOH, these processes have limited applicability due to the corrosive solvent and nature of oxidants required to achieve the catalytic cycle. There are high environmental concerns and these solvents also create hurdles for safety and process engineering. Moreover, the most of the above mentioned are homogeneous catalytic systems which brings disadvantages for an industrial process with downstream processing and product separation. To overcome this, the Periana Pt based catalyst was heterogenised by Palkovitz *et al.* by using a polymer framework based on covalent triazene framework (CTF) [50] as shown in the figure 1.8. This CTF moiety was connected to the bipyramidal Pt species and it required concentrated sulfuric acid according to the conditions described by Periana *et al.* [41].

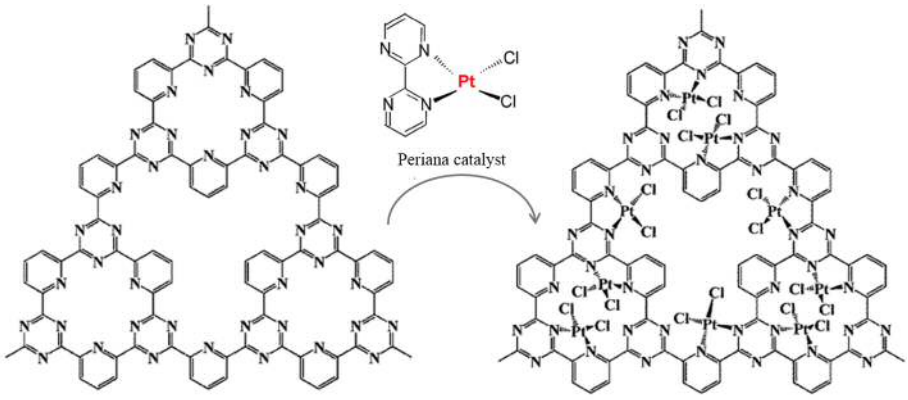

Figure 1.8: CTF-moiety based heterogeneous system for Periana's Pt based catalyst adapted from ref [50].

Next development in catalytic systems was driven by the replacement of harsh protic solvents and oxidants with more benign solvents and oxidants. Methane activation was observed in acetonitrile solution in the presence of $[NBu_4]VO_3$-pyrazine-2-carboxylic acid and H_2O_2 as the promoter in the presence of air by Shulpin and co-workers [51]. Different Fe(III) complexes were also investigated for methane oxidation by the same group [52]. Pyrazine-2-carboxylic acid was shown to have a positive effect on the catalytic activity which was attributed to the formation of ferryl ion [52]. In contrast to the previous Shilov type electrophilic activation, formation of hydroxyl and hydroperoxy radical species was considered as the mechanism for these processes formed due to the interaction with H_2O_2.

An aqueous-phase approach was reported by Yuan *et al.* in which a number of transition metal chloride catalysts like $OsCl_3$ and $HAuCl_4$ were studied for selective oxidation of methane and ethane, which again was showed radical based mechanism [53].

Zeolites for methane oxidation

Several catalysts have been developed with bio-mimetic approaches considering iron based active sites at low temperature using milder conditions such as aqueous systems and benign oxidants. One of the notable example was demonstrated by use of metal-phthalocyanine complexes of Fe and Cu encapsulated within zeolites [54]. Raja and Ratnasamy successfully catalysed methane to a mixture of methanol and formaldehyde at ambient and sub-ambient (0 °C) in liquid phase with O_2/TBHP (tert-butyl hydroperoxide) oxidant mixtures [54]. Though they obtained very low over-oxidation to CO_2, a maximum 2% was obtained within 12 hours with Fe-phthalocyanine encapsulated within zeolite X in acetonitrile. Significant activity was only obtained in chemically reactive organic solvents while a much lower activity of the same catalyst was obtained in water. Further research was carried out by Sorokin et al. with SiO_2 supported metal-phthalocyanine complexes [55, 56]. H_2O_2 was used as the oxidant and reaction was carried out at ambient temperature forming methanol, formaldehyde and formic acid. A μ-nitrido iron phthalocyanine complex grafted on silica was also investigated for methane oxidation with H_2O_2 in water and was found to be unstable during reaction conditions [57]. Un-modified silica support was also found to be active and moreover, Fe/SiO_2 was found to have similar activity as Fe-phthalocyanine grafted on silica with high selectivities and much higher stability suggesting a Fenton type chemistry.

Other catalysts containing iron and copper have also been investigated for methane oxidation inspired by monooxygenase enzyme. Most notably, zeolites have gained a lot of attention in this field. As discussed earlier, zeolites have been employed gas phase methane oxidation with N_2O and O_2. But gas phase methane oxidation leads to lower selectivities due to methane over-oxidation. Liquid phase methane oxidation with zeo-

lites has also been studied extensively. The most notable example of this is ZSM-5 based catalysts [32, 58]. H-ZSM-5 (30) which has been calcined at high temperatures (550 °C) was found to be active for methane oxidation with H_2O_2, achieving a conversion of 0.3 % with a selectivity of 95 % to oxygenated products. Elemental analysis carried out on the samples showed trace amount of iron present in the framework. With addition of extra-framework iron, there was an increase in the catalytic activity which resulted in a methane conversion of 0.7 %, still maintaining a high selectivity of methane and limited selectivity to deep oxidation products *i.e.* CO_2 following the oxidative pathway shown in scheme in figure 1.9.

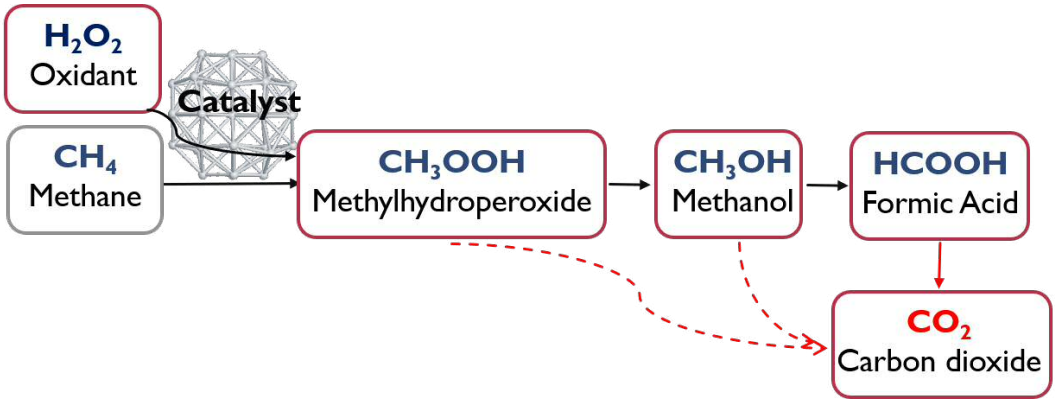

Figure 1.9: Proposed reaction scheme for selective oxidation of methane using ZSM-5 (30) with H_2O_2 [59].

Methylhydroperoxide is proposed to be the primary reaction product which can undergo selective conversion to methanol or non-selective conversion to formic acid. Formic acid and carbon dioxide are consecutive over-oxidation products of methanol. With 2.5% of Fe loading in Fe/ZSM-5 (30) catalyst, the major products found were formic acid (72 %), methanol (10 %), methylhydroperoxide (1 %) and total oxidation product *i.e.* CO_2 (17 %) [59]. With addition of extra-framework or homogeneous Cu^{+2} in addition to iron, a change in selectivity was noticed towards methanol as the major product (85 %) which occurred by shutting off the methanol to formic acid transformation. EPR studies showed Cu^{+2} acting as a scavenger of ·OH which was shown to play a role in the over-oxidation of methanol to formic acid and CO_2 [59]. Though, the Fe-Cu/ZSM-5 catalyst showed similarity to iron and copper based methane monooxygenase enzymatic catalyst, it showed no catalytic activity with molecular oxygen limiting its commercial significance.

Recently, mononuclear rhodium (Rh) species anchored on ZSM-5 catalyst was reported to catalyse the direct conversion of methane to methanol and acetic acid, using oxygen and carbon monoxide under mild conditions [60]. The acidity of the zeolite has been reported to promote the selectivity of Cu-ZSM-5 catalysts for acetic acid and a high methanol selectivity was achieved using Na-ZSM-5. The reaction was carried out in batch reactor where catalysts were suspended in water. Methane pressure of 20 bar and CO pressure of 5 bar was used. O_2 pressure was varied to vary the product selectivity. Upon optimisation of the reaction, a yield of 22,000 μmoles of acetic acid per gram of catalyst or 230 μmoles of methanol per gram of catalyst can be formed in three hours with selectivities of 60 % and 100 % respectively at 150 °C [60]. It was hypothesised that isolated Rh^+ cations facilitated activation of methane with O_2 to form Rh-CH_3 species. Rh-OCH_3 species were then observed in presence of CO suggesting role of CO as co-catalyst. It was also involved in regeneration of Rh-ZSM-5 catalysts. Single atom Rh/ZrO_2 catalysts were also recently investigated for methane oxidation to methanol at mild aqueous conditions at 70 °C in liquid phase and to ethane with O_2 in gas phase at 300 °C [61].

Zeolites have proved to be an important class of heterogeneous catalysts and are being studied extensively for methane oxidation. They have been found to be active for methane oxidation at mild conditions using environmentally favourable oxidants like H_2O_2 and benign solvents like water. However, use of H_2O_2 is not economically viable and industrially favourable since the cost of H_2O_2 is too great in comparison to the value of the product, methanol. Use of molecular oxygen which is not only environmentally benign but also readily available and inexpensive is required which has not been reported in many cases.

1.5 Gold-Palladium Catalysis

Gold was regarded as a poor catalyst due to its inertness in bulk form but catalysis by gold has gained a lot of attention in the past few decades since Haruta's discovery of gold being an excellent catalyst for CO oxidation in 1985 [62] and Hutchings' prediction of

gold being an excellent catalyst for acetylene hydrochlorination [63]. The latter has also led to commercialisation of gold supported on activated carbon, as an active catalyst for acetylene hydrochlorination to synthesise vinyl chloride monomer [64]. Since then, there has been a rapid increase in use and study of different gold based catalysts for various reactions.

The productivity of a gold catalysed reaction has been modified in certain reactions by adding a second metal or sometimes even a third metal component to synthesise bimetallic or trimetallic catalysts [65–67]. In many cases, palladium has been found to have an enhancing effect on the activity of the gold nanoparticles since gold and palladium show a synergistic effect towards many substrates [68, 69]. Palladium itself has been used in oxidation chemistry for many relevant industrial reactions such as the Wacker process for the oxidation of ethylene to acetaldehyde [70]. The 2010 Nobel prize in Chemistry was awarded for palladium catalysed cross coupling reactions in organic synthesis [71]. Hutchings and co-workers have previously shown that supported Au-Pd nanoparticles are highly effective catalysts for the direct synthesis of H_2O_2 [72], the oxidation of alcohols like benzyl alcohol [73],and the oxidation of primary C-H bonds in toluene [74]. Some of the examples of gold, palladium and gold-palladium bimetallic catalysis has been described in sections below with particular emphasis on direct synthesis of H_2O_2 and methane oxidation.

1.5.1 Synthesis of Hydrogen Peroxide

Hydrogen peroxide (H_2O_2) is widely used as environmentally friendly oxidant in various processes such as bleaching agents or disinfectant. Currently, H_2O_2 is commercially produced through sequential hydrogenation and oxidation of alkyl anthraquinone to produce a diol using a nickel and palladium catalyst [75]. This process is only viable at a large scale, and so entails the hazardous storage and transportation of the concentrated H_2O_2 solutions whereas only small quantities are required for the much finer chemical industry. Moreover, H_2O_2 synthesis route involves an expensive solvent system and loss of

anthraquinone, all of which point to a need for a direct, green and atom efficient process.

An alternative process is direct synthesis of H_2O_2 with hydrogen and oxygen. Though this simple concept is highly atom efficient, it comes with its own set of challenges mainly due to formation of water either by combustion or hydrogenation reaction as shown in Figure 1.10 [67]. In addition, stability of H_2O_2 is also an issue. It can easily undergo decomposition to form water and all these side reactions can be catalysed by the catalyst active for direct synthesis of H_2O_2. Furthermore, the efficiency of the reaction is limited by mixing of H_2 and O_2 creating inherently hazardous mixtures. Therefore, only low concentrations of H_2 can be employed, thus limiting the H_2O_2 yield [76].

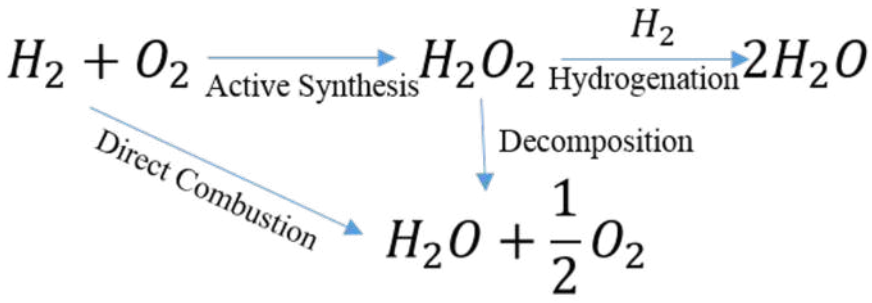

Figure 1.10: Reaction scheme for direct synthesis of H_2O_2 showing side decomposition and hydrogenation pathways [67].

Initial catalytic developments for catalytic synthesis was based on Pd based catalysts [77]. Though they were found to be active, additives like halides and acids were required to attain high activity and selectivity which is undesirable for upscale of processes [78]. Gold based catalysts were also reported to be active for direct synthesis of H_2O_2. Earlier studies were based on Au supported on oxide based supports such as alumina and silica [79, 80]. A high activity dependence on support and particle size was observed. Edwards *et al.* reported higher H_2O_2 productivity for larger Au nanoparticles supported on TiO_2 prepared by the impregnation rather than smaller particle size formed by deposition-precipitation [69, 73]. Increase in rates of H_2O_2 formation along with higher H_2 selectivity was observed by alloying Pd with Au showing high synergistic effect between the two metals. Even with small sized Au-Pd nanoparticles synthesised with sol-immobilisation, much higher activity was observed compared to monometallic Au or Pd. This high activity

was also observed with 80 % lower metal loading [72]. Even with this bimetallic synergy, side-reactions leading to lower selectivity could not be switched off leading to lower yields.

Various parameters were considered and tested to switch off hydrogenation and decomposition reactions to improve H_2 selectivity and H_2O_2 yields. Reaction conditions such as temperature, pressure, H_2/O_2 ratios and solvent were found to play an important role [81] towards H_2O_2 productivity, but at the same time, catalyst preparation and pre-treatment were studied to be able to use more industrially favourable reaction conditions and solvents [82]. Calcination steps were designed and used to increase catalytic stability and to avoid leaching. Pre-treatment of support with acid was also tested and it was found to be switching off hydrogenation reactions thereby increasing total productivities [83]. Other metals such as Pt were added to Au-Pd bimetallic system to increase the activity and efficiency of the reaction [84]. With these developments in catalytic systems, it is possible to synthesise H_2O_2 in solvents like water without acid or halide additives which opens up many suitable applications for these processes like greywater cleaning, medical applications which utilise very clean hydrogen peroxide and in fine chemicals which require clean oxidant.

1.5.2 Activation of Primary C-H Bond

Selective oxidation of the primary C-H bond in aliphatic saturated hydrocarbons such as cyclohexane to their corresponding alcohols, alkenes such as cyclohexene, and aromatic compounds like toluene is significant not only for the synthesis of high-tonnage commodities and agrochemicals, high-value fine chemicals and pharmaceuticals but it also opens up a route to activate and exploit abundant feedstock materials such as natural gas. However; the oxidation processes are usually inefficient from a chemical perspective. At present the commercial processes for cyclohexane oxidation are carried out in air or molecular oxygen at 150-160 °C and 1-2 MPa but these still have about a 4 % conversion with 70-80 % selectivity [85]. And oxidation of cyclohexane to the cyclohexanol and

cyclohexanone gives important intermediates for production of adipic acid and carprolactum which are further processed to produce Nylon-6 and Nylon-6,6. Thus, a lot of C-H activation studies have been performed with cyclohexane as a trial substrate. Several cobalt, manganese and metal substituted aluminosilicate zeolites [86] and aluminophosphates [54, 87] have been used to improve catalytic activity, but many of these systems suffer leaching or not show no appreciable increases in efficiency. Compared to Co, Mn and Fe as the active metal, Au based catalytic systems were also tested and studied. One of the initial systems studied was the Au/ZSM-5 catalyst which successfully oxidised cyclohexane with a 16 % conversion and 92 % selectivity in a solvent free system using oxygen at the oxidant [88]. The catalyst could be recycled without any appreciable loss of activity. Other supports such as mesoporous silica such as SBA and MCM-41 supported Au catalysts were also studied for solvent-free aerobic selective oxidation of cyclohexane [89, 90]. Use of mesoporous supports gave comparable activity and easier product diffusion from active sites makes large-scale processing feasible.

Similarly, selective oxidation of toluene has been widely studied. A range of valuable oxygenate compounds like benzyl alcohol, benzaldehyde, benzoic acid and benzyl benzoate (Figure 1.11) could be produced by this process which have a commercial value for many industrial applications. For example, benzaldehyde is an industrially important aromatic aldehyde and used as raw material for pharmaceutical drugs like ampicillin. Current industrial processes of producing benzaldehyde include hydrolysis of benzyl chloride or the air-oxidation of toluene [91]. The former involves chlorination of toluene making it environmentally unfavourable. Thus, air-oxidation of toluene, both in the gas and liquid phase is the widely used industrial method which requires high temperatures and pressures yielding low amounts of benzaldehyde [74]. The use of catalysts based on Cu, Mn, Co and Cr have been investigated but all of these have low turnover numbers and work at temperatures of around 200 °C. Many reports have shown higher activities using initiators and co-oxidants like H_2O_2 and TBHP which limits the industrial applicability.

Alloyed Au-Pd supported nanoparticles were demonstrated to be active for the oxida-

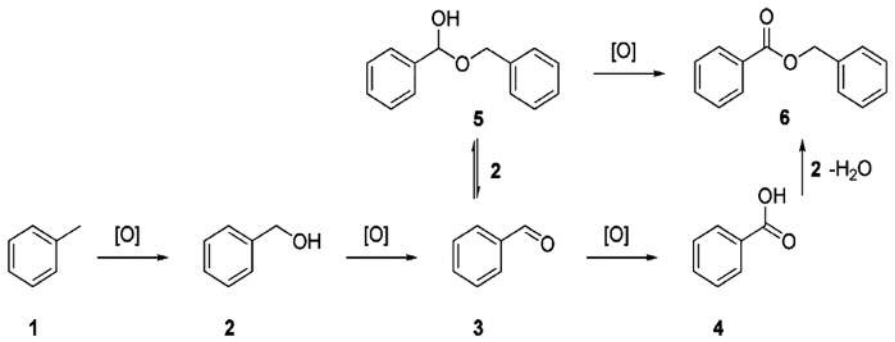

Figure 1.11: Reaction scheme for oxidation of toluene (1) leading to benzyl alcohol (2), benzaldehyde (3), benzoic acid (4), hemi-acetal (5) and benzyl benzoate (6) as shown in reference [74].

tion of primary C-H bonds in toluene under solvent-free conditions using O_2 at 160 °C [74]. A synergy between Au and Pd was observed with catalytic conversion of 5.3 % whereas monometallic catalysts achieved a conversion of 0.2 % with Au and 1.6 % with Pd. The activity of catalysts prepared by impregnation was minimal compared to sol-immobilisation, which produces narrower size distribution with smaller size particles and far greater activity. Conversions as high as 94 % with no CO_2 as over-oxidation product was achieved over long reaction times. Oxidation of toluene under the milder conditions (80 °C) have also been achieved using TBHP as an oxidant with Au-Pd/TiO_2 [92]. The ability of Au-Pd/TiO_2 to selectively oxidise toluene was the proof of concept to test methane oxidation with these nanoparticles since it is considered that these reactions are linked by the formation of a hydroperoxy intermediate from O_2 [92]. The formation of hydroperoxy intermediate was found to be active for methane oxidation formed using H_2O_2 [93].

1.5.3 Methane Oxidation

The efficacy of supported Au-Pd nanoparticles for catalytic activity for alcohol oxidation, primary C-H bond activation and direct synthesis of H_2O_2 led to the investigation of these nanoparticles for methane oxidation with H_2O_2 as the source of oxygen. 5 wt% Au-Pd/TiO_2 catalysts prepared by impregnation were found to be active for methane oxidation at low temperatures of 50 °C with H_2O_2 as the oxidant in aqueous conditions with

high oxygenate selectivity (90%) although low productivity (0.28 $moles_{(products)}kg^{-1}_{(cat)}h^{-1}$) [93]. Reactions were also performed with only O_2 as the oxidant but no oxygenated products were obtained in that case. Methylhydroperoxide was found to be the primary product following the reaction scheme shown in Figure 1.9 which can be converted to methanol. Oxidation of both methylhydroperoxide and methanol led to formic acid and carbon dioxide was the total oxidation product detected.

Since Au-Pd/TiO_2 catalyst prepared by impregnation was shown to be active for direct synthesis of H_2O_2, it was proposed that hydroperoxy species can be formed *in-situ* from gaseous H_2 and O_2 to oxidise methane. Thus methane oxidation was carried out under a mixture of CH_4, H_2 and O_2 diluted with N_2 to avoid flammable mixtures. Similar productivity with a higher methanol selectivity (68 % compared to 49 % in earlier case) was observed when using the *in-situ* generated H_2O_2 [93]. Au-Pd/TiO_2 catalysts prepared by sol immobilisation were also tested for the reaction. Though they were also active, the activity was five times lower than that of catalysts prepared by impregnation. This was probably due to high rates of H_2O_2 decomposition associated with nanoparticles formed by sol immobilisation. On increasing the metal loading, a similar effect in increasing H_2O_2 decomposition without an increase in methane oxidation activity was observed. But on varying the metal composition, a synergistic effect was also observed in this case. An equivalent monometallic Au catalyst displayed much lower activity. On adding Pd, there was an increase observed in activity, methanol selectivity but also in H_2O_2 consumption [94]. The highest activity was observed in 1:1 molar ratio which is used in this thesis for further studies. Stabiliser-free sol-immobilisation Au-Pd/TiO_2 catalysts were also investigated to understand and improve upon as-prepared catalysts which show low catalytic activity along with higher H_2O_2 consumption rates [95]. Heat treatments by high temperature calcinations to modify nanoparticle sizes and rutile-anatase TiO_2 supports were studied to maximise the efficiency and performance of the resulting catalysts.

Following from the methane oxidation activity of bimetallic Au-Pd catalysts, trimetallic Au-Pd-Cu catalysts supported on TiO_2 were investigated for low temperature selective

oxidation of methane with H_2O_2 at 50 6°C [65]. The rate of methane oxidation for these Au-Pd-Cu/TiO_2 was found to be enhanced by a factor of 5 with high oxygenate selectivity of more than 95 %. These catalysts were prepared by impregnation and characterisation showed that Au and Pd alloy in an Au-core-Pd-shell structure whilst Cu was highly dispersed as reduced species as Cu or Cu_2O [65, 93]. Though the productivity and gain factor (moles of oxygenates produced per mole of H_2O_2 consumed) of the methane oxidation reaction with commercial H_2O_2, there was a decrease in the rate of methane oxidation with H_2O_2 generated *in-situ* from H_2 and O_2. This decrease in the methane oxidation activity was attributed to lower H_2O_2 synthesis rates along with Cu-catalysed H_2O_2 conversion reactions which was higher than oxidation reaction.

1.6 Catalysis using Unsupported Nanoparticles

As seen in the previous section, although the catalytic properties of supported gold, palladium and gold-palladium nanoparticles are of much interest, their origin of this catalytic activity is still not fully understood. It was assumed that most of the catalytic activity of the supported nanoparticles was due to the influence of the support and there was a misconception that the activity of colloidal nanoparticles is negligible without the cooperation of the support. Thus, colloidal nanoparticles have been extensively studied to show their intrinsic catalytic activity and to elucidate the catalytic mechanism for hydrogenation, oxidation, coupling reactions etc. [96]. These nanoparticles mimic the metal surface activation and catalysis at the nanoscale typically observed in heterogeneous catalysis but also are soluble in classic solvents (unlike solid catalysts) and can be used as catalysts in homogeneous systems. Thus, nanoparticle catalysis involves both the homogeneous and heterogeneous catalysis communities, and these catalysts are sometimes therefore called *semi - heterogeneous* [97].

1.6.1 Synthesis of Colloidal Nanoparticles

Au, Pd and Au-Pd colloidal nanoparticles have been synthesised by chemical reduction of metal salt precursors using different reducing agents to facilitate better control over shape and size of the particles formed. This strategy was inspired by Faraday who demonstrated the formation of red Au nanoparticles by reduction of tetrachloroaurate $[\mathrm{AuCL_4}]^-$ using phosphorous as the reducing agent [97]. Conventionally, citrate reduction is one of the more popular methods but it yields large particle size of about 20 nm. Much smaller particles with reduced dispersity and controlled size were prepared by the Brust-Schiffrin method using $NaBH_4$ reduction of the metal precursor in a biphasic organic solvent-water system in the presence of tetraoctylammonium bromide ($[N(C_8H_{17})_4]Br$) as the the phase-transfer reagent followed by the addition of a thiol that stabilises the nanoparticle as a thiolate ligand [98]. The stabiliser prevents the metal nanoparticles from aggregating, thus controlling the size and dispersion. The stabilisation can be electrostatic, steric or electrosteric (a combination of steric and electrostatic) depending on the choice of ligand or stabiliser. Nanoparticles can also be synthesised by atomic metal vaporisation and electrochemical synthesis [98, 99]. Physical methods such as finely dividing bulk metal and thermal decomposition of metal precursors in the presence of stabilising polymers are also popular synthetic methods. Polymers not only provide stabilisation due to their steric interaction by its bulk framework but also by weak binding to the nanoparticle surface by the hetero-atom. Some polymers commonly used are poly vinyl alcohol (PVA), poly(allylamine) (PAA), poly(N-vinyl-2-pyrrolidone) (PVP) and poly(2,5-dimethylphenylene oxide) (PPO) (Figure 1.12) because they fulfil both steric and ligand requirements [100]. Furthermore, polymer concentration also plays an important role in particle size control.

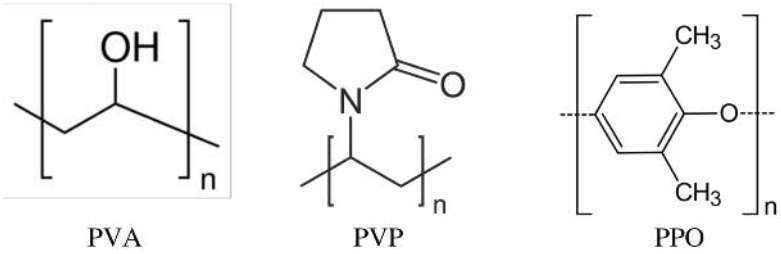

PVA PVP PPO

Figure 1.12: Examples of polymers used stabilisers for metal nanoparticles [97].

1.6.2 Catalysis by Colloidal Nanoparticles

Nano-sized gold colloids display interesting optical properties together with high catalytic activities. They are intensely coloured due to the surface plasmon resonance phenomenon, with the particular colour of the colloid depending not only on the size and shape of the nanoparticles but also on the properties of the solution like the dielectric constant of the dispersion medium [96]. Au and Au-Pd nanoparticles have been shown to exhibit catalytic activities without the presence of a support for oxidation reactions for substrates as benzyl alcohol [101], glycerol [102], glucose [103, 104], styrene and CO [105, 106]; oxidative polymerisation of aniline and pyrrole [107, 108]; hydrogenation of cinnamaldehyde and benzalacetone [109, 110]; and epoxidation and allylic oxidation [111]. Monodispersed PVP stabilised Au nanoparticles were synthesised and investigated by Tsukuda and co-workers for aerobic oxidation of benzylic alcohols and homocoupling of phenylboronic acid [101, 112]. The catalyst was prepared by rapid reduction using $NaBH_4$ into an aqueous solution of $[AuCl_4]^-$-PVP complex which synthesised nanoparticles with 1.3 nm mean diameter. The catalyst was treated with Na_2SO_3 to increase the particle size to study the effect of particle size on catalytic activity.

This size effect on catalytic activity was further investigated under the influence of identity and concentration of the stabilising ligand used to prepare the colloids. The role of the ligand was also studied in the enhancement or suppression of the catalytic activity while avoiding particle aggregation. It has been considered that strong Au-ligand interactions could decrease the particle size and avoid particle aggregation but could also decrease the catalytic activity considerably by partially or completely blocking access of the reactant

molecules to the metal surface [96, 113]. A compromise between the activity and re-usability has to be established with respect to the type of stabilising ligand used and its concentration. For example, the effect of the type of stabiliser used to prepare colloidal catalysts on glycerol oxidation has been investigated by Prati and co-workers [102]. An increase in the catalytic activity was observed with decrease in the particle size when catalysts were prepared using PVA, tetrakishydroxypropylphosphonium chloride (THPC) and citrate as protecting agents. Citrate stabilised Au nanoparticles with mean particle size of 9.8 nm showed the least activity compared to particles stabilised by PVA and THPC which gave much lower particle size of 2 nm and 2.5 nm respectively. But on ageing PVA and citrate showed much less agglomeration compared to THPC stabilised which indicated that electrostatic stabilisers were much less effective as a protective agent compared to steric stabilisers. Bulky steric stabilisers though prevented agglomeration and hence was active over longer use but was found to be much less active compared with THPC probably again due to its steric congestion and limiting active site accessibility. In another report, stabiliser free nanoparticles were synthesised but due to their instability in solution over an extended period of time, were supported onto TiO_2 and tested for glycerol oxidation. Again, a decrease in activity was observed with increase in particle size and also a difference in selectivities was observed with PVP, PVA and stabiliser free catalysts [114]. PVP-stabilised gold nanoparticles were shown to display enhanced catalytic activity compared to the colloids prepared by PAA for aerobic oxidation which was attributed due to electron donation properties observed for PVP [115].

Similarly, the metal:polymer ratio was varied to probe the effect of polymer concentration on particle size and catalytic activity. Particle size was confirmed using electron microscopy and the highest polymer to Au ratio of 50:1 gave small size particles with very narrow particle size distribution in the range of 1.8 - 2.8 nm [116]. On the other hand, much broader particle size distribution from 2 to 12 nm was obtained with polymer to Au ratio of 3:1. Particles prepared with 50 times polymer concentration showed the best activity towards the reduction of nitrophenol compared to the Au catalyst with bigger sizes. Similarly, mean diameter of mono-dispersed Pd nanoparticles was controlled

from 1.7 to 3.0 nm by changing the amount of PVP added during synthesis [117].

Along with the catalytic activity and selectivity, ageing and reuse of the unsupported nanoparticles was also studied. De Vos *et al.* studied the stability of the Au colloids for oxidation of 1,2-propanediol [118]. It was observed that significant level of activity (>50 %) was maintained even after extended periods of ageing (24 days). Another point noted was the recovery and reuse of the colloidal catalysts after consecutive runs. This was addressed by using a poly(dimethylsiloxane) (PDMS) membrane to recover the sol by nanofiltration, by which over 99 % of metallic colloid could be retained [119].

These studies indicate the intrinsic activity of the unsupported nanoparticles and supporting material does not necessarily improve catalytic activity or selectivity. Colloidal catalysts can be used for a various types of reactions with stability and reused with properly designed processes. More research is required to understand and improve on efficiency of the colloidal catalysts and further investigation is required to understand the role of support and metal-support interface. Along with the experimental exploration of Au-Pd unsupported catalysis, a lot of theoretical studies was performed as well with Au and Pd clusters to understand the interactions between substrate and metallic clusters to elucidate the reaction mechanism and understand the active sites involved in the process to enhance catalytic development.

1.7 Oxygen Interactions with Au-Pd: A Theoretical Study

As described in previous sections, gold and palladium have been been shown for many different reactions including oxidation reactions, especially for low temperature methane oxidation. Since liquid phase methane oxidation could not be carried out with molecular oxygen, H_2O_2 was used as the oxygen source or the oxidant for the reaction. H_2O_2 is also an important chemical commodity and direct synthesis using H_2 and O_2 has also been studied with gold and palladium. A combination of these two processes was employed by generating *in-situ* H_2O_2 for methane oxidation. Thus probing into the active sites and

interaction between metallic clusters and O_2/ H_2O_2 is vital to elucidate reaction mechanism. Theoretical chemistry is becoming an increasingly powerful tool which allows this probing and compliments experimental investigations. Ab-initio quantum mechanical and chemical calculations such as density functional theory (DFT) and simulations such as molecular dynamics have been used to provide geometries, electronic structure, reactivity of the catalysts as well as the evolution of reaction at the metal/substrate interface. Nowadays hybrid methods with both quantum mechanical methods (QM), which are more powerful and computationally expensive, are combined with fast molecular mechanics (MM) methods which can be easily used on larger systems are used [120]. The Nobel prize in chemistry in 2013 was awarded for the creation of such a hybrid method called *QM-MM*, "for development of multi-scale models for complex chemical systems" [121]. Micro-kinetic modelling is also used to analyse the set of relevant elementary steps for an overall chemical transformation which presents possible reaction paths which then can be examined by first-principle calculations to determine activation energies. Though it primarily is used alongside DFT, it can also take experimental observations into consideration by comparing with rate constants and turnover frequencies.

1.7.1 Proposed Reaction Mechanisms

Direct synthesis of H_2O_2 is generally assumed to occur via a two-step hydrogenation mechanism [122]. In this process, several parallel and consecutive side reactions are involved. A number of elementary steps are considered which appear to add H atoms sequentially to O_2 to form H_2O_2 while avoiding production of H_2O by irreversible O-O bond rupture in any intermediate [123, 124]. For the reactant O_2 after being adsorbed on the surface, first hydrogenation gives OOH group (Equation 1.13).

$$O_2{}^* + H^* \rightarrow OOH^* \tag{1.13}$$

The asterisks indicate these species to be surface species. Additionally, the adsorbed O_2 can also dissociate to give two surface atoms (Equation 1.14)

$$O_2{}^* \rightarrow O^* + O^* \tag{1.14}$$

For the intermediate OOH, the second hydrogenation could result in formation of H_2O_2 as shown in equation 1.15. But at the same time, hydrogenation of OOH can also yield H_2O and an O atom (Equation 1.16) or two OH groups (Equation 1.17).

$$OOH^* + H^* \rightarrow H_2O_2{}^* \tag{1.15}$$

$$OOH^* + H^* \rightarrow H_2O^* + O^* \tag{1.16}$$

$$OOH^* + H^* \rightarrow 2OH^* \tag{1.17}$$

As shown in equation 1.18, the OOH can also dissociate to give an O atom and an OH group.

$$OOH^* \rightarrow O^* + OH^* \tag{1.18}$$

As with all the other surface species, the product H_2O_2 can desorb from the metal surface (Equation 1.19). But it may also dissociate into two OH groups (Equation 1.20) which could then desorb from the surface.

$$H_2O_2{}^* \rightarrow H_2O_2 \tag{1.19}$$

$$H_2O_2{}^* \rightarrow 2OH^* \tag{1.20}$$

All side reactions involve O-O bond cleavage contributing to unselective formation of H_2O [125]. Thus, DFT calculations can be used to screen how these elementary steps proceed and compete on the surface of the catalyst which can be used to manipulate the activity and selectivity of the catalyst. This requires kinetically trapping unstable surface intermediates such as O_2* and *OOH as well as H_2O_2 to prevent thermodynamically preferred intermediates (O*, OH*) that lead to H_2O [123].

Since, Au, Pd and Au-Pd systems are widely studied experimentally for direct synthesis of H_2O_2, various computational studies have also been performed to elucidate reaction mechanism on catalytic surface and calculate different thermodynamic and kinetic parameters for the above elementary steps. In these studies, monometallic or bimetallic surfaces are mainly considered as catalysts in lieu of large particles because it is computationally expensive to use large size particles. Smaller monometallic clusters such as Au_{12}, Pd_{31} or Au_{20} are also studied [126–128]. Since higher productivities are reported with Au-Pd bimetallic colloids [129], mix-metal clusters have also been optimised and studied [128]. Earlier studies suggested the first step is preferential adsorption and facile dissociation of H_2 on Pd even in Au-Pd(111) and it wasn't blocked or delayed due to presence of Au atoms [130]. It was also suggested that pre-activation of O_2 is not required and it did not facilitate hydrogenation. On the other hand, pre-activation of O_2 molecule on metal surfaces weakened the O-O bond which eased its cleavage [131]. In addition, on the surface covered with H atoms, the reaction takes place with O_2 which is adsorbed on the Au-Pd junction as shown in the figure 1.13 [132]. Meyer and co-workers also showed that by changing the surface from Pd to Pt to Au, the step that governs the non-selective formation of water shifted from O_2 dissociation to OOH dissociation to H_2O_2 decomposition [133]. Mean field micro-kinetic modelling was also used by Plauck *et. al.* to elucidate decomposition of H_2O_2 on Pd(111) and Pd(100) which demonstrated that O-O scisson to be the major pathway for decomposition of H_2O_2 [134]. The presence of Au atoms on Au-Pd surface was found to block this dissociation (Figure 1.13) due to the weaker Au-O bond when compared to the O-O bond [122].

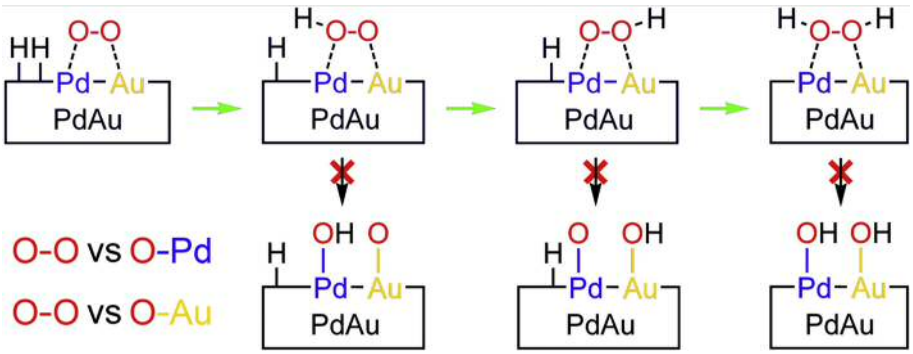

Figure 1.13: Schematic mechanism of H_2O_2 synthesis and side reactions for non-selective formation of H_2O adapted from references [130, 132].

Recently, the H_2O_2 synthesis mechanism was re-evaluated in the absence of secondary decomposition pathways on Pd clusters by Flaherty and co-workers [123, 135]. Experimental rate dependence on H_2 and O_2 pressures was found to be inconsistent with the often invoked Langmuir-Hinshelwood mechanism which is shown in figure 1.13. On the contrary, it provided evidence for heterolytic reaction pathways similar to the two-electron oxygen reduction reaction (ORR) [135]. The mechanism which took into account Pd cluster size and solvent properties was proposed, where the H_2 chemical potential was shown to act as the external electric potential and as the thermodynamic force behind O_2 reduction which then kinetically reacted with H^+ to produce H_2O_2.

1.7.2 Effect of Solvent and Additives

Experimentally, H_2O_2 rates and selectivities have been shown to be highly effected by not only H_2 and O_2 pressures but also by the choice of solvent and additives such as halide salts, mineral acids and diluent gas [78, 83] (Figure 1.14). Therefore it is vital to understand the influence of these additives on oxygen binding energies and metal surfaces or how they help in stabilising certain adsorption configurations thus modifying selectivities. Kinetic dependence measurements have been performed on reactant pressures, protic and aprotic nature of solvent and concentration and identification of proton donors [135]. Complementing these experimental investigations, experimental ORR and gas-phase electronic structure calculations were also performed to obtain details about interactions and influence of the co-adsorbed species like halides on Pt clusters due to spectator ions present in the reaction solution on synthesis of H_2O_2 and reduction to H_2O. [136]. Iwamoto *et. al.* also studied adsorption of HBr on different sites such as unsaturated corner and edge or more saturated (111) face on Pd clusters and its effect on catalytic performance [127, 132]. The energy profiles suggested higher production of H_2O_2 on (111) face sides in these clusters which was enhanced by the strong adsorption of H^+ and Br^- ions on unsaturated corner and edge sites thereby suppressing undesired reactions on these sites. This could explain the increase in H_2O_2 yield observed with

halide additives [78, 127].

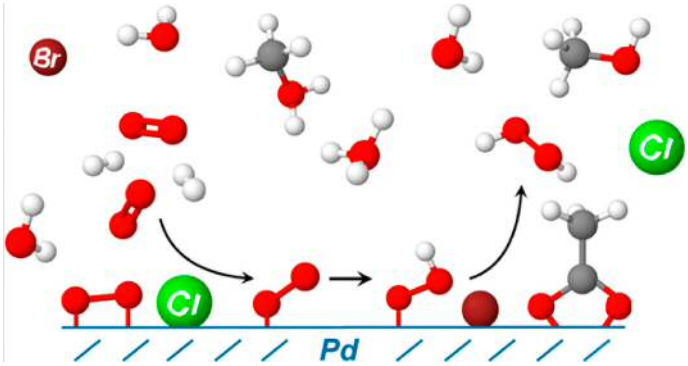

Figure 1.14: Typical reaction mixture for direct synthesis of H_2O_2 in mixture of aqueous solvents containing different additives and diluent gases taken from reference [123].

Though such gas-phase calculations are helpful to elucidate reaction mechanism, the interface formed between the metal or catalyst surface and the reaction solution is important and creates a unique reaction environment based on its properties and composition. This effect of solvent influences the reactivity of molecules and thereby effecting the reaction kinetics and thermodynamics. While these systems are far from the a detailed model that includes all relevant parameters which influence reactivity, these theoretical calculations and modelling provides some information about active sites and adsorption, bond-breaking and forming mechanisms and energies associated with these interactions.

1.8 Thesis Aims

The aims of this thesis are outlined below.

1. Au-Pd nanoparticles supported on TiO_2 have been shown to be as effective catalysts for the oxidation of methane with H_2O_2. In this work, the intrinsic methane oxidation activity of Au-Pd nanoparticles will be measured to investigate differences between the supported and unsupported catalysts.

2. Investigations into methane oxidation with Au-Pd colloids will be carried out with H_2O_2 and O_2 with the aim of using O_2 as the oxidant. Different preparation and testing parameters will be varied to understand the reaction mechanism.

3. The last part of this thesis will focus on computational investigation into interactions with gold and palladium clusters with O_2, H_2 and H_2O. DFT will be used to understand the direct synthesis of H_2O_2. Effect of H_2O as the solvent and reactant will also be studied.

Bibliography

(1) J. G. De Vries and S. D. Jackson, *Catalysis Science & Technology*, 2012, **2**, 2009–2009.

(2) V. Smil, *Nature*, 1999, **400**, 415.

(3) A. D. McNaught and A. Wilkinson, *IUPAC Compendium of Chemical Terminology*, 1997.

(4) K. J. Laidler and J. H. Meiser, *Physical chemistry*, Menlo Park, Calif. : Benjamin/Cummings Pub. Co, 1982.

(5) A. Abad, P. Concepción, A. Corma and H. García, *Angewandte Chemie - International Edition*, 2005, **44**, 4066–4069.

(6) International Energy Agency, *Natural Gas Information 2017*.

(7) BP, *BP Statistical Review of World Energy*, 2017, 52.

(8) International Energy Agency, *Resources to Reserves 2013 - Oil, Gas and Coal Technologies for the Energy Markets of the Future*, 2013, pp. 1–270.

(9) G. Hammer, T. Lübcke, R. Kettner, M. R. Pillarella, H. Recknagel, A. Commichau, H.-J. Neumann and B. Paczynska-Lahme, in *Ullmann's Encyclopedia of Industrial Chemistry*, Wiley-VCH Verlag GmbH & Co. KGaA, 2012.

(10) R. G. Bergman, *Nature*, 2007, **446**, 391–394.

(11) A. I. Olivos-Suarez, À. Szécsényi, E. J. M. Hensen, J. Ruiz-Martinez, E. A. Pidko and J. Gascon, *ACS Catalysis*, 2016, **6**, 2965–2981.

(12) G. A. Olah, A. Goeppert and G. K. S. Prakash, in *Beyond Oil and Gas: The Methanol Economy*, Wiley-VCH Verlag GmbH & Co. KGaA, 2009, pp. 179–184.

(13) J. Moulijn, M. Makkee and A. van Diepen, *Chemical Process Technology*, Wiley, 2013.

(14) J. Topp-Jorgensen, in *Methane Conversion*, ed. D. Bibby, C. Chang, R. Howe and S. Yurchak, Elsevier, 1988, vol. 36, pp. 293–305.

(15) D. Sheldon, *Johnson Matthey Technology Review*, 2017, **61**, 172–182.

(16) D. Wilhelm, D. Simbeck, A. Karp and R. Dickenson, *Fuel Processing Technology*, 2001, **71**, Fuel science in the year 2000: Where do we stand and where do we go from here?, 139–148.

(17) S. J. Blanksby and G. B. Ellison, *Accounts of Chemical Research*, 2003, **36**, 255–263.

(18) J. Ott, V. Gronemann, F. Pontzen, E. Fiedler, G. Grossmann, D. B. Kersebohm, G. Weiss and C. Witte, in *Ullmann's Encyclopedia of Industrial Chemistry*, Wiley-VCH Verlag GmbH & Co. KGaA, 2012.

(19) M. J. da Silva, *Fuel Processing Technology*, 2016, **145**, 42–61.

(20) R. Balasubramanian, S. M. Smith, S. Rawat, L. A. Yatsunyk, T. L. Stemmler and A. C. Rosenzweig, *Nature*, 2010, **465**, 115–119.

(21) J. Colby, D. I. Stirling and H. Dalton, *Biochem. J*, 1977, **165**, 395–402.

(22) A. A. Shteinman, *Russian Chemical Bulletin*, 2001, **50**, 1795–1810.

(23) K. Otsuka and Y. Wang, *Applied Catalysis A: General*, 2001, **222**, 145–161.

(24) H. D. Gesser, N. R. Hunter and C. B. Prakash, *Chemical Reviews*, 1985, **85**, 235–244.

(25) G. Walker, J. A. Lapszewicz and G. A. Foulds, *Catalysis Today*, 1994, **21**, 519–526.

(26) S. Bhatia, *Zeolite Catalysts: Principles and Applications*, Taylor & Francis, 1989.

(27) R. P. Townsend and E. N. Coker, in *Introduction to Zeolite Science and Practice*, ed. H. van Bekkum, E. Flanigen, P. Jacobs and J. Jansen, Elsevier, 2001, vol. 137, pp. 467–524.

(28) V. Sobolev, K. Dubkov, O. Panna and G. Panov, *Catalysis Today*, 1995, **24**, 251–252.

(29) M. V. Parfenov, E. V. Starokon, L. V. Pirutko and G. I. Panov, *Journal of Catalysis*, 2014, **318**, 14–21.

(30) C. Y. Kit, D. N. F., C. J. H., M. R. J., A. R. D., W. Christopher, S. Greg, Y. Sara, B. M. M., W. D. J., T. S. H. and H. G. J., *ChemPhysChem*, **19**, 402–411.

(31) E. V. Starokon, M. V. Parfenov, S. S. Arzumanov, L. V. Pirutko, A. G. Stepanov and G. I. Panov, *Journal of Catalysis*, 2013, **300**, 47–54.

(32) J. Xu, R. D. Armstrong, G. Shaw, N. F. Dummer, S. J. Freakley, S. H. Taylor and G. J. Hutchings, *Catalysis Today*, 2016, **270**, C1 Catalytic Chemistry, 93–100.

(33) M. H. Groothaert, P. J. Smeets, B. F. Sels, P. A. Jacobs and R. A. Schoonheydt, *Journal of the American Chemical Society*, 2005, **127**, 1394–1395.

(34) P. Tomkins, A. Mansouri, S. E. Bozbag, F. Krumeich, M. B. Park, E. M. C. Alayon, M. Ranocchiari and J. A. Vanbokhoven, *Angewandte Chemie - International Edition*, 2016, **55**, 5467–5471.

(35) K. Narsimhan, K. Iyoki, K. Dinh and Y. Román-Leshkov, *ACS Central Science*, 2016, **2**, 424–429.

(36) V. L. Sushkevich, D. Palagin, M. Ranocchiari and J. A. v. Bokhoven, *Science*, 2017, **356**, 523–527.

(37) A. E. Shilov and G. B. Shul'pin, *Russian Chemical Reviews*, 1987, **56**, 442.

(38) M. Lin, C. Shen, E. A. Garcia-Zayas and A. Sen, *Journal of the American Chemical Society*, 2001, **123**, PMID: 11456645, 1000–1001.

(39) J. A. Labinger and J. E. Bercaw, *Nature*, 2002, **417**, 507–514.

(40) R. A. Periana, D. J. Taube, E. R. Evitt, D. G. Loffler, P. R. Wentrcek, G. Voss and T. Masuda, *Science*, 1993, **259**, 340–343.

(41) R. A. Periana, D. J. Taube, S. Gamble, H. Taube, T. Satoh and H. Fujii, *Science*, 1998, **280**, 560–564.

(42) A. Sen, M. A. Benvenuto, M. Lin, A. C. Hutson and N. Basickes, *Journal of the American Chemical Society*, 1994, **116**, 998–1003.

(43) E. Gretz, T. F. Oliver and A. Sen, *Journal of the American Chemical Society*, 1987, **109**, 8109–8111.

(44) B. Michalkiewicz, K. Kałucki and J. G. Sośnicki, *Journal of Catalysis*, 2003, **215**, 14–19.

(45) C. Jones, D. Taube, V. R. Ziatdinov, R. A. Periana, R. J. Nielsen, J. Oxgaard and W. A. Goddard, *Angewandte Chemie*, 2004, **116**, 4726–4729.

(46) L. C. Kao, A. C. Hutson and A. Sen, *Journal of the American Chemical Society*, 1991, **113**, 700–701.

(47) E. D. Park, Y.-S. Hwang, C. W. Lee and J. S. Lee, *Applied Catalysis A: General*, 2003, **247**, 269–281.

(48) M. Lin and A. Sen, *Journal of the American Chemical Society*, 1992, **114**, 7307–7308.

(49) M. N. Vargaftik, I. P. Stolarov and I. I. Moiseev, *J. Chem. Soc., Chem. Commun.*, 1990, 1049–1050.

(50) R. Palkovits, M. Antonietti, P. Kuhn, A. Thomas and F. Schüth, *Angew. Chem. Intl. Ed.*, 2009, **48**, 6909–6912.

(51) N. Galina V., S.-F. Georg and S. Georgiy B., *Chem. Commun.*, 1997, 397–398.

(52) G. B. Shul'pin, G. V. Nizova, Y. N. Kozlov, L. Gonzalez Cuervo and G. Süss-Fink, *Advanced Synthesis & Catalysis*, 2004, **346**, 317–332.

(53) Q. Yuan, W. Deng, Q. Zhang and Y. Wang, *Advanced Synthesis and Catalysis*, 2007, **349**, 1199–1209.

(54) R. Raja and P. Ratnasamy, *Applied Catalysis A: General*, 1997, **158**, L7–L15.

(55) A. Sorokin, E. Kudrik, L. Alvarez, P. Afanasiev, J. Millet and D. Bouchu, *Catalysis Today*, 2010, **157**, 149–154.

(56) A. B. Sorokin, E. V. Kudrik and D. Bouchu, *Chem. Commun.*, 2008, 2562–2564.

(57) M. M. Forde, B. C. Grazia, R. Armstrong, R. L. Jenkins, M. H. A. Rahim, A. F. Carley, N. Dimitratos, J. A. Lopez-Sanchez, S. H. Taylor, N. B. McKeown and G. J. Hutchings, *Journal of Catalysis*, 2012, **290**, 177–185.

(58) C. Hammond, S. Conrad and I. Hermans, *ChemSusChem*, 2012, **5**, 1668–1686.

(59) C. Hammond, M. M. Forde, M. H. Ab Rahim, A. Thetford, Q. He, R. L. Jenkins, N. Dimitratos, J. A. Lopez-Sanchez, N. F. Dummer, D. M. Murphy, A. F. Carley, S. H. Taylor, D. J. Willock, E. E. Stangland, J. Kang, H. Hagen, C. J. Kiely and G. J. Hutchings, *Angewandte Chemie - International Edition*, 2012, **51**, 5129–5133.

(60) J. Shan, M. Li, L. F. Allard, S. Lee and M. Flytzani-Stephanopoulos, *Nature*, 2017, **551**, 605–608.

(61) Y. Kwon, T. Y. Kim, G. Kwon, J. Yi and H. Lee, *Journal of the American Chemical Society*, 2017, **139**, 17694–17699.

(62) H. Masatake, K. Tetsuhiko, S. Hiroshi and Y. Nobumasa, *Chemistry Letters*, 1987, **16**, 405–408.

(63) G. Hutchings, *Journal of Catalysis*, 1985, **96**, 292–295.

(64) G. J. Hutchings and M. Haruta, *Applied Catalysis A: General*, 2005, **291**, 2–5.

(65) M. H. Ab Rahim, R. D. Armstrong, C. Hammond, N. Dimitratos, S. J. Freakley, M. M. Forde, D. J. Morgan, G. Lalev, R. L. Jenkins, J. A. Lopez-Sanchez, S. H. Taylor and G. J. Hutchings, *Catal. Sci. Technol.*, 2016, **6**, 3410–3418.

(66) G. J. Hutchings and C. J. Kiely, *Accounts of Chemical Research*, 2013, **46**, 1759–1772.

(67) J. K. Edwards and G. J. Hutchings, *Angewandte Chemie International Edition*, 2008, **47**, 9192–9198.

(68) P. Landon, P. J. Collier, A. J. Papworth, C. J. Kiely and G. J. Hutchings, *Chem. Commun.*, 2002, 2058–2059.

(69) J. K. Edwards, S. J. Freakley, R. J. Lewis, J. C. Pritchard and G. J. Hutchings, *Catalysis Today*, 2015, **248**, 3–9.

(70) R. Jira, *Angewandte Chemie International Edition*, 2009, **48**, 9034–9037.

(71) *The Nobel Prize in Chemistry 2010.*

(72) J. K. Edwards, S. J. Freakley, A. F. Carley, C. J. Kiely and G. J. Hutchings, *Accounts of Chemical Research*, 2013, **47**, 845–854.

(73) J. Pritchard, L. Kesavan, M. Piccinini, Q. He, R. Tiruvalam, N. Dimitratos, J. A. Lopez-Sanchez, A. F. Carley, J. K. Edwards, C. J. Kiely and G. J. Hutchings, *Langmuir*, 2010, **26**, 16568–16577.

(74) L. Kesavan, R. Tiruvalam, M. Hasbi, A. Rahim, M. Izham, D. I. Enache, R. L. Jenkins, N. Dimitratos, J. A. Lopez-sanchez, S. H. Taylor, D. W. Knight, C. J. Kiely and G. J. Hutchings, *Science*, 2011, **331**, 195–199.

(75) In, *Ullmann's Encyclopedia of Industrial Chemistry*, Wiley-VCH Verlag GmbH & Co. KGaA, 2000.

(76) J. M. Campos-Martin, G. Blanco-Brieva and J. L. G. Fierro, *Angewandte Chemie International Edition*, 2006, **45**, 6962–6984.

(77) J. H. Lunsford, *Journal of Catalysis*, 2003, **216**, 40th Anniversary Commemorative Issue, 455–460.

(78) V. R. Choudhary and C. Samanta, *Journal of Catalysis*, 2006, **238**, 28–38.

(79) T. Ishihara, Y. Ohura, S. Yoshida, Y. Hata, H. Nishiguchi and Y. Takita, *Applied Catalysis A: General*, 2005, **291**, 215–221.

(80) B. E. Solsona, J. K. Edwards, P. Landon, A. F. Carley, A. Herzing, C. J. Kiely and G. J. Hutchings, *Chemistry of Materials*, 2006, **18**, 2689–2695.

(81) M. Piccinini, E. Ntainjua N., J. K. Edwards, A. F. Carley, J. A. Moulijn and G. J. Hutchings, *Phys. Chem. Chem. Phys.*, 2010, **12**, 2488–2492.

(82) D. A. Crole, S. J. Freakley, J. K. Edwards and G. J. Hutchings, *Proceedings of the Royal Society of London A: Mathematical, Physical and Engineering Sciences*, 2016, **472**.

(83) J. K. Edwards, B. Solsona, E. N. N, A. F. Carley, A. A. Herzing, C. J. Kiely and G. J. Hutchings, *Science*, 2009, **323**, 1037–1041.

(84) J. K. Edwards, J. Pritchard, L. Lu, M. Piccinini, G. Shaw, A. F. Carley, D. J. Morgan, C. J. Kiely and G. J. Hutchings, *Angewandte Chemie International Edition*, 2014, **53**, 2381–2384.

(85) U. Schuchardt, D. Cardoso, R. Sercheli, R. Pereira, R. S. da Cruz, M. C. Guerreiro, D. Mandelli, E. V. Spinacé and E. L. Pires, *Applied Catalysis A: General*, 2001, **211**, 1–17.

(86) H.-X. Yuan, Q.-H. Xia, H.-J. Zhan, X.-H. Lu and K.-X. Su, *Applied Catalysis A: General*, 2006, **304**, 178–184.

(87) G. Sankar, R. Raja and J. M. Thomas, *Catalysis Letters*, 1998, **55**, 15–23.

(88) R. Zhao, D. Ji, G. Lv, G. Qian, L. Yan, X. Wang and J. Suo, *Chem. Commun.*, 2004, 904–905.

(89) K. Zhu, J. Hu and R. Richards, *Catalysis Letters*, 2005, **100**, 195–199.

(90) G. Lü, R. Zhao, G. Qian, Y. Qi, X. Wang and J. Suo, *Catalysis Letters*, 2004, **97**, 115–118.

(91) In, *Ullmann's Encyclopedia of Industrial Chemistry*, Wiley-VCH Verlag GmbH & Co. KGaA, 2000.

(92) M. I. Binsaiman, G. L. Brett, R. Tiruvalam, M. M. Forde, K. Sharples, A. Thetford, R. L. Jenkins, N. Dimitratos, J. A. Lopez-Sanchez, D. M. Murphy, D. Bethell, D. J. Willock, S. H. Taylor, D. W. Knight, C. J. Kiely and G. J. Hutchings, *Angewandte Chemie - International Edition*, 2012, **51**, 5981–5985.

(93) M. H. Ab Rahim, M. M. Forde, R. L. Jenkins, C. Hammond, Q. He, N. Dimitratos, J. A. Lopez-Sanchez, A. F. Carley, S. H. Taylor, D. J. Willock, D. M. Murphy, C. J. Kiely and G. J. Hutchings, *Angewandte Chemie*, 2013, **125**, 1318–1322.

(94) M. H. Ab Rahim, M. M. Forde, C. Hammond, R. L. Jenkins, N. Dimitratos, J. A. Lopez-Sanchez, A. F. Carley, S. H. Taylor, D. J. Willock and G. J. Hutchings, *Topics in Catalysis*, 2013, **56**, 1843–1857.

(95) C. Williams, J. H. Carter, N. F. Dummer, Y. K. Chow, D. J. Morgan, S. Yacob, P. Serna, D. J. Willock, R. J. Meyer, S. H. Taylor and G. J. Hutchings, *ACS Catalysis*, 2018, **8**, 2567–2576.

(96) Y. Mikami, A. Dhakshinamoorthy, M. Alvaro and H. Garcia, *Catal. Sci. Technol.*, 2013, **3**, 58–69.

(97) D. Astruc, in *Nanoparticles and Catalysis*, Wiley-VCH Verlag GmbH & Co. KGaA, 2008, pp. 1–48.

(98) M.-C. Daniel and D. Astruc, *Chemical Reviews*, 2004, **104**, 293–346.

(99) C.-J. Jia and F. Schuth, *Phys. Chem. Chem. Phys.*, 2011, **13**, 2457–2487.

(100) J. S. Bradley, in *Clusters and Colloids*, Wiley-VCH Verlag GmbH, 2007, pp. 459–544.

(101) H. Tsunoyama, H. Sakurai, Y. Negishi and T. Tsukuda, *Journal of the American Chemical Society*, 2005, **127**, 9374–9375.

(102) A. Villa, D. Wang, D. S. Su and L. Prati, *ChemCatChem*, 2009, **1**, 510–514.

(103) M. Comotti, C. Della Pina, R. Matarrese and M. Rossi, *Angewandte Chemie International Edition*, 2004, **43**, 5812–5815.

(104) M. Comotti, C. D. Pina and M. Rossi, *Journal of Molecular Catalysis A: Chemical*, 2006, **251**, 89–92.

(105) L. Hu, X. Cao, J. Yang, M. Li, H. Hong, Q. Xu, J. Ge, L. Wang, J. Lu, L. Chen and H. Gu, *Chem. Commun.*, 2011, **47**, 1303–1305.

(106) Y. Iizuka, T. Tode, T. Takao, K.-i. Yatsu, T. Takeuchi, S. Tsubota and M. Haruta, *Journal of Catalysis*, 1999, **187**, 50–58.

(107) Z. Chen, C. D. Pina, E. Falletta, M. L. Faro, M. Pasta, M. Rossi and N. Santo, *Journal of Catalysis*, 2008, **259**, 1–4.

(108) C. D. Pina, E. Falletta, M. L. Faro, M. Pasta and M. Rossi, *Gold Bulletin*, 2009, **42**, 27–33.

(109) Y. Zhu, H. Qian, A. Drake, Bethany and R. Jin, *Angewandte Chemie International Edition*, 2010, **49**, 1295–1298.

(110) I. Biondi, G. Laurenczy and P. J. Dyson, *Inorganic Chemistry*, 2011, **50**, 8038–8045.

(111) M. Boualleg, K. Guillois, B. Istria, L. Burel, L. Veyre, J.-M. Basset, C. Thieuleux and V. Caps, *Chem. Commun.*, 2010, **46**, 5361–5363.

(112) H. Tsunoyama, H. Sakurai, N. Ichikuni, Y. Negishi and T. Tsukuda, *Langmuir*, 2004, **20**, 11293–11296.

(113) K. M. Koczkur, S. Mourdikoudis, L. Polavarapu and S. E. Skrabalak, *Dalton Trans.*, 2015, **44**, 17883–17905.

(114) L. Abis, S. J. Freakley, G. Dodekatos, D. J. Morgan, M. Sankar, N. Dimitratos, Q. He, C. J. Kiely and G. J. Hutchings, *ChemCatChem*, 2017, **9**, 2914–2918.

(115) H. Tsunoyama, N. Ichikuni, H. Sakurai and T. Tsukuda, *Journal of the American Chemical Society*, 2009, **131**, 7086–7093.

(116) I. Biondi, G. Laurenczy and P. J. Dyson, *Inorganic Chemistry*, 2011, **50**, 8038–8045.

(117) T. Teranishi and M. Miyake, *Chemistry of Materials*, 1998, **10**, 594–600.

(118) P. G. N. Mertens, I. F. J. Vankelecom, P. A. Jacobs and D. E. De Vos, *Gold Bulletin*, 2005, **38**, 157–162.

(119) P. G. N. Mertens, M. Bulut, L. E. M. Gevers, I. F. J. Vankelecom, P. A. Jacobs and D. E. D. Vos, *Catalysis Letters*, 2005, **102**, 57–61.

(120) A. Warshel and M. Levitt, *Journal of Molecular Biology*, 1976, **103**, 227–249.

(121) *The Nobel Prize in Chemistry 2013*.

(122) J. Li, A. Staykov, T. Ishihara and K. Yoshizawa, *The Journal of Physical Chemistry C*, 2011, **115**, 7392–7398.

(123) D. W. Flaherty, *ACS Catalysis*, 2018, **8**, 1520–1527.

(124) J. Li, T. Ishihara and K. Yoshizawa, *The Journal of Physical Chemistry C*, 2011, **115**, 25359–25367.

(125) J. Li and K. Yoshizawa, *Catalysis Today*, 2015, **248**, 142–148.

(126) L. C. Grabow, B. Hvolbæk, H. Falsig and J. K. Nørskov, *Topics in Catalysis*, 2012, **55**, 336–344.

(127) T. Deguchi and M. Iwamoto, *The Journal of Physical Chemistry C*, 2013, **117**, 18540–18548.

(128) A. V. Beletskaya, D. A. Pichugina, A. F. Shestakov and N. E. Kuzamenko, *The Journal of Physical Chemistry A*, 2013, **117**, 6817–6826.

(129) Y. Nomura, T. Ishihara, Y. Hata, K. Kitawaki, K. Kaneko and H. Matsumoto, *ChemSusChem*, 2008, **1**, 619–621.

(130) A. Staykov, T. Kamachi, T. Ishihara and K. Yoshizawa, *The Journal of Physical Chemistry C*, 2008, **112**, 19501–19505.

(131) D. C. Ford, A. U. Nilekar, Y. Xu and M. Mavrikakis, *Surface Science*, 2010, **604**, 1565–1575.

(132) T. Deguchi, H. Yamano and M. Iwamoto, *Catalysis Today*, 2015, **248**, 80–90.

(133) R. Todorovic and R. Meyer, *Catalysis Today*, 2011, **160**, 242–248.

(134) A. Plauck, E. E. Stangland, J. A. Dumesic and M. Mavrikakis, *Proceedings of the National Academy of Sciences*, 2016, **113**, E1973–E1982.

(135) N. M. Wilson and D. W. Flaherty, *Journal of the American Chemical Society*, 2016, **138**, 574–586.

(136) I. Katsounaros, W. B. Schneider, J. C. Meier, U. Benedikt, P. U. Biedermann, A. Cuesta, A. A. Auer and K. J. J. Mayrhofer, *Physical Chemistry Chemical Physics*, 2013, **15**, 8058.

2 | Experimental Details

This chapter outlines the experimental procedures followed when preparing, testing and characterising the materials subsequently discussed in this thesis. It is followed by an explanation of the basics of Density Functional Theory used for all the computational calculations in this thesis and the Vienna Ab-initio Simulation Package (VASP) which is used for simulations.

2.1 Reagents

The following reagents were used during the experiments. All reagents were used as received without further purification, unless otherwise stated.

- ^{12}C Methane (99.999%, Air Products)
- ^{13}C Methane (Research Grade, BOC Gases)
- ^{16}O Oxygen (99.999%, BOC Gases)
- ^{18}O Oxygen (Research Grade, BOC Gases)
- Nitrogen (99.999%, BOC Gases)
- Helium (99.999 %, BOC Gases)
- Hydrogen (99.999%, BOC Gases)
- Hydrogen Peroxide (50 wt.% in water, Sigma Aldrich)
- Methanol (HPLC Grade, Sigma Aldrich)

- Deuterium Oxide (99.9 atom% D, Sigma Aldrich)
- ^{13}C Methanol (Research Grade, Sigma Aldrich)
- Formic Acid (98%, Sigma Aldrich)
- Potassium Titanium Oxide Oxalate Dihydrate (Sigma Aldrich)
- Tetrachloroauric Acid ($HAuCl_4 \cdot xH_2O$, 99.999% trace metal basis, Sigma Aldrich)
- Palladium Chloride ($PdCl_2$, 99.999% trace metal basis, Sigma Aldrich)
- TiO_2 – Degussa P25 (99.5% trace metal basis, 20-30 nm particle size)
- Sodium Borohydride (Research Grade, Sigma Aldrich)
- Polyvinylpyrrolidone, PVP (Molecular Weights 3.5 kDa, 10 kDa, 40 kDa, 53 kDa, 360 kDa, 1300 kDa, Sigma Aldrich)
- Polyvinyl Alcohol, PVA (Sigma Aldrich)

2.2 Catalyst Preparation

2.2.1 Preparation of Colloids

Monometallic gold (Au), monometallic palladium (Pd) and bimetallic gold palladium (Au-Pd) nanoparticles were prepared by standard colloidal method [1]. Colloidal route is a method of preparation in which zero-valent metal is stabilised in solution by the presence of a protecting agent. An aqueous solution of total metal concentration of 0.16 mM of the metal precursors was prepared with molar ratio of gold to palladium being 1:1. This involved dissolution of 1.225 ml of aqueous solution of $HAuCl_4$ precursor (12.25 mg/ml Au) and 1.273 ml of acidic solution of $PdCl_2$ precursor (6 mg/ml in 0.5 M HCl) in 800 mL of de-ionised water. Typically, 2.4 mL of stabiliser solution (1 wt.% in water) was added to the solution to give the metal-to-stabiliser wt. ratio of 1:1.2. Generally, polyvinylpyrrolidone (PVP) was used as the stabiliser in this work. After 2-3 min of stirring, 6.6 mL of freshly prepared sodium borohydride ($NaBH_4$, 0.1 M)

solution was added such that the molar ratio of metal-to-$NaBH_4$ was 1:5. The required 6.6 ml was added as two 3.3 ml aliquots. This produced a dark brown colloid which was the left stirring for 30 minutes to ensure full reduction of the metal precursors. The colloid was concentrated using a roto-evaporator at the vacuum pressure of 30 mBar and bath temperature of 35 °C to give a nominal metal loading of 0.66 mM. The colloid was stored in glass media bottles away from direct light prior to use. Polyvinyl alcohol (PVA) stabilised and stabiliser-free colloids were also prepared using the same method. For stabiliser-free colloids, no polymer was added during the preparation and reduction was carried out.

2.2.2 Preparation of Supported Nanoparticles by Sol Immobilisation

For supported catalysts, the sol prepared as described above was immobilized onto 1.98 g of TiO_2 support material [1, 2]. A sufficient amount of support material was added to ensure a 1% wt metal loading and the solution was acidified to pH 1 using sulphuric acid to achieve more homogeneous deposition of nanoparticles. The supernatant solution became clear over a 1 h period after support addition, indicating the deposition process was complete. The sol-immobilized catalyst was then filtered, washed thoroughly with distilled water and then left to dry in an oven at 110 °C overnight.

2.3 Catalyst Characterisation

This section briefly describes the theory behind each characterisation technique employed throughout the project, along with the experimental details of the analysis.

2.3.1 Ultraviolet-Visible Spectroscopy

Ultraviolet-visible spectroscopy (UV-vis) is an analytical technique which concerns the molecular absorption of electromagnetic radiation in the ultraviolet and visible spectral regions (190 nm to 800 nm) [3]. Within this spectral region, molecules can undergo electronic transitions upon excitation from the ground state to a higher energy state. The energy difference between these two states can be calculated based on the frequency of the electromagnetic radiation that caused the excitation which is given by

$$\Delta E = h\nu \tag{2.1}$$

where h is the Planck's constant and ν is the frequency of incident radiation. These energy states are discreet and are affected by the surrounding electronic environment and the energies associated with the transitions such as d-d transitions, ligand-metal charge transfer and metal-ligand charge transfer typically fall within the region of UV-visible region of electromagnetic spectrum. Additionally, the Beer-Lambert law states that the electromagnetic radiation absorbed by the species is proportional to its concentration;

$$\mathrm{A} = \epsilon.[\mathrm{c}].\mathrm{l} \tag{2.2}$$

where A is the absorbance recorded, ϵ is the molar extinction coefficient, [c] is the solution concentration and l = path length of the sample cell. This is one of the main advantages of this technique, since essentially, the intensity of an absorbance can be linked to the concentration of the absorbing species. And thus, this technique can provide quantitative analysis of species in solution or on a solid. This technique is used to determine concentration of H_2O_2 in this study using a yellow coloured pertitanic acid complex which is explained later.

Gold nanoparticles display a characteristic feature in the visible region of the electromagnetic spectra, an intense absorption band is observed which arises due to a phenomenon

known as the surface plasmon resonance [4]. Surface plasmon resonance occurs when the wavelength of radiation leads to coherent excitation of all free conduction band electrons resulting in a collective in-phase oscillation. It is particularly prominent in small sized nanoparticles of coinage metals like Ag, Au and Cu because as the particle size increases the resonance band narrows as scattering length increases.

Experimental procedure

UV-vis spectroscopy measurements were carried out on *Agilent Cary 60* UV-visible spectrophotometer over the range of 200-700 nm at a data interval of 1 nm. Samples were placed in quartz cuvettes for analysis which was carried out at room temperature. The procedure used for H_2O_2 analysis is described later.

2.3.2 Electron Microscopy

The resolving power of a microscope is limited by the wavelength of its incidence beam. Thus, nano-sized structures cannot be imaged with optical microscopy as the wavelength of light is greater than structure trying to be imaged. The wavelength of electrons is less than 1 angstrom, so for structures less than 10 nm, far greater resolution can be achieved using electron microscopes compared to light microscope [5]. As such, electron microscopy can be used to determine the size, orientation and morphology of particles in a sample. It can also provide information on the nature and structuring of the atoms present within the particles. Different detectable signals are produced on interaction between the electron beam and sample as shown in figure 2.1. The type of electron microscopy is determined by the type of signal that is analysed.

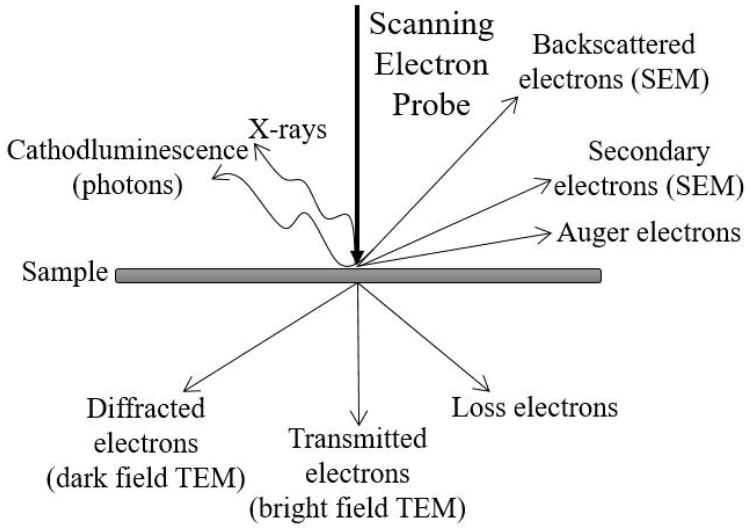

Figure 2.1: Interaction between the incident electron beam and a sample

One of the most commonly used techniques is scanning transmission electron microscopy (STEM) which can provide the information about morphology of catalyst particles at the atomic scale [6]. It is based on analysing the electron beam which has passed (or been transmitted) through a sample as shown in figure 2.1. It employs an intense high energy electron beam emitted by a cathode which is focused on a small area of sample with detectors positioned around the sample to produce different images. Bright field (BF) images are generated by detecting electrons which pass straight through the sample and therefore are unaffected by collisions as shown in figure 2.2. Bright field imaging can provide a 2 dimensional projection of where the metal particles are located since the beam attenuation is dependent on the sample density and thickness along with the direction of the electron beam. Dark field images are created by the diffracted electron beam which is detected slightly off angle to the incident beam. It is particularly useful when the electron beam passes through a crystalline species such as an oxide support or supported metal particle. Due to heavy elements such as supported metal nanooparticles, scattering can be detected at even higher angles which is known as high angle annular dark field (HAADF) imaging and these detection regions are shown in figure 2.2.

STEM analysis was carried out by Prof. Chris Kiely's research group at Lehigh University. Bright field and HAADF-STEM analysis was carried out on fresh and used; sup-

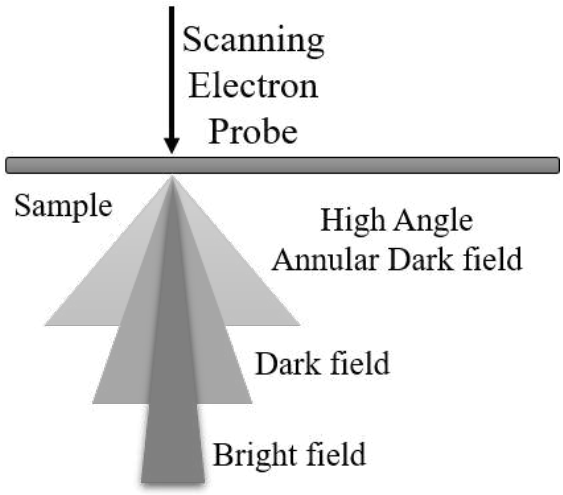

Figure 2.2: Detection regions of a STEM microscope

ported and unsupported gold-palladium catalysts to determine particle size, morphology and composition of the catalyst materials. Samples were prepared by dispersion of the above mentioned materials onto on a lacey carbon film supported over a 300-mesh copper TEM grid. These materials were examined using BF- and HAADF-STEM imaging mode in an aberration corrected JEOL ARM-200CF scanning transmission electron microscope operating at 200 kV. This microscope was also equipped with a Centurio silicon drift detector (SDD) system for X-ray energy dispersive spectroscopy (XEDS) analysis.

2.3.3 X-ray Photoelectron Spectroscopy

X-ray photoelectron spectroscopy (XPS), also known as electron spectroscopy for chemical analysis (ESCA) is a surface-sensitive characterisation technique which can give information about composition and oxidation state of species present on the surface of the catalyst to a depth of about 0-10 nm [7]. XPS is based on the photoelectric effect which is the emission of electrons when a sample is irradiated. When a sample is irradiated with radiation of sufficient energy (X-ray radiation), an atom absorbs this high energy X-ray radiation and as a consequence ejects a core electron with a characteristic amount of kinetic energy. This kinetic energy of the ejected electron depends on the energy of the incident X-rays, the binding energy of the core electron and the work function of the spec-

trometer being used. Binding energies of each element are specific for each core electron, and this depends also on the oxidation state of the sample. The higher the oxidation state of the sample the higher the binding energy of its core electrons. The work function of the spectrometer is the energy needed to eject an electron from the Fermi level into the vacuum. Therefore, to eject a core electron, the energy of the incident X-rays have to higher than the binding energy of that electron combined with the work function and the excess energy is measured as the kinetic energy as described in the equation 2.3

$$E_k = h\nu - E_b - \phi \tag{2.3}$$

where E_k is the kinetic energy of the electron, $h\nu$ is the incident photon energy (h is the Planck's constant and ν is the radiation frequency), ϕ is the work function.

Figure 2.3 shows simplified energy level diagram which was shown in equation 2.3. This shows the photon energy to eject an electron is equal to the binding energy, work function and kinetic energy combined. So, by keeping the energy of the incident X-ray photons constant, we can record XPS spectra of intensity of detected photoelectrons vs binding energy by detecting electrons of a certain kinetic energy. This provides information about the composition of the sample being analysed. In addition, since the binding energy also depends on the oxidation state of the element as the electrons in a positively charged cation are more tightly bound, subtle changes in binding energy also allows the determination of the oxidation state of the elements present on the sample surface.

XPS analysis of all samples was performed using *Kratos Axis Ultra DLS* photoelectron spectrometer utilising monochromatic Al Kα radiation operating at 120 W power. For sample preparation, colloid was deposited onto a clean Si wafer. The solvent was then evaporated under vacuum overnight in the fast entry lock of the spectrometer. Measurements were performed at pass energies of 40 and 160 eV for high resolution and survey scans, with step sizes of 0.1 and 1 eV respectively. All samples were analysed using a slot aperture and in hybrid spectroscopy mode, which utilises both magnetic and electrostatic lenses. The analysis area is a 700 μm x 300 μm rectangle in this mode. For all samples,

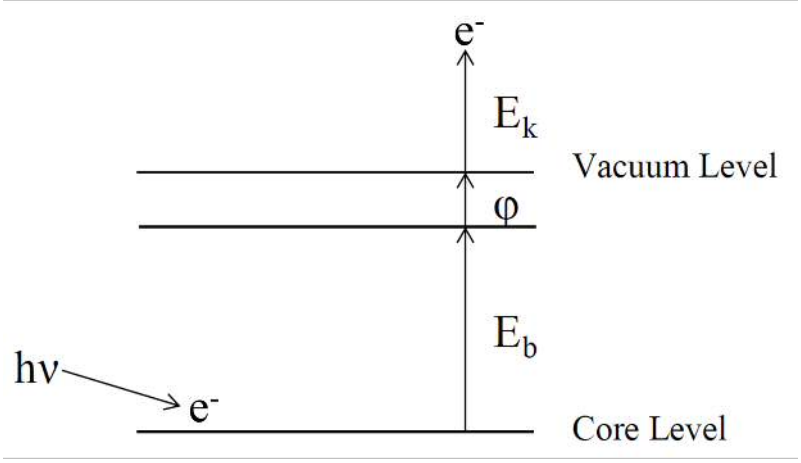

Figure 2.3: Energy level diagram to illustrate the energy barriers associated with the photoelectric effect

the Kratos immersion lens system was used for charge neutralisation and the spectra were subsequently referenced to the C(1s) line taken to be 285 eV. The samples also exhibited a peak at 99.4 eV which corresponded to the elemental Si(2p) peak arising from the Si substrate.

2.4 Catalyst Testing

2.4.1 Liquid Phase Methane Oxidation

Methane oxidation was carried out in a 50 mL glass liner fitted in a stainless steel Parr autoclave reactor equipped with an overhead stirrer and temperature and pressure sensors (fig 2.4). The reactor was charged with 10 mL of colloid (6.6 μmol of metal) and different amounts of H_2O_2 (typically, 50 μmol). The charged autoclave was sealed and purged three times with 30 bar methane. During standard reactions, it was pressurised with 30 bar methane and 5 bar oxygen to remain within oxygen lean limits to avoid a flammable mixture [8]. The mixture was stirred at 1500 rpm and heated to the desired reaction temperature (usually 50 °C) at the ramp rate by computer tuning of 2.25 °C/min and maintained at the reaction temperature for a fixed time (usually 30 min). At the end of

the reaction, the autoclave was cooled in ice to a temperature below 10 °C in order to minimise the loss of volatile products. The reaction gas was taken in a gas sampling bag to be analysed by GC (described in subsection 2.5.2.) The resultant solution was analysed by ^{1}H-NMR and GC-MS (described in subsections 2.5.1 and 2.5.3) respectively. The H_2O_2 consumed was analysed by spectrophotometric analysis explained in subsection 2.5.4. For isotopic reactions, O_2 added to the gas phase was replaced by ^{18}O enriched O_2 and the same procedure was used. The presence of labelled O in liquid oxygenates was analysed by GC-MS.

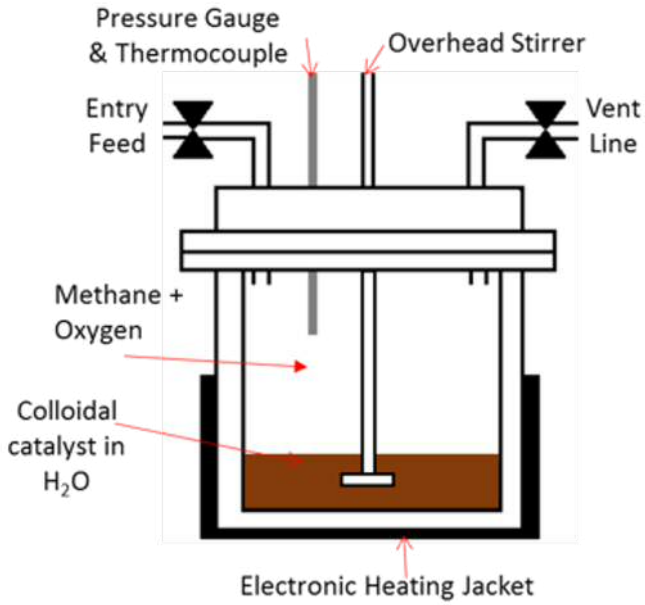

Figure 2.4: Schematic representation of an autoclave reactor

In cases where sol-immobilised catalysts were used, the reactor was charged with 100 mg of catalyst in 10 mL solution of de-ionised water and H_2O_2. At the end of the test, the reaction mixture was filtered before analysis.

2.5 Product Analysis

Liquid phase oxygenates were analysed using ^{1}H-nuclear magnetic resonance (NMR) spectroscopy and gas chromatography-mass spectrometry (GC-MS). Gas phase products

were detected and quantified using GC. H_2O_2 was quantified using titanium oxalate spectrophotometric method which are discussed in this section.

2.5.1 ^{1}H-Nuclear Magnetic Resonance (NMR) Spectroscopy

NMR spectroscopy is a powerful analytical technique that enables identification and quantification of organic molecules. It is a non-destructive analytical tool which utilises the behaviour of atomic nuclei in local magnetic fields. Nuclei of many elemental isotopes have a non-zero characteristic net spin (I) and an associated angular momentum due to uneven number of protons and/or neutrons(e.g. ^{1}H, ^{13}C, ^{15}N) [7]. Due to non-zero spin, these nuclei have spin states which are degenerate *i.e.* they have the same energy. Thus, for molecules such as ^{1}H, ^{13}C or ^{19}F, the nucleus has two possible spin states : m = 1/2 or m = -1/2 (also referred as spin-up and spin-down) which have same energy. But when the nucleus is placed in a magnetic field, the interaction between this external magnetic field and the nuclear moment leads to removal of degeneracy (Figure 2.5).

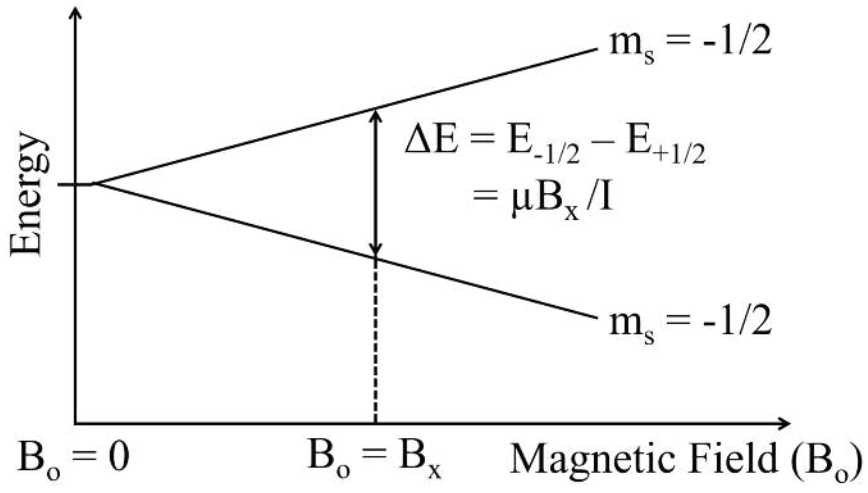

Figure 2.5: Energy level diagram to illustrate splitting of nuclei states in an external magnetic field

There is a small energy difference between the the two spin states which is dependent on the external magnetic field strength and magnetic moment of the nuclei (μ). When electromagnetic radiation of the correct frequency is applied to the nucleus which matches

the energy difference, the photon is absorbed. It is this magnetic resonant absorption which is detected in NMR. The signal that matches this transfer is measured and processed in order to yield an NMR spectrum for the nucleus concerned. It can also be used as an analytical tool since the magnitude of the signal produced is proportional to the number of nuclei present and hence depends on the concentration of the sample.

The exact resonance frequency of this energy transition is dependent on the effective magnetic field at the nucleus. Magnetic field at the nucleus is generally reduced due to the "shielding" effect created by the magnetic moment of the electrons which is opposite to the magnetic field produced by the nucleus. As a result, the energy gap is reduced, and the frequency required to achieve this resonance is also reduced. This shift in the NMR frequency depends on the chemical environment of the nucleus and electronic density distribution and hence used to probe chemical structures. This shift is commonly referred as chemical shift. Since, resonant frequency is dependent on external magnetic field and no two magnets will have exactly the same field, different resonance signals will be obtained for same molecule. Thus, NMR signals in a spectrum are reported relative to a reference standard compound. Thus, information about the chemical environment can be determined by the resonance frequency which in translated to chemical shift by using a reference molecule. Tetramethylsilane ($(CH_3)_4Si$) is used as the reference molecule for ^{1}H-NMR and ^{13}C-NMR analysis for organic compounds.

^{1}H-NMR (Bruker 500 MHz spectrometer) was used to identify and quantify liquid phase reaction products. It is equipped with a solvent suppression system to suppress the signal arising due to reaction solvent, water in this case. The chemical shifts of the analytes were reported in ppm relative to the tetramethylsilane (TMS, Me_4Si) standard (s, $\delta = 0$). The oxygenated species identified were methanol (s, $\delta = 3.4$), methylhydroperoxide (s, $\delta = 3.9$) and formic acid (s, $\delta = 8.4$) as shown in figure 2.6. In a previous study by Chadwick and co-workers, formaldehyde was also observed as a product[9]. But in these reactions, formaldehyde was not observed in the NMR analysis (s, $\delta = 4.89$). But it is also possible that the signal is obscured by H_2O signal in the spectrum (Figure 2.6), its

presence or absence could not be confirmed. Analysis was also carried on 600 MHz NMR spectrometer with enhanced water suppression which enables identification of formaldehyde signal. But, peak for formaldehyde was not observed in the analysis as well.

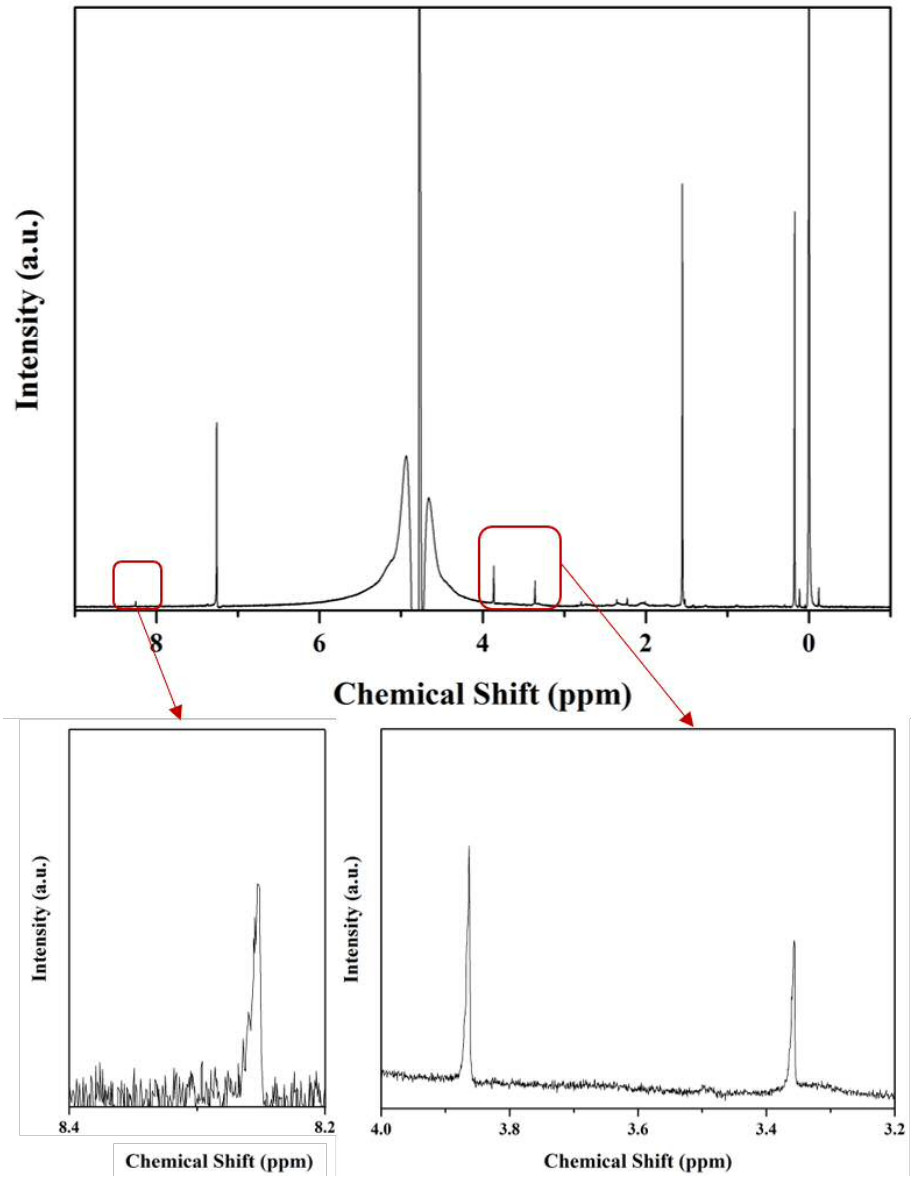

Figure 2.6: ^{1}H-NMR spectrum obtained from a typical reaction mixture. The oxygenated species identified were methylhydroperoxide (s, $\delta = 3.9$) and methanol (s, $\delta = 3.4$) shown in the zoomed inset along with formic acid (s, $\delta = 8.4$). The relative intensities in insets are arbitrarily shown. The other signals present corresponds to tetramethylsilane (s, $\delta = 0$), $CHCl_3$ (s, $\delta = 7.3$), H_2O in $CDCl_3$ (s, $\delta = 1.5$) and dissolved CH_4 (s, $\delta = 0.2$)

^{1}H-NMR analysis was performed as follows. Typically, 0.7 mL of sample and 0.1 mL of D_2O (for lock) were placed in an NMR tube for analysis. The oxygenates present were quantified against a 1% TMS in $CDCl_3$ internal standard contained within a sealed

glass ampule, which was also placed inside the NMR tube. This internal standard was calibrated against known methanol standards and example of such calibration curve is shown in figure 2.7. The residual water peaks in $CDCl_3$ arise due to the water present in sealed tube.

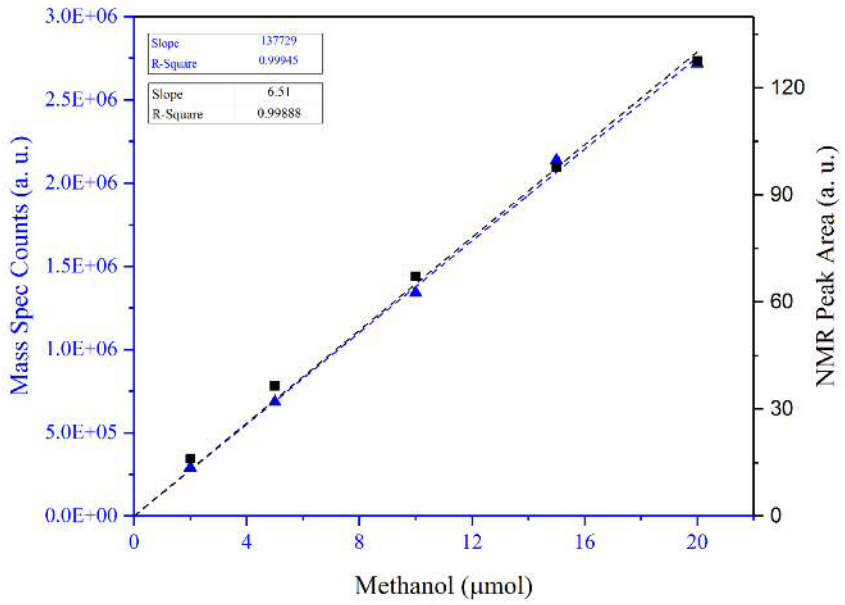

Figure 2.7: NMR and GC-MS calibration curves obtained for standard solution of methanol

2.5.2 Gas Chromatography

Chromatography is a technique used to separate a mixture of chemical compounds. Gas chromatography (GC) is one of the most common analytical techniques used to detect and analyse mixtures of gases or products that can be easily vaporised [10]. GC can provide both qualitative and quantitative information about the mixtures and also help to identify impurities or side products. The separation of these chemical substances relies on partitioning behaviour between a flowing mobile phase and a stationary phase. A typical GC system (figure 2.8) involves introducing the sample mixture into a carrier gas which is the mobile phase. This carrier gas is passed through a sample loop and and injected into a column containing an adsorbant material which acts as the stationary phase. This

is usually held at a specific temperature using an oven as shown in the figure 2.8.

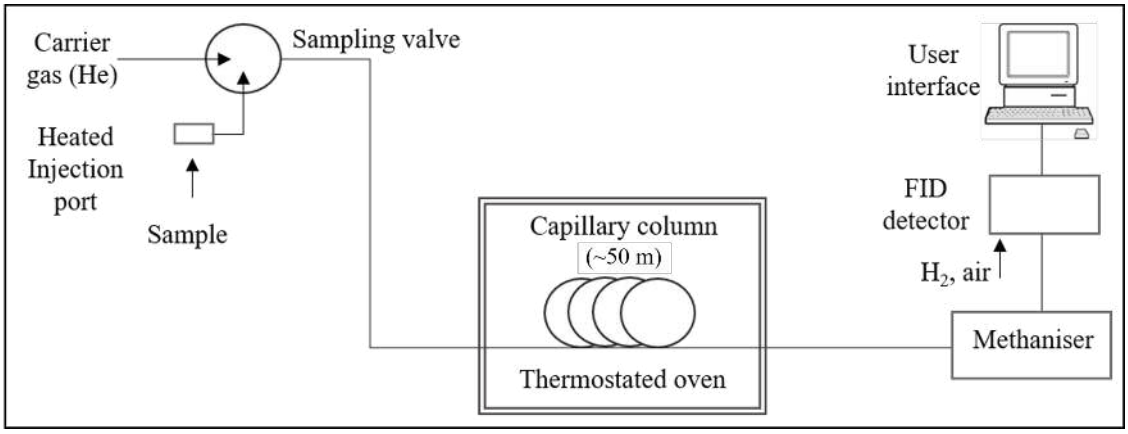

Figure 2.8: Schematic of the GC setup used

The separation of compounds is based on the exchange-equilibria between the analytes present in the sample and the column which defines the speed at which sample is carried through the column. This exchange-equilibria is dependent on the nature of the analyte present in the mobile-phase (polarity), and the interaction between analyte and stationary phase (H-bonding, dipole interaction). The component having stronger interaction with the adsorbant column will remain in the column for longer time compared to the one with weak interaction. This results in the separation of the compounds as the compounds leave the column at different times which is known as the retention time. Then they enter the detector.

Since separation of compounds depends on interaction between analyte in mobile phase and stationary phase column, several factors such as carrier gas flow rate, column temperature and column type affect this separation. These are all parameters that can be optimised to give the most effective separation of components. The carrier gas typically is an inert gas with high purity and made moisture free by passing it through a molecular sieve before entering the GC system. Generally, helium, nitrogen and argon are used depending on the detector and components that need to be analysed. The carrier gas flow rate dictates how long components are retained in the system and can affect the analysis. The higher the flow rate the faster the analysis, but the lower the separation between analytes. Thus the flow rate needs to be selected to ensure separation but minimise length

of analysis. Samples enter the column by passing through an injection port, which is held at a high enough temperature to vaporise the components of the mixture if they are not already in the gas phase. Thus, the compounds that need to be vaporised must have sufficient volatility but also thermal stability to avoid thermal decomposition.

Similarly column type and temperature also has an effect on analyte separation and elution. There are mainly two types of separation columns; packed columns and capillary columns. Packed columns are usually made of glass or stainless steel and contains stationary phase packed into them. They typically have an internal diameter of 2-5 mm and shorter length of 1-10 m compared to capillary column which are usually made of flexible material and can be very long, upto 50 m. The internal diameter of capillary column is usually tenths of millimetres and the internal wall is coated with the stationary phase. Various stationary phase are used for separation of components and many columns are readily available to separate the desired mixture of compounds. Similar to carrier flow rate, the column temperature is also optimised; as a low column temperature produces the greatest level of separation, but can result in very long elution times, whereas a high temperature gives fast analysis times but shorter retention times and less product separation.

Separately eluted products are individually detected by the chosen detector. Usually thermal conductivity detector (TCD) or flame ionisation detector (FID) are used. For this study, FID was used which detects compounds through combustion. On passing through a flame, the compound is oxidised and forms fragmented ions which can be detected by oppositely charged plates. On correlating the response of the ions with retention times and amount of standards, both qualitative and quantitative information can be extracted. Since, pyrolysis relies on combustion and oxidation of a compound, maximum response is generated with low oxidation state carbon. This means, CO_2 with high oxidation state C will have minimal or zero detectability. This problem is overcome by placing a methaniser after analyte separation which comprises of Ni-Co catalyst which reduces the effluent stream with H_2 to CH_4. In this study, GC analysis was performed by a *Varian 450-GC* fitted with a CP-Sil 5CB capillary column (50 m length, 0.32 mm diameter, carrier gas =

He), a methaniser unit and both FID detector as shown is figure 2.8. CO_2 was quantified against a calibration curve obtained using commercial standards (Figure 2.9).

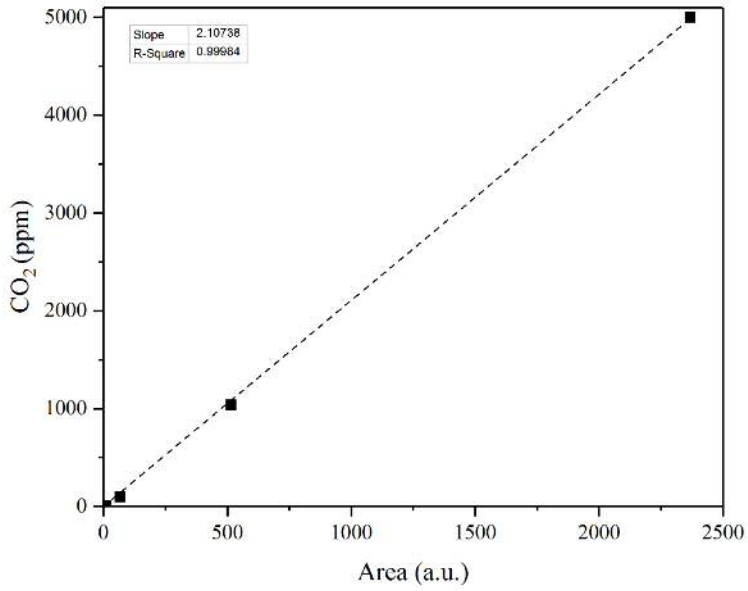

Figure 2.9: Calibration curve obtained for carbon dioxide

2.5.3 GC-Mass Spectrometry

Mass spectrometry (MS) is an analytical technique widely used to identify and characterise different chemical compounds and is applied to pure samples or complex mixtures [10]. It ionises chemical species and sorts the ions based on their mass-to-charge ratio. A mass spectrum is a plot of ion signal as a function of this mass-to-charge ratio and can also be used to study isotopic signature of a sample which was performed in this study. GC-MS is basically an analytical method that combines the features of gas-chromatography and mass spectrometry within a test sample. Combining these two processes also reduces the possibility of error in identifying constituents of an analyte, as it is unlikely that two different molecules will behave in the same way in both a gas chromatograph and a mass spectrometer. Traditional detectors in a GC such as FID cannot differentiate between multiple molecules with same retention time which co-elute. Such molecules can be easily seen separately with a MS detector such as electron ionisation (EI) detector which is

much more sensitive to mass-to-charge ratio and can also detect much lower quantities.

EI also known as electron impact ionisation and electron bombardment ionisation is an ionisation method which uses energetic electron beam to interact with the analyte sample to produce ions. These electrons are generated through thermionic emission and have kinetic energy higher than the ionisation energy of the sample. The positively charged ions produced from sample are then directed towards the mass analyser by a repeller electrode.

In this study, analysis of $^{18}O_2$ isotope labelling reactions was analysed using GC-MS. Oxygen has only one naturally occurring NMR active nucleus, ^{17}O which has a very low natural abundance and low receptivity in NMR rendering. Thus for isotopic labelling experiments, $^{18}O_2$ was used and analysis took place using GC-MS fitted with EI source. Since, in GC, volatile compounds are vaporised, methylhydroperoxide when vaporised in the injector, converted to methanol [11, 12].

As shown in figure 2.10, good agreement was was observed between the combined amount of methanol and methylhydroperoxide as determined by NMR and the amount of methanol determined by GC-MS. Calibration was performed with methanol standards as shown above in figure 2.7. In some cases, methylhydroperoxide was converted to methanol using $NaBH_4$ before injection into the GC system. In these cases also, the amounts of methanol produced by reduction of methylhydroperoxide was measured by NMR and found to in agreement. The "as-is" pre-reduced reaction mixture containing methylhydroperoxide was also injected into the GC-MS for comparison.

2.5.4 Hydrogen Peroxide Determination

The amount of H_2O_2 present in the reaction solution was determined by spectrophotometric method [13]. In this case, H_2O_2 was reacted with potassium titanium oxalate in acid solution to form the yellow pertitanic acid complex. This coloured complex is measured spectrophotometrically using *Agilent Cary 60* UV-visible spectrophotometer at 390 nm.

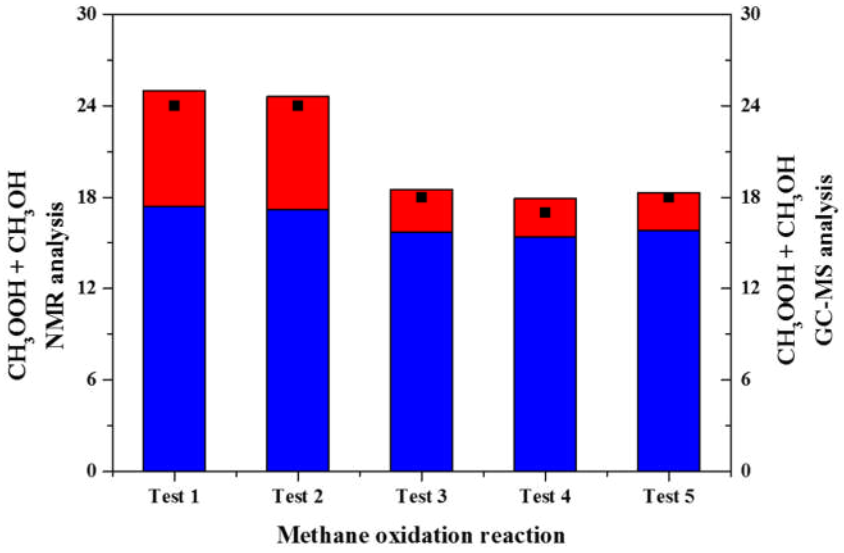

Figure 2.10: NMR and GC-MS quantification analysis for test reaction solutions. Liquid phase products were quantified by both mass spectrometry and NMR quantitative analysis of the reaction solutions. Within experimental error, the amount of methylhydroperoxide (blue bar) + methanol (red bar) in the NMR analysis corresponded to the amount of methanol (black box) measured in the GC-MS analysis. Test conditions: Pressure (CH_4) = 30 bar, pressure (O_2) = 5 bar, catalyst: 10 mL AuPd-PVP colloid, 6.6 μmol of metal (1:1 metal molar ratio), 1000 μmol H_2O_2, 50 °C (ramp rate of 2.25 °C/min), 1500 rpm, 30 min.

This method is suitable for determination of low amounts of H_2O_2 in the range 0.1 - 50 μg/mL and the peroxotitanium complex is specific to H_2O_2, so usually free from interference. However, background colour due to colloid colour which can be compensated by zeroing out a blank sample of colloidal sample. A 0.5 % solution of potassium titanium oxalate solution was made in water by dissolving 5 g in 100 ml.

To measure the amount of H_2O_2, 0.05 to 1 mL of reaction sample was acidified using dilute H_2SO_4 and 1 ml of potassium titanium oxalate solution was added to form the yellow complex which was analysed. A calibration curve was obtained by similar procedure by adding known amounts of H_2O_2 in 1 ml of colloid which was acidified with dil. H_2SO_4 (Figure 2.11)

Some definitions used throughout the thesis

- Oxygenate Selectivity = (moles of oxygenates (CH_3OOH + CH_3OH)/ total moles

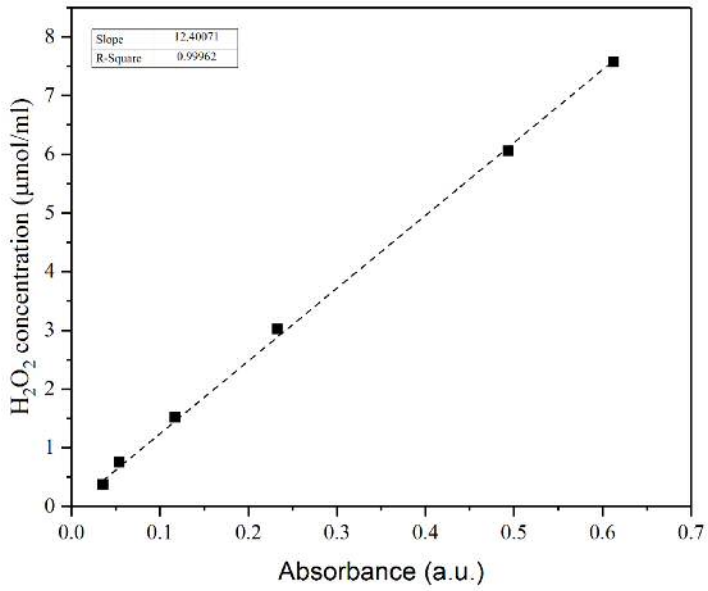

Figure 2.11: Calibration curve obtained for hydrogen peroxide

of products) $\times$ 100

- Gain Factor = moles of oxygenate (CH_3OOH + CH_3OH) produced/ moles of H_2O_2 consumed
- Oxygenate Productivity = $\text{moles}_{(\text{oxygenates}(CH_3OOH + CH_3OH))}\text{kg}^{-1}_{(\text{metal})}\text{h}^{-1}$
- Total Productivity = $\text{moles}_{(\text{products}(CH_3OOH + CH_3OH + HCOOH + CO_2))}\text{kg}^{-1}_{(\text{metal})}\text{h}^{-1}$

As shown in Figure 2.10, methane oxidation has been performed several times under identical multiple conditions. These tests show high degree of reproducibility. Standard error was calculated to be 2% on the amount of products using NMR and 5% in H2O2 determination by UV-Vis. Thus, the uncertainty error in gain factor was calculated as 5.4% by propagation of error.

2.6 Density Functional Theory

Density Functional Theory (DFT) is one of the most widely used method to computationally investigate systems containing moderate to large numbers of atoms. DFT basically

describes the electronic states of atoms, molecules and materials in terms of the 3 dimensional electronic density of the system with N electrons. It has now become a preferred method for electronic structure theory and this popularity stems in part because its cost scales well with the system size compared to wave function theory (WFT) which involves 3N-dimensional wave function for the same system; and yet similar levels of accuracy is achieved except for very small systems [14]. It is particularly useful for metals because of inclusion of static electron correlation and hence used extensively to investigate transition states and active sites in catalysis.

DFT was used to perform the computational calculations that have been discussed through the study. It underpins methods like geometry optimisation, transition state search though nudged elastic band calculations (NEB), vibrational frequency analysis and Bader charge analysis which are used in this study. This section will outline the underlying theory of DFT and how it has been applied to the work performed in this thesis. Vienna Ab Initio Simulation Package (VASP) which is a plane-wave DFT code has been used to implement these simulations. Inside the VASP package, there are various extensions and functions used alongside standard DFT like, DFT-D3, DFT-vtst for NEB methods etc. These methods will be discussed very briefly in this thesis and the theory behind these methods are well established in the literature and outlined in various computational chemistry textbooks [15–19] and beyond the scope of this thesis. For simplicity, a majority of the derivations of various equations have been left out.

2.6.1 Ab-initio Codes and Hartree-Fock Method

Ab-Initio (or *first-principles*) codes which are based on Schrödinger equation (equation 2.4) describe the interactions between nuclei and electron to interpret properties of various systems.

$$\hat{H}\Psi(r_e, r_n, t) = E\Psi(r_e, r_n, t) \tag{2.4}$$

Where $\hat{H}$ is the Hamiltonian operator, Ψ is the wave function, E is the energy of the system and the parameters r_e and r_n are the coordinates of the electron and nucleus respectively, and t is time. In theory, equation 2.4 can be solved for every atom in a system and give a full representation of interactions between them, but it is practically impossible for any system larger than hydrogen atom as variable scaling expands exponentially with complexity. In order to simplify, *time-independent* Schrödinger equation can be used by only studying the ground state of electrons . To simplify further, the nuclei of the system can be ignored as well. Based on Born-Oppenheimer approximation, the energy of the electrons and the nuclei can be decoupled (Equation 2.5). Born-Oppenheimer approximation can be used due to the difference between nuclear and electronic masses.

$$E_{atom} = E_{nucleus} + E_{electron} \tag{2.5}$$

Equation 2.5 shows the energy of the atom is the sum of nuclear and electronic energies. On applying these simplifications to the equation2.4, the *time-independent* Schrödinger Equation 2.6

$$\hat{H}(r)\Psi(r) = E\Psi(r) \tag{2.6}$$

in which the Hamiltonian operator $\hat{H}$, and the wave function Ψ are now only functions of the electron coordinate r. Equation 2.6 shows that the information relating to the energy of the system E is contained within the wave-function Ψ which implies by selecting the correct Hamiltonian operator $\hat{H}$ and the wave-function Ψ, the energy of the system E can be calculated.

One of the first method for calculating this energy is Hartree-Fock (HF) approach, which attempts to solve equation 2.6 using some assumptions like Born-Oppenheimer approximation, neglecting relativistic effects, and treating a solution as a linear combination of finite orbitals. Under these assumptions, it is possible to build a set of initial guess wave-functions, calculate the value of the function at that point and then vary the values of the function until the value converges. Essentially, on optimisation of the wave-function is performed in order to calculate the true wave-function, and hence calculate the energy

of the system. HF approach also assumes that any trial function that is being used for calculating the energy will always have an energy equal to greater than the true value.

2.6.2 Origins of DFT

HF method works well for simple systems of several atoms, however they do not fully incorporate electronic interactions. It leads to high energy calculations and is not very useful.Now a days, new post-Hartree Fock methods have been developed taking such interactions into account. Hohenberg and Kohn [20] provided the next breakthrough by two theories which showed it was possible to use the electron density instead of the wave-function in order to calculate the energy of the interacting system. The first theory was that the ground state electron density of the system will provide a unique external potential (interaction between nuclei and electrons) i.e.

$$\rho(r) \iff U_{ext} \tag{2.7}$$

with $\rho(r)$ is the electron density of the system, and U_{ext} is the external potential. Thus, first theorem states that the ground state properties of a system can be determined by the electron density. The electron density itself depends on 3 spatial coordinates. Therefore, 3N spatial coordinates of a many electron system to three. The second principle states that the minimised density obtained by optimising the density functional corresponds to the true ground state energy.

The above theorems indicated the density can determine the external potential U_{ext}, which can then determine a $\hat{H}$ which subsequently can determine the wave-function. With the wave-function and Hamiltonian, energy and properties of the system can be evaluated. While this theory is powerful, it is limited since, actually calculating the true value of ground state electron density is difficult.

Expanding on the Hohenberg and Kohn method, the *Kohn-Sham* [21] method was devel-

oped, which formed the basis of modern DFT. They developed a system which was built up by using single electrons as a sum of electron operators as a set of non-interacting electrons. Using the $\hat{H}$ from n-electron system from the *time-independent* Schrödinger equation used in HF, the energy of the system can be considered as a summation of the following individual energies:

$$E = E_{kin} + E_{ext} + E_H + E_x \tag{2.8}$$

with the four energy terms representing the kinetic, external, Hartree and exchange energies respectively. Since, the electrons in their one-electron system are non-interacting, energy components can be split into interacting and non-interacting components such as,

$$E = E_{kin}^{non} + E_{ext} + E_H + E_{xc} \tag{2.9}$$

where E_{kin}^{non} is the kinetic energy of the non-interacting system, and the term E_{xc} is the exchange correlation energy of the system, which is made up of the correlation and exchange energies:

$$E_{xc} = E_x + E_c \tag{2.10}$$

$$E_c = E_c^{int} + E_{kin}^{int} \tag{2.11}$$

where E_x is the exchange energy related to the same spin electrons arising from Pauli's exclusion principle and E_c is the correlation energy related to the opposite spin electrons occupying the same orbital which again is composed of correlation due to electron-electron interactions and kinetic energy due to these interactions.

To calculate the Energy in equation 2.9, the first three terms can be computed using Kohn-Sham equations, but the exchange correlation E_{xc} energy has no explicit solution, meaning it has to be approximated.

2.6.3 Exchange Correlation Energy

Exchange correlation energy is approximated by employing many varieties of functionals. There are two main methods for performing this estimate, known as Local Density Approximation (LDA) and Generalised Gradient Approximation (GGA) [22]. In LDA, the total electron density for a system can be split into smaller uniform pieces with uniform electron density. And the total E_{xc} is the sum of individual energies. Since, it's a summation approach, it has issues like over-predicting binding between atoms, causing incorrect lattice parameters and improper estimation. To avoid this, GGA is used which removes the homogeneity of the LDA by taking the gradient of the electron density. Since, it's a more realistic picture of the electron density, the density functional obtained is considered to be more accurate and therefore, the energies are more accurate.

The GGA approximation is well established with codes like VASP with most common functionals used are Becke (B88) [23], Perdew and Wang (PW91) [24] and Perdew, Burke and Enzerhof (PBE) [25]. PBE is extensively used throughout the thesis. GGA often performs poorly with strongly correlated systems such as transition metals but corrections are introduced in such cases to increase the accuracy. For such strongly correlated systems, there are penalty functions added to DFT energy to account for Coloumb and exchange interactions (U and J respectively) [26].

2.6.4 Vienna Ab-initio Simulation Package

VASP (Vienna Ab-initio Simulation Package) has been used for simulation package for DFT calculations performed in this thesis. The code has been used for simulations of materials and their geometry optimisation, interactions between catalyst and substrate and molecular dynamics and solvation. VASP has the pseudopotentials contained within a basis set with plane wave called Projector Wave Method (PAW). Pseudopotentials are effective potentials used as approximations for core electrons which take into account

effect of nucleus in accurate manner. If all electrons were included within a calculation, the computational cost would prohibit all but the simplest of systems to be studied. Since, properties of a chemical reaction are governed by valence states and not core electrons, use of pseudopotentials eases the DFT calculations. In VASP, PAW functionals are used for PBE which are taken from existing database. All these pseudopotentials are contained in a file named POTCAR which is read by VASP.

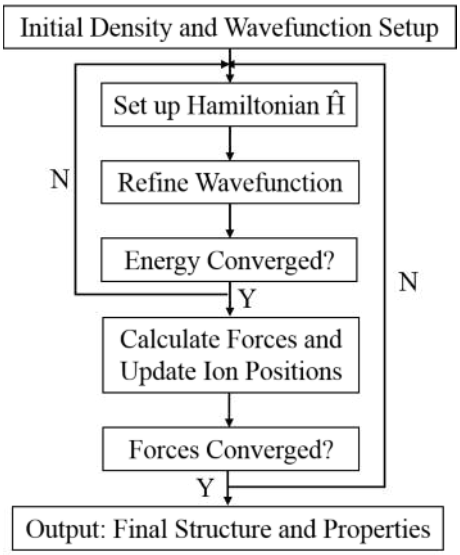

Figure 2.12: Flow chart of DFT optimisation in VASP

The optimisation of the density functional in VASP consists of two loops (figure 2.12). The density and wave function are optimised in the inner loop, and then the forces and atom positions are optimised in the outer loop. To optimise the wave-function, *ALGO = Fast* was used. For the optimisation of the outer loop *i.e.* movement of ion positions, the *IBIRON* tag is used to specify which method to use. IBRION tag basically defines how the ions are updated and moved. For all of the calculations in this thesis *IBIRON = 2* has been used, which uses a conjugate gradient method for the minimisation of the forces and atomistic positions [22], which is the recommended setting in VASP. Initial atomic positions are provided with POSCAR file.

2.6.5 Dispersion Interactions

With previously mentioned parameters, structure and energy optimisation is possible in VASP, but for more accurate representation of structure, extra corrections are required with standard DFT. One such correction used in this thesis is for long range dispersion (van der Waals) forces. These attractive interactions are important components to the energies of inert gas interactions, catalytic surface/adsorbate systems and DNA structures. The common method to include these corrections is to use summation of standard KS energy using DFT and the energy arising from dispersion correction:

$$E_{DFT-D3} = E_{DFT} + E_{D3} \tag{2.12}$$

where E_{DFT-D3} is the corrected system energy, E_{DFT} is the standard DFT energy and E_{D3} is the dispersion correction energy. The popular dispersion correction used throughout this thesis is known as Grimme D3 correction which is based on the Leonard-Jones interaction energy plot [27]. In VASP, D3 correction is included by setting the tag *IVDW = 11* and including the following tags:

```
VDW_RADIUS     = Cutoff radius for pair interactions
VDW_CNRADIUS   = Cutoff radius for calculation coordination number
VDW_S6         = Functional dependant damping parameter
VDW_S8         = Functional dependant damping parameter
VDW_SR         = Functional dependant damping parameter
```

The first two tags are system dependant, and have been set at 15Å and 10Å respectively throughout the work. Cut-off radii are usually kept large (around 10-15 Å) to account of all possible interactions between different molecules even if they are not in close contact. The final three tags depend on the functional used and in this case have been set as 1.0, 0.722 and 1.217 respectively for PBE functional.

2.6.6 Transition State Searches

To understand any reaction, it is vital to understand the evolution of reaction mechanism and activation energy barriers associated with the elementary steps. Energy of the transition state is required to calculate the activation energy which is difficult since the structure of the transition state is majorly unknown. One of the method developed to attempt to find the structure of the transition state and hence the minimum energy path is developed by Henkelmen and co-workers known as the Nudged Elastic Band (NEB) [28] method usually used with climbing image modifier [29]. NEB method works by taking the start and end point of a reaction mechanism (the two minima) and interpolating a number of images between them.

The images are connected to one another by a spring, so that on optimising the structures, the images do not fall into either the start or the end. The NEB force acting on image i comprises of two independent components [30]:

$$F_i^{NEB} = F_i^{Perpendicular} + F_i^{Parallel} \tag{2.13}$$

where $F_i^{Perpendicular}$ is the component of force arising due to the potential perpendicular to the band and $F_i^{Parallel}$ is component of the spring force parallel to the band. The relaxation and optimisation of images is continued along the images until a minima is reached and at this point, the minima energy pathway (MEP) is said to be found. The climbing image modifier is applied to make sure the highest energy lies on the transition state found on the MEP [29, 31].

Implementation of NEB in VASP is through an extension available called VASP-vtst (VASP Transition State Tools) which is more accurate and reliable for such calculations [28–31]. The general methodology is to perform optimisation using a Quick Minima (QM) method which is similar to VASP geometric optimisation to get acceptable starting points and use more accurate methods of force minimisation such as Limited-memory

Broyden-Fletcher-Goldfarb-Shanno (LGFBS) and Conjugate Gradient Method (CGA) to find the transition state and MEP. Example INCAR files with NEB tags are shown in the appendix 7.1 to 7.3.

2.6.7 Vibrational Frequency Analysis

Vibrations in a molecule can be considered as simple harmonic motion between the atoms bonded together. The time period in such case can be defined by

$$T = 2\pi\sqrt{\frac{\mu}{k}} \tag{2.14}$$

where mass of atoms can be expressed as reduced mass μ and spring constant is k. VASP is used in this work to compute vibrational frequencies by invoking IBRION = 5 or 6 in the INCAR file. IBRION = 5 considers displacement of all the atoms in Cartesian coordinates whereas IBRION = 6 utilizes symmetry which decreases the computational cost. But usually computational costs can be decreased also by fixing the fixed atoms which are not studied by using *selective dynamics* in POSCAR and then fixing atoms by assigning F to the coordinates of those atoms.

A valid transition state corresponds to a maximum on the potential energy surface or MEP and therefore should contain a single negative or imaginary frequency corresponding to the mode or bond which is maximised in the transition state. Thus, a transition state can be confirmed to a valid state by performing frequency analysis.

2.6.8 Implicit Solvation

Most computational calculations are performed on gas phase molecules. As many experimental measurements and reactions are performed in the aqueous phase (or different solvents), it is important to study the interactions with the solvent and it's effect on energetics of the reaction to get a more accurate representation of the mechanism. In order

to counteract the errors arising due to solvent interactions, there are two main methods which are usually undertaken, the first is to use a fully ab-initio approach by explicitly modelling and averaging different solvent molecule configurations which is known as explicit solvation model. The second is to apply an implicit solvation model which is a parameterised approach in which the solvent molecules are replaced with a continuum dielectric. Thus the system which is being studied is placed in a homogeneous polarisable continuum which basically implies that the molecular configurations of the solvent are embedded in the model parameters. Though both methods have shown to accurately recreate experimental systems, a full explicit model is considered to give a more detailed representation of the system but it is also computationally expensive. The implicit solvation is a good compromise for including the effect of solvation for a system but is highly dependent on the accuracy of the model provided.

Solvation energy is calculated by additional terms in KS potential and energy. Electrostatic and cavitation interactions (cavity surface tension) are accounted for by smoothly varying the relative permittivity function over the solute-solvent boundary [32]. For solvent calculations, gas phase optimised ion positions and wavefunctions are taken as a starting point and the electronic contribution to solvation energy is measured by

$$E_{sol} = E_{tot:sol} - E_{tot:vac} \tag{2.15}$$

where $E_{tot:sol}$ is the energy of the system with implicit solvation model and $E_{tot:vac}$ is the energy of the system in gas phase. Implicit solvation has been used in this work and has been implemented through an extension called VASP-sol [32]. It is generally turned on by tag LSOL in INCAR. Other VASP input parameters that are defined include

```
EB_K     = Relative permittivity of the bulk solvent
SIGMA_K  = Width of the dielectric cavity
NC_K     = Cut-off charge density
TAU      = Cavity surface tension
```

Default solvent is considered to be water for which parameters are taken as 78.4, 0.6, 0.0025 and 0.000525. Water has been used as the solvation solvent throughout this work.

Bibliography

(1) J. A. Lopez-Sanchez, N. Dimitratos, P. Miedziak, E. Ntainjua, J. K. Edwards, D. Morgan, A. F. Carley, R. Tiruvalam, C. J. Kiely and G. J. Hutchings, *Phys. Chem. Chem. Phys.*, 2008, **10**, 1921–1930.

(2) J. A. Lopez-Sanchez, N. Dimitratos, C. Hammond, G. L. Brett, L. Kesavan, S. White, P. Miedziak, R. Tiruvalam, R. L. Jenkins, A. F. Carley, D. Knight, C. J. Kiely and G. J. Hutchings, *Nature Chemistry*, 2011, **3**, 551–556.

(3) T. Owen, *Fundamentals of UV-visible Spectroscopy: A Primer*, Hewlett Packard, 1996.

(4) S. Eustis and M. A. El-Sayed, *Chem. Soc. Rev.*, 2006, **35**, 209–217.

(5) S. Amelinckx, D. van Dyck, J. van Landuyt and G. van Tendeloo, in *Electron Microscopy*, Wiley-VCH Verlag GmbH, 2007, pp. 305–497.

(6) S. Amelinckx, D. van Dyck, J. van Landuyt and G. van Tendeloo, in *Handbook of Microscopy*, Wiley-VCH Verlag GmbH, 2008, pp. 563–594.

(7) J. W. Niemantsverdriet, *Spectroscopy in Catalysis Third Edition*, John Wiley & Sons, 2007.

(8) C. M. Cooper and P. J. Wiezevich, *Industrial and Engineering Chemistry*, 1929, **21**, 1210–1214.

(9) S. Al-Shihri, C. J. Richard and D. Chadwick, *ChemCatChem*, **9**, 1276–1283.

(10) G. Schwedt, in, John Wiley & Sons, 1997, pp. 142–173.

(11) N. Galina V., S.-F. Georg and S. Georgiy B., *Chem. Commun.*, 1997, 397–398.

(12) C. Hammond, S. Conrad and I. Hermans, *ChemSusChem*, 2012, **5**, 1668–1686.

(13) R. M. Sellers, *Analyst*, 1980, **105**, 950–954.

(14) C. J. Cramer and D. G. Truhlar, *Phys. Chem. Chem. Phys.*, 2009, **11**, 10757–10816.

(15) R. G. Parr and W. Yang, *Density functional theory of atoms and molecules*, Oxford University Press, 1989.

(16) F. Jensen, *Introduction to computational chemistry*, John Wiley & Sons, 2013.

(17) C. J. Cramer, *Essentials of computational chemistry: theories and models*, John Wiley & Sons, 2013.

(18) E. K. Gross and R. M. Dreizler, *Density functional theory*, Springer Science & Business Media, 2013, vol. 337.

(19) W. Koch and M. C. Holthausen, *A chemist's guide to density functional theory*, John Wiley & Sons, 2015.

(20) P. Hohenberg and W. Kohn, *Physical review*, 1964, **136**, B864.

(21) W. Kohn and L. J. Sham, *Physical review*, 1965, **140**, A1133.

(22) K. E. Atkinson, *An introduction to numerical analysis*, John Wiley & Sons, 2008.

(23) A. D. Becke, *Phys. Rev. A*, 1988, **38**, 3098–3100.

(24) J. P. Perdew and Y. Wang, *Physical Review B*, 1992, **45**, 13244.

(25) J. P. Perdew, K. Burke and M. Ernzerhof, *Physical review letters*, 1996, **77**, 3865.

(26) S. L. Dudarev, G. A. Botton, S. Y. Savrasov, C. J. Humphreys and A. P. Sutton, *Phys. Rev. B*, 1998, **57**, 1505–1509.

(27) S. Grimme, J. Antony, S. Ehrlich and H. Krieg, *The Journal of chemical physics*, 2010, **132**, 154104.

(28) D. Sheppard, R. Terrell and G. Henkelman, *The Journal of chemical physics*, 2008, **128**, 134106.

(29) G. Henkelman, B. P. Uberuaga and H. Jonsson, *The Journal of chemical physics*, 2000, **113**, 9901–9904.

(30) D. Sheppard and G. Henkelman, *Journal of computational chemistry*, 2011, **32**, 1769–1771.

(31) G. Henkelman and H. Jonsson, *The Journal of chemical physics*, 2000, **113**, 9978–9985.

(32) K. Mathew, R. Sundararaman, K. Letchworth-Weaver, T. A. Arias and R. G. Hennig, *The Journal of Chemical Physics*, 2014, **140**, 084106.

3 | Selective Oxidation of Methane with Au-Pd Colloids using H_2O_2 and O_2

3.1 Introduction

The direct oxidation of methane to methanol has been the subject of intensive study for many decades [1, 2]. Low temperature selective oxidation of methane has been extensively studied using a wide variety of homogeneous and heterogeneous catalysts [1, 3] including platinum based [4–6], iron based [7] and zeolite based catalysts such as Fe-Cu/ZSM [8, 9], Cu-SSZ-13 [10], Rh-ZSM-5 [11]. Homogeneous Au and Pd have also been investigated for low temperature methane oxidation [12, 13]. However, without strong oxidants such as selenic acid or trifluoroacetic acid, the catalyst was not effective in activating methane to produce oxygenated products. Mild oxidation in aqueous conditions with homogeneous chloroauric acid led to precipitation of Au^0 and deactivation of the catalyst [14]. C-H activation has been also been widely investigated using noble metal Au-Pd catalysts prepared by sol immobilisation following the study demonstrating primary C-H bond activation in toluene using O_2 at elevated temperature (160 °C) [15].

The aforementioned reactions are considered to be linked by the hydroperoxy intermediate which could be formed by oxidants like H_2O_2 and tert-butyl hydroperoxide (TBHP). Since, hydroperoxy intermediate formation was also found in methane oxidation in previous studies [4, 8], Au-Pd nanoparticles were tested for the reaction. TiO_2 supported

bimetallic Au-Pd nanoparticles were shown to be active for methane oxidation at 50 °C using H_2O_2 as the oxidant [16]. The synergistic effect of gold and palladium was found to not only increase the catalytic activity but also improve selectivity and efficiency of the reaction. Since bimetallic Au-Pd catalysts have also been extensively studied for direct synthesis of H_2O_2 [17, 18], they were employed for methane oxidation using *in-situ* produced H_2O_2 by using a mixture of H_2, O_2, CH_4 and N_2. A similar productivity but higher methanol selectivity was observed when using the in-situ generated H_2O_2 compared to commercial ones.

In this chapter, the intrinsic methane oxidation activity of the Au-Pd nanoparticles is investigated. The differences in catalytic activity of the supported and unsupported nanoparticles is studied. And the effect of supporting the nanoparticles is characterised using electron microscopy and x-ray photoelectron spectroscopy. Au-Pd colloidal nanoparticles have been stabilised using PVP polymer to prevent agglomeration and destabilisation during the reaction. Thus, blank reactions were also carried out to measure any contribution of the polymer to liquid oxygenate productivity due to its degradation.

3.2 Comparison Between Supported Au-Pd Catalysts and Colloidal Catalysts

During the previously reported investigations of Au-Pd/TiO_2 catalysts, catalysts prepared by incipient wetness were found to be five times more productive compared to the sol-immobilised catalysts. The sol-immobilised supported catalysts also consumed all of the 5000 μmol H_2O_2 which was added to the reaction as the oxidant compared to the incipient wetness catalyst which consumed 2894 μmol H_2O_2 while producing more products [16]. H_2O_2 consumption is a very important factor to consider in CH_4 oxidation reactions because of the high cost associated with H_2O_2 oxidant. It was suggested that high H_2O_2 decomposition rates which led to lower activity was facilitated by the small size and metallic nature of the Au-Pd nanoparticles. Sol-immobilised catalysts have been pre-

viously shown to have marrower particle size distribution ranging between 4-7 nm compared to the catalysts prepared by incipient wetness where particle size ranged between 2 and 14 nm with occasional larger particles with sizes greater than 25 nm [19]. There is also a size dependent composition variation. Thus, the degree of control of the particle composition was also found to be worse than incipient wetness samples with particles were shown to have Pd-rich morphology. Impregnated catalysts also show lower rates for H_2o_2 decomposition compared to sol-immobilised catalysts which is attributed to the particle size [20]. Thus, this low un-selective methane oxidation with as-prepared sol-immobilised catalysts was ascribed to the particle size and morphology of the supported Au-Pd nanoparticles. Heat treatments were performed to increase the particle size and to modify the nanoparticle morphology to improve the catalytic turnover and decrease H_2O_2 decomposition rates [21]. After high temperature calcination of the TiO_2 support at 800 °C for 3 hours, followed by catalyst calcination at 800 °C for 3 hours, 3.43 μmol of total oxygenates were formed consuming 1785 μmol of H_2O_2 making the reaction highly inefficient. The gain factor, defined as mol of oxygenate produced/mol of H_2O_2 consumed, in this case was calculated to be 2×10^{-3}.

The sol-immobilisation preparation technique can be used to prepare unsupported colloidal nanoparticles which can then be supported on a variety of high surface area support materials. This allows for direct comparison between the nanoparticles of similar size and composition with, and without supports. It also provides a tool to understand the influence of metal-support interactions and active sites in isolation. In the previous study, TiO_2 was used as the support for the majority of the work. Though TiO_2 is well known for activating H_2O_2 to produce peroxo- or hydroperoxo- species, no methane oxidation was observed with TiO_2 as the catalyst without the Au-Pd components. Though the support can affect the conversion and selectivity, due to its influence on shape and morphology of metal nanoparticle, in this case, however, not much of a difference was found in the activity by depositing the Au-Pd nanoparticles on different supports like TiO_2, C, SiO_2, CeO_2, and Al_2O_3 [22]. The productivity with different support ranged from 0.10-0.30 $mol_{(products)}kg^{-1}_{(cat)}h^{-1}$. In the study, the highest H_2O_2 efficiency was achieved with Al_2O_3

but even with Al_2O_3, 2058 μmol was consumed producing 2.74 μmol of total products still with the gain factor of 1.4×10^{-3}. This indicated that the supported catalysts were inherently inefficient towards methane oxidation in spite of the high consumption of H_2O_2.

3.2.1 Degradation of Hydrogen Peroxide

In order to investigate which component of the sol-immobilised catalyst system was responsible for the observed high rates of H_2O_2 consumption during methane oxidation, H_2O_2 degradation reactions were carried out at ambient temperature in glass vials using 6.6 μmol of metal. This was done by using either the supported catalyst or the colloidal solution and 1000 μmol of H_2O_2 (by adding 57 μl of 50 wt.% H_2O_2) and the amount of H_2O_2 was then measured using spectrophotometrically every 10 mins (Figure 3.1). When using the supported Au-Pd nanoparticles, over 90% of H_2O_2 was degraded in 30 mins; in comparison, when the same amount of metal was added in a colloidal solution, less than 10% of the initial H_2O_2 amount was degraded in 30 mins. Control reactions also show that H_2O_2 was stable in the presence of bare TiO_2 and that the thermal contributions also do not account towards high H_2O_2 degradation rates of H_2O_2 alone in the vial (Figure 3.1). Interactions of H_2O_2 with rutile and anatase TiO_2 have been computationally studied and the direct decomposition into hydroxyl groups is not kinetically facile [23]. The high degradation rate was only observed when the nanoparticles were supported on the TiO_2 support material. Though lower rates of H_2o_2 degradation are reported for impregnated catalysts as compared to sol-immobilised catalysts, the rates are higher compared to unsupported catalysts [22, 24]. Higher rates in sol-immobilised catalysts is usually attributed to smaller size compared to impregnated catalysts and the latter have also been shown to have lower H_2O_2 decomposition/hydrogenation rates [20, 22].

Supporting nanoparticles on materials like TiO_2 leads to a change in morphology and faceting of the nanoparticles compared to their equilibrium structure in solution [25, 26]. Higher proportions of close packed (111) and open (100) facets are proposed to be found in supported catalysts. These faceted catalysts show higher O-O bond scisson, readily

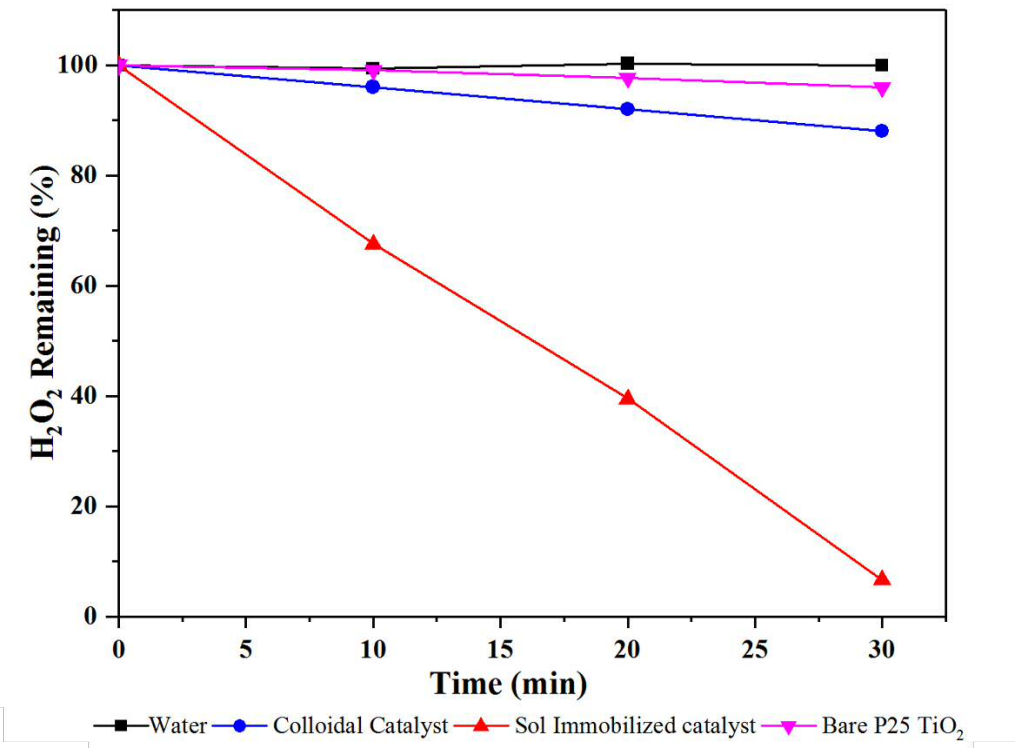

Figure 3.1: Hydrogen peroxide degradation was carried out at ambient pressure and room temperature. 1000 μmol H_2O_2 was added to 10 mL of Au-Pd colloid (blue line), or water containing 100 mg of sol immobilized 1 wt.% Au-Pd/TiO_2 catalyst (red line), pure water (black line) or bare TiO_2 (purple line) in a glass vial. The H_2O_2 concentration was measured every 10 min in this test.

producing *OH and *O species [27]. H-transfer reaction to those species is also thermodynamically favoured to form H_2O. Slower rates of of O-O bond scisson are observed in colloids leading to lower H_2O_2 decomposition. This high H_2O_2 degradation on supported catalyst could also be attributed to the formation of interfacial sites between the nanoparticles and the oxide material which enhances H_2O_2 decomposition [28]. It has been shown that oxygen does not strongly adsorb onto Au or TiO_2, but has a higher binding affinity to Au-Ti^{+4} perimeter dual sites [29]. Theoretical calculations have also shown that at this Au-Ti interface, there is direct electron transfer from Au to Ti and subsequent electron transfer to the 2π* anti-bonding orbitals weakening the O-O bond aiding its scisson [30].

As previously discussed in subsection 1.6.2, stabilising agents play an important role in many reactions with nanoparticles in tuning the activity and selectivity of reactions [31, 32]. Stabilising polymers are not only known to stabilise the bimetallic nanoparticles to avoid aggregation but can also block some of the active sites, hence controlling the

rate of the reaction [32, 33]. PVP (Polyvinylpyrrolidone), one of the most commonly used stabilising agent, also used in this work, is known to bind to the surface of metal nanoparticles through carbonyl groups and/or the nitrogen atom of the pyrrolidone ring [31]. PVP monomer is considered to chemisorb with the oxygen atom in the ring to the Pd nanocrystal surface capped with a large number of PVP molecules [34]. Similarly, Density Functional Theory (DFT) studies suggest PVP units bind to Au surfaces through O atoms with binding energy dominated by Van der Waals interactions [35]. It is likely that the strong metal-polymer binding blocks some of the active sites from the colloidal surface decreasing the rate of H_2O_2 decomposition which will be studied later in this thesis. PVP adsorbed on to TiO_2 also showed no H_2O_2 degradation. In Au-Pd on TiO_2 supported catalysts, it has also been considered that ligand molecules can be locally displaced from the interface region leading to enhanced adhesion and increase in periphery sites which again could increase H_2O_2 decomposition [25].

These interesting results show that PVP-stabilised unsupported Au-Pd nanoparticles do not lead to high degradation of H_2O_2 at ambient temperature and pressure as compared to supported nanoparticles. The effect of high decomposition of H_2O_2 on oxidation reactions is vital to study for development of better catalysts as it is used as an oxidant in reactions such as methane oxidation. It also becomes an important factor to consider, especially industrially, due to the high cost associated with H_2O_2. Since, it has been shown that high degradation of H_2O_2 led to lower activity in supported catalysts [22], it was considered that lower degradation rates of H_2O_2 could translate into higher methane oxidation activity. With that aim in mind, Au-Pd-PVP colloids were tested for methane oxidation.

3.2.2 Methane Oxidation Activity

High H_2O_2 degradation rates not only lead to water formation, but also produce high radical concentrations due to homolytic scisson of O-O bond. High concentration of radicals can cause quick termination of reactive radical species or facilitate recombination reactions to generate water and oxygen. High concentration of ·OH radicals could also be

quenched due to "wall reactions" with the reactor components and metal-support interfacial sites [36]. This could be detrimental to methane oxidation because the rates of radical destruction are too high to allow sufficient interaction with low amount of dissolved CH_4. This lack of reaction between CH_4 and H_2O_2 was responsible for the low activity observed with 1 wt.% Au-Pd/TiO_2. 100 mg of 1 wt.% Au-Pd/TiO_2 sol-immobilised catalyst with total metal loading of 6.6 μmol was tested for methane oxidation in Parr autoclave reactors. The reactor was charged with 1000 μmol of H_2O_2 and 10 ml of water. Standard reaction conditions included a methane pressure of 30 bar and reaction temperature of 50 °C while the reaction was stirred during temperature ramp-up to ensure uniform heating and avoid local heat spots. Quantitative NMR spectroscopy was used to analyse the reaction solutions to quantify liquid phase products and GC was used to quantify CO_2 as described in Chapter 2. The TiO_2 supported Au-Pd nanoparticles produced 1.6 μmol of total products with a very low primary oxygenate selectivity of 26% and consumed 73% of H_2O_2 available in 30 minutes of testing (Figure 3.2). High surface area TiO_2, which is used as the support, is also known to quench radical reactions and might also have contributed to lowering the reaction rates observed [37]. To ensure that loss of methanol does not occur since methanol is known to bind strongly to TiO_2, reactions were carried out by stirring 20 μmol CH_3OH with 100 mg of supported 1 wt.% Au-Pd/TiO_2. The concentration of methanol was measured over time. No loss in CH_3OH concentration was observed over 2 hours. Reaction was also carried out with the supported catalyst and analysis was performed without filtration. In this case, no increase in products was observed. Thus, low methane oxidation activity was associated with supported catalysts.

As seen in figure 3.1, a decrease in H_2O_2 degradation rate was observed with the same amount of metal in Au-Pd aqueous colloidal solution. Thus, the colloidal catalyst was tested for methane oxidation reaction by adding 1000 μmol of H_2O_2 in 10 mL of aqueous colloid with a metal concentration of 6.6 μmol for direct comparison with the supported catalyst while the metal ratio of Au to Pd was also kept as 1:1. Figure 3.2 shows the comparison in the activity between the supported and unsupported Au-Pd nanoparticles with same amount of metal. 16.8 μmol of total products were generated on using aqueous

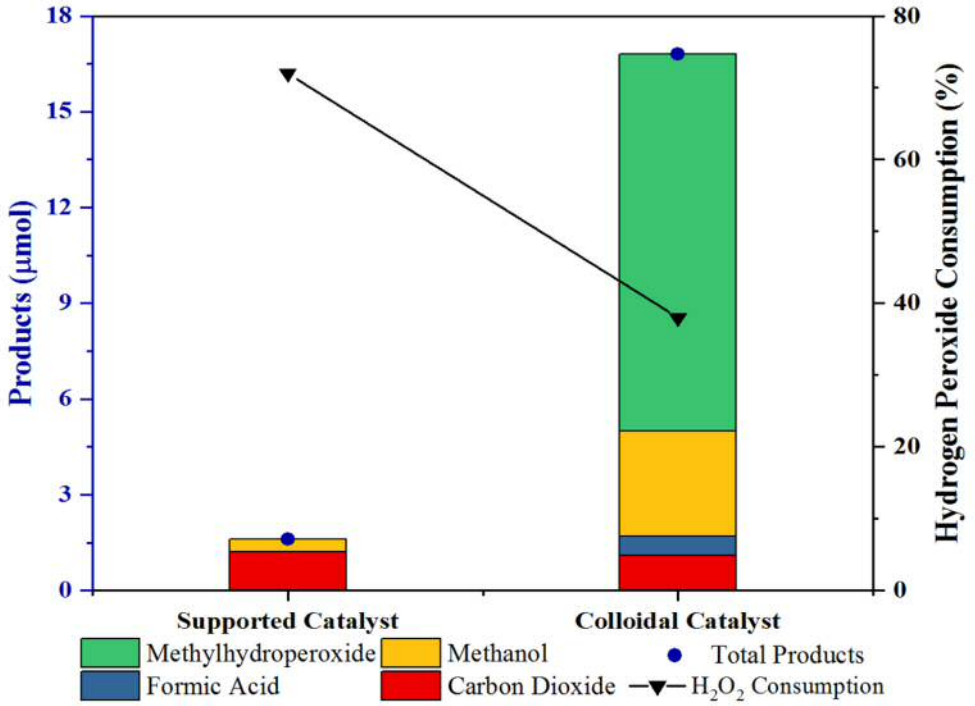

Figure 3.2: Methane oxidation activity of supported and colloidal Au-Pd catalysts using H_2O_2. Test conditions: Pressure (CH_4) = 30 bar, catalyst: 6.6 μmol of metal (1:1 metal molar ratio), 1000 μmol H_2O_2, 50 °C (ramp rate of 2.25 °C/min), 1500 rpm, 30 min.

Au-Pd-PVP colloid with much higher oxygenate selectivity of 90% and only 1.1 μmol of CO_2 was produced. No methane oxidation activity resulting from H_2O_2 auto-oxidation was observed in the absence of colloids or supported catalysts.

The presence of methylhydroperoxide, methanol, formic acid and carbon dioxide in the product stream was found to be consistent with previous studies performed with supported catalysts as shown in figure 3.3 [16]. Au-Pd colloids produced 11.8 μmol of CH_3OOH, 3.3 μmol of CH_3OH and 0.6 μmol of HCOOH as the liquid oxygenates during the reaction. As seen from the product distribution (Figure 3.2) and reaction scheme (Figure 3.3); the primary oxygenates, CH_3OOH and CH_3OH have been formed with highest selectivity while only 6.5% CO_2 was formed which is in contrast to results obtained with a supported catalyst, which formed 75% CO_2.

H_2O_2 consumption was also much lower with unsupported nanoparticles. 38% of available H_2O_2 was used during the reaction with colloids compared to 73% of H_2O_2 which was used with a supported catalyst which made the reaction much more efficient with

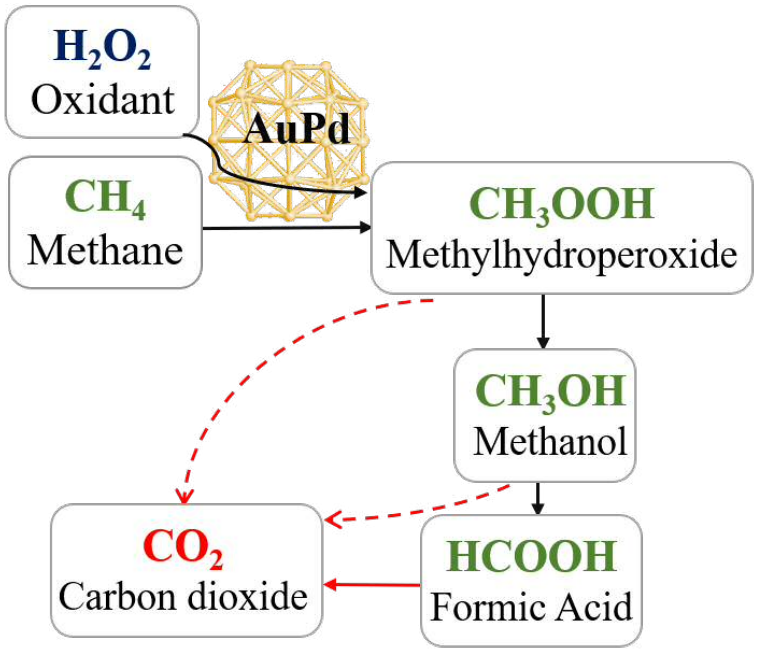

Figure 3.3: Oxidative reaction pathway for methane oxidation

respect to H_2O_2 usage. The oxygenate productivity of the colloidal system was calculated to be 29.4 $mol_{(products)}kg^{-1}_{(cat)}h^{-1}$ compared to 0.03 $mol_{(products)}kg^{-1}_{(cat)}h^{-1}$ when the same amount of metal was supported on TiO_2. The four order of magnitude increase is partly due to difference in the amount of products produced but mainly also due to the extremely low catalyst mass used in colloidal reaction. For this reason, it is useful to compare the catalyst efficiency in terms of gain factor. The colloidal catalyst was found to be one order of magnitude more efficient than supported Au-Pd/TiO_2, with higher gain factor of 3×10^{-2} when compared with 2×10^{-3} for supported catalyst.

These results show that not only Au-Pd unsupported nanoparticles are active for selective oxidation of methane but they also utilise H_2O_2 more efficiently compared to TiO_2 supported Au-Pd sol-immobilised catalysts. In addition, the colloidal catalysts show lower H_2O_2 decomposition without the support indicating that the presence of metal-support interface is not required for this reaction but might be detrimental for its efficacy. The colloidal catalysts also show three times higher selectivity towards the desired products avoiding total oxidation to CO_2.

Though the lower rate of H_2O_2 degradation was considered to be an important factor in

increasing the activity of Au-Pd-PVP colloid, other differences between the unsupported nanoparticles and supported catalysts should also considered. One such possibility was the stabilising polymer (PVP) which used during catalyst preparation. The polymer plays an important role as a stabilising agent for control of particle size and composition [31]. Furthermore, it has also been shown to affect catalytic activity and stability by interacting with metal surface sites. However; in the case of supported catalysts, the polymer stabiliser could be removed from the catalytic surface using a heat-treatment or by reflux [38]. In this case, the nanoparticles are not supported and removal of the polymer is not required. It is also not possible to perform the heating or washing step to remove the polymer from the colloid. Hence, it is essential that the polymer does not degrade or oxidise during the reaction.

During catalyst preparation, the metal to polymer ratio used was 1:1.2 resulting in 120 μl of 1 wt.% PVP solution in 10 ml of aqueous solution. Blank reactions were then carried out in absence of methane under standard conditions. 120 μl of 1 wt.% PVP solution in 10 ml of water and PVP stabilised Au-Pd colloid with total metal concentration of 6.6 μmol of metal were tested for any oxidation/degradation activity. In the absence of methane, no oxidation products were observed with either the colloidal catalyst or the polymer on its own as shown in table 3.1.

Table 3.1: Blank reactions carried out with the Au-Pd-PVP colloid and the PVP ligand.

Entry	Catalyst	Product amount (μmol)				H_2O_2 Consumed / %	Gain Factor
		CH_3OOH	CH_3OH	HCOOH	CO_2		
1	PVP	0	0	0	n.d.	2	0
2	Au-Pd-PVP	0	0	0	n.d.	3	0

Test conditions: 1000 μmol H_2O_2, 50 °C (ramp rate of 2.25 °C/min), 1500 rpm, 30 min. Entry 1: 120 μl of 1 wt.% PVP solution in water, Entry 2: Colloidal Au-Pd-PVP colloid, 6.6 μmol of metal (1:1 metal molar ratio)

The stabilising polymer PVP used in this case did not produce any products under reaction conditions. Reactions were also carried out with PVP solution in presence of 30 bar CH_4

in the gas phase. Similarly, 120 μl of 1 wt.% PVP solution in water was used as the catalyst along with 1000 μmol H_2O_2. The reactor was then pressurised with 30 bar CH_4 and the reaction mixture was characterised by using NMR after the end of the reaction (Figure 3.4). No products were observed in the reaction performed with PVP solution. A peak corresponding to dissolved methane (s, $\delta = 0.2$) was seen in the NMR spectrum which indicated enhanced solubility of methane due to presence of the PVP polymer which is attributed to the organic nature of the polymer.

Furthermore, to ensure that all oxidation products originated from gas phase CH_4 and not from the polymer during reactions with Au-Pd-PVP colloid, reactions were carried out with isotopically labelled CH_4 to identify such products. The reaction was carried out by replacing a portion of $^{12}CH_4$ with $^{13}CH_4$.

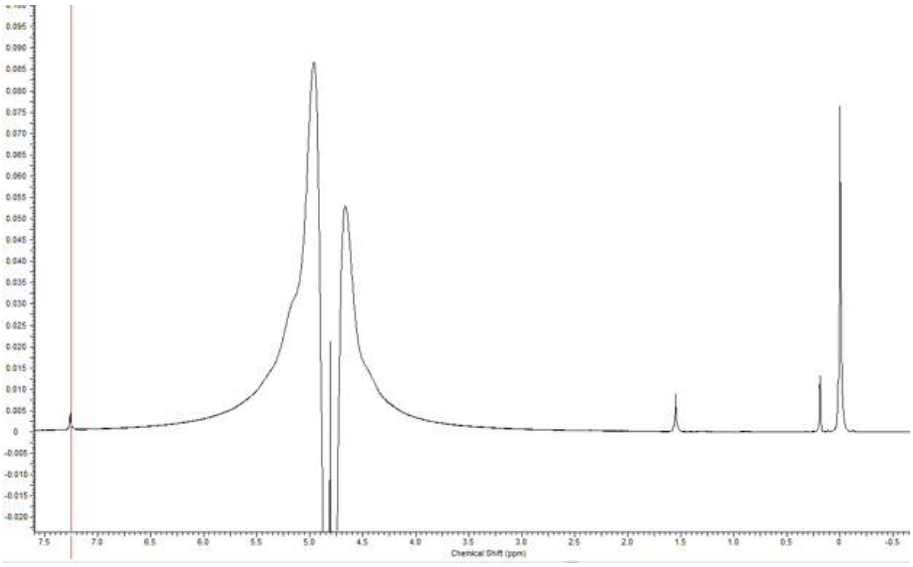

Figure 3.4: NMR spectrum of reaction carried out with PVP in presence of CH_4 showing methane solubility.

NMR analysis was carried out on the reaction mixture and satellite peaks were integrated along with the main peak to quantify the labelled products (Figure 3.5). Satellite peaks for $^{13}CH_3OOH$ (δ = 3.90 and δ = 3.66), $^{13}CH_3OH$ (δ = 3.39 and δ = 3.16) and $H^{13}COOH$ (δ = 8.34 and δ = 7.98) were observed along with main ^{12}C peaks ($^{12}CH_3OOH$ δ = 3.79, $^{12}CH_3OH$ δ = 3.28 and $H^{12}COOH$ δ = 8.17 respectively). On evaluating the peak areas, it was found that the 10% of oxygenates containing ^{13}C isotope corresponded to the 3 bar

of isotopically labelled CH_4 that was added to the reactor.

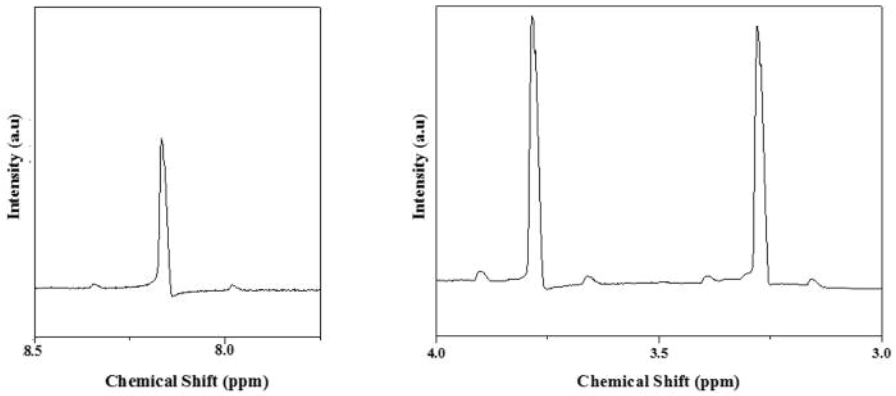

Figure 3.5: ^{13}C isotopically labelled products are observed along with main ^{12}C peaks. Data provided by Dr Rebecca McVicker.

These studies confirmed that PVP could be used as the polymer to prepare Au-Pd unsupported nanoparticles and it was stable under reaction conditions. Furthermore, all products that were detected during methane oxidation originate from gas phase methane without any contribution from oxidation or degradation of PVP. In these cases, organic polymer coating might be assisting CH_4 solubility. Further studies on the effects of stabiliser will be be performed and discussed about throughout the thesis.

3.3 Methane Oxidation with Oxygen using Colloids

Previously, electron paramagnetic resonance (EPR) spin trapping studies were conducted on sol-immobilized Au-Pd/TiO_2 catalysts. The spin trapping experiments showed both hydroxyl (·OH) and methyl (·CH_3) radicals indicating that the reaction proceeds via a radical mechanism [16]. Other oxygen based radicals could not be detected in EPR but they could not be excluded because of experimental and analytical procedure which leads to quick conversion of ·OOH to ·OH [39]. There is also a possibility of formation of superoxide species and radical quenching which is associated with the titania support that could lead to destruction of radicals before they are trapped [15, 37]. Based on these

observations, a methane oxidation reaction mechanism was hypothesised as shown in figure 3.6. Methyl radicals are considered to be generated via H abstraction by hydroxyl radicals which are in-turn produced due to homolytic cleavage of H_2O_2 [40]. CH_3OOH is the primary oxidation product which can be formed either by primary termination step between $\cdot CH_3$ and $\cdot OOH$ radicals or by recombination of $\cdot CH_3$ with dissolved O_2 in the solution followed by protonation [41]. This dissolved O_2 could potentially also originate from H_2O_2 decomposition. The reaction of $\cdot CH_3$ with O_2 has been reported to occur with high rates in gas phase methane oxidation reactions [42].

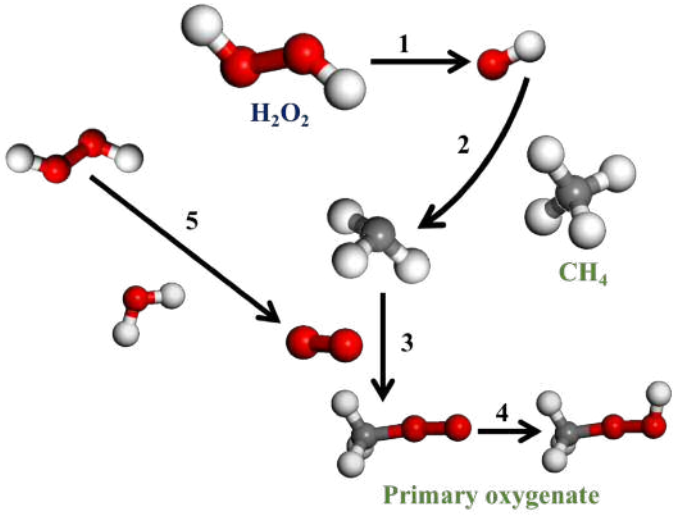

Figure 3.6: Proposed reaction mechanism for methane oxidation to CH_3OOH.

As shown earlier, decomposition of H_2O_2 proceeded at a much slower rate with unsupported colloidal catalysts compared to Au-Pd/TiO_2 sol-immobilised catalyst. The depressed O-O bond cleavage would suggest sluggish generation of $\cdot OH$ radicals, hence producing $\cdot CH_3$ radicals over a longer time scale. Also, O_2 production would be slower in this case. Since, fast reaction between $\cdot CH_3$ and O_2 is known to occur, it was considered that this reaction can be facilitated by adding molecular oxygen. This was tested by adding 5 bar of O_2 along with the 30 bar of CH_4 in gas phase and 1000 μmol H_2O_2 in 10 ml of aqueous Au-Pd-PVP colloid. Oxidation reactions were then carried out at 50 °C under standard conditions. Figure 3.7 shows the comparison in activity and efficiency with and without O_2. On addition of 5 bar O_2 in the gas phase, higher methane oxidation activity was observed. 28.3 μmol of products were generated in presence of O_2 when

compared to 16.8 μmol which were produced in the absence of O_2. The high primary oxygenate selectivity of 88% was maintained and only 1.5 μmol of CO_2 was produced during the reaction. The oxygenate productivity of the colloidal catalysts in presence of O_2 was calculated to be 53.6 $mol_{(products)}kg^{-1}_{(cat)}h^{-1}$ compared to 29.4 $mol_{(products)}kg^{-1}_{(cat)}h^{-1}$ in absence of O_2 with the same amount of metal.

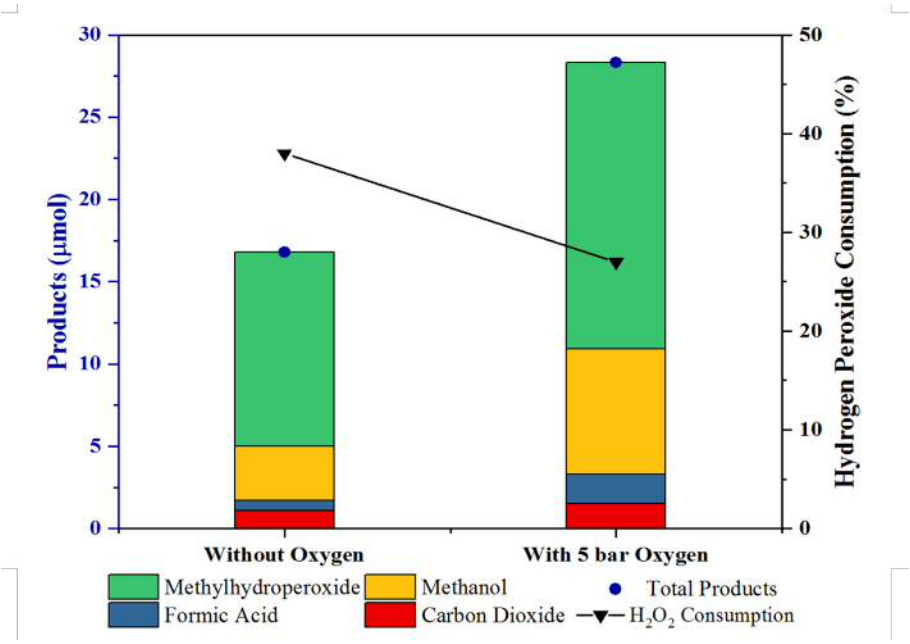

Figure 3.7: Methane oxidation activity of Au-Pd colloid using H_2O_2 and O_2. Test conditions: Pressure (CH_4) = 30 bar, pressure (O_2) = 5 bar, catalyst: 10 mL Au-Pd-PVP colloid, 6.6 μmol of metal (1:1 metal molar ratio), 1000 μmol H_2O_2, 50 °C (ramp rate of 2.25 °C/min), 1500 rpm, 30 min.

Similar to the previous reaction,CH_3OOH, CH_3OH, HCOOH and CO_2 were formed in the product stream. Colloids produced 17.4 μmol of CH_3OOH, 1.8 μmol of CH_3OH and 0.6 μmol of HCOOH as the liquid oxygenates during the reaction in presence of O_2. CH_3OOH and CH_3OH were formed with the high selectivity and only 5.3% CO_2 is formed during the reaction.

The reaction carried out in presence of O_2 was also carried out in presence of 1000 μmol H_2O_2. As shown in figure 3.7, H_2O_2 consumption also dropped down in presence of O_2, consuming only 27% of the available H_2O_2 when compared to 38% that was consumed without gas phase O_2. This led to increase in the reaction efficiency and the gain factor was calculated to be 9×10^{-2}. This gain factor remained an order of magnitude higher

than 2×10^{-3} which was calculated for the supported catalyst and it was also much higher compared to the reaction in absence of O_2 which led to the gain factor of 3×10^{-2}.

Higher productivity and lower H_2O_2 decomposition with gas phase O_2 indicated the role of O_2 in production of products. Since formation of methylhydroperoxy species is also possible by recombination of $\cdot CH_3$ radical with O_2, it is considered that primary product generation is promoted by this additional O_2 which is present in higher concentration than the O_2 originating from the decomposition of H_2O_2. To study the role of gas phase O_2 and probable incorporation of O_2 into primary products, a labelling experiment was performed. The CH_4 oxidation reaction was carried out by replacing the 5 bar of gas-phase molecular O_2 with ^{18}O labelled O_2. 1000 μmol $H_2{}^{16}O_2$ was added in the liquid phase colloid and the reaction was carried out at 50 °C. Since ^{18}O is not an NMR active molecule, the isotope labelled products could not be differentiated using NMR. Thus GC-MS was used to analyse these reaction mixtures, since it could separate and analyse products by masses. As described in the experimental chapter, compounds are vaporised in the injector of GC prior to analysis. CH_3OOH was found to be degraded into CH_3OH due to high injection temperature and good quantitative agreement was found between product quantification through NMR and GC-MS as shown in figure 2.10.

The intensities are measured with the relative to the base peak which has the highest response which is peak at m/z = 31 here. CH_3OH and ^{18}O labelled CH_3OH has been observed by analysing the peaks at m/z 32 and 34 respectively. Figure 3.8 shows the mass spectrometry analysis of the reactions performed with $H_2{}^{16}O_2$ + $^{16}O_2$ showing mass of $CH_3{}^{16}OH$ at 32 m/z and $H_2{}^{16}O_2$ + $^{18}O_2$ with m/z = 34 showing $CH_3{}^{18}OH$.

As shown in Figure 3.8, reactions carried out with $^{18}O_2$ showed that 51% of the observed signal for CH_3OH mass fragments contained the ^{18}O label. This indicated that more than 50% of the product formation was the result of reaction with the gas phase O_2 demonstrating the role of O_2 in formation on primary products. Previous studies have shown the absence of evidence of scrambling between O_2, H_2O_2 and H_2O [43, 44].

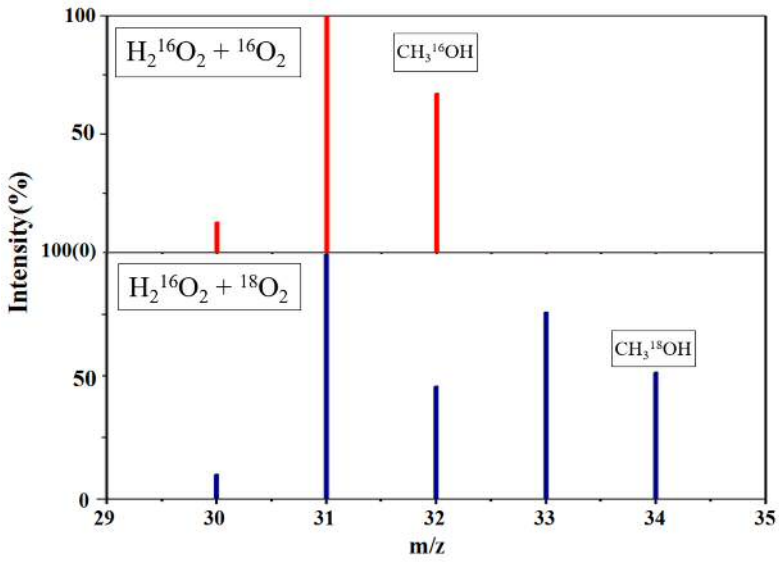

Figure 3.8: GC mass spectrum of methanol formed (m = 32 or 34) during methane oxidation using a Au-Pd-PVP colloid with 1000 μmol $H_2{}^{16}O_2$ + $^{16}O_2$ (*above*) or 1000 μmol $H_2{}^{16}O_2$ + $^{18}O_2$ (*below*). Test conditions: Pressure (CH_4) = 30 bar, pressure (O_2) = 5 bar, catalyst: 10 mL Au-Pd-PVP colloid, 6.6 μmol of metal (1:1 metal molar ratio), 1000 μmol H_2O_2, 50 °C (ramp rate of 2.25 °C/min), 1500 rpm, 30 min.

Reactions carried out in the absence of H_2O_2 with only O_2 showed no product formation confirming the need for H_2O_2 for the reaction to proceed. Since reactions proceed with only H_2O_2 with higher decomposition, it is highly likely that product generation in that case happens due to reaction with O_2 formed due to H_2O_2. Thus control over H_2O_2 decomposition rates along with use of molecular O_2 can be used to create more efficient catalytic systems. Since, Au-Pd/TiO_2 supported catalysts are also considered to show a similar reaction mechanism, CH_4 oxidation reactions were carried out in presence of O_2 and H_2O_2 with 100 mg of 1 wt.% Au-Pd/TiO_2. Data is shown for different amounts of H_2O_2 in table 3.2. But as seen earlier, due to the presence of support, high consumption of H_2O_2 was observed along with no appreciable increase in the activity.

Table 3.2: Methane oxidation activity of Au-Pd supported using H_2O_2 and O_2.

Entry	H_2O_2 Added μmol	Product amount (μmol)				Oxygenate Selectivity	Oxygenate Productivity	H_2O_2 Consumed / %	Gain Factor
		CH_3OOH	CH_3OH	HCOOH	CO_2				
1	1000	0	0.3	0.7	0.3	76.9	0.026	65	0.001
2	50	0	0.1	0.1	0.1	50	0.004	100	0.002

Test conditions:Pressure (CH_4) = 30 bar, pressure (O_2) = 5 bar, catalyst: 100 mg 1 wt.% Au-Pd/TiO_2, 6.6 μmol of metal (1:1 metal molar ratio) , 50 °C (ramp rate of 2.25 °C/min), 1500 rpm, 30 min. [a]Oxygenates productivity = $mol_{oxygenates} kg_{cat}{}^{-1} h^{-1}$

These results conclusively demonstrate the use of O_2 in methane oxidation with high selectivity and minimal over-oxidation to CO_2. Colloids show a much higher efficiency when compared to the supported catalysts which is increased by gas phase O_2. A decrease in H_2O_2 consumption is also noted with substantial incorporation of molecular O_2 in primary oxygenates.

3.4 Effect of H_2O_2 on Reaction Efficiency

In the previous section, a decrease in H_2O_2 consumption was demonstrated with the addition of O_2. And this O_2, which was added to the gas phase, was shown to act as an oxidant to synthesise CH_3OOH. Thus it is also possible to decrease the amount of H_2O_2 that is added in the beginning of the reaction. It is considered that decrease of H_2O_2 concentration and addition of O_2 could decrease the rate of H_2O_2 decomposition rate. Figure 3.9 shows the effect of different amounts of H_2O_2 used in the reaction on the amount of products and the selectivity towards the primary oxygenates. Gain factor was also measured for these reactions to analyse the influence of H_2O_2 concentration on the efficiency of the reaction.

Previous reactions were performed with 1000 μmol H_2O_2. Firstly, increasing the amount of H_2O_2 was investigated. Here , the reaction was carried out by adding 2000 μmol over 60 minutes while maintaining 5 bar of O_2 in gas phase. Upon increasing the amount of H_2O_2 from 1000 to 2000 μmol, the quantity of products formed initially decreased

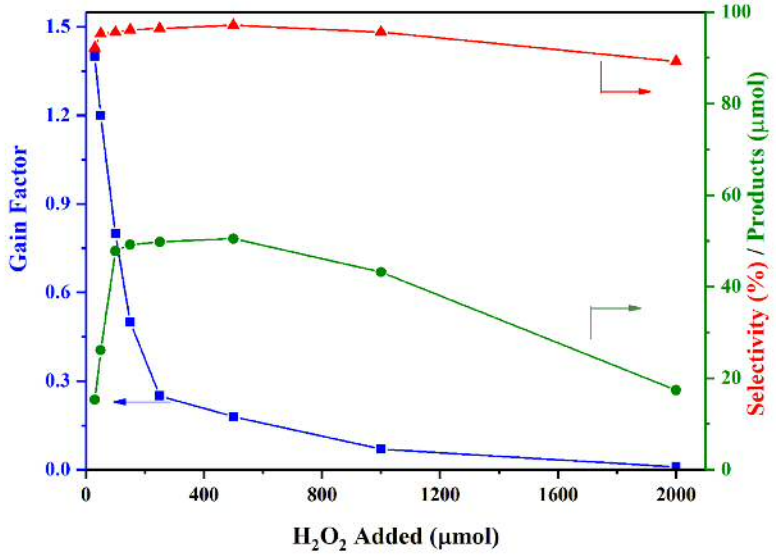

Figure 3.9: Effect of amount of H_2O_2 used on Gain factor (blue squares), product selectivity (red triangles) and total amount of products (green circles). Test conditions:Pressure (CH_4) = 30 bar, pressure (O_2) = 5 bar, catalyst: 10 mL Au-Pd-PVP colloid, 6.6 μmol of metal (1:1 metal molar ratio) , 50 °C (ramp rate of 2.25 °C/min), 1500 rpm, 60 min.

from 43 μmol to 18 μmol. This decrease coincided with increase in the amount of H_2O_2 consumption from 64% to 81%. 1620 μmol of H_2O_2 was consumed out of 2000 μmol in 60 min. A full breakdown with the entire product distribution with different amount of H_2O_2 addition along with oxygenate selectivity is given in table 3.3.

Increasing the H_2O_2 concentration led to a decrease in catalytic efficiency and activity. It can be considered that this is likely due to termination of radical reactions due to an excess of H_2O_2. Since this might limit product formation, reactions were then carried out by decreasing the amount of H_2O_2 added. When the reaction was performed with 500 μmol H_2O_2, there was a slight increase in the reaction products. 50 μmol of reaction products were formed with 97% oxygenate selectivity. There was also a decrease in H_2O_2 consumption. About 50% H_2O_2 was consumed yielding a higher gain factor of 0.2. On further decreasing the amount of H_2O_2 added to 250 μmol, a productivity of 49.2 $mol_{(products)}kg^{-1}_{(cat)}h^{-1}$ was obtained while consuming 165 μmol H_2O_2. Upon the addition of 150 μmol H_2O_2, 49.2 μmol of oxygenates were produced with a gain factor of 0.5. Similar to the reaction oxidative pathway, CH_3OOH was formed with highest selectivity

Table 3.3: Methane oxidation activity of Au-Pd colloid by varying H_2O_2 with O_2.

Entry	H_2O_2 Added μmol	Product amount (μmol)				Oxygenate Selectivity	Oxygenate Productivity	H_2O_2 Consumed	Gain Factor
		CH_3OOH	CH_3OH	HCOOH	CO_2				
1	2000	11	6	0.34	2.1	89	17.3	1622	0.01
2	1000	27.4	12	3.8	2	96	43.2	638	0.07
3	500	31.4	14.5	4.6	1.5	97	50.5	246	0.2
4	250	34.7	10.5	4	1.8	96	49.8	165	0.3
5	150	35	10	4.8	2	96	49.2	93	0.5
6	100	31.1	10.3	6.4	2.2	96	47.8	60	0.8
7	50	18.5	5.4	2.2	1.3	95	26.1	22	1.2
8	30	10.2	3.7	1.4	1.3	92	15.3	11	1.4
9	20	4.4	2.4	0.6	1.2	89	8.6	6 1.43	

Test conditions:Pressure (CH_4) = 30 bar, pressure (O_2) = 5 bar, catalyst: 10 mL Au-Pd-PVP colloid, 6.6 μmol of metal (1:1 metal molar ratio) , 50 °C (ramp rate of 2.25 °C/min), 1500 rpm, 60 min.

while an oxygenate selectivity of 96% was observed.

A very slight decrease in products was observed on addition of 100 μmol H_2O_2. A productivity of 47.8 $mol_{(products)}kg^{-1}_{(cat)}h^{-1}$ was observed with a high oxygenate selectivity of 96%. It was also observed that the change in product formation is not high when compared to the change in H_2O_2 concentration from 1000 μmol to 100 μmol, especially with the 500, 250, 150 μmol addition reactions. It is considered that reaction had become limited by availability of a reactant other that the radical species generated by H_2O_2. It is possible that productivity was limited by CH_4 or O_2 solubility which is dependent on the aqueous media. But a higher gain factor of 0.8 was observed when only 60 μmol H_2O_2 was consumed producing 47.8 μmol of products compared to the scenario when 100 μmol H_2O_2, was added thus making the reaction more efficient.

Since an increase in H_2O_2 efficiency was observed, H_2O_2 concentration was further decreased to analyse the effect of H_2O_2 on catalytic activity and selectivity. The reaction was performed with 50 μmol of H_2O_2. 26.1 μmol of oxygenates were generated consuming 22 μmol of H_2O_2. Oxygenate selectivity of 95% was observed with a gain factor of 1.2. With

slightly lower amount of 30 μmol of H_2O_2, a productivity of 15.3 $mol_{(products)}kg^{-1}_{(cat)}h^{-1}$ was observed with 11 μmol H_2O_2 consumption. Even with lower H_2O_2 consumption, a high selectivity of 92% and a high catalytic efficiency was observed while yielding a gain factor of 1.4. With the lower amount of H_2O_2 (30 μmol), the decrease in product formation is probably due to reduction in the concentration of radicals that is generated. This reduction could lead to the lower productivity observed. Since in the lower H_2O_2 regime (< 150μmol) productivity is observed to depend on H_2O_2 concentration rather than being limited by other reactants, a kinetic analysis was performed. Production of CH_3OOH was studied with different amounts of H_2O_2 as shown in figure 3.10. This was done to avoid CH_3OOH transformation or oxidation to other oxygenates which might consume H_2O_2.

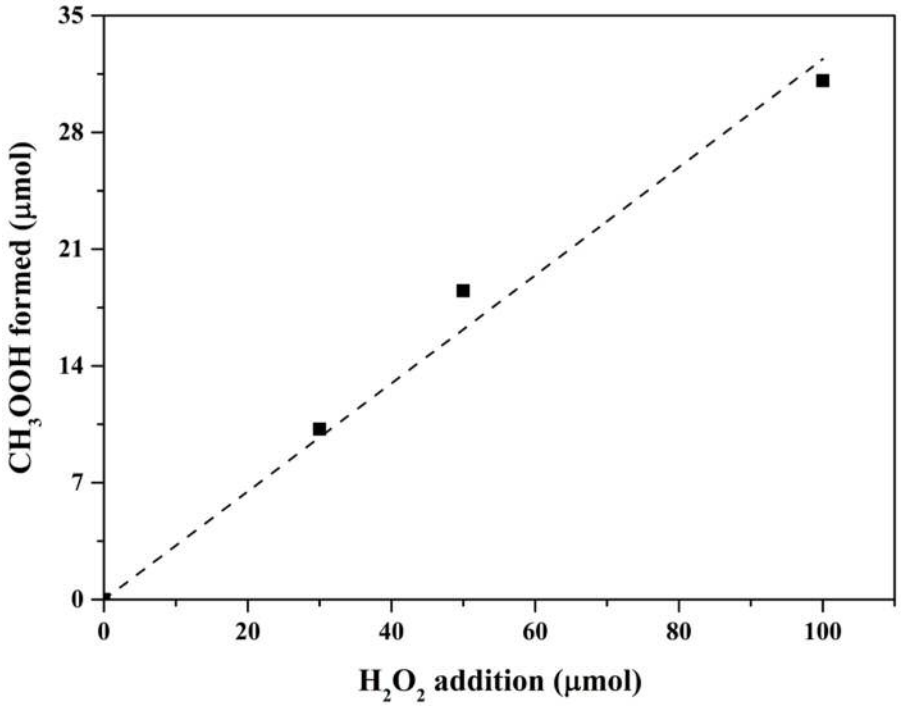

Figure 3.10: Measurement of dependence of primary oxygenate CH_3OOH formation on the amount of H_2O_2 added. Test conditions: Pressure (CH_4) = 30 bar, pressure (O_2) = 5 bar, catalyst: 10 ml Au-Pd-PVP colloid 6.6 μmol of metal (1:1 metal molar ratio), 50 °C (ramp rate of 2.25 °C/min), 1500 rpm, 30 min.

A first order dependence of methane oxidation is observed with H_2O_2. This kinetic dependence was also observed with the supported Au-Pd catalysts[22]. A study of the effect of H_2O_2 concentration is important for process development and reactions involving photocatalysis also need to consider rates of H_2O_2 addition/formation. One such example is photochemical methane partial oxidation where H_2O_2 has been used as hydroxyl source.

In these reactions, it is also known to play a significant role as electron scavenger, thus, excess H_2O_2 was found to be detrimental since it was found to be scavenging and consuming reactive oxygen species (ROS) forming O_2 [45]. Concentration therefore plays an important role in methane oxidation productivity, selectivity and process efficiency.

For the optimised amount of H_2O_2 (50 μmol), a productivity of 39.4 $mol_{(products)}kg^{-1}_{(cat)}h^{-1}$ was generated with 32% of H_2O_2 was consumed yielding a gain factor of 1.2. Oxygen incorporation was measured by performing $^{18}O_2$ isotopic labelling experiment, with 50 μmol H_2O_2 and 5 bar $^{18}O_2$. Mass spectrometry analysis was carried out to analyse ^{18}O labelling in methanol product and the mass spectrum obtained is shown in figure 3.11.

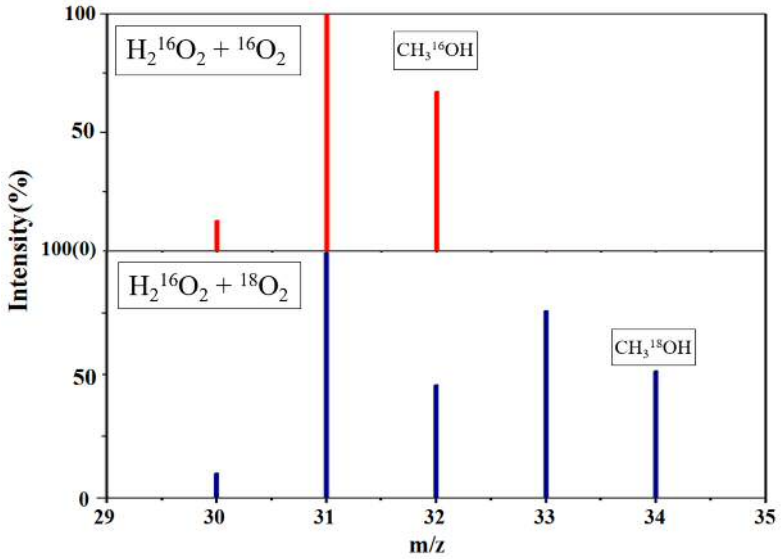

Figure 3.11: GC mass spectrum of methanol formed (m = 32 or 34) during methane oxidation using a Au-Pd-PVP colloid with 50 μmol $H_2{}^{16}O_2$ + $^{16}O_2$ (*above*) or 50 μmol $H_2{}^{16}O_2$ + $^{18}O_2$ (*below*). Test conditions: Pressure (CH_4) = 30 bar, pressure (O_2) = 5 bar, catalyst: 10 mL Au-Pd-PVP colloid, 6.6 μmol of metal (1:1 metal molar ratio), 50 μmol H_2O_2, 50 °C (ramp rate of 2.25 °C/min), 1500 rpm, 30 min.

As shown in figure 3.11, substantial incorporation into primary products, of about 50% was observed. With a gain factor of 1.2, higher incorporation was expected in this case compared to the isotopic labelling experiment, which was performed with 1000 μmol since the gain factor observed in that case was 0.09. It has been previously shown that alcohol production could take place in GC injector from the alkyl hydroperoxide via an alkyl radical generation which could react with $^{16}O_2$ formed by decomposition of remaining H_2O_2 or other ^{16}O sources present in the reaction mixture [7].

Since, in all of the above isotope labelling reactions, CH_3OOH is decomposed to CH_3OH, it was considered that there is a loss of the isotopic label due to the above mentioned thermal decomposition and ^{18}O containing product is being underestimated. To prevent such losses, the reaction solution was reduced before GC-MS analysis using a reducing agent. Since $NaBH_4$ is used in preparation of the catalyst and did not interfere with the reaction or catalyst, it was used as the reducing agent. Quantitative comparison was performed using NMR to ensure no loss of primary oxygenates took place by $NaBH_4$ reduction. The mass spectrometry analysis of the isotope labelling methane oxidation reaction mixture, reduced with $NaBH_4$, is shown in figure 3.12.

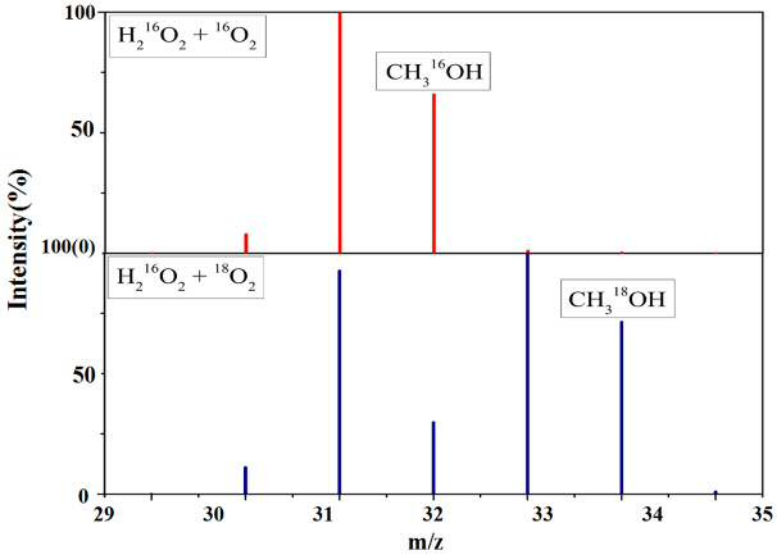

Figure 3.12: GC mass spectrum of methanol formed (m = 32 or 34) during methane oxidation using a Au-Pd-PVP colloid with 50 μmol $H_2{}^{16}O_2$ + $^{16}O_2$ (*above*) or 50 μmol $H_2{}^{16}O_2$ + $^{18}O_2$ (*below*). The reaction was reduced using $NaBH_4$ prior to analysis. Test conditions: Pressure (CH_4) = 30 bar, pressure (O_2) = 5 bar, catalyst: 10 mL Au-Pd-PVP colloid, 6.6 μmol of metal (1:1 metal molar ratio), 1000 μmol H_2O_2, 50 °C (ramp rate of 2.25 °C/min), 1500 rpm, 30 min.

When the reaction performed with 50 μmol H_2O_2 and $^{18}O_2$ was analysed after reducing the reaction mixture with $NaBH_4$, more than 70% of the CH_3OH detected showed incorporation of the ^{18}O label compared to only 50% in the sample analysed without treatment. This indicated the real incorporation of molecular oxygen in primary oxygenates. There is still some ^{16}O product obtained which might correspond to the formation of primary products due to the interaction with $^{16}O_2$ either dissolved in aqueous solution or which is

formed by decomposition of H_2O_2.

Methane oxidation reactions were also performed with very low amounts of H_2O_2, 5 μmol, in presence of O_2 to try and use H_2O_2 as an initiator and probe for more propagation steps. But, in this case, lower gain factor of 0.24 and total consumption of 5 μmol H_2O_2 was observed yielding 1.1 μmol of CH_3OOH and no other liquid phase product. But an issue that becomes significant at lower concentration of H_2O_2 is decomposition of H_2O_2 due to wall reactions with stirrer and dip-tube surfaces. Decomposition carried out with blank solution containing only 5 μmol of H_2O_2 in 10 ml water also showed 2-3 μmol of H_2O_2 is consumed over 30 min at 50 °C. Thus, these reactions show that though use of H_2O_2 cannot be completely eliminated, decreasing the amount of H_2O_2 increases the catalytic efficiency without compromising on product selectivity.

These results clearly demonstrate the effect of H_2O_2 on catalytic activity and selectivity. An exponential increase in gain factor and hence catalytic efficiency can be observed. More than one mol of oxygenate is produced for every mol of H_2O_2 consumed for optimised reactions. Oxygen incorporation is conclusively shown using using the isotope labelling experiment and the incorporation is identified quantitatively by reaction reduction with $NaBH_4$ prior to analysis. These interesting results are important for developing an efficient and effective system. O_2 is preferred oxidant to make the process cost-effective since, H_2O_2 is a costlier reactant. Hence, decreasing H_2O_2 is important for any potential scale-up of any such process. This interesting trend can be particularly utilised in developing a continuous process. Since in a continuous process there is the continuous influx of H_2O_2, this results can be used in creating a continuous stream of $\cdot OH$ and thus $\cdot CH_3$. This could be utilised to understand methane oxidation mechanisms and optimise the reaction process.

3.5 Proposed Reaction Mechanism

Methane oxidation using Au-Pd colloids was carried out with H_2O_2 and O_2 as oxidant. Though the reaction proceeds with only H_2O_2, no oxygenates are formed with O_2 alone. Previous EPR studies performed on supported Au-Pd nanoparticles showed presence of both ·OH and $\cdot CH_3$ radicals. Thus the reaction is likely to proceed via radical mechanism as previously described. Figure 3.13 shows a proposed reaction mechanism in presence of $H_2{}^{16}O_2$ and $^{18}O_2$ based on previous studies.

Since, the reaction only proceeds in presence of H_2O_2, it is considered that the initial activation of CH_4 to $\cdot CH_3$ is likely to occur through a hydrogen abstraction using ·OH. Experiments were performed by trapping these short-lived radicals using spin-trap reagents like 5,5-dimethyl-1-pyrroline-*N*-oxide (DMPO) and phosphorous containing analog of DMPO, 5-(Diethoxyphosphoryl)-5-methyl-1-pyrroline-N-oxide (DEPMPO). Since, ^{31}P is an NMR active atom, NMR shifts in FDMPO with radical species could be employed to study radical trapping and reaction mechanisms. It was noticed that the reaction stopped when ·OH radicals were trapped from the reaction solution and no products were obtained. Structure of the spin trap and the NMR spectra are shown in the appendix 7.1-7.3. Thus, presence of ·OH is essential for product formation and is considered to form $\cdot CH_3$ radicals (Figure 3.13).

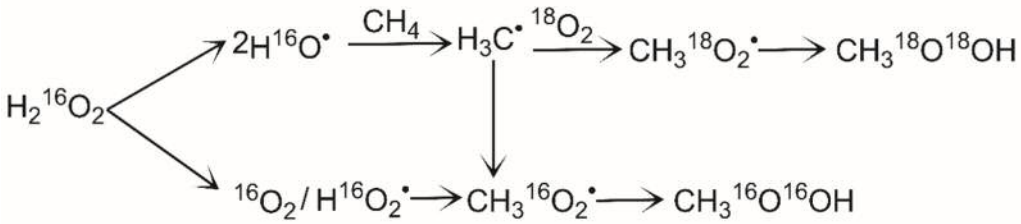

Figure 3.13: Proposed mechanism for methane oxidation in presence of H_2O_2 and molecular $^{18}O_2$

These $\cdot CH_3$ radicals can react quickly with dissolved O_2, which results in incorporation of >70% O_2 into the primary reaction products under optimised conditions. In the optimised reaction, 10 μmol of H_2O_2 and 5 bar of $^{18}O_2$ were required to generate 20 μ mol of

products. Since, the isotopic label was contained in 70% of primary products, it is considered 14 μmol were formed by reaction with $^{18}O_2$ while the remaining 6 μmol contained ^{16}O label. These products are considered to form through radical reactions between $\cdot CH_3$ with either $\cdot ^{16}O^{16}OH$ or $^{16}O_2$ generated from the decomposition of $H_2{}^{16}O_2$ (Figure 3.13). The total consumption of 16 μmol of H_2O_2 seems to be in line with these isotopic ratios and the reaction scheme proposed. It is considered that out of the 16 μmol consumed, 10 μmol H_2O_2 was used to generate $\cdot CH_3$ radicals and 6 μmol was used in ^{16}O products via decomposition. Thus, higher efficiency of reaction is achieved by utilising H_2O_2 to generate $\cdot CH_3$ radicals and O_2 to generate products via oxidation.

Since, $\cdot OH$ radicals are required for C-H activation and formation of $\cdot CH_3$, the product formation takes place readily in the presence of O_2. With this mechanism in mind, an iron-based Fenton type catalyst was tested for methane oxidation which is well known in literature to produce $\cdot OH$ in the presence of H_2O_2. Methane oxidation reaction was performed with Fe(III) based catalyst ($FeCl_3$) in absence of Au-Pd colloid, results of which are shown in table 3.4. Negligible product formation was observed with same amount of metal as compared to Au-Pd colloidal catalysts. Furthermore, no appreciable increase in catalytic activity or efficiency was observed in presence of gas phase O_2.

Table 3.4: Liquid phase oxidation of methane using an Fe-based Fenton's type catalyst using H_2O_2 and O_2.

Entry	O_2 Added (bar)	Product amount (μmol)				Oxygenate Selectivity	Oxygenate Productivity	H_2O_2 Consumed / %	Gain Factor
		CH_3OOH	CH_3OH	HCOOH	CO_2				
1	0	0.7	1.0	0	0.2	89	2.1	22	0.1
2	5	1.0	1.3	0	0.3	88	2.9	18	0.2

Test conditions:Pressure (CH_4) = 30 bar, catalyst: 6.6 μmol of Fe^{+3} metal in 10 ml of water from solid $FeCl_3 \cdot 6\,H_2O$, 50 μmol H_2O_2, 50 °C (ramp rate of 2.25 °C/min), 1500 rpm, 30 min.

Therefore, the presence of the Au-Pd colloidal nanoparticles is also essential for CH_4 activation and product generation. Furthermore, reactions were also performed with monometallic Au or Pd colloid for comparison. Reactions were carried out under optimised conditions with 50 μmol H_2O_2 and 5 bar O_2 with identical metal concentration

of 6.6 μmol as used in Au-Pd bimetallic colloids. No product formation was observed in both of these cases with 11% of H_2O_2 consumed with Au and 22% in case of Pd colloid. The use of Au-Pd bimetallic colloid has many benefits over monometallic colloids. Firstly, it is stable to the reaction conditions; in solution the Pd colloid was found to be unstable under these oxidising reaction conditions and found to agglomerate and precipitate after the reaction. Secondly, it also decomposed H_2O_2 rapidly to unselective termination of the radical chains, whereas Au colloids were found to be poor at initiating H_2O_2.

Recently, leaching of precious metals into the reaction solution have been implicated in catalytic reactions [46]. Single atom and homogeneous metal ions have also been found to be catalytically active for certain oxidation reactions. Therefore metal chloride precursors were also tested for methane oxidation using the same metal concentration and under identical reaction conditions. No reaction products were obtained with $HAuCl_4$ or $PdCl_2$ solution, in addition $HAuCl_4$ was found to be precipitated as Au(0) during the reaction consuming 10% of the available H_2O_2. Reactions performed with $PdCl_2$ also consumed 5% of the added H_2O_2 in 30 min. Thus, alloyed Au-Pd nanoparticles are shown to demonstrate a synergistic effect in terms of activity and stability for the reaction. It is likely that these bimetallic catalysts perform the dual role of breaking H_2O_2 into ROS at a controlled rate likely on a Pd site and activate oxygen non-dissociatively, likely on a Au site which aids the reaction of $\cdot CH_3$ radicals with O_2.

These results demonstrate the efficacy of bimetallic Au-Pd colloidal catalysts for methane oxidation using H_2O_2 and O_2 as an oxidant. The reaction which proceeds via radical mechanism can be tuned using the concentration of H_2O_2, which is shown to be essential for methyl radical generation. These $\cdot CH_3$ radicals react with O_2 to generate primary products. More oxygenated products are shown to form than the amount of H_2O_2 consumed which demonstrates that the controlled breakdown of H_2O_2 is essential to activate methane, which subsequently incorporates molecular oxygen.

3.6 Catalyst Characterisation

It was assumed that supporting nanoparticles might lead to changes in structure and morphology of the nanoparticles thus affecting the catalytic activity. Therefore structure, morphology and composition was examined to understand any differences. Characterisation techniques like electron microscopy and X-ray photoelectron spectroscopy were used to analyse Au-Pd colloids and TiO_2 supported Au-Pd catalyst prepared by sol-immobilisation. Both fresh and used catalysts were characterised to study the differences caused in the catalyst after the reaction.

3.6.1 X-ray Photoelectron Spectroscopy

XPS analysis was carried out for both the fresh colloid and the used colloid under optimised conditions. To carry out the measurements of the colloid, one drop of colloid was deposited on a clean Si wafer and the solvent was evaporated under vacuum. The XPS analysis of a fresh and used bimetallic Au-Pd colloid is shown in figure 3.14. Fresh samples showed both Au and Pd to be metallic in nature. Presence of some cationic gold (6%) (figure 3.14a) and minor $PdCl_2$ (figure 3.14b) components were also detected in the fresh catalyst which is consistent with the trend observed when metallic nanoparticles are stored over time due to some re-oxidation.

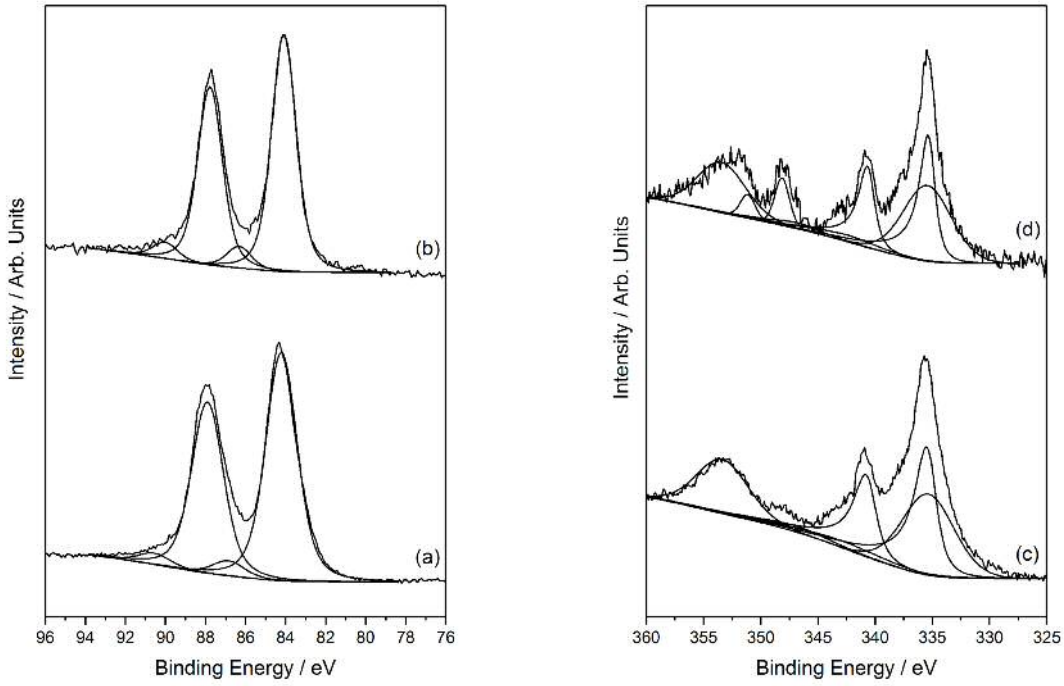

(a) (b)

Figure 3.14: XPS spectra of Au-Pd bimetallic colloid. a) Au(4f) (a-b) and b) Pd(3d) (c-d) spectra of fresh and used colloid. Test conditions: Pressure (CH_4) = 30 bar, pressure (O_2) = 5 bar, catalyst: 10 mL Au-Pd-PVP colloid, 6.6 μmol of metal (1:1 metal molar ratio), 50 μmol H_2O_2, 50 °C (ramp rate of 2.25 °C/min), 1500 rpm, 30 min.

XPS spectra of used colloid catalyst also shows a similar metallic nature. For instance, some cationic gold (8%) (figure 3.14a) and minor $PdCl_2$ (figure 3.14b) components were detected. No leaching was observed since there was no significant increase in the cationic concentration. Plots (c-d) (figure 3.14b) also show presence of Au(4d) signals. In both fresh and used, a shift in binding energies is observed for Au and Pd which indicates interaction between Au and Pd leading to the synergistic effect observed in the catalytic activity.

Similarly, XPS analysis was also performed on Au-Pd nanoparticles supported on TiO_2 catalyst for comparison (figure 3.15). Sample catalysts were deposited on clean Si wafer. Supported catalyst were also found to be mainly metallic in nature with some cationic gold and minor $PdCl_2$ components.

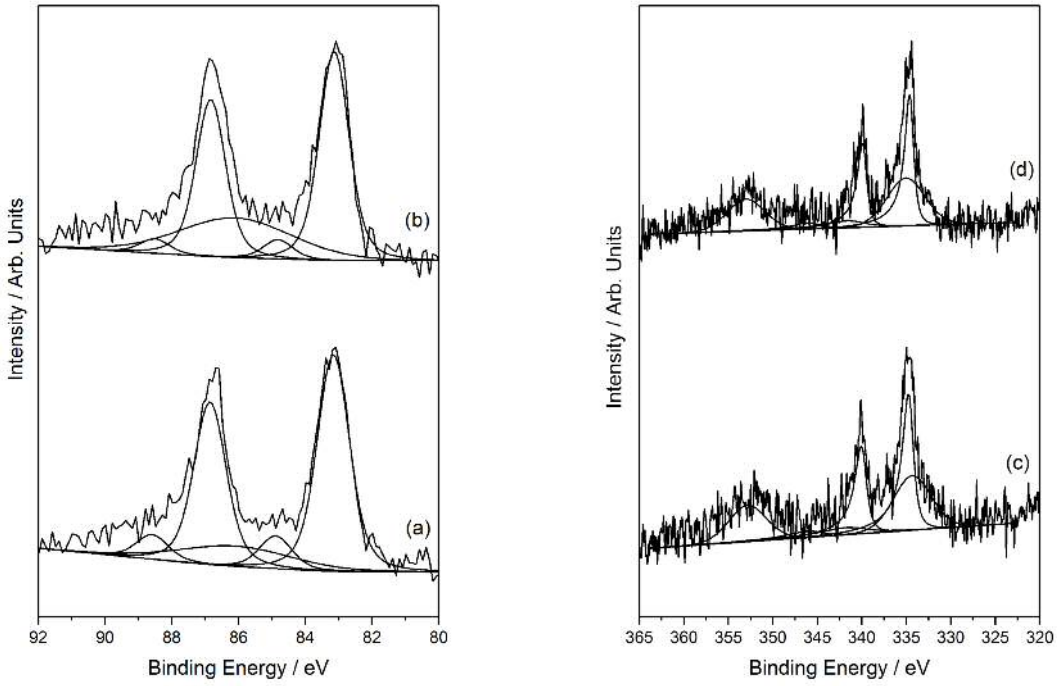

Figure 3.15: XPS spectra of Au-Pd/TiO_2 supported catalyst. a) Au(4f) (a-b) and b) Pd(3d) (c-d) spectra of fresh and used supported catalyst. Test conditions: Pressure (CH_4) = 30 bar, pressure (O_2) = 5 bar, catalyst: 100 mg 1 wt.% Au-Pd/TiO_2, 6.6 μmol of metal (1:1 metal molar ratio), 50 μmol H_2O_2, 50 °C (ramp rate of 2.25 °C/min), 1500 rpm, 30 min.

Fresh catalysts contained about 12% of cationic gold which might be due to the drying step involved in the preparation of the supported catalyst. Post-reaction, no oxidation of metals was observed with only 8% of cationic gold present (figure 3.15a). As seen in colloidal catalysts, there was a minor shift observed in binding energies and plots (c-d) (figure 3.15b) which also show presence of Au(4d) signals. There was also an underlying Ti signal present XPS spectra of the supported catalysts.

3.6.2 Scanning Transmission Electron Microscopy

Morphology, particle size and compositions were investigated using transmission electron microscopy (TEM) by Prof Chris Kiely's group at Lehigh University. Samples were dispersed onto a lacey carbon film supported over a copper TEM grid. Bright field (BF)

imaging was performed on both Au-Pd colloid and 1 wt.% Au-Pd/TiO_2 as shown in the figure 3.16.

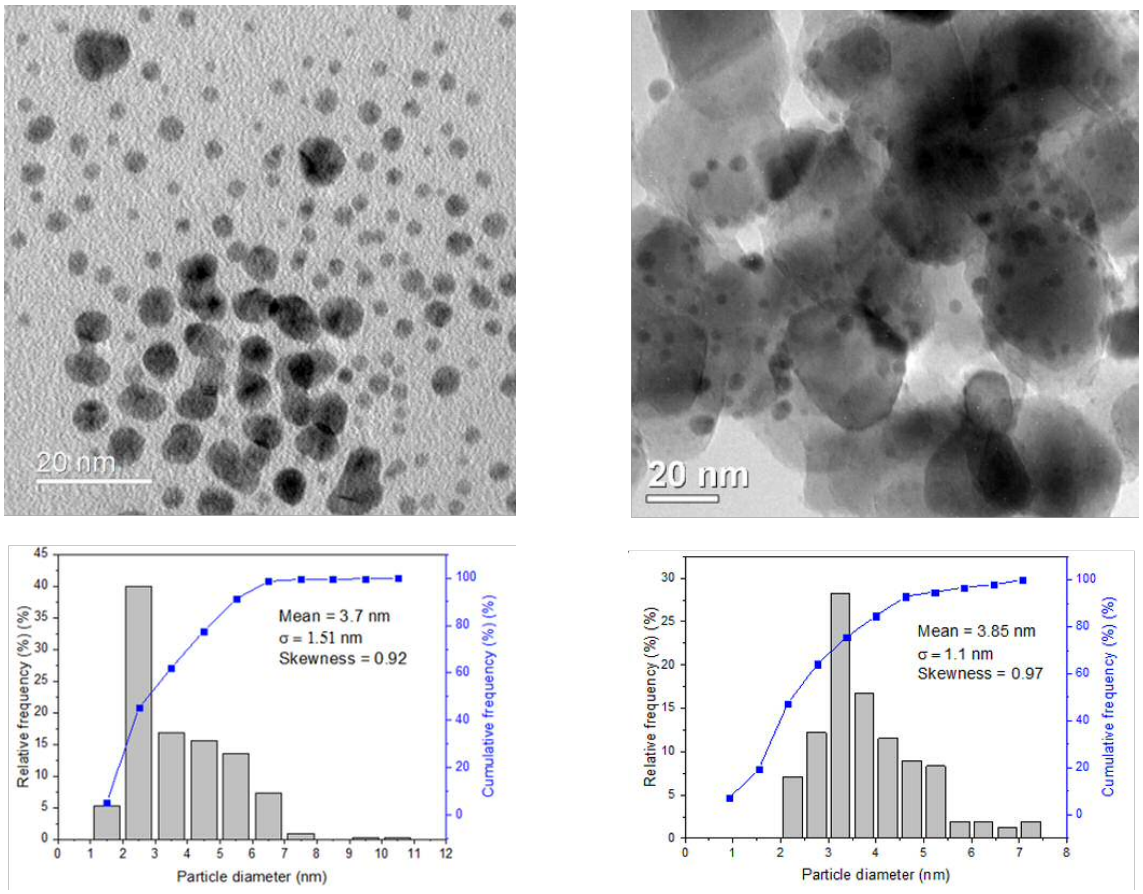

(a) (b)

Figure 3.16: Representative BF-TEM images and particle size distributions for the fresh bimetallic Au-Pd catalysts (1:1 metal molar ratio). a) Au-Pd-PVP colloid and b) 1 wt.% Au-Pd/TiO_2 sol immobilised supported catalyst using PVP stabiliser.

The Au-Pd-PVP colloids ranged in size between 2 and 12 nm with a mean diameter of 3.7 nm (Figure 3.16a). Sol-immobilized Au-Pd/TiO_2 supported samples showed that the Au-Pd nanoparticles have a similar size and morphology to their colloidal counterparts. When compared to the colloidal catalysts, the supported bimetallic catalysts had a mean particle size of 4.1 nm (Figure 3.16b). This slightly larger size is believed to be the result of particle agglomeration probably due to the 120 °C drying treatment which is performed for 16 hours. The drying process can also cause the initially spherical colloidal particles to partially become wet and spread on the support to form particles with distinct metal/support interface [19, 47]. Au-Pd bimetallic colloidal and supported catalysts were also characterised post-reaction as shown in Figure 3.17.

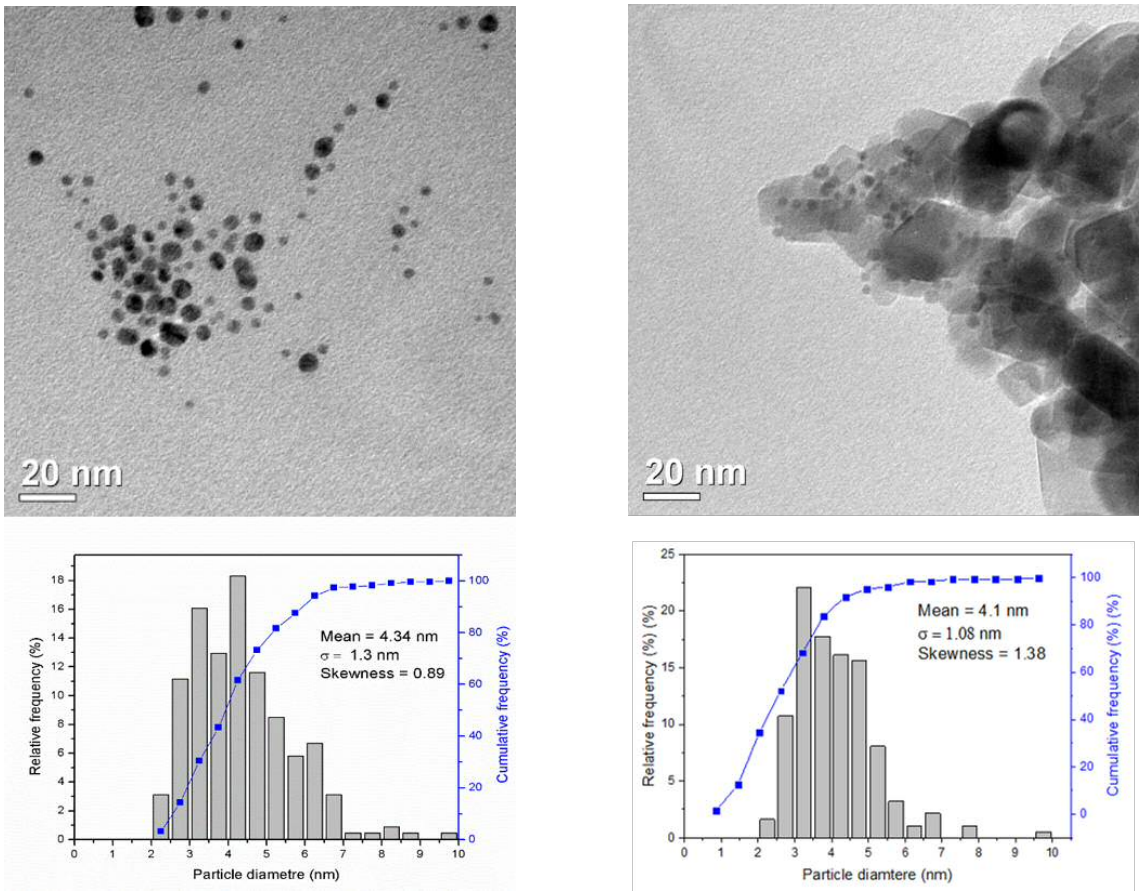

(a) (b)

Figure 3.17: Representative BF-TEM images and particle size distributions for the used bimetallic Au-Pd catalysts (1:1 metal molar ratio). a) Au-Pd-PVP colloid and b) 1 wt.% Au-Pd/TiO_2 sol immobilised supported catalyst using PVP stabiliser. Test conditions: Pressure (CH_4) = 30 bar, pressure (O_2) = 5 bar, catalyst: 10 mL Au-Pd-PVP colloid and 100 mg 1 wt.% Au-Pd/TiO_2, 6.6 μmol of metal (1:1 metal molar ratio), 50 μmol H_2O_2, 50 °C (ramp rate of 2.25 °C/min), 1500 rpm, 30 min.

BF-TEM of used colloidal catalysts revealed an increase in particle size to a mean size of 4.3 nm (Figure 3.17a). In the case of the supported catalysts as shown in Figure 3.17b, a minor increase was noted after use which was smaller than that of unsupported colloids due to metal support interaction which limited its growth. Also no significant morphological changes were detected in the used catalysts.

High-angle annular dark field–scanning transmission electron microscopy (HAADF-STEM) imaging of the fresh Au-Pd–PVP colloids revealed that the nanoparticles primarily have multiply twinned icosahedral structures, and some cuboctahedral shaped nanoparticles were also detected (Figure 3.18a). HAADF-STEM analysis of the used colloid showed

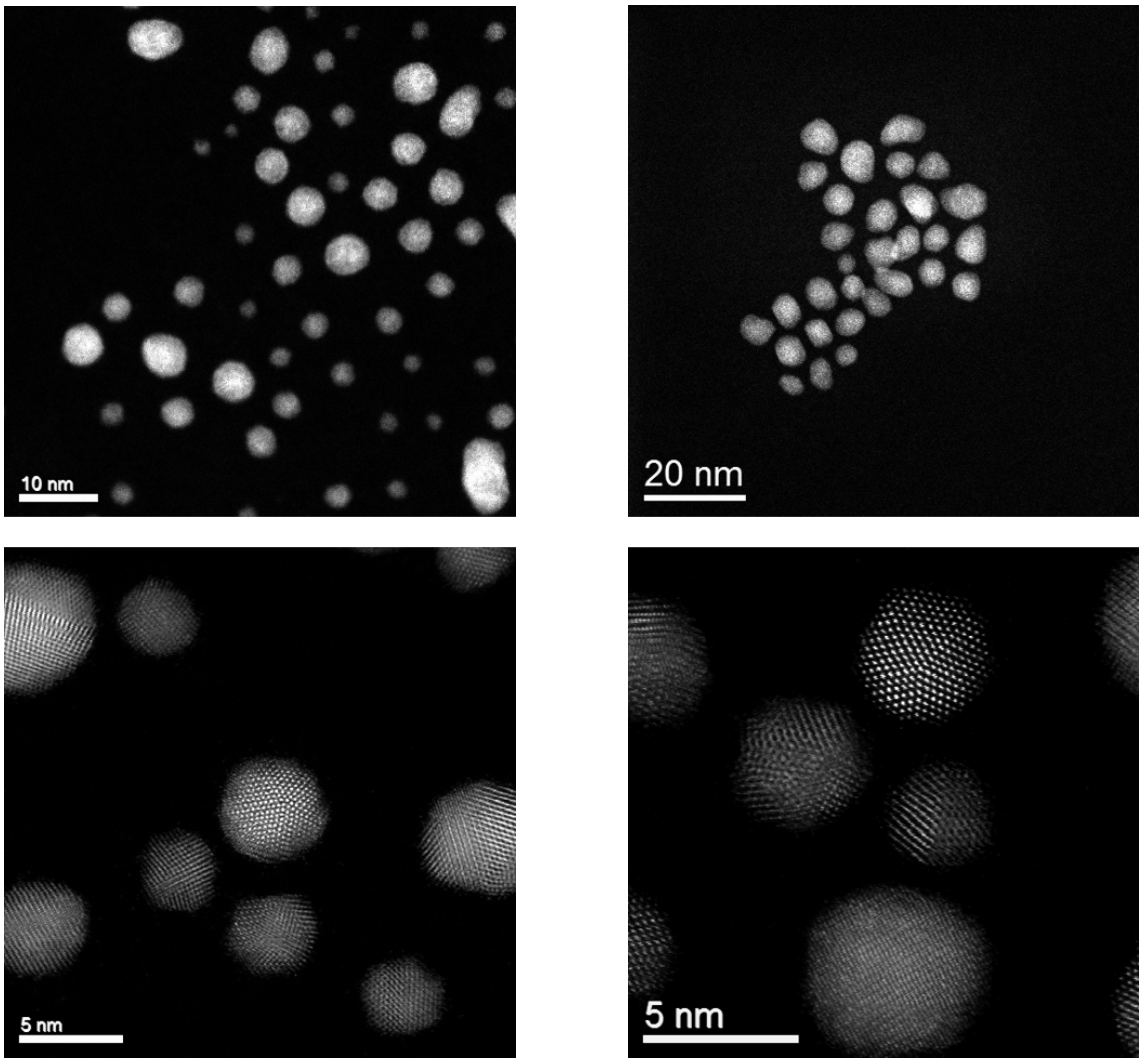

(a) (b)

Figure 3.18: Representative HAADF-STEM images for the unsupported Au-Pd-PVP colloid a) fresh and b) used. Test conditions: Pressure (CH_4) = 30 bar, pressure (O_2) = 5 bar, catalyst: 10 mL Au-Pd-PVP colloid, 6.6 μmol of metal (1:1 metal molar ratio), 50 μmol H_2O_2, 50 °C (ramp rate of 2.25 °C/min), 1500 rpm, 30 min.

some limited particle growth which was also observed in BF-TEM imaging, but no evidence of subnanometer clusters or isolated Au atoms was found after the reaction (Figure 3.18b). STEM–X-ray energy-dispersive spectroscopy (XEDS) compositional analysis was also performed on the colloids to study the composition of the nanoparticles. No compositional variation was observed with the different size particles as shown in Figure 3.19.

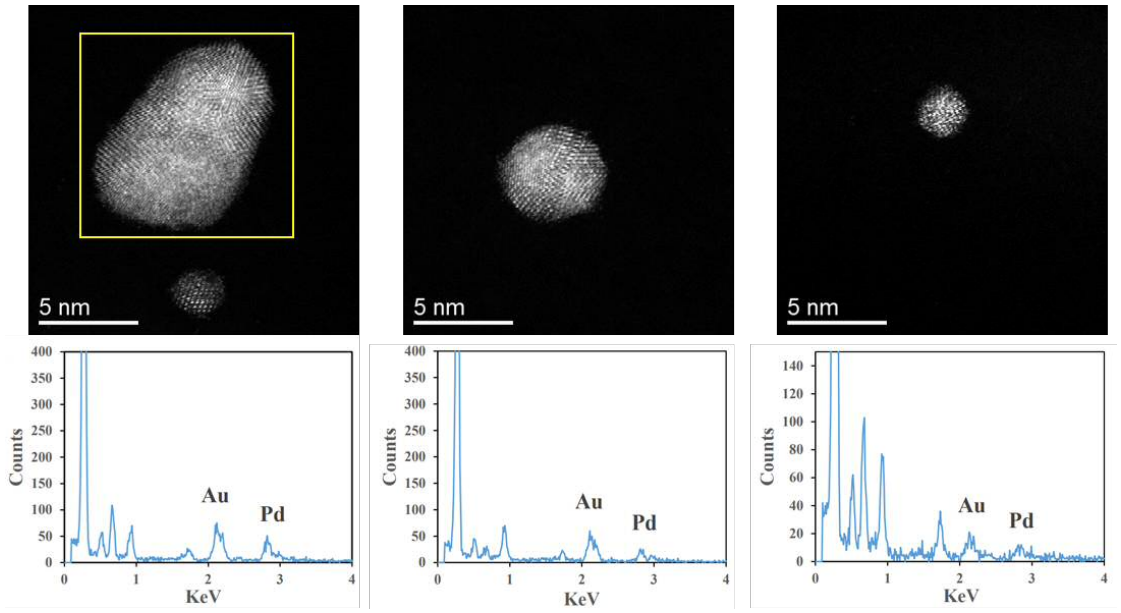

Figure 3.19: Representative XEDS compositional analysis from individual Au-Pd-PVP nanoparticles.

A comparison was performed between the relative heights of the Au M_α and Pd L_α peaks for particle size of 7 nm, 4 nm and 2 nm (Figure 3.19). The relative heights showed that the individual particles had a similar Au:Pd ratio, irrespective of their size. Thus, large particles and small particles have similar Au:Pd ratio showing no compositional variation.

XPS and electron microscopy analysis of colloidal Au-Pd nanoparticles showed similar size, morphology and composition to their supported counterparts. A slight increase in size of supported nanoparticles was observed; however that might be due to the drying treatment. XEDS analysis showed no size dependent composition variation in these bimetallic nanoparticles with similar Au:Pd ratios in different sized particles. Used particles showed slight increase in particle size but no subnanomater clusters or isolated atoms were found. This was also seen by XPS analysis. Both fresh and used samples showed no increase in cation amounts and the vast majority of the metal existed in metallic form.

3.7 Conclusions

Supported Au-Pd/TiO_2 were shown to be active for methane oxidation [16] but showed low activity and H_2O_2 efficiency. This high consumption of H_2O_2 is attributed to the metal support interface, since much lower decomposition was observed with Au-Pd-PVP colloids and bare TiO_2 when compared to Au-Pd/TiO_2. Thus, low temperature selective oxidation of CH_4 using 1000 μmol H_2O_2 was carried out using PVP stabilised Au-Pd nanoparticles. The reaction was found to occur with a high productivity of 29.4 $mol_{(products)}kg^{-1}_{(cat)}h^{-1}$ and oxygenate selectivity of 90%. H_2O_2 consumption was also much lower (38%) in this reaction when compared to 73% which was consumed by supported Au-Pd/TiO_2 with same amount of metal. Oxygenates formation due to degradation or oxidation of stabiliser was also eliminated by performing blank reactions and $^{13}CH_4$ isotope labelling reactions.

The reaction is found to proceed via same radical oxidative pathway as CH_4 oxidation catalysed by supported Au-Pd nanoparticles. In both systems, CH_3OOH is produced as the primary product which undergoes subsequent transformation to CH_3OH. Over-oxidation of these primary oxygenates leads to production of HCOOH before complete oxidation to CO_2. CH_3OOH is proposed to form by reaction of $\cdot CH_3$ radicals with O_2. This hypothesis is tested by performing CH_4 oxidation with H_2O_2 and gas phase O_2. Higher productivity of 53.6 $mol_{(products)}kg^{-1}_{(cat)}h^{-1}$ was achieved in presence of 5 bar O_2 with lower H_2O_2 decomposition of 27% while no reaction was observed in absence of H_2O_2. This incorporation of molecular O_2 was studied using $^{18}O_2$ isotope labelling experiments where CH_3OH mass fragments containing ^{18}O label were responsible for more than 50% of the observed signal. These results show that under mild aqueous conditions, colloidal Au-Pd nanoparticles can catalyse the reaction of H_2O_2 + CH_4 + O_2 with incorporation of O_2 into the primary reaction products.

In the presence of O_2, since lower H_2O_2 was consumed, the effect of decreasing H_2O_2 concentration was measured on the activity and efficiency of the reaction with the aim of

generating more than one primary oxygenate species per molecule of H_2O_2 consumed. An exponential increase was observed in the gain factor on decreasing the amount of H_2O_2 added in the reaction. With colloids, the gain factor reached 1.2 on optimising the reaction with 50 μmol H_2O_2. This represented an increase by three orders of magnitude over the supported 1 wt.% Au-Pd/TiO_2 sol-immobilised catalyst, together with higher selectivity to primary oxygenates. Furthermore, $^{18}O_2$ isotopic labelling experiments were carried out under optimised conditions which exhibited substantial incorporation of $^{18}O_2$ (50%) into primary products. A possibility of under-estimation of the ^{18}O label was proposed due to thermal decomposition of CH_3OOH with H_2O_2 in GC injector. Pre-reduction of reaction mixture was carried out and GC-MS analysis showed much higher O_2 incorporation of 70%. This incorporation and methane oxidation was explained using a radical mechanism.

Monometallic Au and Pd colloids, as well as the corresponding precursor metal chlorides with the same metal concentration showed no activity for CH_4 oxidation and precipitation of Pd colloid and $HAuCl_4$. This demonstrated synergistic effect in terms of activity and stability in alloying Au and Pd, forming bimetallic nanoparticles which was also seen previously in supported Au-Pd catalysts [22, 48]. These bimetallic catalysts were characterised using XPS and STEM. The Au-Pd-PVP colloids ranged in size between 2 and 12 nm and had a mean diameter of 3.7 nm. XEDS compositional analysis showed the Au-Pd-PVP nanoparticles have similar Au:Pd ratio, irrespective of their size while Sol-immobilised Au-Pd/TiO_2 showed similar size and morphology compared to their colloidal counterparts. XPS analysis also showed both Au and Pd were metallic in nature with minor cationic Au. Used catalysts also showed similar XPS spectra with no evidence of clusters or atoms in HAADF-STEM. Only limited particle growth was observed in used catalysts which was slightly higher in colloidal catalysts compared to the supported ones.

Overall, these results demonstrate the intrinsic activity of Au-Pd-PVP nanoparticles for methane oxidation, which is hindered by supporting the nanoparticles. Colloidal catalysts also utilise molecular O_2 as the oxidant along with H_2O_2 which is useful considering

high scale up costs associated with H_2O_2. Since no oxygenates were produced using only O_2, more studies need to be performed, probably with *in-situ* generation of H_2O_2. Further research also needs to be done to see the effect of different reaction and catalyst preparation parameters to optimise the reaction more. However, the aim of this work, which was to study CH_4 oxidation with use of molecular O_2 has been achieved. It is hoped these results will help in understanding liquid phase methane oxidation as well as hydrogen peroxide processes and contribute towards catalytic development.

Bibliography

(1) A. I. Olivos-Suarez, À. Szécsényi, E. J. M. Hensen, J. Ruiz-Martinez, E. A. Pidko and J. Gascon, *ACS Catalysis*, 2016, **6**, 2965–2981.

(2) E. V. Kondratenko, T. Peppel, D. Seeburg, V. A. Kondratenko, N. Kalevaru, A. Martin and S. Wohlrab, *Catal. Sci. Technol.*, 2017, DOI: 10.1039/C6CY01879C.

(3) A. E. Shilov and G. B. Shul'pin, *Russian Chemical Reviews*, 1987, **56**, 442.

(4) R. A. Periana, D. J. Taube, S. Gamble, H. Taube, T. Satoh and H. Fujii, *Science*, 1998, **280**, 560–564.

(5) R. Palkovits, M. Antonietti, P. Kuhn, A. Thomas and F. Schüth, *Angew. Chem. Intl. Ed.*, 2009, **48**, 6909–6912.

(6) M. Lin, C. Shen, E. A. Garcia-Zayas and A. Sen, *Journal of the American Chemical Society*, 2001, **123**, PMID: 11456645, 1000–1001.

(7) N. Galina V., S.-F. Georg and S. Georgiy B., *Chem. Commun.*, 1997, 397–398.

(8) C. Hammond, M. M. Forde, M. H. Ab Rahim, A. Thetford, Q. He, R. L. Jenkins, N. Dimitratos, J. A. Lopez-Sanchez, N. F. Dummer, D. M. Murphy, A. F. Carley, S. H. Taylor, D. J. Willock, E. E. Stangland, J. Kang, H. Hagen, C. J. Kiely and G. J. Hutchings, *Angewandte Chemie - International Edition*, 2012, **51**, 5129–5133.

(9) T. Sheppard, C. D. Hamill, A. Goguet, D. W. Rooney and J. M. Thompson, *Chem. Commun.*, 2014, **50**, 11053–11055.

(10) K. Narsimhan, K. Iyoki, K. Dinh and Y. Román-Leshkov, *ACS Central Science*, 2016, **2**, 424–429.

(11) J. Shan, M. Li, L. F. Allard, S. Lee and M. Flytzani-Stephanopoulos, *Nature*, 2017, **551**, 605–608.

(12) C. Jones, D. Taube, V. R. Ziatdinov, R. A. Periana, R. J. Nielsen, J. Oxgaard and W. A. Goddard, *Angewandte Chemie*, 2004, **116**, 4726–4729.

(13) L. C. Kao, A. C. Hutson and A. Sen, *Journal of the American Chemical Society*, 1991, **113**, 700–701.

(14) Q. Yuan, W. Deng, Q. Zhang and Y. Wang, *Advanced Synthesis and Catalysis*, 2007, **349**, 1199–1209.

(15) L. Kesavan, R. Tiruvalam, M. Hasbi, A. Rahim, M. Izham, D. I. Enache, R. L. Jenkins, N. Dimitratos, J. A. Lopez-sanchez, S. H. Taylor, D. W. Knight, C. J. Kiely and G. J. Hutchings, *Science*, 2011, **331**, 195–199.

(16) M. H. Ab Rahim, M. M. Forde, R. L. Jenkins, C. Hammond, Q. He, N. Dimitratos, J. A. Lopez-Sanchez, A. F. Carley, S. H. Taylor, D. J. Willock, D. M. Murphy, C. J. Kiely and G. J. Hutchings, *Angewandte Chemie*, 2013, **125**, 1318–1322.

(17) J. K. Edwards and G. J. Hutchings, *Angewandte Chemie International Edition*, 2008, **47**, 9192–9198.

(18) J. Pritchard, L. Kesavan, M. Piccinini, Q. He, R. Tiruvalam, N. Dimitratos, J. A. Lopez-Sanchez, A. F. Carley, J. K. Edwards, C. J. Kiely and G. J. Hutchings, *Langmuir*, 2010, **26**, 16568–16577.

(19) J. A. Lopez-Sanchez, N. Dimitratos, P. Miedziak, E. Ntainjua, J. K. Edwards, D. Morgan, A. F. Carley, R. Tiruvalam, C. J. Kiely and G. J. Hutchings, *Phys. Chem. Chem. Phys.*, 2008, **10**, 1921–1930.

(20) J. K. Edwards, B. E. Solsona, P. Landon, A. F. Carley, A. Herzing, C. J. Kiely and G. J. Hutchings, *Journal of Catalysis*, 2005, **236**, 69–79.

(21) C. Williams, J. H. Carter, N. F. Dummer, Y. K. Chow, D. J. Morgan, S. Yacob, P. Serna, D. J. Willock, R. J. Meyer, S. H. Taylor and G. J. Hutchings, *ACS Catalysis*, 2018, **8**, 2567–2576.

(22) M. H. Ab Rahim, M. M. Forde, C. Hammond, R. L. Jenkins, N. Dimitratos, J. A. Lopez-Sanchez, A. F. Carley, S. H. Taylor, D. J. Willock and G. J. Hutchings, *Topics in Catalysis*, 2013, **56**, 1843–1857.

(23) W.-F. Huang, P. Raghunath and M. C. Lin, *Journal of Computational Chemistry*, 2011, **32**, 1065–1081.

(24) R. U. McVicker, Ph.D. Thesis, University of Cardiff, University of Cardiff, 2014.

(25) R. C. Tiruvalam, J. C. Pritchard, N. Dimitratos, J. A. Lopez-Sanchez, J. K. Edwards, A. F. Carley, G. J. Hutchings and C. J. Kiely, *Faraday Discuss.*, 2011, **152**, 63–86.

(26) J. Pritchard, M. Piccinini, R. Tiruvalam, Q. He, N. Dimitratos, J. A. Lopez-Sanchez, D. J. Morgan, A. F. Carley, J. K. Edwards, C. J. Kiely and G. J. Hutchings, *Catal. Sci. Technol.*, 2013, **3**, 308–317.

(27) I. Katsounaros, W. B. Schneider, J. C. Meier, U. Benedikt, P. U. Biedermann, A. Cuesta, A. A. Auer and K. J. J. Mayrhofer, *Physical Chemistry Chemical Physics*, 2013, **15**, 8058.

(28) A. Thetford, G. J. Hutchings, S. H. Taylor and D. J. Willock, *Proceedings of the Royal Society A: Mathematical, Physical and Engineering Sciences*, 2011, **467**, 1885–1899.

(29) I. X. Green, W. Tang, M. Neurock and J. T. Yates, *Accounts of Chemical Research*, 2014, **47**, 805–815.

(30) J.-M. Pan, B. L. Maschhoff, U. Diebold and T. E. Madey, *Journal of Vacuum Science & Technology A: Vacuum, Surfaces, and Films*, 1992, **10**, 2470–2476.

(31) B. Donoeva and P. E. De Jongh, *ChemCatChem*, 2018, **10**, 989–997.

(32) K. M. Koczkur, S. Mourdikoudis, L. Polavarapu and S. E. Skrabalak, *Dalton Trans.*, 2015, **44**, 17883–17905.

(33) A. Villa, D. Wang, D. S. Su and L. Prati, *ChemCatChem*, 2009, **1**, 510–514.

(34) T. Teranishi and M. Miyake, *Chemistry of Materials*, 1998, **10**, 594–600.

(35) S.-H. Liu, W. A. Saidi, Y. Zhou and K. A. Fichthorn, *The Journal of Physical Chemistry C*, 2015, **119**, 11982–11990.

(36) M. Suh, P. S. Bagus, S. Pak, M. P. Rosynek and J. H. Lunsford, *The Journal of Physical Chemistry B*, 2000, **104**, 2736–2742.

(37) K. L. Antcliff, D. M. Murphy, E. Griffiths and E. Giamello, *Physical Chemistry Chemical Physics*, 2003, **5**, 4306.

(38) J. A. Lopez-Sanchez, N. Dimitratos, C. Hammond, G. L. Brett, L. Kesavan, S. White, P. Miedziak, R. Tiruvalam, R. L. Jenkins, A. F. Carley, D. Knight, C. J. Kiely and G. J. Hutchings, *Nature Chemistry*, 2011, **3**, 551–556.

(39) G. R. Buettner, *Free Radic Res Commun.*, 1993, **19**, 79–87.

(40) J. Korchowiec, S.-i. Kawahara, K. Matsumura, T. Uchimaru and M. Sugie, *The Journal of Physical Chemistry A*, 1999, **103**, 3548–3553.

(41) P. P. Olivera, E. M. Patrito and H. Sellers, *Surface Science*, 1995, **327**, 330–357.

(42) V. T. Minasyan, L. G. Grigoryan and B. A. Nalbandyan, *Oxidation Communications*, 1998, **11**, 87–97.

(43) J. Edwards and P. Fleischauer, *Inorganica Chimica Acta Reviews*, 1968, **2**, 53–63.

(44) R. C. Jarnagin and J. H. Wang, *Journal of the American Chemical Society*, 1958, **80**, 786–787.

(45) A. Lopez-Martin, A. Caballero and G. Colon, *Journal of Photochemistry and Photobiology A: Chemistry*, 2017, **349**, 216–223.

(46) J. Oliver-meseguer, J. R. Cabrero-antonino, I. Domínguez, A. Leyva-pérez and A. Corma, *Science*, 2012, **338**, 3–7.

(47) J. Pritchard, M. Piccinini, R. Tiruvalam, Q. He, N. Dimitratos, J. A. Lopez-Sanchez, D. J. Morgan, A. F. Carley, J. K. Edwards, C. J. Kiely and G. J. Hutchings, *Catal. Sci. Technol.*, 2013, **3**, 308–317.

(48) M. Sankar, Q. He, M. Morad, J. Pritchard, S. J. Freakley, J. K. Edwards, S. H. Taylor, D. J. Morgan, A. F. Carley, D. W. Knight, C. J. Kiely and G. J. Hutchings, *ACS Nano*, 2012, **6**, 6600–6613.

4 | Further Investigations into Au-Pd Colloids as Catalysts for Methane Oxidation

4.1 Introduction

In the previous chapter, the methane oxidation activity of unsupported Au-Pd-PVP colloidal catalyst was determined with H_2O_2 and O_2 and compared with supported Au-Pd/TiO_2 catalysts prepared by sol immobilisation. It was established that colloids can be used to carry out this reaction and O_2 incorporation was demonstrated using isotopic labelling experiments. The reaction could be carried out in mild aqueous conditions with 50 μmol H_2O_2 and 5 bar O_2 and colloids performed better in the absence of TiO_2.

Unsupported catalysts have been previously shown to be active for a variety of chemical reactions such as CO oxidation [1], hydrogenation of cinnamaldehyde [2], direct synthesis of H_2O_2 [3] among other examples and have been revised extensively by Yusuke *et. al.* [4]. Factors such as the particle size and composition in bimetallic systems were shown to effect catalytic activity and selectivity. In colloidal systems without the stability of anchoring the particles to the support material, ageing is also a parameter that needs to be considered and was studied on Au colloids for oxidation of 1,2-propanediol [5] and a recovery of more than 50% rates was observed upon reuse. Thus, reaction and synthesis

parameters are important to study to understand the intrinsic activity of colloids, and such studies are undertaken in this chapter to investigate methane oxidation activity of Au-Pd colloids.

Another important factor to be considered is the effect of the polymer stabiliser. Polymers such as PVP can serve as a surface stabiliser, growth modifier, nanoparticle dispersant and sometimes as reducing agent [6]. Ligands can enhance catalytic activity by controlling particle size and composition but can also disfavour or decrease the rate of reaction by partially blocking active sites. The effect of PVP stabilisation on colloids and its effect on methane oxidation is also examined a bit further in this thesis.

4.2 Extended Reactions and Stability of Au-Pd-PVP colloids

Methane oxidation catalysed using Au-Pd-PVP colloids was carried out in the presence of H_2O_2 and O_2 over increasing time scales to investigate how the reaction rate and product selectivity evolved over time to determine the reaction pathway. Since, it was observed that 16 μmol H_2O_2 was consumed out of the initial 50 μmol under optimised conditions over 30 minutes, reactions for the time-on-line were carried out with 50 μmol H_2O_2 an an initial oxidant concentration. Evolution of total products along with primary oxygenate selectivity (selectivity for primary oxygenates which includes CH_3OOH and CH_3OH) is shown in figure 4.1. H_2O_2 consumption was also measured as a function of time. Liquid oxygenates were observed even before the reaction reached the set temperature of 50 °C. 6.6 μmol of products were formed with 100% selectivity even before 50 °C was reached which is referred as t = 0. There is a 12 minute temperature ramp to reach 50 °C with a ramp rate of 2.25 °C/min. This suggests a lack of induction period.

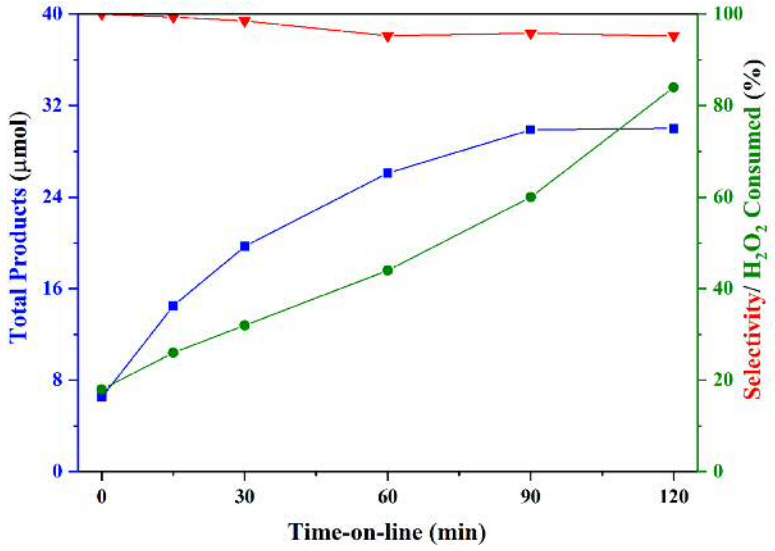

Figure 4.1: Time-on-line analysis for methane oxidation using Au-Pd-PVP colloid with H_2O_2 and O_2. This figure shows total products (blue squares), oxygenate selectivity (red triangles) and H_2O_2 consumption (green circle) as a function of reaction time. Test conditions: Pressure (CH_4) = 30 bar, pressure (O_2) = 5 bar, catalyst: 10 mL Au-Pd-PVP colloid, 6.6 μmol of metal (1:1 metal molar ratio), 50 μmol H_2O_2, 50 °C (ramp rate of 2.25 °C/min), 1500 rpm.

Recently, leaching of precious metals into the reaction solution to generate clusters of 3-5 atoms have been observed and implicated in catalytic reactions [7]. These reactions are characterised by long induction periods which are absent in this case. Also it is likely that the reaction is not mass transfer limited due to colloidal nature of the catalyst rather than the typically used solid powders where stirring is needed to initiate the reaction. An increase in the amount of products with time while maintaining high selectivity (>94%) was observed in 2 hours. A full breakdown of products is shown in table 4.1.

As expected, the highest selectivity is observed for CH_3OOH which is formed almost exclusively in first 15 minutes. It slowly starts to transform into CH_3OH and the amount of CH_3OH increases from 0.3 μmol to 5.4 μmol in 60 min to 10.1 μmol in 2 hours suggesting that this is a consecutive transformation. Even then, the selectivity towards CH_3OOH is high which indicates its likely continuous formation. Over-time, formation of HCOOH is observed which increases to 1.2 μmol in 30 min, 2.2 μmol in 60 min and 3.9 μmol

Table 4.1: Product distribution for the time-on-line reactions of liquid phase oxidation of CH_4 using Au-Pd-PVP colloids using H_2O_2 and O_2 for varying times up to 120 mins

Entry	Catalyst	Product amount (μmol)				Oxygenate Selectivity / %	H_2O_2 Used/ μmol
		CH_3OOH	CH_3OH	HCOOH	CO_2		
1	0	6.2	0.3	0	n.d.	100	9
2	15	11.9	1.7	0.9	0.1	99	13
3	30	15.7	2.8	1.2	0.3	98	16
4	60	18.5	5.4	2.2	1.3	95	22
5	90	13.8	11.5	2.6	1.3	95	30
6	120	14	10.1	3.9	1.5	95	42

Test conditions: Pressure (CH_4) = 30 bar, pressure (O_2) = 5 bar, catalyst: 10 mL Au-Pd-PVP colloid, 6.6 μmol of metal (1:1 metal molar ratio), 50 μmol H_2O_2, 50 °C (ramp rate of 2.25 °C/min), 1500 rpm.

in 120 minutes. Overall, in 2 hours, a high selectivity of 95% is observed for liquid oxygenates with only 1.5 μmol CO_2 formed. Initially, no CO_2 is observed leading to 100% selectivity towards CH_3OOH and CH_3OH. Thus, these results are interesting and suggest a highly efficient continuous system could be utilised to suppress subsequent reaction although separation is challenging. It is also observed that H_2O_2 efficiency or gain factor is maintained over time.

As seen from the figure 4.1, decreasing reaction rates is observed over 90-120 min. The total amount of products is observed to plateau at 120 min which coincided with H_2O_2 depletion. There is also an increase in conversion of CH_3OOH to CH_3OH which suggests that this process is a decomposition of CH_3OOH rather than being initiated by H_2O_2. It also suggests that this process is in competition for active sites on catalysts which are more available when there is low amount of H_2O_2.

Thus a reaction was carried out by adding an additional 50 μmol H_2O_2 after 120 minutes of reaction at 50 °C. The reactor was depressurised and opened but not cooled down after 120 minutes of reaction. 50 μmol H_2O_2 was added and the reactor was sealed. The

reactor was then pressurised with 30 bar CH_4 and 5 bar O_2 and the reaction was continued for different lengths of time before stopping and cooling it down. Figure 4.2 shows the amount of products formed during the reactions performed for extended periods of time after 120 minutes of reaction.

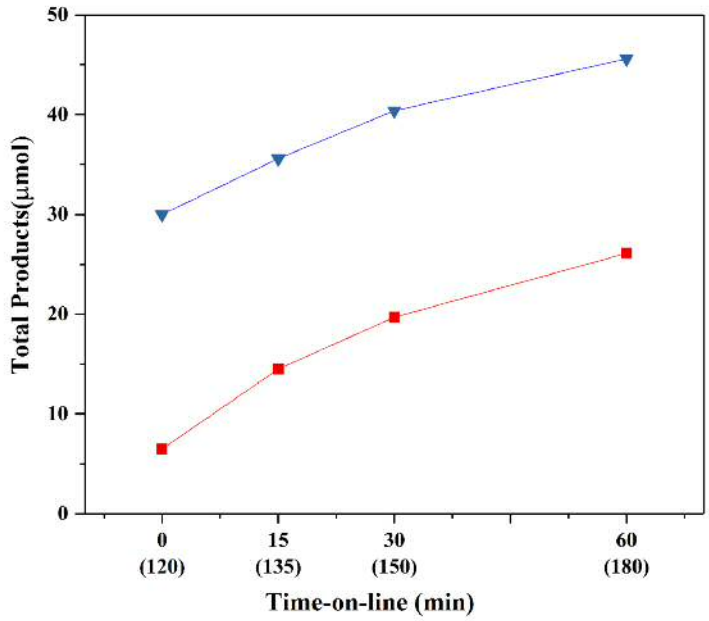

Figure 4.2: Re-use (shown with blue triangles) for methane oxidation using Au-Pd-PVP colloids studied by addition of 50 μmol of H_2O_2 at 50 °C after 120 min of initial reaction (shown with red squares). Test conditions: Pressure (CH_4) = 30 bar, pressure (O_2) = 5 bar, catalyst: 10 mL Au-Pd-PVP colloid, 6.6 μmol of metal (1:1 metal molar ratio), 50 °C (ramp rate of 2.25 °C/min), 1500 rpm.

After adding more H_2O_2 after 120 minutes, generation of more products was observed. 7.9 μmol of products were further generated in 15 minutes of reaction. This is comparable with the initial reaction rates that were measured where 8.1 μmol of products were generated in 15 minutes of reaction after the set temperature of 50 °C was achieved. Similar oxidation rate was thus observed with the Au-Pd-PVP colloid which indicated the colloid was stable during the reaction time and can be re-used by adding reactants.

Evolution of individual products over this re-use is shown in figure 4.3 as a function of time. Initially, again a high selectivity is observed for CH_3OOH, but soon CH_3OH increases due to CH_3OOH conversion which is accelerated at high temperature. A cross-over in selectivites is observed beyond 180 minutes. But even with higher conversion, the

oxygenate selectivity remains high and only limited over-oxidation was observed with time. There is some increase in rate of formation of HCOOH and 12.2 μmol of HCOOH is formed in 4 hours. Total products of 57 μmol are formed in 4 hours with high oxygenate selectivity of 94%. Even after a long reaction, only 3.4 μmol of CO_2 was formed. CO_2 was counted as sum of CO_2 formed after 120 minutes and CO_2 formed after the end of re-use reaction.

The catalyst was found to be stable after 4 hours of reaction with no visible aggregation or precipitation. The time-on-line and re-use studies demonstrate stability and efficacy of the colloidal catalysts where even after some over-oxidation, total level of CO_2 remained less than 6% of the total products achieved.

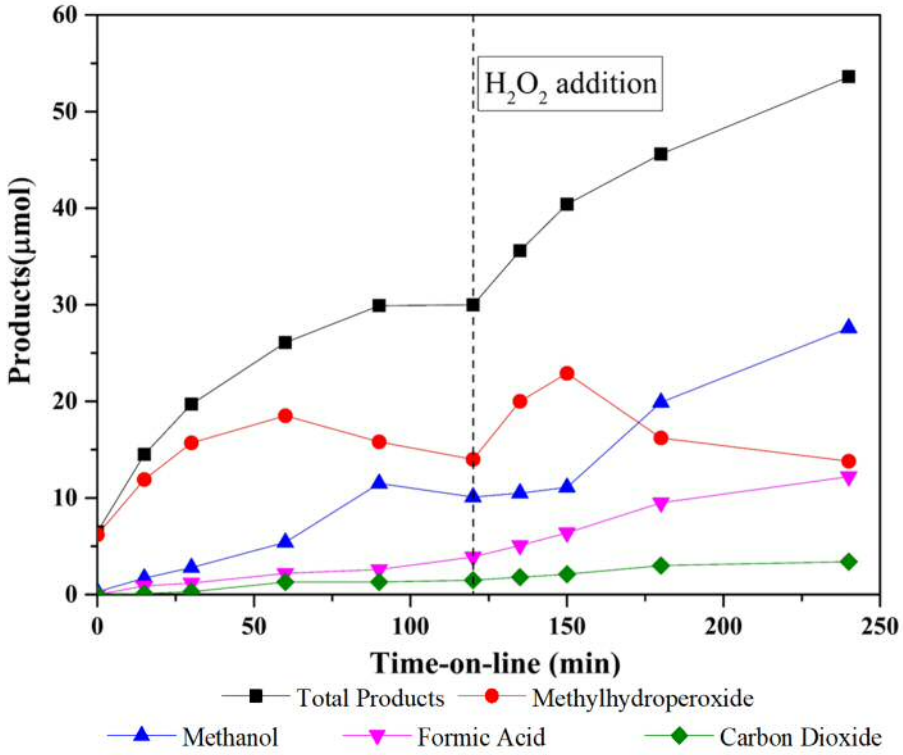

Figure 4.3: Time-on-line and reuse study for methane oxidation using Au-Pd-PVP colloid with H_2O_2 and O_2. Re-use of colloid is studied upon on adding 50 μmol of H_2O_2 at 50 °C after 120 min of initial reaction shown by black dotted line. Test conditions: Pressure (CH_4) = 30 bar, pressure (O_2) = 5 bar, catalyst: 10 mL Au-Pd-PVP colloid, 6.6 μmol of metal (1:1 metal molar ratio), 50 °C (ramp rate of 2.25 °C/min), 1500 rpm.

Time-on-line reaction were also performed with 30 μmol H_2O_2 and similar trend was observed (Figure 4.4). Similar to above, an increase in the amount of products was observed

with increase in time with high selectivity. A decrease in the rate of oxygenate production is observed after 60 minutes which corresponded with increase in H_2O_2 selectivity and slight over-oxidation.

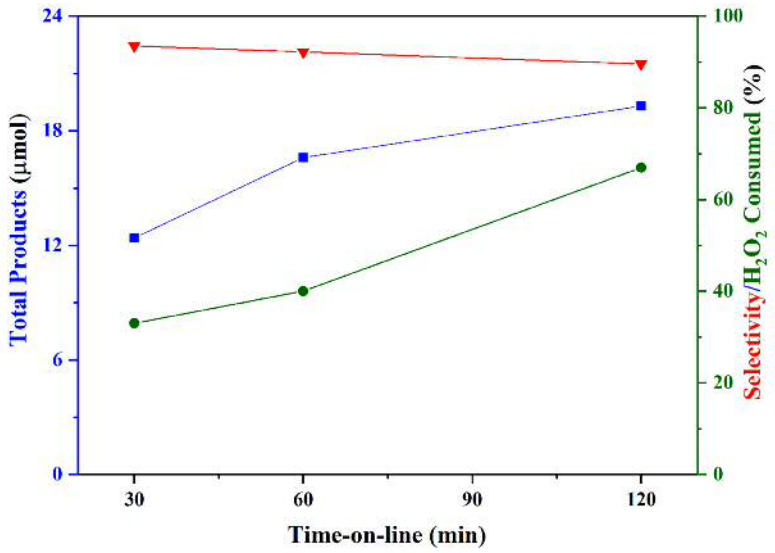

Figure 4.4: Time-on-line analysis for methane oxidation using Au-Pd-PVP colloid with H_2O_2 and O_2. This figure shows total products (blue squares), oxygenate selectivity (red triangles) and H_2O_2 consumption (green circle) as a function of reaction time. Test conditions: Pressure (CH_4) = 30 bar, pressure (O_2) = 5 bar, catalyst: 10 mL Au-Pd-PVP colloid, 6.6 μmol of metal (1:1 metal molar ratio), 30 μmol H_2O_2, 50 °C (ramp rate of 2.25 °C/min), 1500 rpm.

These time-on-line reactions studies indicate the high stability and re-usability of the colloids. Since, rate of reaction is maintained with similar amount of H_2O_2 addition, these catalysts can also be utilised for continuous phase reactions to achieve higher productivity. In order to do so, more studies are required utilising this by finding ways for product separation.

4.3 Effect of Reaction Temperature

Since, no induction period was observed with these colloidal catalysts and product formation took place before 50 °C was reached, it is considered that the colloidal catalyst could perform at lower temperatures. Thus, reactions were carried out at room temperature (23

°C) with and without the addition of O_2 as a part of the reaction mixture (Figure 4.5).

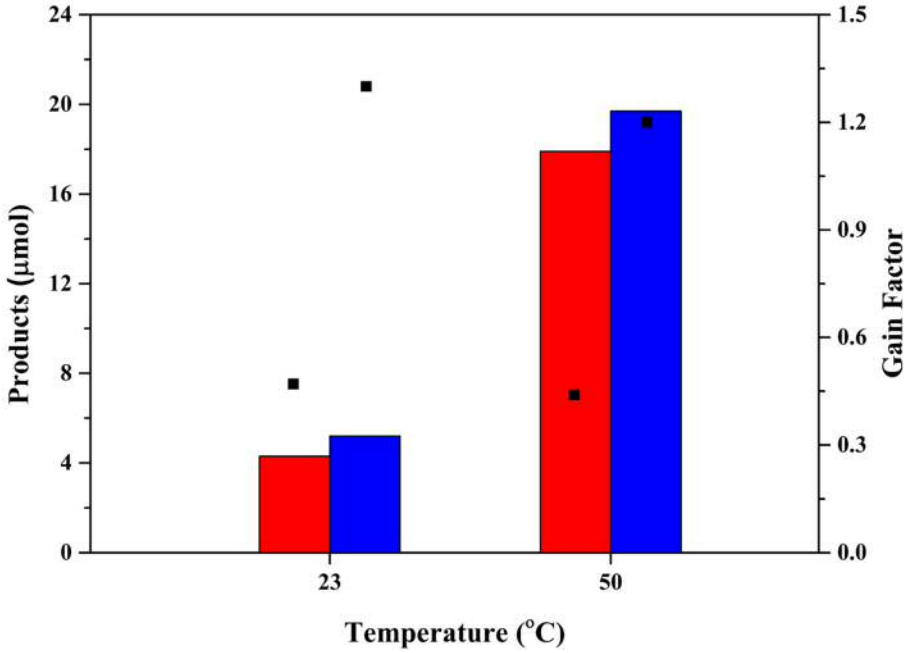

Figure 4.5: Oxidation of CH_4 performed at 23 °C and 50 °C with 50 μmol of H_2O_2. Blue and red bars represent reactions performed with and without 5 bar of O_2 pressure, respectively. Black squares indicate their respective gain factors. Test conditions: Pressure (CH_4) = 30 bar, pressure (O_2) = 5 bar, catalyst: 10 ml Au-Pd-PVP colloid 6.6 μmol of metal (1:1 metal molar ratio), 50 μmol, 1500 rpm, 30 min.

Indeed, Au-Pd-PVP bimetallic colloids were found to catalyse methane oxidation at room temperature. Though a decrease in productivity was observed showing that the reaction was temperature dependent; the efficiency of the reaction was found to be same at 23 °C and 50 °C. High oxygenate selectivity was also observed at room temperature which was of similar levels as that of the reaction carried out at 50 °C. A gain factor of 1.3 was observed at room temperature in presence of O_2 producing 5.4 μmol of products with only 4 μmol of H_2O_2 consumption, corresponding to a productivity of 10.4 $mol_{(products)}kg^{-1}_{(cat)}h^{-1}$. Methane oxidation activity for the methane mono-oxygenase system from *Methylococcus capsulates* (Bath) which selectively oxidises methane to methanol is reported to be 5.05 $mol_{(methanol)}kg^{-1}_{(cat)}h^{-1}$. The catalytic activity of Au-Pd colloidal system compares favourably with these methanotropic micro-organisms.

Since, no change in gain factor is observed with change in temperature, it is considered that the reaction proceeds through the same path once the activation step has taken place.

Since the reaction slows down on decreasing temperature, the reaction is considered to have an activation energy. This activation energy can be calculated using Arrhenius equation,

$$\mathrm{K} = Ae^{\frac{-E_a}{RT}} \tag{4.1}$$

where k is the reaction rate constant, A is the pre-exponential factor called the frequency factor, E_a is the activation energy, R is universal gas constant and T is the absolute temperature of the reaction. E_a can be evaluated by the variation in reaction rate coefficient as a function of time, given by

$$ln(\mathrm{K}) = ln(A) - \frac{E_a}{R}(\frac{1}{T}) \tag{4.2}$$

Thus, by plotting ln(k) as a function of $\frac{1}{T}$ as shown in the figure 4.6, the slope of the graph can be used to determine E_a. The activation energy for Au-Pd-PVP catalysed methane oxidation was determined to be 39 $\pm$ 3 kJ/mol. Previously, the activation barrier for H_2O_2 dissociation on Au@Pd(111) has been calculated as 25 kJ/mol [8]. Hydroxyl generation has been considered to be a fast reaction whereas abstraction of H from CH_4 has been considered as a slow step. The activation energy of H abstraction by O species has been calculated between 15-40 kJ/mol on Au and Pd surfaces [9]. The activation of oxygen leading to formation of methylhydroperoxy radical has been shown to have no intrinsic activation barrier which is in line with the mechanism proposed.

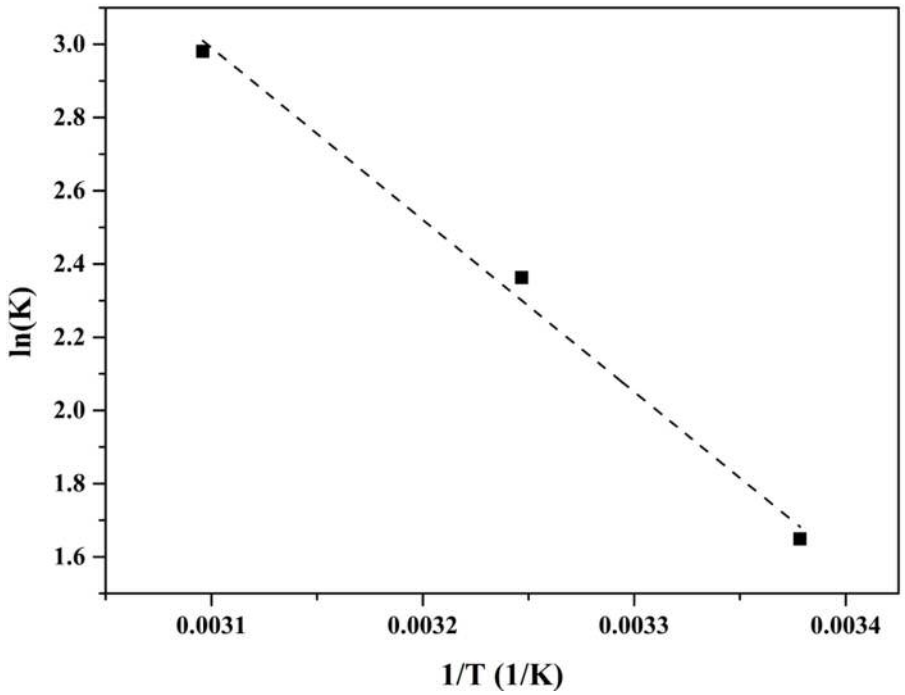

Figure 4.6: Arrhenius plot used to estimate the reaction barrier for methane oxidation in Au-Pd-PVP colloid based on initial rate constants based on initial consumption of H_2O_2 at each temperature. Test conditions: Pressure (CH_4) = 30 bar, catalyst: 10 ml Au-Pd-PVP colloid 6.6 μmol of metal (1:1 metal molar ratio), 50 μmol, 1500 rpm, 30 min.

Methane oxidation using colloids was shown earlier during the ramp-up period (before t=0) with high selectivity and stability. Now, it has been demonstrated that methane oxidation reaction takes place at room temperature. To evaluate the reactivity of the catalyst at room temperature in shorter time scales mimicking ramp up, a reaction was carried out for 10 minutes with 50 μmol H_2O_2. Compared to the reactions carried out for 30 minutes, lower gain factor of 0.57 was observed with production of 1.7 μmol of products was observed. This might be due to insufficient solubility of CH_4 or lack of radical concentration and interaction time given. Though the productivity is lower, these results indicate that colloidal catalysts can be utilised over a range of temperature and its activity can be tuned based on contact time without loss in selectivity. These parameters are important for optimisation of the reaction and scale up.

4.4 Effect of Reaction Pressure

A further kinetic investigation was carried out by conducting reactions using colloidal Au-Pd nanoparticles where different gas pressures of CH_4 and O_2 were used. Firstly, reactions were carried out with different pressures of CH_4 between 20 and 40 bar with constant pressure of 5 bar for O_2. The pressure range was chosen to keep the variation between CH_4 and O_2 relatively low to avoid reaction limitation due to O_2 concentration. The results of these reactions are shown in figure 4.7.

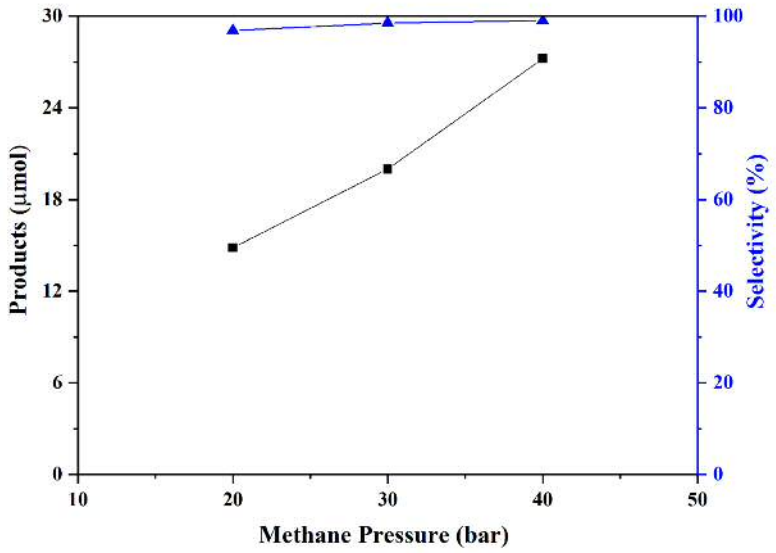

Figure 4.7: Kinetic studies showing dependence of primary oxygenate CH_3OOH formation on the methane pressure. Test conditions: Pressure (O_2) = 5 bar, catalyst: 10 ml Au-Pd-PVP colloid 6.6 μmol of metal (1:1 metal molar ratio), 50 μmol, 50 °C (ramp rate of 2.25 °C/min), 1500 rpm, 30 min.

From these reactions, it was found that increasing CH_4 pressure from 20 to 40 bar resulted in increase from 15 μmol to 27 μmol in the product amount. The oxygenate selectivity remained high (> 98%) even with the lower pressure of 20 bar demonstrating the efficacy of the catalyst. These observations are consistent with previous studies of increasing CH_4 leading to increase in productivity and oxygenate selectivity [10, 11]. An increase in CH_4 pressure has been shown to increase its solubility which might be responsible for this increase in productivity [12]. Reactions were then carried out by changing the O_2

pressure along with 30 bar of CH_4. Reactions were carried out with 3-5 bar of O_2. There was an upper limitation on O_2 pressure to keep the reaction within O_2 lean concentrations to avoid flammable mixtures of CH_4 and O_2. The results of the reaction are shown in the figure 4.8.

As shown in the figure, no substantial decrease in the amount of products was observed by decreasing the O_2 pressure. Zero order kinetic dependence is observed with O_2 pressure. Even in the absence of O_2, though the decrease in the product amount was not substantial, but as seen in Figure 4.5, there was a decrease in gain factor, hence higher consumption of H_2O_2 was observed. This fits well with the mechanism proposed in figure 3.13 in the previous chapter that H_2O_2 can also be consumed to generate O_2 which could then react with $\cdot CH_3$ to produce CH_3OOH. The selectivity was also maintained above 95% when the O_2 pressure was decreased. Previous studies performed with Pd/PdO systems for methane oxidation using CH_4 and O_2 also show similar zero order kinetic dependence on O_2 [13, 14].

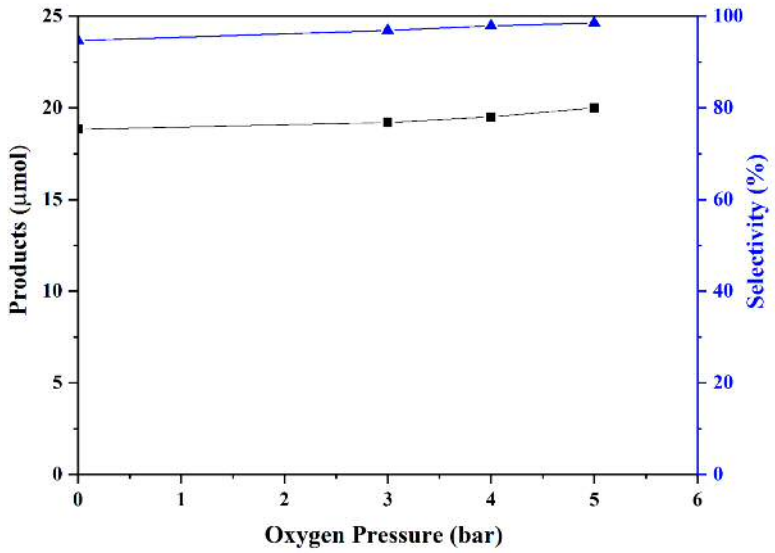

Figure 4.8: Kinetic studies showing dependence of primary oxygenate CH_3OOH formation on the methane pressure. Test conditions: Pressure (CH_4) = 30 bar, catalyst: 10 ml Au-Pd-PVP colloid 6.6 μmol of metal (1:1 metal molar ratio), 50 μmol, 50 °C (ramp rate of 2.25 °C/min), 1500 rpm, 30 min.

These reactions clearly show the dependence of reaction rates on CH_4 concentration. And

it is also seen that effective utilisation of H_2O_2 is dependent on O_2 pressure. These results can again be used for reaction optimisation to increase productivity and H_2O_2 efficiency while remaining within non-flammable mixtures.

4.5 Effect of Catalyst Preparation

In order to understand the Au-Pd colloidal system in more detail, the effect on the catalytic activity was studied by altering the catalyst and preparation parameters. In this section, CH_4 oxidation reactions are carried out with H_2O_2 and O_2 with a slight variation from the standard Au-Pd catalyst and the effect of that variation on the catalytic activity is investigated. The role of stabiliser is also investigated in this section by performing reactions in the absence of the stabiliser. Previous studies on supported Au-Pd/TiO_2 for methane oxidation with H_2O_2 have shown the effect of varying the metal ratio on catalytic activity and efficiency with a 1:1 metal molar ratio displayed the highest activity. Combined with minimal activity observed for monometallic colloids, catalysts were synthesised with 1:1 metal ratio and tested for these studies as well.

4.5.1 Effect of Metal Concentration

Reactions were generally performed with a metal concentration 6.6 μmol. An investigation into the effect of metal concentration was carried out on CH_4 oxidation reactions with H_2O_2 and O_2 using Au-Pd-PVP colloid was carried out (Figure 4.9).

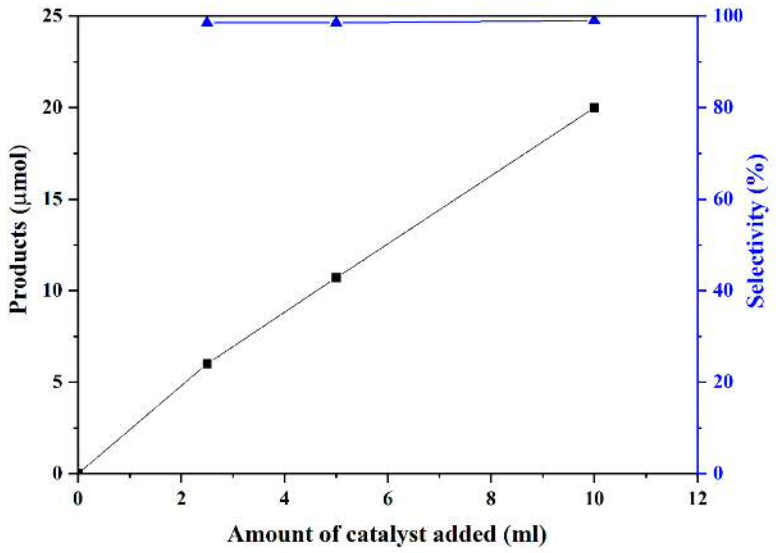

Figure 4.9: CH_4 oxidation reactions carried out with O_2 and H_2O_2 and Au-Pd colloids of various concentrations. Test conditions: Pressure (CH_4) = 30 bar, pressure (O_2) = 5 bar, catalyst: Au-Pd-PVP colloid, (1:1 metal molar ratio), 50 μmol H_2O_2, 50 °C (ramp rate of 2.25 °C/min), 1500 rpm, 30 min.

Samples of a typical Au-Pd colloid (metal concentration 6.6 μmol) were diluted to 3.3 μmol and 1.65 μmol and used to carry out CH_4 oxidation reactions. It was considered preferable to dilute a standard colloid than to prepare colloids by different concentration to avoid changing the preparation protocols. It was done to prevent inducing any change in particle size or composition that might affect catalytic activity. As shown in the figure 4.9, the amount of total products changes linearly with the amount of catalyst without any change in product selectivity. It also showed a first-order relationship between the total amount of oxygenated products produced after 30 min and the catalyst amount. The reaction with a metal concentration of 1.65 μmol produced 6 μmol, this number increased to 20 μmol when the metal concentration was increased to 6.6 μmol. These results demonstrated that under the standard conditions, the reaction operates under kinetic regime without significant diffusion limitations. This was expected as it is considered that removal of solid support could lead to removal of mass transport limitations on catalysis.

The colloidal catalyst was prepared in 800 ml of water and then rota-evaporation was

performed to increase the metal concentration. In these cases, final solution volume was concentrated to 200 ml. Thus to evaluate the difference in catalyst prepared with and without rota-evaporation, catalysts were prepared with same metal concentration of 6.6 μmol without performing the evaporation step. This was done by adding both metal precursors to 200 ml of water. The same procedure was then followed by performing polymer stabilisation and $NaBH_4$ reduction. Figure 4.10 shows the microscopy images of the fresh catalyst prepared in this method.

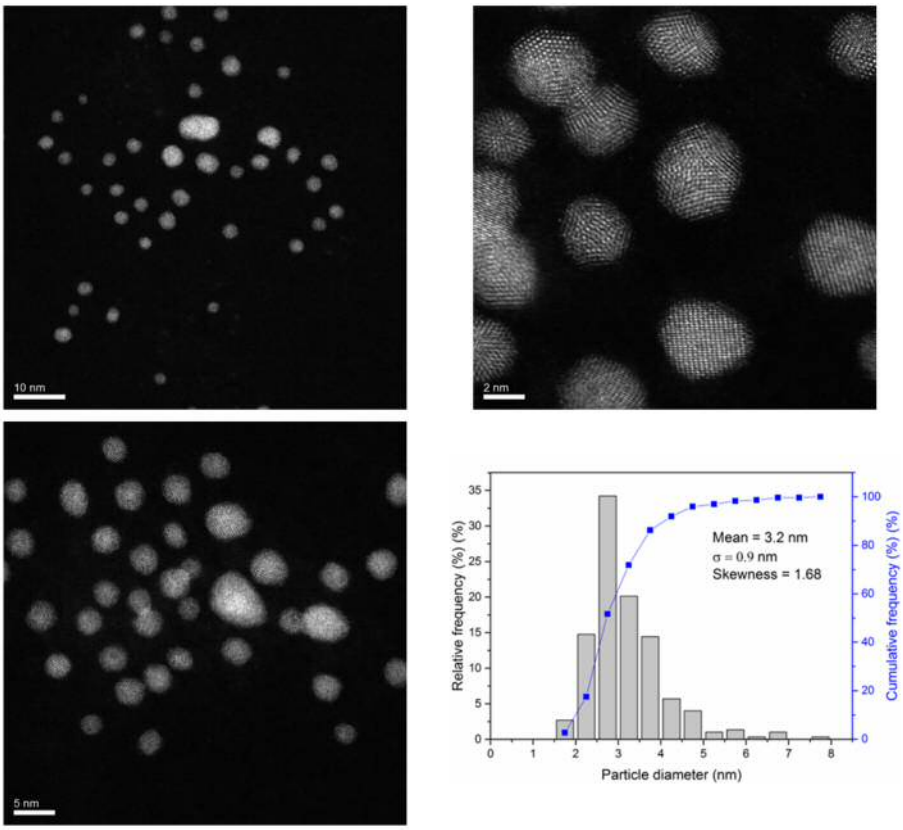

Figure 4.10: Representative HAADF-STEM images for the unsupported fresh Au-Pd-PVP colloid prepared without rota-evaporation.

The catalysts in this case were also found with uniform particle size with mean size of 3.2 nm along with a few large particles (>5 nm) similar to the catalysts obtained after rota-evaporation. Similar morphology of multi-twinned icosahedral was also observed. But here, some occasional truncated cub-octahedral nano-structures were also found. No dispersed atoms or clusters were observed in HAADF-STEM.

These catalysts were then used for methane oxidation. Testing was carried out with 10 ml

of this colloidal solution using 50 μmol H_2O_2 and 5 bar O_2. A similar productivity of 39.2 $moles_{(products)}kg^{-1}_{(metal)}h^{-1}$ was observed in 30 minutes with these catalysts as well as a high selectivity of 80% with only 0.3 μmol of CO_2 was produced. These used catalysts were then characterised using HAADF-STEM to understand the effect of reactants on these catalysts stability. HAADF-STEM images of used catalysts is shown in figure 4.11.

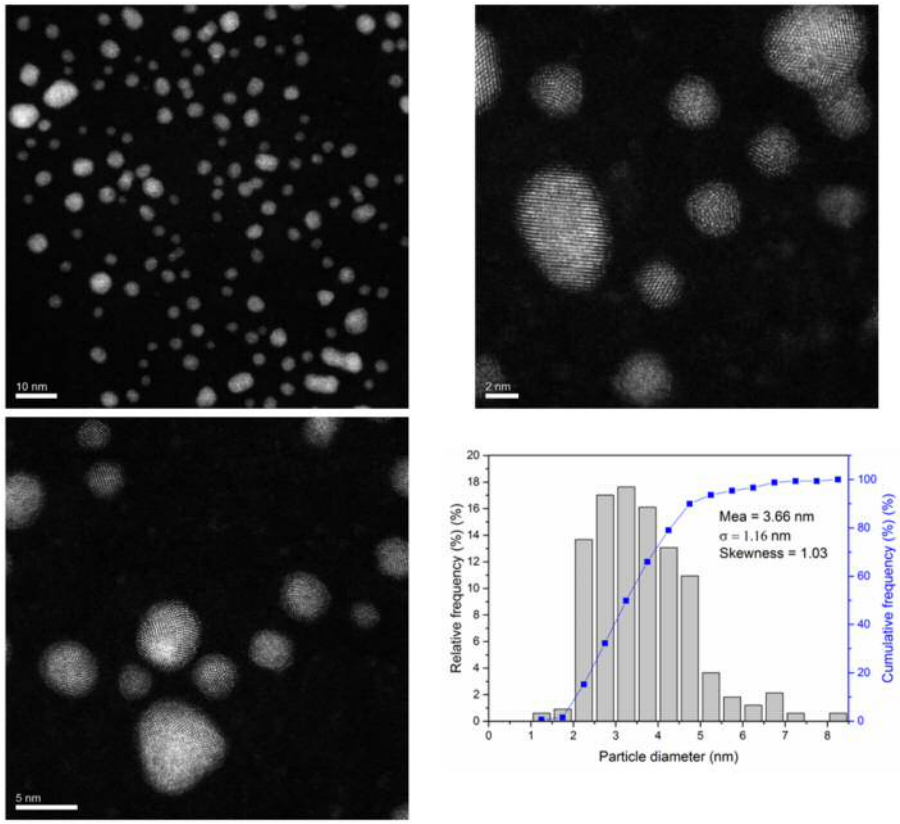

Figure 4.11: Representative HAADF-STEM images for the unsupported used Au-Pd-PVP colloid prepared without rota-evaporation. Test conditions: Pressure (CH_4) = 30 bar, pressure (O_2) = 5 bar, catalyst: 10 mL Au-Pd-PVP colloid, 6.6 μmol of metal (1:1 metal molar ratio), 50 μmol H_2O_2, 50 °C (ramp rate of 2.25 °C/min), 1500 rpm, 30 min.

Au-Pd-PVP colloids without rota-evaporation used for methane oxidation showed evidence of particle growth and agglomeration. The mean particle size was observed to be around 3.7 nm and a greater number of large particles (> 5 nm) was also observed. These observations are consistent with previous characterisation made regarding the used colloidal nanoparticles. Similar to the fresh samples, HAADF images revealed similar icosahedral and cub-octahedral Au-Pd-PVP nanoparticle structures and morphologies. But used samples also showed evidence of sub-nm clusters and some dispersed atoms. Since they are not present in the fresh catalysts, it is considered that leaching occurred in

the used catalysts. It was found that some of the particles developed a core-shell structure with Pd rich shell possibly caused by being exposed to oxidative conditions. This leaching was not observed in used catalysts formed by rota-evaporation. The effect of this leaching on the activity and stability was studied by performing reactions for extended periods of time. Reactions were performed for 60 and 120 minutes and the product distribution is showed in figure 4.12.

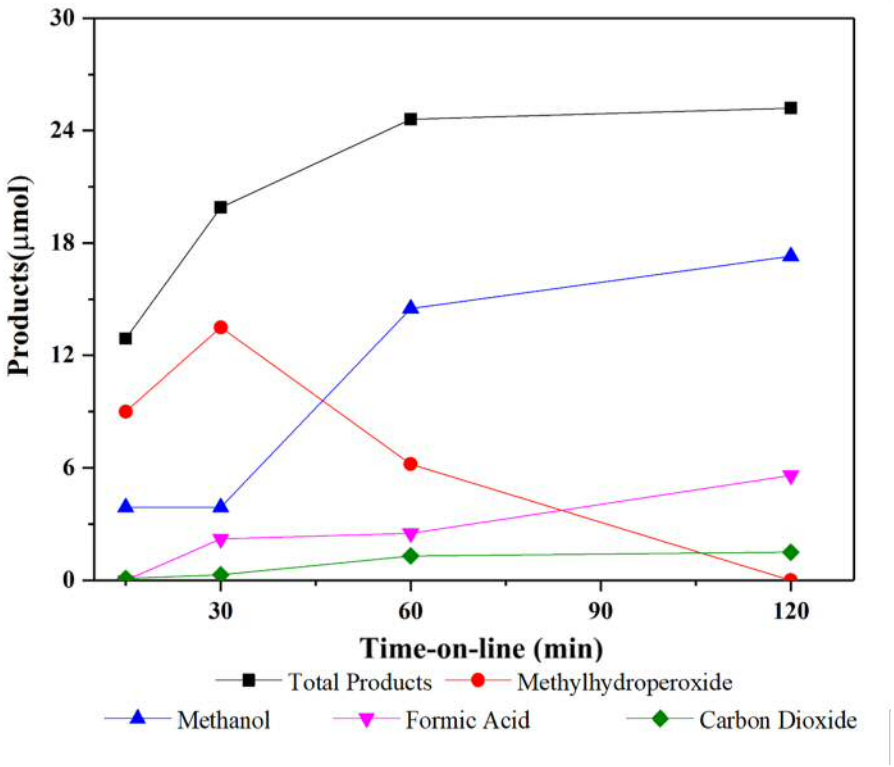

Figure 4.12: Time-on-line for methane oxidation of the unsupported Au-Pd-PVP colloid prepared without rota-evaporation with H_2O_2 and O_2. Test conditions: Pressure (CH_4) = 30 bar, pressure (O_2) = 5 bar, catalyst: 10 mL Au-Pd-PVP colloid, 6.6 μmol of metal (1:1 metal molar ratio), 50 μmol H_2O_2, 50 °C (ramp rate of 2.25 °C/min), 1500 rpm.

On comparing the time-on-line of these catalysts prepared without rota-evaporation to the rota-evaporated catalysts prepared throughout the thesis, a major difference in oxygenate selectivity was observed. As seen in figure 4.3, a rise in CH_3OH selectivity was observed after 90 minutes. But in this case, as shown in figure 4.12, a sharp decrease in CH_3OOH accompanied by an increase in CH_3OH was observed in 60 minutes of reaction. This might be due to an increase in Pd surface sites which is observed in used catalysts probably due to leaching. Pd surface active sites are known to dissociate O-O

bonds which might lead to CH_3OOH conversion to CH_3OH. In 30 minutes of reaction, 13.5 μmol of CH_3OOH and 3.9 μmol of CH_3OH was formed whereas in contrast to this, a crossover in these selectivities takes place in a 60 minute reaction. 6.2 μmol of CH_3OOH and 14.5 μmol of CH_3OH was formed. Slightly higher amount of over-oxidation product of HCOOH is also formed but limited selectivity was observed to the total oxidation product. After 120 minutes of reaction, 2.3 μmol CO_2 was measured.

These reactions indicate though the catalyst shows a limited structure-activity dependence, the product selectivities are dependent on surface site composition. These reactions are important to minimise over-oxidation but maximise CH_3OH selectivity without introducing new thermal or reduction steps. But rota-evaporating the colloid to increase the metal concentration is considered to form more stable catalysts compared to the colloids prepared by reducing a more concentrated metal solution as metallic clusters and dispersed atoms were observed in the used catalysts in the latter case. The effect of metal concentration on sols have been previously reported demonstrating a decrease in sol stability with increase in metal concentration [15, 16]. In case of the samples prepared by rota-evaporation, initial concentration of 0.16 M of metal precursors is used in 800 ml of water. The catalyst is formed after stable nanoparticle formation is rota-evaporated to remove water to increase the over-all metal concentration to 0.66 M in 200 ml. Whereas, without the rota-evaporation protocol, metal precursor solution of 0.66 M is used in 200 ml of water thereby forming a less stable colloidal solution. These reactions demonstrate the importance of tuning the catalyst preparation parameters like metal concentration for longer lifetime of the catalyst without compromising on the activity and selectivity of the reaction.

4.5.2 Effect of Metal Reduction

Colloidal nanoparticles are synthesised using chemical reduction methods [17]. The Brust-Schiffrin method of $NaBH_4$ reduction has gained popularity due to its ability to synthesis small sized particles narrow size distribution and dispersity [18, 19]. In this

work, a chemical reduction using $NaBH_4$ has been performed to synthesise bimetallic Au-Pd nanoparticles. A molar ratio of 1:5 (metal:$NaBH_4$) was used to ensure complete reduction. To achieve this, 6.6 ml of 0.1 M $NaBH_4$ was used. This solution was added using a pipette in two aliquots of 3.3 ml each. The colloidal solution was left to stir to ensure complete reduction took place.

Electron microscopy and X-ray photoelectron spectroscopy studies demonstrated that complete reduction took place after the addition as no dispersed atoms or clusters were observed. However, a mixture of particle sizes varying between 2 and 12 nm were measured with mean particle size of 3.7 nm. Though most of the particles were sized between 2 and 3 nm, some large sized particles between 3.5 nm to 4.5 nm were also observed. More detailed particle analysis was performed on the catalyst and it was possible to show a separated bi-modal distribution of particles size was plotted (Figure 4.13). Both smaller and larger sized particles can be seen in microscopy analysis. HAADF-STEM showed that all particles had similar morphology. XEDS analysis performed on particles with varied sizes such as 2 nm, 4 nm and 7 nm also showed that the composition of all these particles was same and no size dependent composition variation was present.

As seen from the particle size distribution, two dispersions of particles were observed. Smaller particles with a mean size of 2.4 nm and larger particles with a mean size of 4.7 nm were observed. It is considered this separated distribution of particles was formed due to the two aliquot addition performed during metal reduction. Larger particles are probably formed due to growth on the small sized nanoparticle "seeds" during the addition of second aliquot of the reductant. This type of seed mediated growth of nanoparticles is widely studied with gold nanoparticles [20]. But limited growth is observed with very few particles with very few particles with particle size greater than 6 nm and majority of particle sizes ranged between 2-4 nm.

To evaluate the effect of two aliquot $NaBH_4$ addition on the catalytic activity, catalysts were prepared by modifying the reduction procedure. Colloids were prepared with same metal concentration and same ratio of $NaBH_4$ reductant but by adding 6.6 ml of 0.1 M

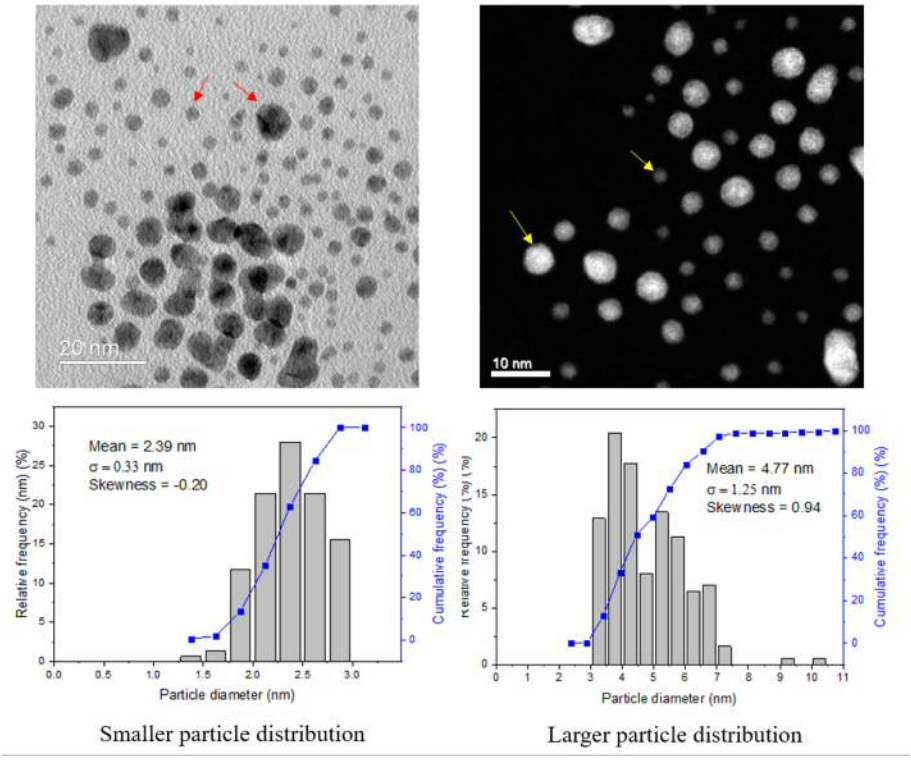

Figure 4.13: Representative BF and HAADF-STEM images for the unsupported fresh Au-Pd-PVP colloids prepared by adding two 3.3 ml aliquots of 0.1 M $NaBH_4$ showing smaller and larger particles and their particle size distributions.

$NaBH_4$ in one aliquot. The catalyst was then characterised using electron microscopy as shown in figure 4.14 and the particle size distribution was also measured.

As seen in the figure 4.14, both these catalysts showed similar multiply-twinned icosahedral morphology. Though STEM images indicated that this catalyst had relatively uniform particle size distribution and far fewer larger particles were observed with single aliquot $NaBH_4$ addition. The bimodality was not so much pronounced which might be due to the single aliquot addition. Though some of the particles were found to develop Pd rich surface, but no leaching of any metal was found in the catalyst as no dispersed atoms or sub-nanometer clusters were observed in HAADF-STEM. CH_4 oxidation activity was evaluated for this catalyst by testing this catalyst under standard conditions.

A reaction was first performed for 30 minutes. Similar productivity of 38.8 $moles_{(products)} kg^{-1}_{(metal)} h^{-1}$ was observed along with high oxygenate selectivity of 94% with only 0.4 μmol of CO_2. The activity and selectivity was found to be similar to the catalyst prepared by addition

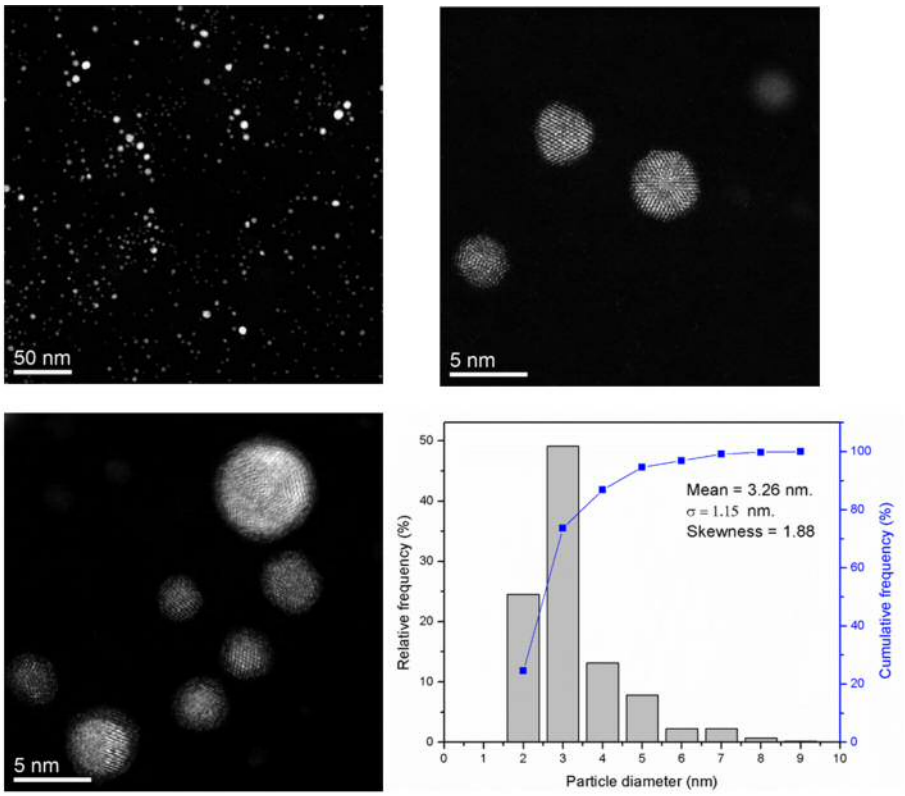

Figure 4.14: Representative HAADF-STEM images for the unsupported fresh Au-Pd-PVP colloid prepared by adding one 6.6 ml aliquot of 0.1 M $NaBH_4$ with its particle size distribution.

of two aliquots. This might be due to similarity in structure and morphology of the particles. The majority of particles in both the catalysts were also found to be sized between 2-4 nm. Also, there was no compositional variation in particles of different sizes, thus catalysts are considered to be similar in composition.

To compare the stability of this catalyst, time-on-line studies were performed with the catalyst (Figure 4.15). Productivity and selectivity obtained with this catalyst over 90 minutes was observed to be similar to the one prepared by addition of two aliquots which was shown in figure 4.3. A high oxygenate selectivity (> 85%) is maintained over 90 minutes with 2.3 μmol of CO_2 is produced. The amount of CO_2 is slightly higher compared to the previous case which might be due to the over-oxidation assisted by increased amount of Pd surface sites.

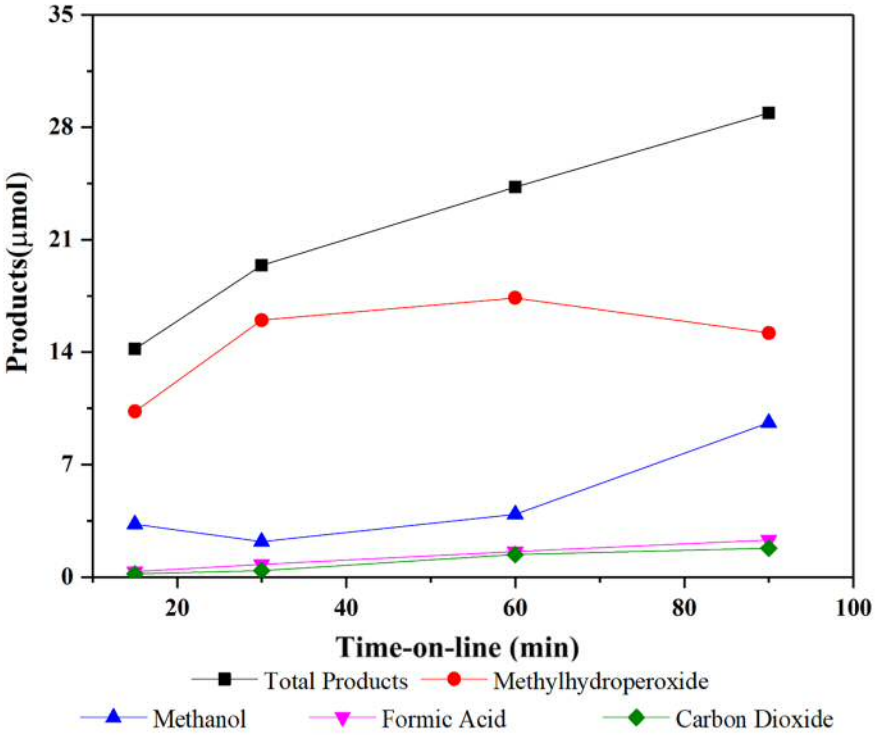

Figure 4.15: Time-on-line for methane oxidation of the unsupported Au-Pd-PVP colloid prepared by adding one 6.6 ml aliquot of 0.1 M $NaBH_4$ with H_2O_2 and O_2. Test conditions: Pressure (CH_4) = 30 bar, pressure (O_2) = 5 bar, catalyst: 10 mL Au-Pd-PVP colloid, 6.6 μmol of metal (1:1 metal molar ratio), 50 μmol H_2O_2, 50 °C (ramp rate of 2.25 °C/min), 1500 rpm.

In contrast to the previous case where a cross-over of CH_3OOH and CH_3OH selectivity was observed (Figure 4.12), in this case, highest selectivity was calculated for CH_3OOH, followed by CH_3OH. These results suggest a lack of effect of particle size on the activity of the catalyst within a narrow range when there is no compositional variation with different particle sizes. Since, majority of particles have similar particle sizes, the concentration of active surface sites is also considered to be similar which led to similar activity and selectivity in both the catalysts. Thus, a stable catalyst with narrow particle size distribution was synthesised by tuning the preparation protocol which was found to be active for methane oxidation with high productivity and selectivity. These results are useful to understand structure-activity relationship and elucidate reaction mechanism.

4.5.3 Effect of Polymer Stabiliser

In the previous chapter, it was shown that PVP polymer did not decompose or oxidise to form any liquid oxygenates. But the effect of polymer is unclear on the catalyst activity and stability. In this section the role of stabilising polymers is investigated by performing the reactions with stabiliser free Au-Pd colloid (Au-Pd-SF). Synthesis of Au-Pd-SF was performed by reduction of metal precursors using $NaBH_4$. But in these cases, PVP solution was not added prior to reduction. Previous studies have shown that the nanoparticles have similar particle sizes and morphology [21]. Reactions were carried out with the same metal concentration of 6.6 μmol. CH_4 oxidation activity of Au-Pd-SF is shown in figure 4.16 in comparison to Au-Pd-PVP colloid. A much lower activity was observed the colloids in the absence of stabilising polymer. Along with this, complete consumption of H_2O_2 was also observed with the Au-Pd-SF catalyst.

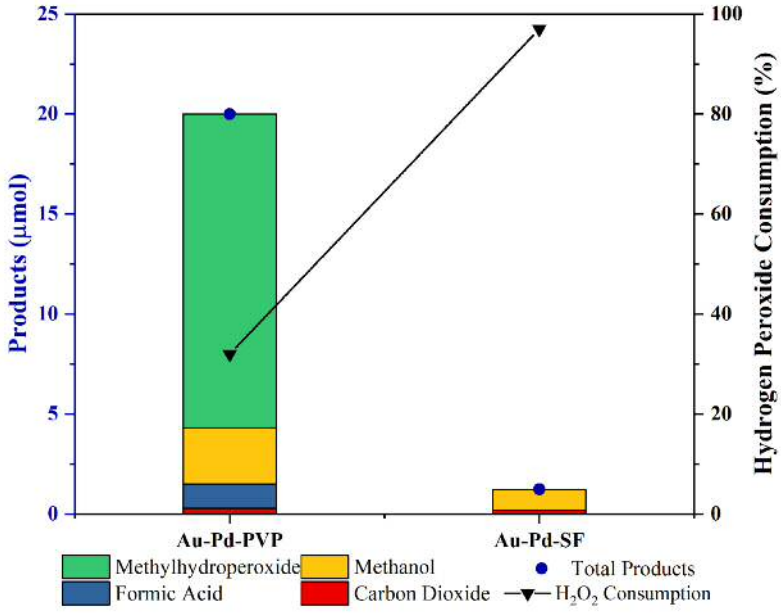

Figure 4.16: CH_4 oxidation activity of PVP stabilised and stabiliser free Au-Pd colloids using H_2O_2 and O_2. Test conditions: Pressure (CH_4) = 30 bar, pressure (O_2) = 5 bar, catalyst: 10 ml colloid 6.6 μmol of metal (1:1 metal molar ratio),, 50 μmol H_2O_2, 50 °C (ramp rate of 2.25 °C/min), 1500 rpm, 30 min.

As shown in the figure 4.16, 1.05 μmol of total products were formed with oxygenate selectivity of 84%. CH_3OH was found to be the major liquid oxygenate which might

have formed due to CH_3OOH transformation. Due to high consumption of H_2O_2, a low value of gain factor of 0.02 was observed. Compared to the gain factor of 1.2 for Au-Pd-PVP, stabiliser-free catalysts display much lower activity and efficiency. Au-Pd-SF nanoparticles were also found to be agglomerated after the end of the reaction. Abis *et. al.* have previously synthesised polymer free colloid for glycerol oxidation but it needed to be supported to avoid destabilisation and aggregation [21]. Thus, the polymer is shown not only to increase the stability of the reaction but also enhance the rates of the methane oxidation reaction. Polymers such as PVP are known to interact with different metallic sites. Interactions between Pd and PVP have been previously shown to block some of these sites. It is possible that in CH_4 oxidation, apart from increasing the stability of the colloids; PVP polymer also interacts with metal surface thus controlling the rate of the reaction by allowing selective interaction between the active sites and reactants.

In order to investigate the interactions between the metal nanoparticles and stabilising polymer PVP and its effect on CH4 oxidation activity, reactions were carried out using Au-Pd-SF colloidal catalysts with PVP solution in the reaction mixture along with H_2O_2 and O_2. To perform these reactions, 120 μl of 1 wt. % PVP solution was added to the reaction mixture to achieve same ratio which was used during preparation of Au-Pd-PVP colloid (metal:PVP::1:1.2).

Figure 4.17 shows the CH_4 oxidation activity performed with Au-Pd-SF nanoparticles with and without the PVP solution in the reaction mixture with H_2O_2 and O_2. 16.3 μmol products were obtained with the reaction containing PVP polymer solution. This was accompanied with reduction in H_2O_2 consumption to 48%. Thus a gain factor of 0.7 was obtained which is 35 times higher compared to reaction performed with Au-Pd-SF in the absence of PVP solution in the reaction mixture. Compared to Au-Pd-PVP colloidal catalysts, the activity and efficiency obtained is lower, but similar selectivity of 97% is observed.

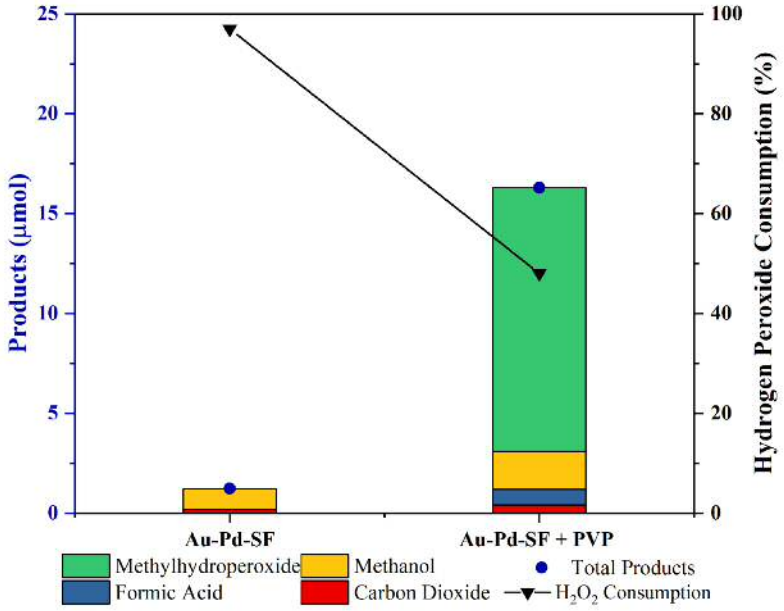

Figure 4.17: CH_4 oxidation activity of Au-Pd-SF colloids using H_2O_2 and O_2 with and without PVP polymer solution. Test conditions: Pressure (CH_4) = 30 bar, pressure (O_2) = 5 bar, catalyst:10 ml Stabiliser free Au-Pd colloid 6.6 μmol of metal (1:1 metal molar ratio), 120 μl of 1 wt.% PVP solution in water, 50 μmol H_2O_2, 50 °C (ramp rate of 2.25 °C/min), 1500 rpm, 30 min.

The Performance of stabilising polymer free colloids was assessed with addition of different amount of PVP solution, thus decreasing the ratio of PVP to metal from 1:1.2 which was used during catalyst preparation. Thus reactions were carried out with 120, 60, 10 μl of 1 wt. % PVP solution. The same metal concentration of 6.6 μmol was used by employing stabiliser free Au-Pd colloid. The results of these reactions are shown in figure 4.18. As seen from the figure, there is a slight decrease in the total amount of products from 16.3 μmol to 14.9 μmol when ratio is decreased from 1:1.2 to 1:0.1 maintaining high selectivity (> 97%) with a maximum production of CO_2 of 0.4 μmol. There is a sharp increase in H_2O_2 consumption to 90% on decreasing the PVP polymer amount to 10 μl decreasing the gain factor to 0.3. Agglomeration and precipitation of the colloid was also found post-reaction.

Table 4.2 shows the product distribution obtained in the reactions. Reactions performed with 120 and 60 μl PVP showed similar product distribution as obtained with PVP sta-

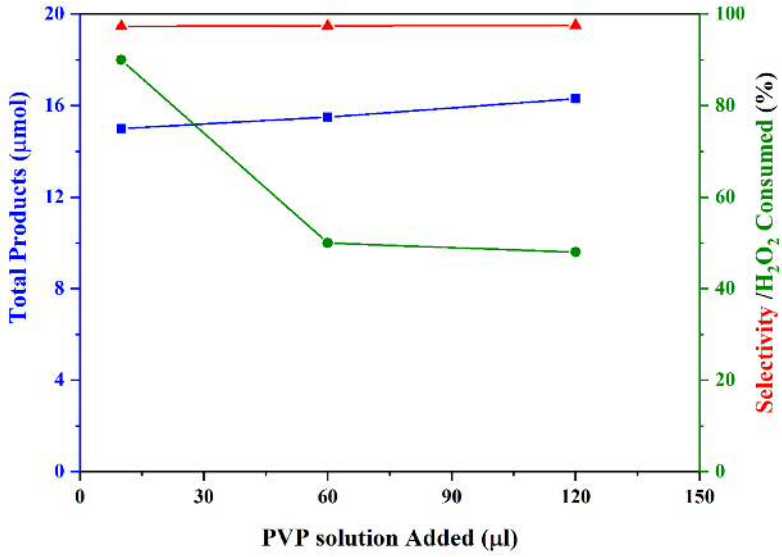

Figure 4.18: CH_4 oxidation activity of Au-Pd-SF colloids using H_2O_2 and O_2 with different amounts of PVP polymer solution. Test conditions: Pressure (CH_4) = 30 bar, pressure (O_2) = 5 bar, catalyst:10 ml Stabiliser free Au-Pd colloid 6.6 μmol of metal (1:1 metal molar ratio), 1 wt.% PVP solution in water, 50 μmol H_2O_2, 50 °C (ramp rate of 2.25 °C/min), 1500 rpm, 30 min.

bilised Au-Pd colloid with highest selectivity was observed for CH_3OOH followed by CH_3OH. Some over-oxidation to HCOOH was also observed along with minimal total oxidation product of CO_2. This trend is not observed with very low amount of 10 μl of PVP solution, where highest selectivity was observed for CH_3OH. 5.8 μmol of CH_3OOH and 6.3 μmol of CH_3OH was formed during the reaction. In contrast, 11.7 μmol of CH_3OOH and 2.7 μmol of CH_3OH was formed in reaction with 60 μl of PVP solution. A higher consumption in H_2O_2 was also observed in conjunction to higher over-oxidation. This trend was also observed with longer reactions where H_2O_2 consumption was used for CH_3OOH conversion and oxidation. The catalyst was also found to be destabilised and agglomerated after 30 minutes of reaction.

Since an increase in reaction productivities and gain factor was observed on increasing the amount of PVP that was added, reactions were carried out with 240 μl of 1 wt.% PVP solution to evaluate the activity difference. Figure 4.19 shows the comparison between reactions performed with Au-Pd-SF with metal:PVP ratio 1:1.2 and 1:2.4. No significant increase in productivity was observed on increasing the amount of PVP, thus indicating

Table 4.2: Methane oxidation activity of stabiliser free Au-Pd colloid by varying the amount of 1 wt.% PVP solution added.

Entry	PVP Added μl	Product amount (μmol)				Oxygenate Selectivity	Oxygenate Productivity	H_2O_2 Consumed	Gain Factor
		CH_3OOH	CH_3OH	HCOOH	CO_2				
1	1:1.2 (120)	13.2	1.9	0.8	0.4	92.6	31.8	48	0.7
2	1:0.6 (60)	11.7	2.7	0.7	0.3	93.5	30.2	50	0.6
3	1:0.1 (10)	5.8	6.3	2.6	0.6	81.2	29.8	90	0.3

Test conditions:Pressure (CH_4) = 30 bar, pressure (O_2) = 5 bar, catalyst: 10 mL Au-Pd-SF colloid, 6.6 μmol of metal (1:1 metal molar ratio), 1 wt.% PVP solution in water, 50 °C (ramp rate of 2.25 °C/min), 1500 rpm, 60 min.

the limitation on activity of stabiliser free colloidal catalysts. Oxygenate productivity of 32.4 $moles_{(oxygenates)}kg^{-1}_{(metal)}h^{-1}$ was observed with similar product distribution as observed with reactions with 120 μl of PVP solution. The highest selectivity was observed for CH_3OOH (14.1 μmol) followed by CH_3OH (1.3 μmol) and formic acid (0.8 μmol). Low total oxidation product of CO_2 of 0.4 μmol was observed leading to high selectivity of 97%. A slight decrease in H_2O_2 consumption from 48% to 44% was observed in this case. But as compared to Au-Pd-PVP colloids, H_2O_2 consumption is still higher leading to lower gain factor of 0.7.

These reactions indicate that the presence of polymer is essential to selectively expose the active sites to the reactants present in the solution. The absence of PVP polymer stabilisation led to high H_2O_2 consumption and low activity for methane oxidation. A suppression in H_2O_2 decomposition is observed with addition of PVP solution in the reaction media. It is considered that the polymer interacts with the metal sites thus providing a pathway to control H_2O_2 decomposition rates. Such kinetic control over reaction rates have been demonstrated in different reactions such oxidation of n-butanol where a decrease in activity was observed on increasing the amount of polymer present [22]. Such reactions are important to understand not only the structure of the catalyst and stabiliser effect but also helps in understand the active sites for reaction mechanism in oxidation chemistry.

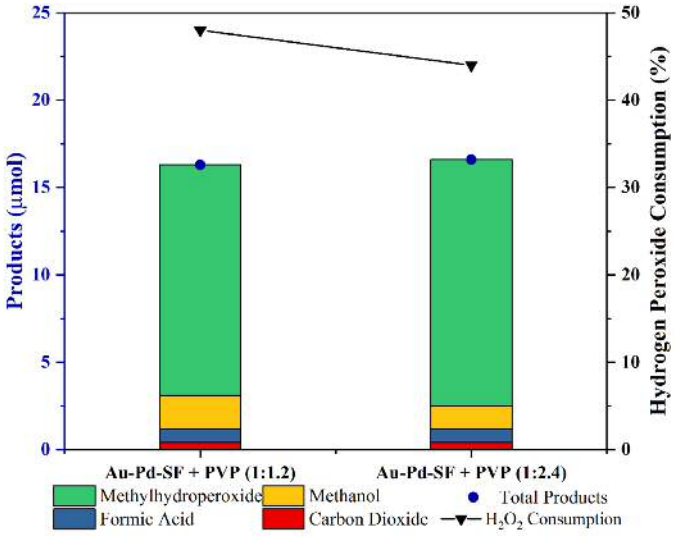

Figure 4.19: CH_4 oxidation activity of Au-Pd-SF colloids using H_2O_2 and O_2 with higher amount of PVP polymer solution. Test conditions: Pressure (CH_4) = 30 bar, pressure (O_2) = 5 bar, catalyst:10 ml Stabiliser free Au-Pd colloid 6.6 μmol of metal (1:1 metal molar ratio), 1 wt.% PVP solution in water, 50 μmol H_2O_2, 50 °C (ramp rate of 2.25 °C/min), 1500 rpm, 30 min.

4.6 Conclusions

Following the preliminary investigations into methane oxidation with H_2O_2 and O_2 with Au-Pd-PVP colloids, the focus in chapter has been to identify and elucidate the effect of key catalyst preparation and testing parameters. Longer reactions have been carried out to check the stability of the catalyst. After 2 hours of reaction, a plateau was observed in reaction rates which coincided with consumption of available H_2O_2. Though a shift is observed in selectivity with longer time, but selectivity to liquid oxygenates remain high even after 2 hours of reaction. Revival of reaction rates was observed on addition of more H_2O_2 after 120 minutes of methane oxidation activity. Thus, the colloid catalyst is stable for longer use and reuse. Even after 4 hours of reaction, total level of CO_2 remained less than 6% of the total products.

Furthermore, no induction period was observed and products were obtained even before 50 °C was attained. Thus reactions were carried out at lower temperatures successfully

and activation energy of the reaction was calculated as 39 ± 3 kJ/mol. Catalytic activity of Au-Pd-PVP colloidal system compared favourably with the methanotropic microorganisms at room temperature. The colloidal system was found to operate in kinetic regime since amount of products was found to be proportional to concentration of colloid. It was also found to be dependent on methane pressure and concentration of H_2O_2 but independent of gas phase O_2. This observation was in agreement with the scheme presented.

First order relationship was observed between the total amount of oxygenates and the metal concentration. This metal concentration was varied by diluting a colloidal solution of 0.66 μmol/ml. The catalyst itself was concentrated by rota-evaporation. The effect of rota-evaporation was evaluated on activity and stability of the colloid. Though the colloid was found to be active and similar productivity was obtained after 30 minutes of reaction, evidence for leaching was observed post reaction. Colloid was also prepared by modifying the reduction process and no change in activity or stability was observed.

Finally, the effect of stabiliser was investigated for colloidal catalysts. Stabilising polymer is known to prevent agglomeration of the catalyst and interacts with the metal surface sites affecting the activity and selectivity of the reaction. With Au-Pd colloids, polymer free catalysts were found to be unstable and diminished methane oxidation activity was observed. High H_2O_2 consumption was also observed in the absence of PVP stabilising polymer. Consumption was seen to be depressed on addition of PVP polymer solution to the reaction mixture. This was accompanied by increase in the methane oxidation activity to levels similar to the PVP stabilised Au-Pd colloids. Though the gain factor was found to be slightly lower, it is possible that polymer in the solution interacts with the metal surface sites thus controlling the rate of production of radicals.

Overall, the bimetallic Au-Pd colloidal catalysts have been found to be highly active and selective for methane oxidation with H_2O_2 and O_2 and a better understanding of the system has been attained through the systematic investigation of various aspects of the catalytic preparation and reaction parameters. It has been shown that Au-Pd colloids display high level of intrinsic activity for methane oxidation and its chemical properties make it

an interesting material and catalyst to study other oxidation reactions and chemical transformations.

Bibliography

(1) Y. Iizuka, T. Tode, T. Takao, K.-i. Yatsu, T. Takeuchi, S. Tsubota and M. Haruta, *Journal of Catalysis*, 1999, **187**, 50–58.

(2) I. Biondi, G. Laurenczy and P. J. Dyson, *Inorganic Chemistry*, 2011, **50**, 8038–8045.

(3) Y. Nomura, T. Ishihara, Y. Hata, K. Kitawaki, K. Kaneko and H. Matsumoto, *ChemSusChem*, 2008, **1**, 619–621.

(4) Y. Mikami, A. Dhakshinamoorthy, M. Alvaro and H. Garcia, *Catal. Sci. Technol.*, 2013, **3**, 58–69.

(5) P. G. N. Mertens, I. F. J. Vankelecom, P. A. Jacobs and D. E. De Vos, *Gold Bulletin*, 2005, **38**, 157–162.

(6) K. M. Koczkur, S. Mourdikoudis, L. Polavarapu and S. E. Skrabalak, *Dalton Trans.*, 2015, **44**, 17883–17905.

(7) J. Oliver-meseguer, J. R. Cabrero-antonino, I. Domínguez, A. Leyva-pérez and A. Corma, *Science*, 2012, **338**, 3–7.

(8) J. Li, A. Staykov, T. Ishihara and K. Yoshizawa, *The Journal of Physical Chemistry C*, 2011, **115**, 7392–7398.

(9) P. P. Olivera, E. M. Patrito and H. Sellers, *Surface Science*, 1995, **327**, 330–357.

(10) M. H. Ab Rahim, M. M. Forde, C. Hammond, R. L. Jenkins, N. Dimitratos, J. A. Lopez-Sanchez, A. F. Carley, S. H. Taylor, D. J. Willock and G. J. Hutchings, *Topics in Catalysis*, 2013, **56**, 1843–1857.

(11) C. Hammond, R. L. Jenkins, N. Dimitratos, J. A. Lopez-Sanchez, M. H. A. Rahim, M. M. Forde, A. Thetford, D. M. Murphy, H. Hagen, E. E. Stangland, J. M. Moulijn, S. H. Taylor, D. J. Willock and G. J. Hutchings, *Chemistry – A European Journal*, **18**, 15735–15745.

(12) Z. Duan, N. Møller, J. Greenberg and J. H. Weare, *Geochimica et Cosmochimica Acta*, 1992, **56**, 1451–1460.

(13) F. Ribeiro, M. Chow and R. Dallabetta, *Journal of Catalysis*, 1994, **146**, 537–544.

(14) C. F. Cullis, D. E. Keene and D. L. Trimm, *Trans. Faraday Soc.*, 1971, **67**, 864–876.

(15) J. Turkevich, *Gold Bulletin*, 1985, **18**, 86–91.

(16) M. Chow and C. Zukoski, *Journal of Colloid and Interface Science*, 1994, **165**, 97–109.

(17) C.-J. Jia and F. Schuth, *Phys. Chem. Chem. Phys.*, 2011, **13**, 2457–2487.

(18) M. Brust, M. Walker, D. Bethell, D. J. Schiffrin and R. Whyman, *J. Chem. Soc., Chem. Commun.*, 1994, 801–802.

(19) M.-C. Daniel and D. Astruc, *Chemical Reviews*, 2004, **104**, 293–346.

(20) W. Leng, P. Pati and P. J. Vikesland, *Environ. Sci.: Nano*, 2015, **2**, 440–453.

(21) L. Abis, S. J. Freakley, G. Dodekatos, D. J. Morgan, M. Sankar, N. Dimitratos, Q. He, C. J. Kiely and G. J. Hutchings, *ChemCatChem*, 2017, **9**, 2914–2918.

(22) G. Inaki, M. P. J., N. Ewa, D. Mark, M. D. J., H. G. J. and T. S. H., *ChemSusChem*, **8**, 473–480.

5 | Theoretical investigations into H_2O_2 and Au and Pd using DFT

5.1 Introduction

The previous chapters have demonstrated methane oxidation using H_2O_2 and O_2 with Au-Pd nanoparticles. It has been shown that Au-Pd nanoparticles have high activity and selectivity for methane oxidation. It was also shown that H_2O_2 is essential for the reaction and reaction efficiency is dependent on H_2O_2 consumption. H_2O_2 is also an important commodity chemical used as bleaching agent or disinfectant. As discussed in Chapter 1, the current method for the industrial production of H_2O_2 is the anthraquinone process. Direct synthesis of H_2O_2 from molecular O_2 and H_2 is an atom efficient and greener approach and has been investigated widely. Design of catalysts with high activity and selectivity requires fundamental, multi-level knowledge of mechanism for H_2O_2 formation on metal clusters. This is where computational tools are very useful. First principle calculations and molecular dynamics have been previously used to examine different reaction pathways and their energetics on various sites [1, 2].

The reaction mechanism for the production of hydrogen peroxide from O_2 and H_2 has been previously investigated using extended metal surfaces [3, 4]. Adsorption energies for O_2 and H_2 and activation energies for different reaction steps were calculated but with the aim of evaluating the effect of alloying Au and Pd together. Staykov *et. al.* utilised

periodic Pd and Pd/Au surfaces to understand the role of Au in decreasing the dissociation of O_2 which leads to formation of water on Pd(111) surface [5]. Though these results are useful for catalytic development, it is important to understand the role of different active sites in Pd and Au and the difference among the activity of atoms located at different facets, edges and corners [2, 6].

Another significant area of research is the effect of the solvent on the reaction. Though most of the DFT studies are based on gas phase calculations; a solvent like water and methanol, and additives like halides and acids have been shown to greatly influence the activity and selectivity under the experimental conditions [7, 8]. Some studies have been performed by including additives such as H^+ and Br^- with Pd clusters in gas phase calculations where adsorption of Br^- has been shown to suppress decomposition of H_2O_2 [6]. Flaherty and co-workers have proposed a mechanism involving the proton from solvent molecule for H_2O_2 formation where electrons are provided by heterolytic hydrogen oxidation [8] (Figure 5.1). The mechanism resembles the oxygen reduction reaction (ORR) commonly observed in electrocatalysis and is consistent with previously reported Lunsford mechanism for Pd based systems [9]. However, more theoretical studies are required to understand the mechanism at this liquid-solid interface to understand the role of solvent and additives [10].

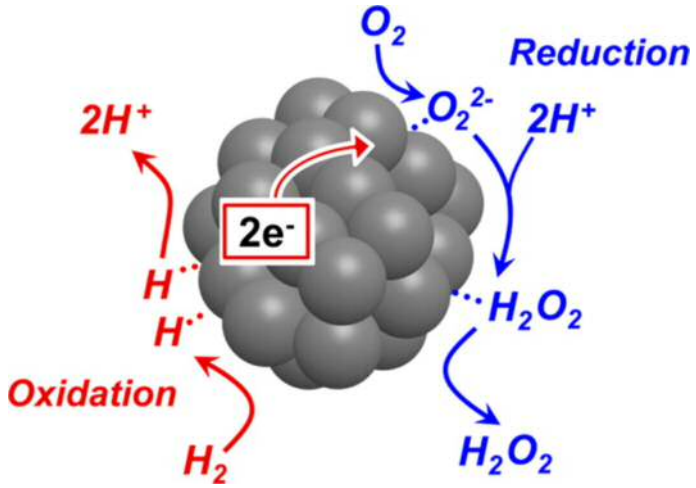

Figure 5.1: Schematic showing both O_2 reduction and heterolytic H_2 oxidation on Pd cluster to form H_2O_2 taken from ref [8]

In this chapter, computational studies are performed on isolated Au and Pd clusters in order to understand the reactivity of different sites for direct synthesis of H_2O_2. Adsorption of O_2 and H_2 will be studied and the activation energy of different reaction steps would be monitored. The effect of protic solvent would be studied by first adding water molecule as a reactant and later by implicit solvation.

5.2 Computational Details

All calculations were performed using the Vienna Ab Initio Simulation Package (VASP 5.4.1/5.4.1-tst-/5.4.1-sol). Details of various parameters used in the thesis are explained in chapter 2. Pure gold and palladium metal particles containing 38 atoms are investigated in this thesis. The metallic clusters were separately placed within a cubic periodic box with a side length of 25 Å. The distance was sufficient to avoid physical interaction between neighbouring particles. *Plane Wave Cut off*: It is important to calculate a cut-off energy E_{encut} to accurately account for interactions in the system while avoiding large computational costs which would result with too large cut-off value. In VASP, the ENCUT tag is used to modify these plane wave cut-off energies. For both Au and Pd system, an evaluation of the plane wave cut-off was performed initially by varying the total energy of the system with different cut-off energies (Figure 5.2). A plane wave cut-off of 500 eV was found to be suitable for treatment of both Au and Pd particles as total energy has converged at this point. Further expansion produces total energies with a difference of 0.008 eV, thus confirming suitability of 500 eV cut off.

This value will be used for all further calculations. The generalised gradient approximation (GGA) is used to perform all the calculations using the PBE functional (Perdew, Burke and Ernzerhof) [11, 12]. Another functional commonly used is PW91 but it was not chosen as a suitable functional as it has been reported to overestimate binding energy of small molecules to metal surfaces [13]. As explained earlier long range dispersion corrections were included for correct approximation of adsorption energies. The PBE

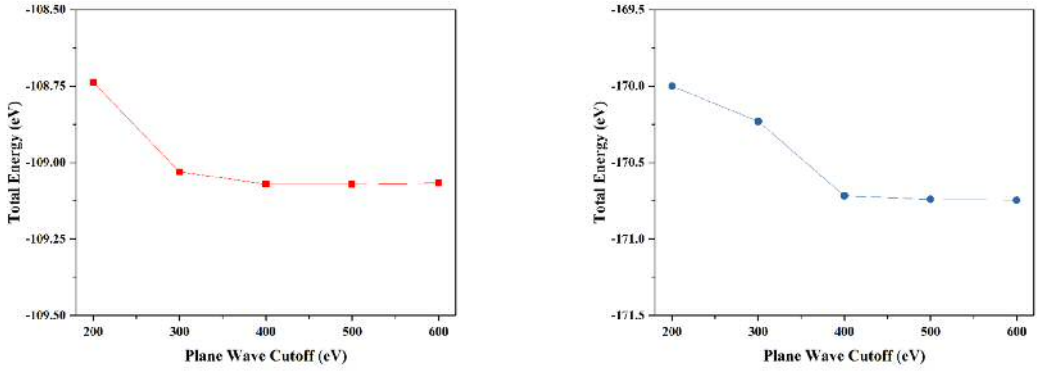

(a) (b)

Figure 5.2: Total energy vs plane wave cut off for (a) Au_{38} and (b) Pd_{38} particles.

functional within VASP also provides an option to include these interactions using D3 method of Grimme [14].

All calculations are spin unrestricted with Projector Wave method (PAW) pseudopotentials. As mentioned earlier in chapter 2, explicit treatment of all electrons is unfeasible. Therefore the electron energy levels are divided into core and valence states. This is employed by using metal POTCAR in which Au contains 60 core and 19 valence electrons and Pd contains 36 core and 10 valence electrons. Since, the modelling of these clusters and molecules is performed in isolation in a large (15625 $Å^3$) periodic box and properties of localised nanoparticles is investigated, Monkhorst-Pack k-point grid density was set to a mesh of $1 \times 1 \times 1$ to avoid large computational costs. A small sample mesh along with adequately sized periodic box prevents self-interaction between the periodic images. These metal particles are different from bulk metal as they contain discreet orbital energies as opposed to continuous bands observed within bulk metal. To avoid this electronic smearing at Fermi level which leads to these continuous band formation, the Gaussian smearing of very small width of 0.0001 is employed. This is done by setting the SIGMA tag within VASP. Finally, all geometric relaxations were performed with electronic convergence set to 10^{-4} eV and force convergence criteria set to -0.05 $eVÅ^{-1}$. Activation barriers for various reaction mechanisms were obtained using the nudged elastic band method (NEB) briefly explained in subsection 2.6.6. In the process of NEB calculations

five images were used between the starting and ending geometries. The transition states were verified by performing a frequency calculation on the proposed transition state system to locate a single imaginary frequency mode and confirm that there was only a single imaginary mode. VESTA (**V**isualisation for **E**lectronic and **St**ructural **A**nalysis) to analyse and visualise the computed DFT electron density distribution [15]. Charge density files were created by the tag LCHARG in the INCAR file after geometry optimisation.

5.3 Optimisation of Metal Particles

Metallic clusters are well studied in literature and used to catalysis on different types of active sites [16]. But there is a massive range of sizes and shapes of nano-clusters which can be used. The cuboctahedral geometry of the clusters was selected based on Sutton-Chen global minima in transition metals [17]. The size of the cluster in the Sutton-Chen potential studies was varied upto 80 atoms but specific clusters were found to be more stable than others like 6, 17, 38 and 75 as shown in figure 5.3 [17].

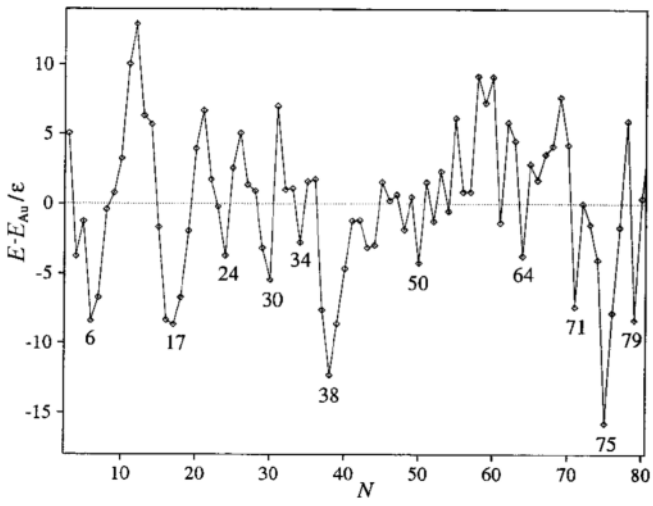

Figure 5.3: Energies of various nano-clusters normalised to cluster size (taken from reference [17])

Au and Pd monometallic clusters containing 38 atoms were selected to investigate due to their high symmetry and availability of various facets sites. As shown in the figure 5.4, these clusters are highly symmetrical and exhibit both square (100) and trigonal (111)

facets. The facets have been identified as active sites where different reagents could adsorb and potentially react. Though bimetallic Au-Pd alloys with random or core-shell structure have also been studied for oxygen adsorption, dissociation and oxidation reactions but it is vital to understand the role of different active sites present in individual metals and role of these sites independently. Hence, preliminary studies are performed here with Au and Pd mono-metallic clusters.

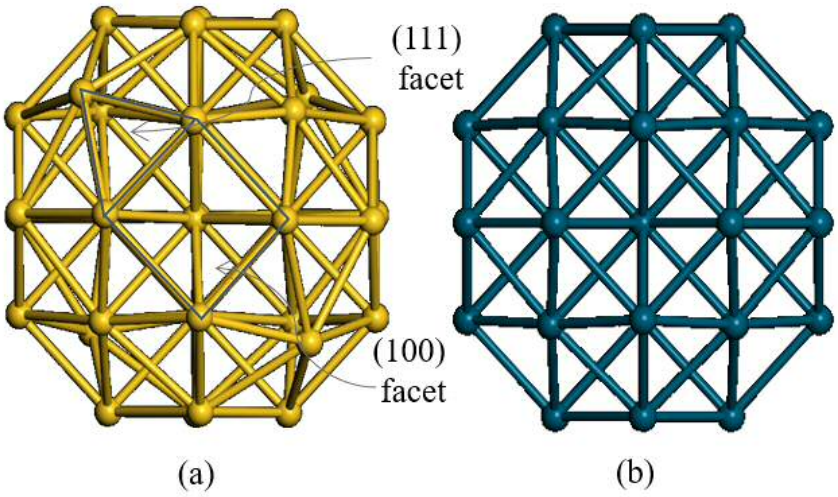

Figure 5.4: Metal particles investigated during this thesis showing surface facets for (a)Au_{38} and (b) Pd_{38}. Atoms have been coloured: Au in yellow and Pd in blue.

Using VASP, these structures were fully relaxed and energies obtained are denoted as $E_{Cluster}$. On each particle surface, different bonds can be identified on surface planes and edges. Symmetrical bonds are easier to identify in the Pd cluster since in Au cluster, slight distortion in bonds is observed (Figure 5.4). Those are bonds on the edge of square and trigonal facets and the (111) trigonal surface bonds. The Pd-Pd edge bond in the Pd_{38} nanoparticle was 2.68 Å whereas in the case of Au_{38}, the Au-Au edge bond varied from 2.73 Å - 2.87 Å due to some distortion that was observed on optimising the cluster. Trigonal (111) surface bonds for Pd_{38} ranged from 2.684 Å - 2.690 Å whereas higher variation was observed for Au_{38} with bond lengths varying from 2.82 Å - 2.89 Å. Surface bonds on (111) facet were longer compared to the edge bonds. And The Pd-Pd bonds are approximately 0.15 Å shorter compared to the Au-Au surface bonds.

5.4 Oxygen Interaction with Metal Particles

The optimised metal nanoparticles were used to study the adsorption of oxygen on various surface sites. Only molecular oxygen was also placed within the periodic cell of the same size and fully relaxed. Spin restricted calculations were performed for singlet and triplet oxygen states. Spin unrestricted calculations were also performed showing the ground state of oxygen as triplet with same energy as spin restricted ones. The energy of molecular oxygen was calculated to be -9.86 eV and denoted as E_{O_2}. Since, the molecular oxygen is in triplet state, it also gives the bond energy *i.e.* the energy for O_2 = 2O. The O atom is also in triplet state. Then, the molecular oxygen was adsorbed onto different sites in order to deduce most favourable mode of oxygen adsorption. It has also been previously shown that the junction between (100) and (111) facet is an important site where binding of molecular oxygen is preferred on Au cluster [18]. Thus, three distinct sites were investigated; site A, site B and site C (Figure 5.5). Site A is considered where oxygen is adsorbed at the junction of two (111) facets (top-a-top-b). Adsorption site B is adsorption at the junction of a (100) and (111) facet (top-a-bridge-b) and finally adsorption site C is the one in which molecular oxygen is parallel to and centred over the (100) facet (bridge-a-bridge-b).

The adsorbed geometries were also relaxed and the energy produced was denoted as E_{Clus+X} where X = O_2. Using equation 5.1, adsorption energies ($E_{ads\text{-}X}$) can be determined.

$$E_{ads\text{-}X} = E_{Clus+X} - (E_{Clus} + E_X) \tag{5.1}$$

where E_{Clus} is energy of the optimised metal particle and E_X is energy of X in this case O_2. Favourable adsorption is indicated by a negative calculated value. Table 5.1 shows calculated adsorption energies for molecular oxygen onto the metal clusters investigated.

Adsorption energies calculated in table 5.1 indicate that the adsorption of O_2 is favourable onto all three sites as each value is negative. The adsorption with higher negative value

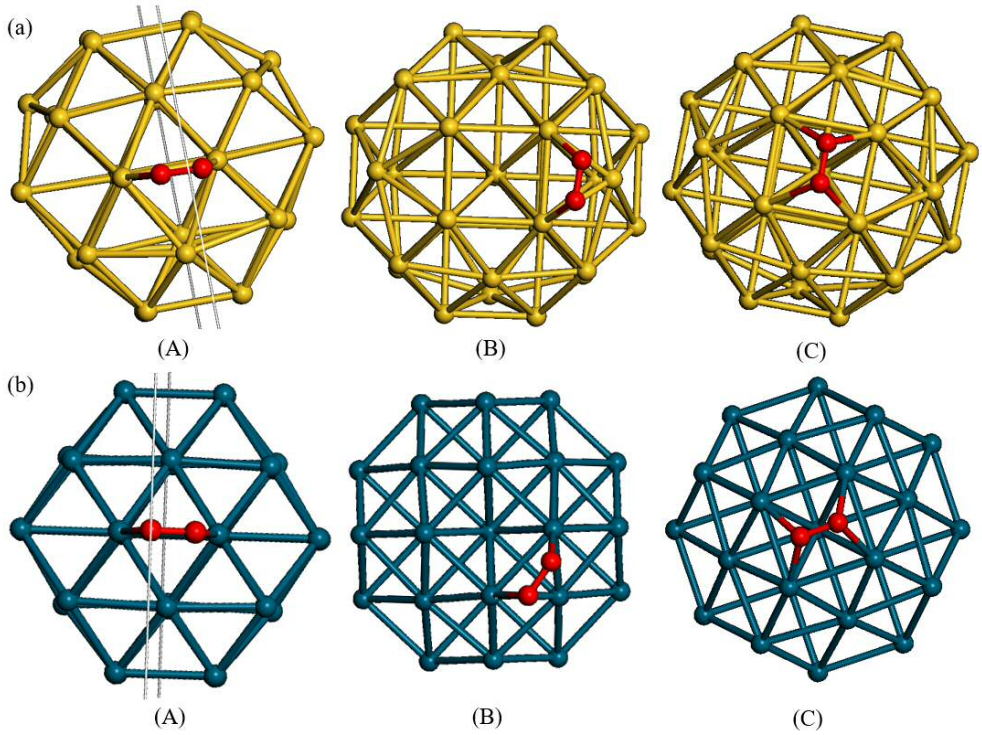

Figure 5.5: Molecular oxygen adsorbed onto sites A, B and C for both metal particle (a)Au_{38} and (b)Pd_{38}. Atoms have been coloured: Au in yellow, Pd in blue and O in red.

Table 5.1: Adsorption energies calculated for oxygen adsorbed in three different positions onto the clusters studied

	$E_{ads\text{-}O_2}$ (eV)		
	A	B	C
Au_{38}	-0.73	-0.96	-0.77
Pd_{38}	-1.39	-1.38	-2.43

corresponds to stronger interaction. It is observed that this value is higher for site B for for the Au_{38} clusters, however the adsorption site C for Pd_{38} shows the highest negative $E_{ads\text{-}O_2}$. Adsorption energies at other sites are also more negative for Pd indicating greater adsorption affinity for Pd compared to Au. Previous studies performed on Au cluster also show similar trend in the adsorption energies [19].

The distribution of the electron density and the effect of O_2 adsorption was studied by calculating the charge density difference ($\Delta\rho$) of the system. This charge density difference

$\Delta\rho_{\text{Clus+O}_2}$ of the system Clus+O_2 is given by equation 5.2

$$\Delta\rho_{\text{Clus+O}_2} = \rho_{\text{Clus+O}_2} - (\rho_{\text{Clus}} + \rho_{\text{O}_2}) \tag{5.2}$$

Where the atomic positions for the latter two quantities are fixed at the positions they have in the relaxed structure system Clus+O_2. Figure 5.6 shows the isosurface of the charge density difference performed for Au and Pd clusters with O_2 adsorption at the three sites.

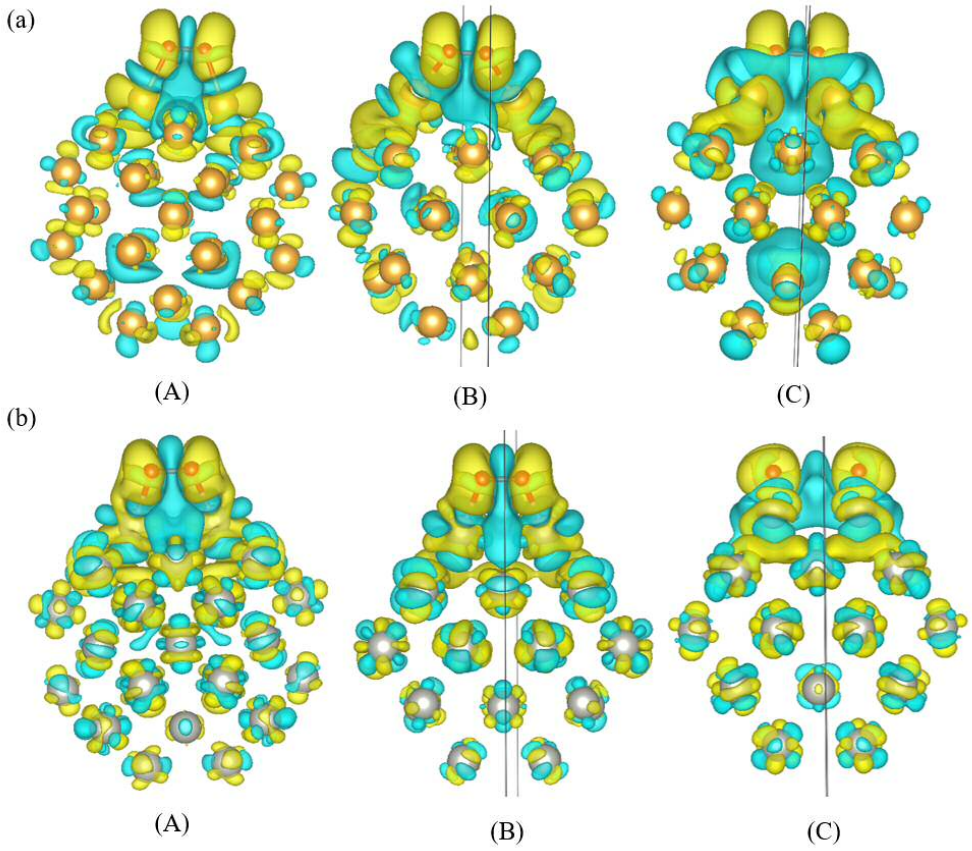

Figure 5.6: Electron density difference isosurfaces resulting from O_2 surface adsorption on Au and Pd clusters (Au_{38} and Pd_{38}). Positive electron density is denoted with yellow colour whilst negative electron density is denoted with blue colour

As shown in figure 5.6, the electron density is reorganised with negative electron density on oxygen atoms and positive electron density is present on the surface atoms. There is some reorganisation in the core atoms but mainly interaction and electron transfer is observed from the surface atoms. There is greater degree of charge transfer that is observed in adsorption at site C. But in all the cases, there is electron donation that is observed to the oxygen molecule. Adsorption is considered to be a balance between donation of the

electron density from the O_2 molecule to the metal particle and back donation to the π^* orbitals present on the O_2 molecule. Since, there is an increase in the electron density on oxygen, it is probable, that back donation component is predominant here. Back donation will cause a decrease in the overall bond order of O_2 as it increases the electron density in anti-bonding π orbitals weakening and increasing the bond distance. Table 5.2 shows the O-O bond length on adsorption on different sites and the change in equilibrium bond distance where a positive value indicates an elongation of the O-O bond.

Table 5.2: O-O bond distance for O_2 onto sites A, B and C for both cluster compositions along with the difference from the equilibrium bond distance.

	r_{O-O} Adsorption / Å			δr_{O-O} Equilibrium / Å		
	A	B	C	A	B	C
Au_{38}	1.352	1.351	1.461	0.118	0.117	0.227
Pd_{38}	1.366	1.345	2.817	0.132	0.111	1.583

The positive change in bond distances clearly indicate bond elongation in all these cases. But most elongation is observed in site C, which also indicates maximum electron back donation into anti-bonding π orbitals. This elongation in site C also suggests that adsorption occurs in superoxo state supporting negatively charged adsorbed O_2 species. In case of Pd adsorption of O_2 at site C which is parallel and centred over (100) facet, a spontaneous dissociation is also observed with an interatomic distance for the resulting O atoms of 2.817 Å. The relaxed geometry and electron density difference plot is shown in figure 5.7. Even by adsorbing O_2 with different orientation over (100) facet, a high elongation of 0.244 Å was observed.

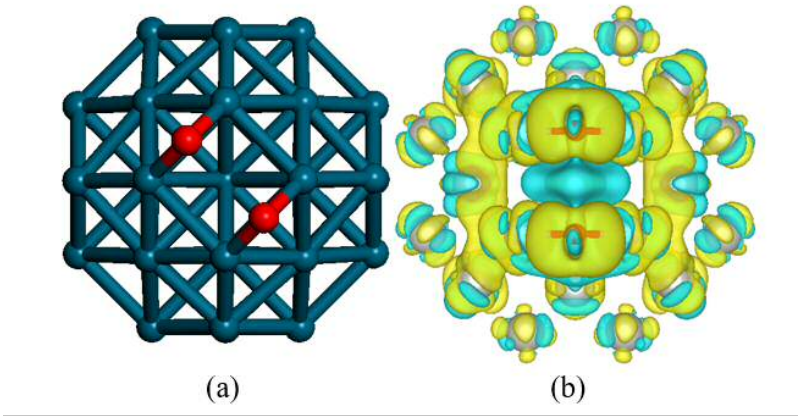

Figure 5.7: Adsorption of O_2 on site C in Pd nanoparticle showing (a) bond elongation and (b) electron density distribution. Atoms have been coloured: Pd in blue and O in red. Positive electron density is denoted with yellow colour whilst negative electron density is denoted with blue colour.

Considering the adsorption energies and configurations, it is clear that all sites are feasible for oxygen adsorption. In case of Au, site B adsorption showed the highest negative energy. Hence it was the most stable configuration while preserving the O-O bond. In case of Pd, though the highest energy was found when oxygen was adsorbed onto Site C but that led to elongation and breaking of O-O bond. But since, the interest lies in preserving the O-O bond while synthesising OOH species, adsorption via site B would be investigated and used for further adsorption configurations.

5.5 Hydrogen Interaction with Metal Particles

Two possible routes have been suggested for H_2O_2 formation [3]. The first one is adsorption of O_2 and H_2 on the cluster followed by H_2 bond breaking into two H atoms and transfer of the H atoms to adsorbed O_2 to form H_2O_2 via OOH species. The second route is breaking of the adsorbed O_2 and H_2 into two O atoms and two H atoms. This would be followed by reformation of hydroxyl groups to form H_2O_2. The second route requires additional O-O bond cleavage which possesses an energy barrier [19]. Also as seen in previous section that though spontaneous bond cleavage was observed on one site on Pd

but only molecular adsorption was observed in Au which means there must be a barrier to molecular dissociation. Also, since cleavage of H_2O_2 into hydroxyl groups is quite favourable, reverse process is highly unlikely. The first step in the reaction mechanism is adsorption of H_2. Thus hydrogen adsorption was performed on these clusters. Adjacent positions were chosen for H_2 adsorption and the structures were relaxed (Figure 5.8).

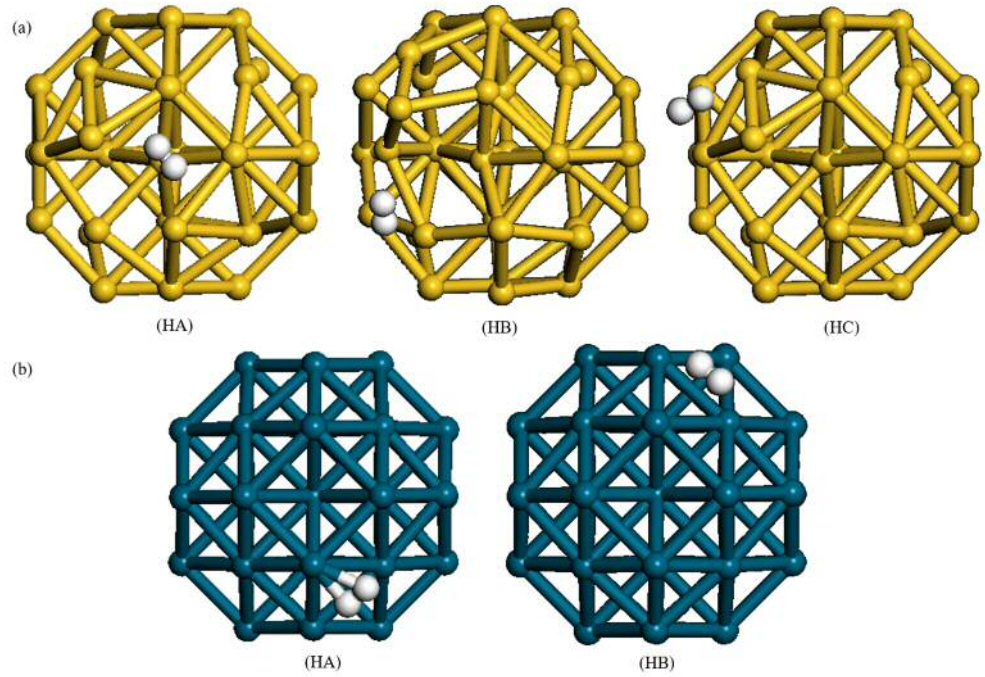

Figure 5.8: Hydrogen adsorbed onto different sites for both metal particle (a)Au_{38} and (b) Pd_{38}. Atoms have been coloured: Au in yellow, Pd in blue, O in red and H in white.

For the gold cluster, site HA refers to adsorption of H_2 parallel to and centred over (100) facet. HB site is considered as adsorption on the junction of (111) and (100) facet and HC as adsorption on the junction of two (100) facets. For the palladium cluster, adsorption at the HA site is considered as adsorption on the junction of (111) and (100) facet and HB as adsorption on the junction of two (100) facets. The structures were optimised and E_{Clus+H_2} was measured. To calculate the adsorption energies for H_2, only one hydrogen molecule was also placed within the periodic cell of the same size and fully relaxed. The energy of molecular hydrogen was calculated to be -2.23 eV and denoted as E_{H_2}. Using equation 5.1, $E_{ads\text{-}H_2}$ was calculated. The adsorption energies for hydrogen on the cluster are tabulated in table 5.3. These energies indicate that hydrogen adsorption is highly favourable. Compared to oxygen adsorption, higher negative energy values were

obtained with hydrogen. H_2 adsorption was found to be more favourable on Pd clusters compared to Au.

Table 5.3: Adsorption energies calculated for hydrogen adsorbed on different positions onto the clusters studied

	$E_{ads\text{-}H_2}$ (eV)		
	HA	HB	HC
Au_{38}	-4.95	-4.73	-4.56
Pd_{38}	-5.61	-5.57	

Facile adsorption and negative binding energy has been previously reported with Au(111), Pd containing Au(111) surface and 55-atom Au@Pd icosahedral nanoparticle [20, 21]. In the case of Au clusters, highest negative energy was observed for site HA. But in this case, it was observed that hydrogen splitting took place with H-H distance increased from 0.740 Å to 4.200 Å. This was not observed in the other two sites with bond distances being 0.752 Å and 0.746 Å for HB and HC sites respectively. The site HC with least adsorption energy and the bond distance closest to H_2 molecule was observed to be binding very weakly to the cluster. Though H_2 splitting is shown to be uncommon in extended Au(111) surfaces, it has been shown to occur in some adsorption sites in clusters [20, 22]. In the case of Pd, hydrogen splitting has been commonly demonstrated which is also observed here [23]. The distance between the H atoms is observed to be 2.739 Å and 2.675 Å for the two sites. These adsorption sites will be later used as reaction sites with O_2.

5.6 Water Interaction with Metal Particles

Recent studies by Flaherty and co-workers have demonstrated the involvement of the proton from solvent molecules in H_2O_2 formation [8]. Formation rates were shown to be sensitive to H_2 pressure but also required protic solvent since no activity was observed in aprotic solvent. To examine such reaction steps, it is essential to understand the adsorption of water on these clusters. Adsorption of H_2O was performed on different sites of Au and

Pd clusters. For both clusters, WA adsorption site refers to intersection between (100) and (111) facets, WB site refers to adsorption centred over (100) facet and WC site refers to adsorption of H_2O centred over (111) trigonal facet. The structures were then relaxed and energy of the system was calculated (E_{Clus+H_2}).

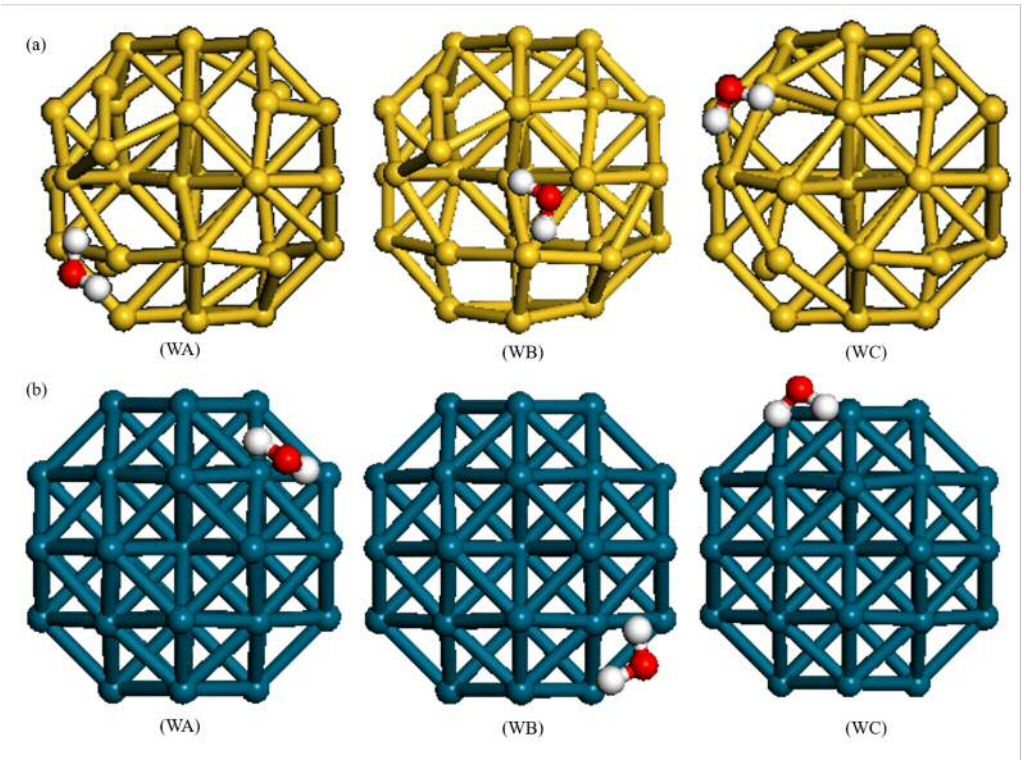

Figure 5.9: Water (O atom shown in red and H atom shown in white) adsorbed onto different sites for both metal particle (Au_{38} and Pd_{38})

To calculate the adsorption energies for water, only one water molecule was also placed within the periodic cell of the same size and fully relaxed. The energy of the isolated water molecule was calculated to be -14.21 eV and denoted as E_{H_2O}. The adsorption energy $E_{ads\text{-}H_2O}$ was calculated using the equation 5.1. The adsorption energies for water on the cluster are tabulated in table 5.4. These energies indicate that water adsorption is slightly favourable. Compared to oxygen and hydrogen adsorption, a much lower negative energy values were obtained with water. H_2O adsorption was found to be similar on Au and Pd clusters. A low binding energy has previously been observed by Phatak *et al.* on Au(111) and Pd(111) surfaces [24].

In the case of Au clusters, the adsorption energy was calculated to be between -0.17 eV

Table 5.4: Adsorption energies calculated for water adsorbed on different positions onto the clusters studied

	$E_{ads\text{-}H_2O}$ (eV)		
	WA	WB	WC
Au_{38}	-0.27	-0.21	-0.17
Pd_{38}	-0.05	-0.25	-0.24

and -0.27 eV with Au-O distances between 2.8 Å - 2.6 Å respectively. Similar bond lengths have also been previously reported by King and co-workers [25]. They also showed water molecule to be nearly flat to Au (111) metal surface with OH bonds only very slightly tilted up which was also observed with (111) facet of Au clusters in this case (site WB). Bond length elongation was not observed with average bond length in all cases being 0.977-0.981 Å. Similarly, for Pd clusters, a low adsorption energy was observed. In the case of site WA, an adsorption energy of -0.05 eV was calculated. This coincided with the increase in Pd-O distance to 3 Å. For the other two sites, E_{ads3} was observed to be -0.25 eV and -0.24 eV with Pd-O distance as 2.73 Å and 2.8 Å. No elongation in water bond length was observed. These reaction sites will be later used on oxygenated clusters to form hydroperoxy species.

5.7 Synthesis of Hydroperoxy Species

It has been ascertained that oxygen adsorbs favourably and site B will be used in this thesis for further calculations. It was also showed that hydrogen and water also adsorbs with negative adsorption energies. Now a systematic study will be performed to investigate the mechanism of OOH formation using O_2, H_2 and H_2O. Different routes of OOH synthesis are designed with H_2 on oxygenated clusters and H_2O on oxygenated clusters. NEB calculations as discussed in chapter 2 (subsection 2.6.6) were used to determine the transition state and associated energy of the transition state to form OOH species. NEB calculations are performed by interpolating the bond structure between two stable minima

and finding a minimum energy path (MEP) between the structures. The transition state is given by the point with highest energy on MEP.

In the following cases, the initial starting point is taken as hydrogen or water adsorbed on oxygenated metal clusters. The end point is taken as the structure in which OOH is formed by movement of H from the initial reactant. Each of these start and end points were relaxed and optimised in VASP. A representation of the transition state is shown in all of the calculations. In order to cross a reaction barrier and overcome the energy required for the reaction, the barrier calculated should not be substantially higher than the adsorption energy of the reactants. Energy barriers for OOH synthesis with H_2 and O_2 are detailed in figures 5.11 - 5.13. Figure 5.10 shows the reaction pathway on Au_{38} cluster with H_2 adsorbed at site B. The end point configuration is found to be more stable with exothermic energy as 0.58 eV. The barrier energy of 0.23 eV was observed.

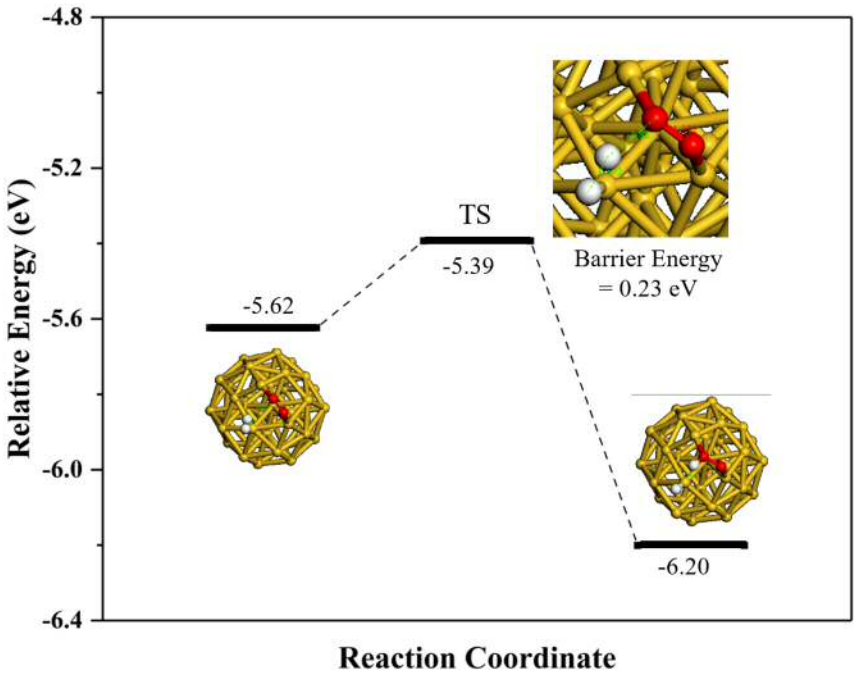

Figure 5.10: Reaction pathway for OOH synthesis using adsorbed O_2 and H_2(Site HB) on Au_{38}. Zero energy is set relative to the isolated gold cluster, isolated molecular oxygen and isolated molecular hydrogen. TS corresponds to the transition state energy.

In the case of H_2 adsorption on site A, H-H bond elongation was observed. But when H_2 was adsorbed on site A on the Au_{38} cluster with molecular O_2 already adsorbed, hydrogen splitting was not observed. It was also used to create OOH end point and optimised. NEB

analysis showed the barrier energy to about 1.22 eV with only slight increase in stability in the end point (Figure 5.11).

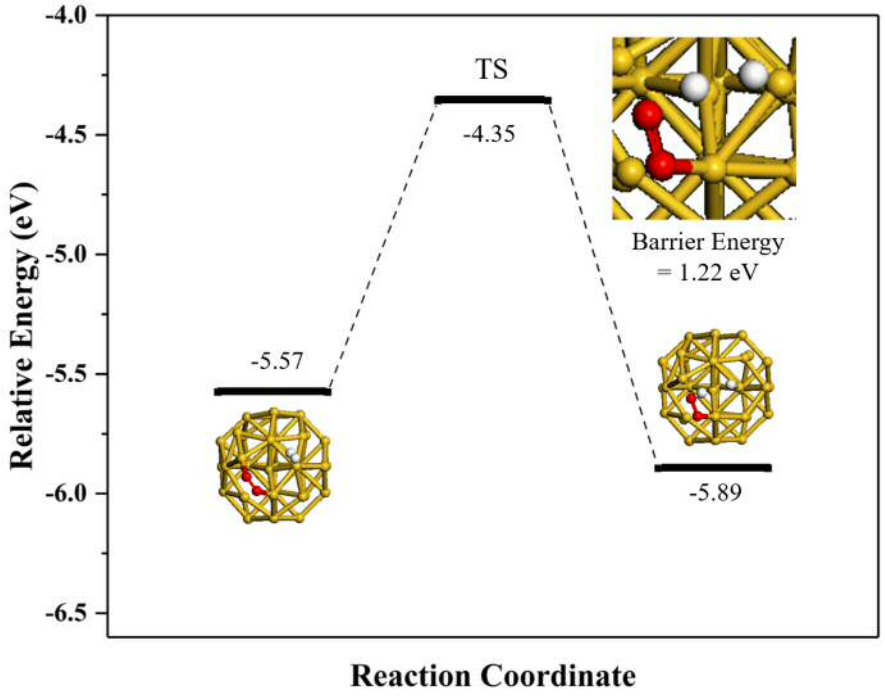

Figure 5.11: Reaction pathway for OOH synthesis using adsorbed O_2 and H_2(Site HA) on Au_{38}. Zero energy is set relative to the isolated gold cluster, isolated molecular oxygen and isolated molecular hydrogen. TS corresponds to the transition state energy.

Weak adsorption was observed with H_2 adsorption on site C. Hence it was considered as free H_2. The system with free H_2 was also optimised and transition state search was performed which is shown in figure 5.12. The end point is stabilised more with H atom adsorbed on the gold cluster. The barrier energy was calculated to be 1.11 eV with.

From the above reaction pathways, figure 5.10 showed the minimum energy barrier and will be used for further calculations. As discussed earlier, hydrogen splitting was facilitated on Pd clusters. Thus the starting configuration contains split H atoms adsorbed over oxygenated clusters. For Pd cluster, one successful product formation could be optimised without the H atom going back. Figure 5.13 shows the reaction pathway for OOH synthesis. Slightly lower energy was found for the end point with difference being 0.08 eV. The barrier energy was calculated to be 1.05 eV.

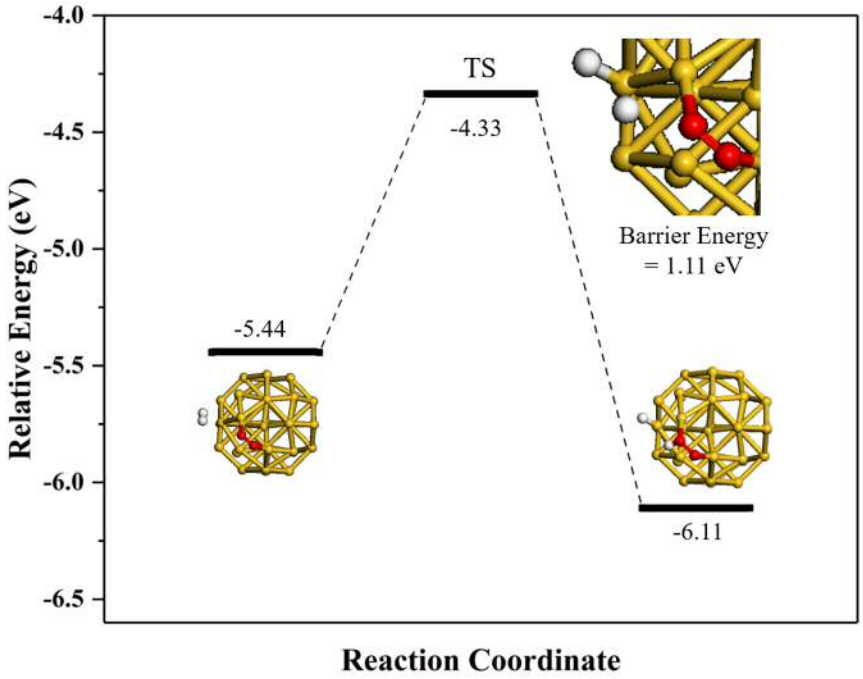

Figure 5.12: Reaction pathway for OOH synthesis using adsorbed O_2 and free H_2(Site HC) on Au_{38}. Zero energy is set relative to the isolated gold cluster, isolated molecular oxygen and isolated molecular hydrogen. TS corresponds to the transition state energy.

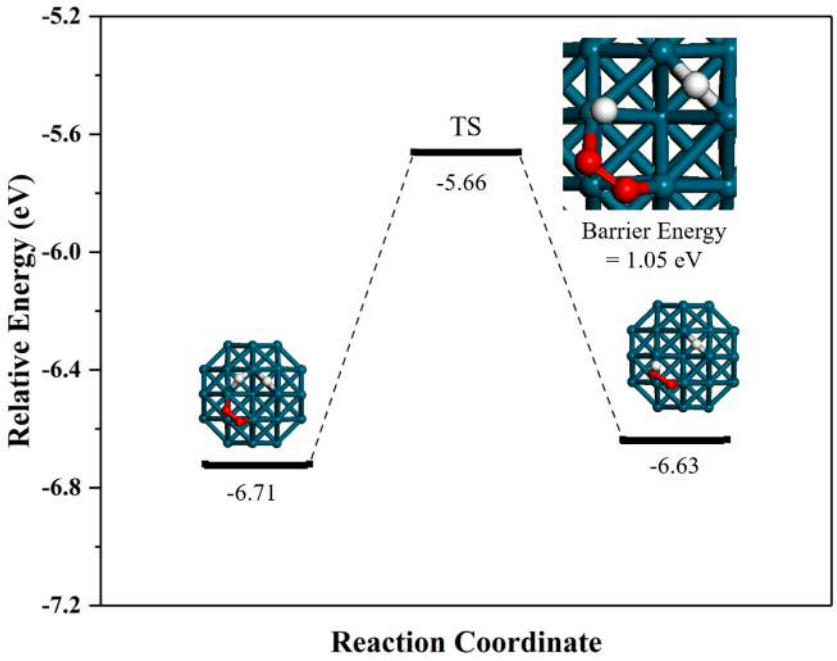

Figure 5.13: Reaction pathway for OOH synthesis using adsorbed O_2 and H_2 on Pd_{38}. Zero energy is set relative to the isolated palladium cluster, isolated molecular oxygen and isolated molecular hydrogen. TS corresponds to the transition state energy.

Earlier gas-phase calculations performed on Pd and Au/Pd extended surfaces have ex-

plored the possibility of H_2O_2 formation by hydrogenation of O_2 by H_2 co-adsorbed on the cluster [1, 3]. But, H_2O_2 formation was shown to be only possible in protic solvents with increase in the H_2O_2 production with halide and acid additives.

The smallest and simplest unit of metal-aqueous interface involves a single metal atom in contact with a single molecule of water. However, using a single metal atom does not have the same energy structure as compared to metal cluster or extended surface. Thus instead of single atom, metallic clusters have been used [26]. But the electronic character of water in isolation is not very different from condensed phase. Thus initial adsorption and reactivity of a water molecule on the metallic cluster can be studied with single molecule of water. It provides initial insights into electronic interactions which govern the adsorption and reactivity of water [27]. Thus, OOH formation was also performed with H_2O adsorption on oxygenated clusters. Figure 5.14 and 5.15 show the reaction pathways for O-H bond breaking and O-O-H bond synthesis.

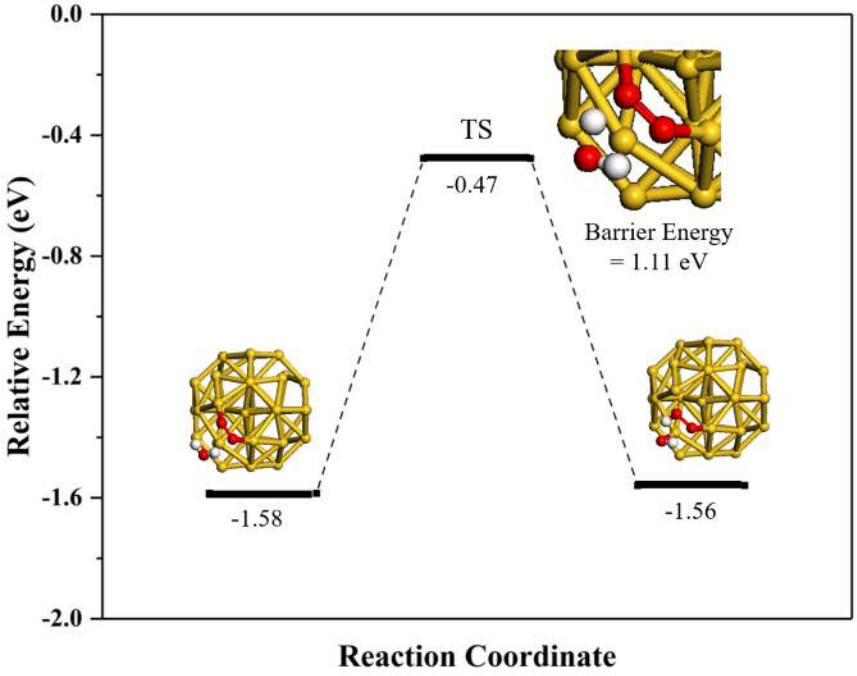

Figure 5.14: Reaction pathway for OOH synthesis using adsorbed O_2 and surface bound H_2O on Au_{38}. Zero energy is set relative to the isolated gold cluster, isolated molecular oxygen and isolated water molecule. TS corresponds to the transition state energy.

As seen from the figure 5.14, movement of H can be seen across the cluster to form OOH species. The barrier energy was found to be 1.11 eV. The start and end point geometries

were shown to be of similar energy. Similarly, systems were optimised with H_2O adsorption on oxygenated Pd cluster which was then used to create and optimise the end point geometry. As seen from the figure 5.15, the reaction was found to be slightly endothermic. The barrier energy in this case was calculated to be 3.5 eV making this reaction unfeasible.

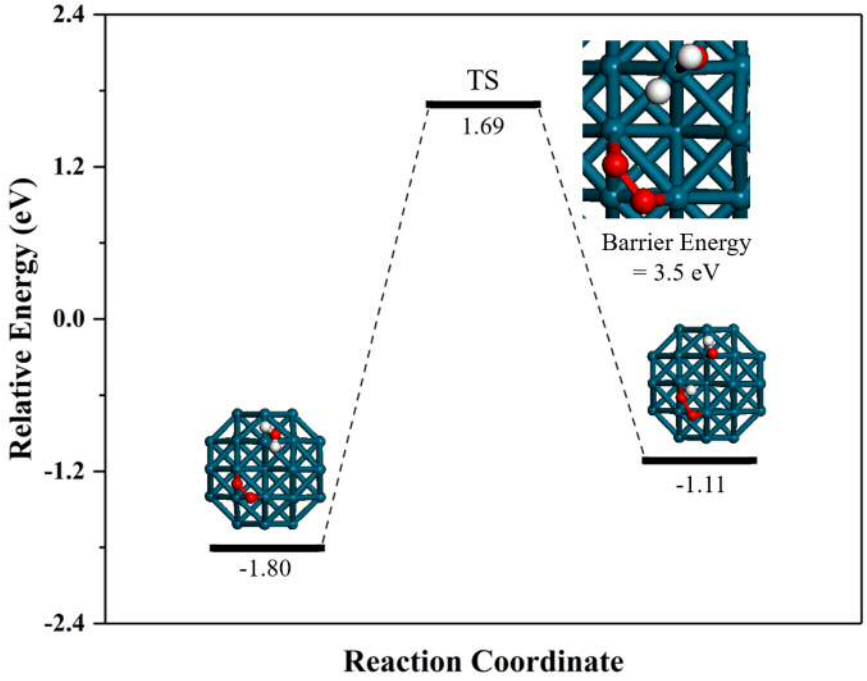

Figure 5.15: Reaction pathway for OOH synthesis using adsorbed O_2 and surface bound H_2O on Pd_{38}. Zero energy is set relative to the isolated palladium cluster, isolated molecular oxygen and isolated water molecule. TS corresponds to the transition state energy.

These reaction pathways demonstrate the feasibility of OOH formation with H_2 on oxygenated clusters due to low barrier energy and higher end point energies. Reaction pathways with surface H_2O showed higher barrier energies. The effect of solvent will be studied using free H_2O rather than surface bound.

5.8 Effect of Solvent on Transition State Energy

The reactivity of the metal to some extent is controlled by availability of delocalised and partially localised electron density at Fermi level [26]. Though, gas phase calculations provide insights into reaction pathway and its energetics, these interactions can differ

in an aqueous reaction environment. In an aqueous reaction environment, these localised electron density can readily reorganise due to dipole interactions with water, thus affecting its energy [6]. Thus it is important to consider the solvent effect while analysing catalytic activity. Jacob and Goddard showed that under gas phase conditions the calculations were quite different from those under solvated conditions while performing theoretical calculations for water formation on Pt and Pd clusters [28]. The complexity of solvent was gradually increased. After performing NEB calculations with surface bound H_2O with Au and Pd clusters, the next set of calculations were performed by including free water molecule in the simulations. Figure 5.16 and 5.17 show the presence of free H_2O along with surface adsorbed H_2 on an oxygenated cluster.

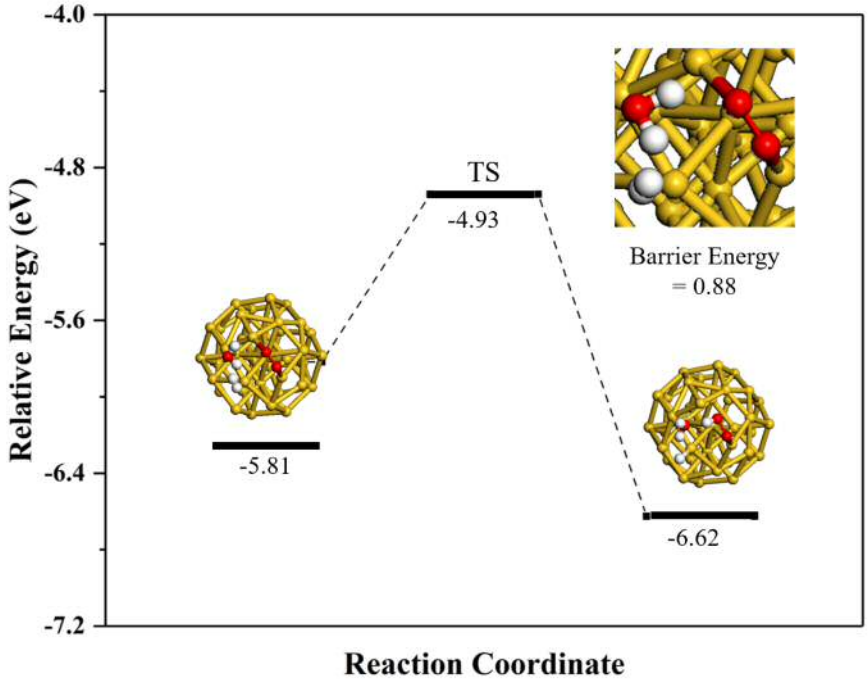

Figure 5.16: Reaction pathway for OOH synthesis using adsorbed O_2 and H_2 with free H_2O on Au_{38}. Zero energy is set relative to the isolated gold cluster, isolated molecular oxygen, isolated molecular hydrogen and isolated water molecule. TS corresponds to the transition state energy.

As seen in figure 5.16, H movement was performed across the free water molecule. In this case, a slight increase in the barrier energy was observed with the energy being 0.88 eV. The end point geometry is also found to be more stable with an energy difference of 0.8 eV compared to the initial structure with H_2, H_2O and O_2 co-absorbed. But in the case of

the Pd cluster, a much lower energy barrier of 0.75 eV was observed. This barrier energy is lower than gas phase OOH formation with H_2 on Pd cluster. The end point geometry also shows higher stability with higher energy difference of 0.33 eV. This demonstrates the effect of water as a reactant in direct synthesis of H_2O_2.

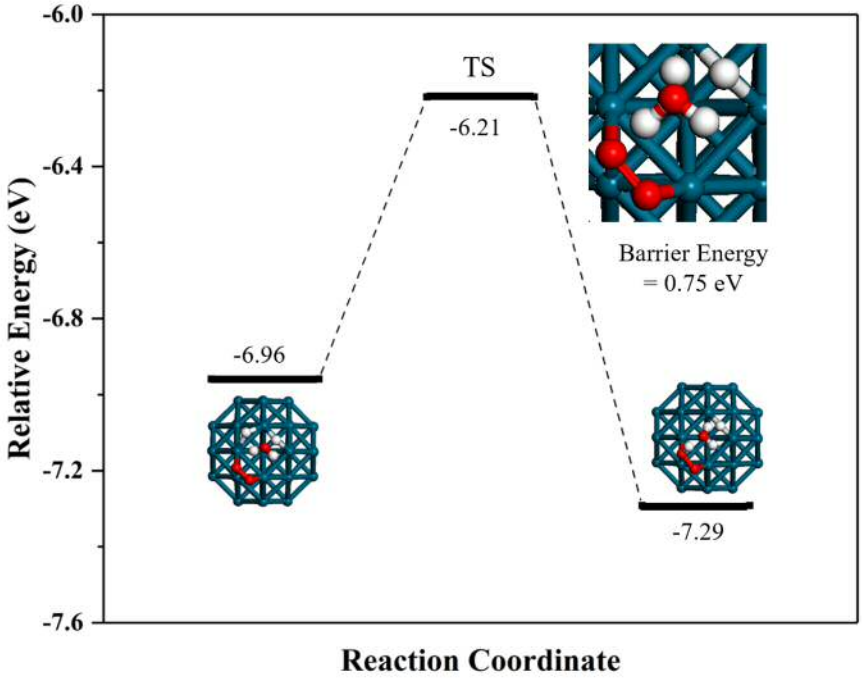

Figure 5.17: Reaction pathway for OOH synthesis using adsorbed O_2 and H_2 with free H_2O on Pd_{38}. Zero energy is set relative to the isolated palladium cluster, isolated molecular oxygen, isolated molecular hydrogen and isolated water molecule. TS corresponds to the transition state energy.

Similar to the previous section, transition state search was also performed with free H_2O on oxygenated clusters with surface bound H_2O. Figure 5.18 depicts the reaction pathway on Au_{38} cluster with bound and free H_2O. A low barrier energy of 0.19 eV was calculated for this reaction pathway. Such low barrier energy will facilitate such a reaction path. Similar calculations were also performed on Pd cluster. As seen in figure 5.19, barrier energy of 0.35 eV was calculated. In both cases, the end point energy is higher making it slightly less stable than the starting points. These reactions clearly demonstrate lowering of barrier energy in presence of water as a solvent which could participate in the reaction. This observation is in agreement with mechanism proposed by Flaherty and co-workers which showed a dependence on protic solvent for H_2O_2 formation [8].

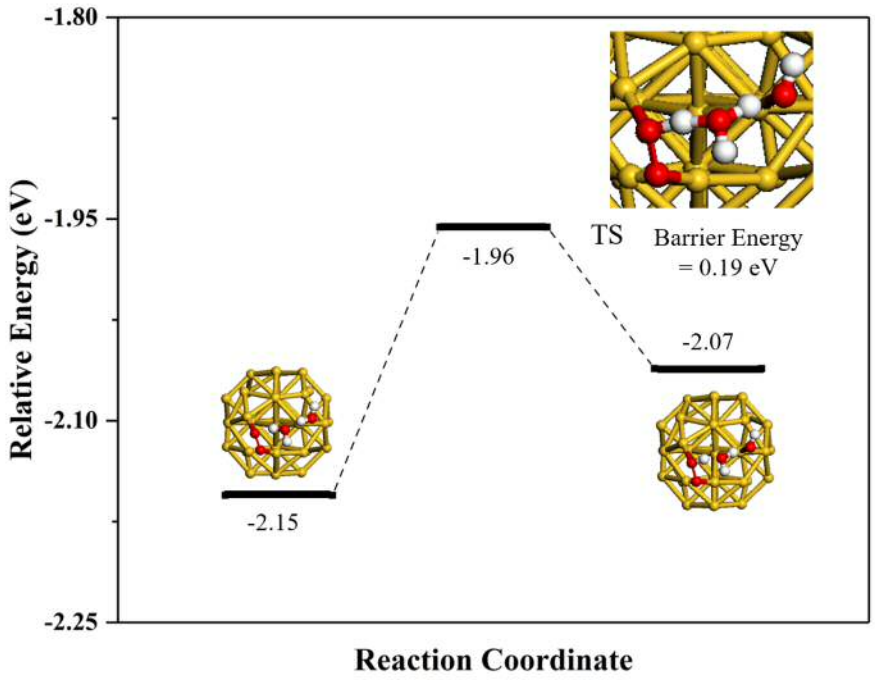

Figure 5.18: Reaction pathway for OOH synthesis using adsorbed O_2 and surface bound H_2O with free H_2O on Au_{38}. Zero energy is set relative to the isolated gold cluster, isolated molecular oxygen and isolated water molecules. TS corresponds to the transition state energy.

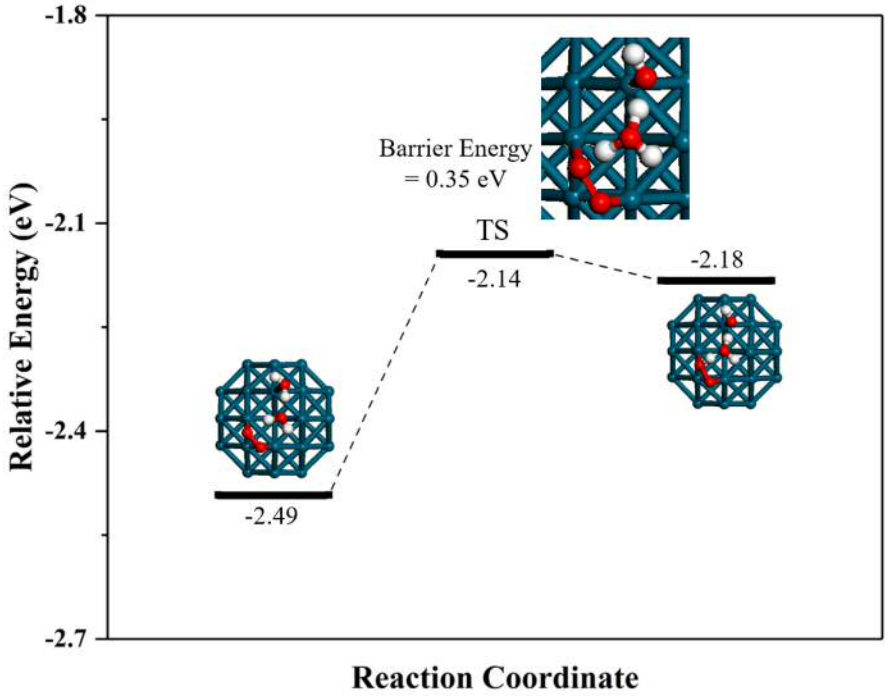

Figure 5.19: Reaction pathway for OOH synthesis using adsorbed O_2 and surface bound H_2O with free H_2O on Pd_{38}. Zero energy is set relative to the isolated gold cluster, isolated molecular oxygen and isolated water molecules. TS corresponds to the transition state energy.

Another step towards understanding the reaction under close to experimental conditions is including more than a single H_2O molecules. This is usually done by "soaking" the catalytic system in a water-containing box where about 50 to 200 water molecules are added. But performing ab-initio calculations on such systems is computationally expensive and can be applied to only well defined systems which is not possible with this high number of H_2O with different orientations [29].

Also, such approaches might lead to plausible results but they do not describe a completely solvated system. Ensemble-sampling methods like molecular dynamics or Monte Carlo are also sometimes used which can be applied to larger systems. But to utilise rigour of ab-initio-DFT calculations in the bond breaking and making without performing ab-initio molecular dynamics simulations, implicit solvation has been employed [26]. Though explicit solvent molecules involves possible participation of water, in this case that has been demonstrated by treatment with free H_2O. Implicit solvation is used to understand relaxation of the system with fully solvated systems. In implicit solvation model, solvent is considered as a continuum dielectric. Electronic contribution to the solvation energy is measured using the equation 5.3

$$E_{\text{Solvation}} = E_{\text{system: solvated}} - E_{\text{system: gas phase}} \tag{5.3}$$

Figure 5.20 shows the $E_{\text{system: solvated}}$ and $E_{\text{system: gas phase}}$ for the metal clusters with O_2 and H_2 with and without H_2O. Total output energy values for the start and end point configurations along with the transition state are reported for all cluster configurations for comparison of stability of the configurations. As seen from figure 5.20, solvated systems have higher negative energy compared to gas phase systems *i.e.* they are more thermodynamically stable compared to gas phase systems. The energy difference with free H_2O was calculated to be higher than in the absence of it. This demonstrates the further stabilisation and participation of H_2O in direct synthesis of H_2O_2.

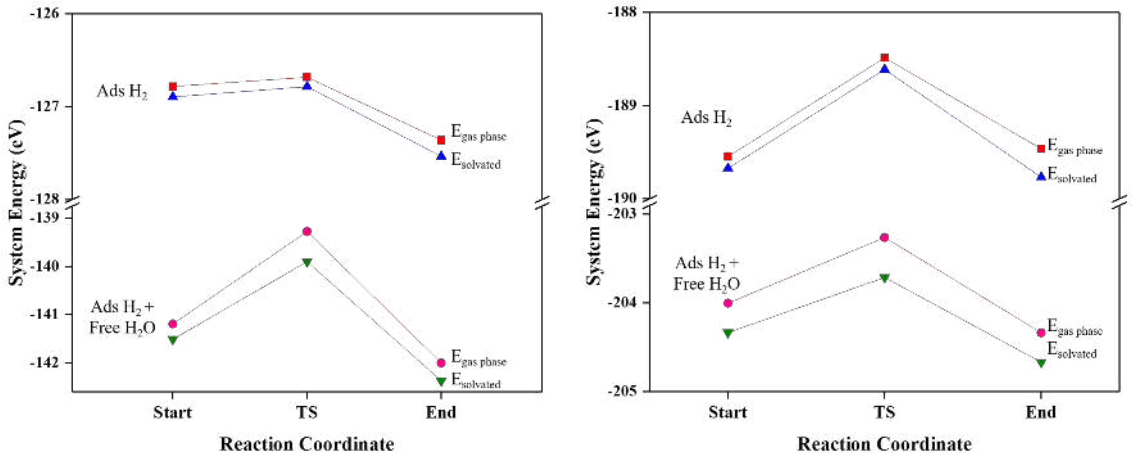

(a) (b)

Figure 5.20: Energies of the start point, transition state and end point in gas phase and solvated in water for oxygenated a) gold and b) palladium cluster + H_2 with and without free H_2O.

The solvation energies calculated for all the configurations in different reaction pathways is tabulated in table 5.5. A negative solvation energy is observed in both cluster systems in all the cases. Similar range of solvation energies has also been observed in oxygen reduction reaction catalysed on Pt clusters [29].

Table 5.5: Solvation energy for the reaction pathway configurations for OOH synthesis

	$E_{Solvation}$ / eV					
Reactants	H_2			H_2-H_2O		
Configurations	Start	TS	End	Start	TS	End
Au_{38}	-0.11	-0.10	-0.18	-0.32	-0.63	-0.37
Pd_{38}	-0.13	-0.13	-0.31	-0.33	-0.45	-0.33
Reactants	H_2O			H_2O-H_2O		
Configurations	Start	TS	End	Start	TS	End
Au_{38}	-0.23	-0.38	-0.26	-0.39	-0.33	-0.33
Pd_{38}	-0.50	-0.79	-0.40	-0.39	-0.40	-0.40

Solvation energies calculated for start, transition state and end point for reaction of H_2; H_2 and free H_2O; adsorbed H_2O; and adsorbed H_2O and free H_2O on oxygenated Au_{38} and Pd_{38} clusters to form OOH.

As seen from the table, similar barrier energies are observed for the H_2 containing systems in the absence of free H_2O with slightly higher stability of the end point configuration. But in the case of addition H_2O, a higher negative $E_{Solvation}$ was observed for transition state configuration leading to a decrease in the barrier energy for these reaction pathways. These results show the feasibility of such reaction step under experimental conditions. Similar calculations were also performed for the cluster configurations containing O_2 and surface adsorbed H_2O. Again, differences in solvation were measured in the presence of free H_2O mimicking participation of solvent (Figure 5.21).

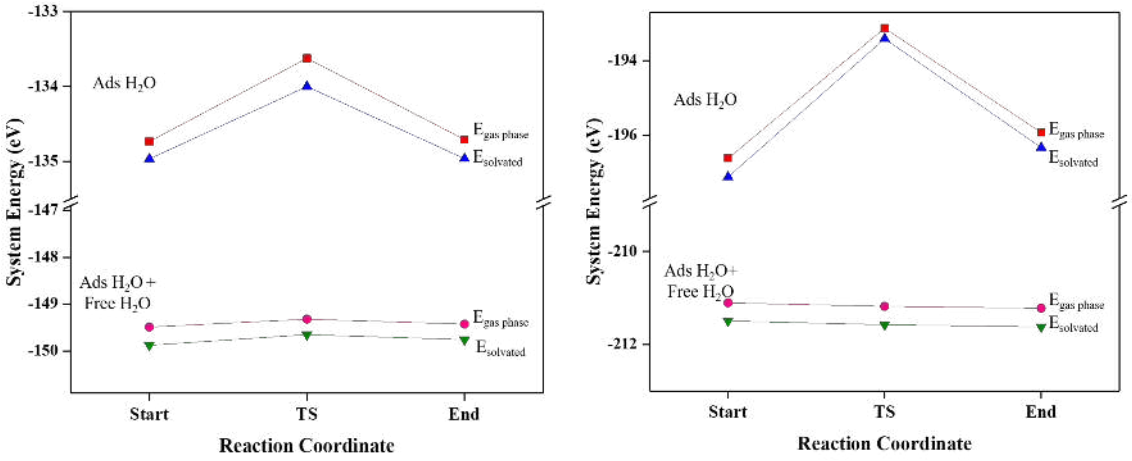

(a) (b)

Figure 5.21: Energies of the start point, transition state and end point in gas phase and solvated in water for oxygenated a) gold and b) palladium cluster + adsorbed H_2O with and without free H_2O.

Total energy output values are shown to compare the stability of the different configurations and higher negative $E_{system:\ solvated}$ was measured in all the compositions. Slightly higher $E_{solvation}$ was observed for the transition state configuration with adsorbed H_2O, thereby decreasing the barrier energy for these reaction pathways. Calculation of the reaction pathways is crucial to understand the reaction mechanism for direct synthesis of H_2O_2. Involvement of water as explicit reactant, participating solvent and continuous homogeneous media sheds light on mechanism taking place at metal active sites under experimental conditions.

5.9 Conclusions

Hydrogen peroxide is a major commodity chemical with uses as an antiseptic and bleach. Direct synthesis of H_2O_2 using H_2 and O_2 has been of interest for research for a long time primarily with an aim to synthesis OOH species over dissociation of O_2. Gold and palladium have been shown to catalyse the production of H_2O_2 at low temperatures. Much of computational interest lies in elucidating reaction mechanism over Pd and Au/Pd extended surfaces and Au@Pd clusters [3]. Previous studies have also tried to explain the synergistic effect shown by alloying Au and Pd to display higher activity and selectivity. Changes in adsorption energy of the reactants and energy barriers for different steps in bimetallic systems have been calculated to understand the difference [2]. This chapter was focused on basic understanding of the reactivity of different active sites like edges, corners and facets on metallic clusters using Density Functional Theory. VASP with planewave basis set has been used to perform all the calculations.

Computational studies have been carried out on 38 atom containing metallic clusters which show (111) and (100) facets. Adsorption of O_2, H_2 and H_2O was studied on both Au and Pd cluster. O_2 adsorption on the junction of (111) and (100) facet (top-a-bridge-b) position was found to be most stable in Au_{38}. Charge density analysis for these configurations was also carried out. Though for Pd_{38} cluster, configuration containing molecular oxygen parallel and centred over (100) facet showed the highest negative energy, it was shown that this site facilitated O_2 dissociation leading to H_2O formation. Thus, top-a-bridge-b position was selected in both cases for further studies. Similarly, H_2 and H_2O was adsorbed on various sites and their adsorption energies were calculated. Then transition state theory was used and hydroperoxy species were synthesised. Transition state search was carried out by interpolating structures between two minima namely the start and end of the reaction. NEB interpolation and optimisation was used to create the energy path and highest energy structure was located. Transition state energy and configurations are showed for synthesis of OOH species with H_2 and H_2O on oxygenated cluster.

The last part of the chapter explains the effect of solvent on these reaction pathways and cluster configurations. The reactivity of a catalyst is controlled to a great extent by the conditions it is used under. A higher activity and selectivity has been observed with Au-Pd catalysts with protic solvents such as methanol and water; and with halide and acid additives [7]. Immeasurably low activity has been recorded under aprotic solvents [8]. Thus it is vital to study reaction pathways with involvement of water. H_2O was studied as a reactant with O_2 and H atom from H_2O was moved across the cluster to form OOH. In these cases, participation of H_2O in the reaction was studied as a solvent by employing free H_2O in the reaction pathways and monitor the effect on transition state energies. Differences in transition state and energetics was measured and much lower barrier energy was calculated in cases with surface adsorbed H_2O and free H_2O where H atom was seen as a shuttle between the H_2O molecules. An implicit solvation model was also employed to measure the stabilisation caused due to solvent media rather than vacuum. Lowering of barrier energy was also observed in this case. These reactions clearly demonstrate the participation and feasibility of reactions under aqueous conditions bringing theoretical calculations closer to the experimental observations.

Bibliography

(1) T. Deguchi, H. Yamano and M. Iwamoto, *Catalysis Today*, 2015, **248**, 80–90.

(2) A. V. Beletskaya, D. A. Pichugina, A. F. Shestakov and N. E. Kuzamenko, *The Journal of Physical Chemistry A*, 2013, **117**, 6817–6826.

(3) J. Li and K. Yoshizawa, *Catalysis Today*, 2015, **248**, 142–148.

(4) R. Todorovic and R. Meyer, *Catalysis Today*, 2011, **160**, 242–248.

(5) A. Staykov, T. Kamachi, T. Ishihara and K. Yoshizawa, *The Journal of Physical Chemistry C*, 2008, **112**, 19501–19505.

(6) T. Deguchi and M. Iwamoto, *The Journal of Physical Chemistry C*, 2013, **117**, 18540–18548.

(7) J. K. Edwards and G. J. Hutchings, *Angewandte Chemie International Edition*, 2008, **47**, 9192–9198.

(8) N. M. Wilson and D. W. Flaherty, *Journal of the American Chemical Society*, 2016, **138**, 574–586.

(9) S. Chinta and J. H. Lunsford, *Journal of Catalysis*, 2004, **225**, 249–255.

(10) D. W. Flaherty, *ACS Catalysis*, 2018, **8**, 1520–1527.

(11) K. E. Atkinson, *An introduction to numerical analysis*, John Wiley & Sons, 2008.

(12) J. P. Perdew, K. Burke and M. Ernzerhof, *Physical review letters*, 1996, **77**, 3865.

(13) J. P. Perdew and Y. Wang, *Physical Review B*, 1992, **45**, 13244.

(14) S. Grimme, J. Antony, S. Ehrlich and H. Krieg, *The Journal of chemical physics*, 2010, **132**, 154104.

(15) K. Momma and F. Izumi, *Journal of Applied Crystallography*, 2008, **41**, 653–658.

(16) J. H. Lunsford, *Journal of Catalysis*, 2003, **216**, 40th Anniversary Commemorative Issue, 455–460.

(17) J. P. Doye and D. J. Wales, *New journal of chemistry*, 1998, **22**, 733–744.

(18) M. Boronat and A. Corma, *Dalton Trans.*, 2010, **39**, 8538–8546.

(19) A. Staykov, D. Derekar and K. Yamamura, *International Journal of Quantum Chemistry*, 2016, **116**, 1486–1492.

(20) M. G. Sandoval, R. Luna, G. Brizuela, A. O. Pereira, C. R. Miranda and P. Jasen, *The Journal of Physical Chemistry C*, 2017, **121**, 8613–8622.

(21) W.-Y. Yu, G. M. Mullen and C. B. Mullins, *The Journal of Physical Chemistry C*, 2013, **117**, 19535–19543.

(22) S. Venkatachalam and T. Jacob, *Phys. Chem. Chem. Phys.*, 2009, **11**, 3263–3270.

(23) H. L. Tierney, A. E. Baber, J. R. Kitchin and E. C. H. Sykes, *Phys. Rev. Lett.*, 2009, **103**, 246102–246106.

(24) A. A. Phatak, W. N. Delgass, F. H. Ribeiro and W. F. Schneider, *The Journal of Physical Chemistry C*, 2009, **113**, 7269–7276.

(25) A. Michaelides, V. A. Ranea, P. L. de Andres and D. A. King, *Phys. Rev. Lett.*, 2003, **90**, 216102.

(26) C. D. Taylor and M. Neurock, *Current Opinion in Solid State and Materials Science*, 2005, **9**, 49–65.

(27) A. Ignaczak and J. Gomes, *Journal of Electroanalytical Chemistry*, 1997, **420**, 209–218.

(28) T. Jacob and W. A. Goddard, *ChemPhysChem*, 2006, **7**, 992–1005.

(29) Y. Sha, T. H. Yu, Y. Liu, B. V. Merinov and W. A. Goddard, *The Journal of Physical Chemistry Letters*, 2010, **1**, 856–861.

6 | Conclusions and Future Work

As already discussed in Chapter 1, methane oxidation is one of the grand challenges of modern day catalysis. It is the main component of natural gas and also a significant by-product of oil refining and chemical processing. Thus methane valorisation to energy-dense liquid derivatives like methanol is a highly desirable endeavour. In this work, bimetallic gold-palladium based catalysts have been investigated for low temperature selective oxidation of methane. Previously, Au-Pd nanoparticles supported on TiO_2 have been shown to be effective catalysts for the oxidation of methane with H_2O_2. Though the catalysts were found to be active, the productivity was found to be low and the reaction was accompanied by high consumption of H_2O_2. In this work, intrinsic methane oxidation activity of Au-Pd nanoparticles was measured to investigate the difference between supported and unsupported catalysts. Though a difference in H_2O_2 consumption is shown with supported and unsupported nanoparticles, this result should be explored further by understanding the H_2O_2 direct synthesis, hydrogenation and degradation. Au-Pd-PVP colloids have been demonstrated as highly active and selective catalysts for methane oxidation under mild conditions i.e aqueous solvents and low temperatures such as 50 °C. While establishing the methane oxidation activity of colloidal Au-Pd, O_2 was used as the co-oxidant and the incorporation of molecular O_2 was demonstrated in Chapter 3. Once the methane oxidation was established by Au-Pd colloid with H_2O_2 and O_2, further investigations were carried out by altering the parameters of the reaction conditions to understand the reaction mechanism and the role of H_2O_2 and O_2. The catalyst preparation parameters and effects of the polymer was also investigated (Chapter 4). The results

obtained in these chapters investigating CH_4 oxidation with O_2 show very promising results and the conclusions reached in these chapters not only show that low temperature methane oxidation process has exciting prospects of being used at a larger scale but also provides an interesting and challenging reaction to conduct studies upon catalysis.

Chapter 3 delves into liquid phase methane oxidation with Au-Pd-PVP colloids. The benchmark system for a selective low temperature oxidation process is biological methanotropic micro-organisms having the enzyme methane mono-oxygenase (MMO) which selectively converts methane to methanol in aqueous medium at mild temperatures < 100 °C. Along with high methanol selectivity under green conditions, another advantage of MMO enzyme is it's ability to perform this reaction with molecular oxygen. Though the scaling up of enzymatic systems has proven to be difficult, different catalysts have been developed inspired by MMO which utilise H_2O_2 as the oxidant. Through this work, it has been shown that Au-Pd-PVP colloids can catalyse methane oxidation using O_2 and H_2O_2 and insertion of molecular oxygen in products has been demonstrated using isotope labelling experiment. Methane oxidation activity of biological MMO system from *Methylococcus capsulates* (Bath) is reported as 5.05 $mol_{(methanol)}kg^{-1}_{(cat)}h^{-1}$ [1]. Catalytic activity of Au-Pd colloidal system has been shown to compare favourably with these methanotropic micro-organisms with productivity of 10.4 $mol_{(products)}kg^{-1}_{(cat)}h^{-1}$ at room temperature (Chapter 4). Both fresh and used colloids were characterised using electron microscopy and x-ray photoelectron microscopy. The catalyst was found to be stable after use with no significant agglomeration observed. An absence of dispersed atoms and sub-nanometer clusters also indicated a lack of leaching from metal nanoparticles. Further investigations were carried out into the effects of temperature, methane and oxygen pressure and concentration of H_2O_2. The reaction was successfully carried out at room temperature and the activation energy was calculated as 39 kJ/mol. First order kinetic dependence was measured for methane pressure and zero-order for oxygen pressure. First order dependence was also observed for H_2O_2 but only upto a certain concentration level. Higher concentration of H_2O_2 was found to be detrimental for the reaction which was investigated by performing a series of experiments. These results are useful in optimising the catalytic process to

obtain higher productivity without increasing over-oxidation.

Reactions were also performed in the absence of H_2O_2 but no activity was observed. In optimised reactions, a gain factor of 1.2 was observed. Thus for every mol of H_2O_2 consumed, 1.2 mol of products were obtained. One of the downsides of this catalytic system is the use of H_2O_2 and the costs associated with it. Commercial viability will hinge on the use of no or catalytic amounts of H_2O_2 and only air or O_2 as the oxidant. Rather than using H_2O_2, other processes could be devised by coupling Au-Pd colloid with photochemical [2, 3] or electrochemical methods [4, 5] which could generate similar radical species. Recently, a small-scale decentralised reactor was built to generate H_2O_2 electrochemically by oxygen reduction [6]. Such devices can be combined with Au-Pd colloidal systems to oxidise methane without use of pre-formed H_2O_2. Similarly, gas phase production of H_2O_2 was recently demonstrated using Au-Pd nanoparticles in a fixed bed reactor [7]. Thus, it would be useful to couple H_2O_2 generation and CH_4 oxidation in a continuous flow reactor. Initial investigation can also be performed with pre-formed H_2O_2 in which contact time between different reactants and colloids can be tuned to increase the catalytic efficiency and gain factor. The colloid could be circulated through the reactor to increase the product concentration in stream. One of the other concerns apart from H_2O_2 costs during scaling-up that needs to be addressed is product separation. This concern is related to the nature of the solvent system. Although, water provides a clean, green and non-reactive reaction medium, separation of methanol from water is highly problematic given the high solubility of methanol in water and their similar boiling points. Alternative solvents need to be used which would not only be utilised for colloid preparation but also facilitate product separation. Biphasic systems could also be employed with non-reactive organic solvents. Alternatively, methods need to be designed to 'strip' methanol from water or reaction needs to be performed in solvent-less system.

Through this work, it has been shown that supporting nanoparticles in this case is detrimental for the catalytic activity. Industrially however, heterogeneous catalysts have been preferred given the ease of re-usability of the catalysts. Thus, future work could also be

looking at non-conventional supports which do not cause H_2O_2 degradation like polymer resins. More research also needs to be performed in the role of polymer stabiliser on the activity and selectivity of colloidal catalysts. Methane oxidation reaction can be used as a model reaction to understand hydrocarbon oxidation with such colloidal catalysts. Different preparation techniques and substrates like ethane, cyclohexane can also be employed to understand this vast field of catalysis.

The last part of this thesis focused on computational investigations into interactions between gold and palladium clusters with O_2, H_2 and H_2O. Computational chemistry is a powerful tool to probe reaction mechanism and substrate-active site reaction. It can be used to compliment and explain experimental observations. In this work Density Functional Theory is used to understand the adsorption of O_2 on various facets of Au_{38} and Pd_{38}.Then H_2 and H_2O are adsorbed onto adjacent atoms to facilitate OOH synthesis. This step is essential to understand the surface reactions and the mechanism for direct synthesis of H_2O_2 which, as discussed in the introduction, is not only an important commodity chemical but used as an oxidant in many processes including methane oxidation. In such molecular simulations, calculating barriers is not an elementary concept since it involves simulating the potential energy surface to search for a transition state. From the energy of transition state, the energy barrier is then calculated. Nudged Elastic Band (NEB) technique was used to calculate the energy barrier between the defined start and end configuration to simulate the potential energy surface. Using this, energy barriers were calculated for OOH synthesis from O_2 and H_2 on both gold and palladium nanoparticles. A possible future work would be to employ bimetallic systems as done recently in interactions between O_2 and core-shell Au-Pd clusters [8]. More studies are also needed to be performed on nano-alloys and core-shell bimetallic Au-Pd nanoparticles. Higher sized clusters which contains more facets like 75 atom cluster containing (110) facet could also be employed to study more reaction pathways.

Bridging the gap between gas phase computational calculations and liquid phase experimental measurements, some complexity is introduced by including the effect of H_2O

on OOH synthesis and activation energies. This is performed by starting with surface bound H_2O molecules to participate in the reaction which is followed by the inclusion of free H_2O. Though a notable difference was not calculated between the reaction barrier for OOH synthesis with H_2 and bound-H_2O, a significant drop in transition state energy was observed with inclusion of free H_2O molecule. This demonstrates the use of protic solvent in direct synthesis of H_2O_2 which has been previously shown during kinetic investigations [9, 10]. To evaluate effects of solvent media on the reaction, implicit solvation model, which uses solvent properties like permittivity to model system was applied. Solvation energy was calculated for the systems and though a decrease was observed compared to the energy in vacuum, not much difference was observed within the different configurations. Slight lowering of barrier energy was observed with free H_2O. Thus, future work would be to include ab-initio approaches to simulate exact effects of solvents. The idea would be to gradually increase the complexity of the system to save computation time and develop realistic models by involving molecular dynamics of solvent molecules at second stage after gas phase energetics calculations. The other approach would be to combine these dynamic simulations with transition state search to perform dynamic transition state search sampling. This increases the sampling on the potential energy surface for the transition state. This approach often gives more information regarding the reaction mechanism which could not be derived by NEB method of transition state search. But it is also computationally expensive and could be employed at later stages.

6.1 Final Conclusions

In summary therefore, this work has addressed one of the great challenges in catalysis to design catalyst and catalytic system to oxidise methane. In this thesis, experimental investigations have been performed to understand and evaluate Au-Pd nanoparticles for low temperature selective oxidation for methane using hydrogen peroxide and oxygen which is highly productive, highly effective and green. Alongside this, computational studies have been carried out into interactions between gold and palladium clusters and reactant

molecules such as oxygen, hydrogen and water. Reaction energetics were calculated to understand the mechanism of direct synthesis of hydrogen peroxide. This will greatly enhance our understanding of the reaction kinetics and influence of solvent on reactions.

Though, the catalysts have shown high productivity and utilises molecular oxygen, a significant amount of further research is required before any industrial impact can be considered. These include investigations into process design (solvent, reactor design) and the catalyst itself (polymer supports, additives). More computational studies are also required to complement experimental studies to understand the process and increase its applicability to other oxidation processes.

Bibliography

(1) R. Balasubramanian, S. M. Smith, S. Rawat, L. A. Yatsunyk, T. L. Stemmler and A. C. Rosenzweig, *Nature*, 2010, **465**, 115–119.

(2) M. Gondal, A. Hameed and A. Suwaiyan, *Applied Catalysis A: General*, 2003, **243**, 165–174.

(3) R. P. Noceti, C. E. Taylor and J. R. D'Este, *Catalysis Today*, 1997, **33**, 199–204.

(4) A. Tomita, J. Nakajima and T. Hibino, *Angewandte Chemie - International Edition*, 2008, **47**, 1462–1464.

(5) K. Frese, *Langmuir*, 1991, **7**, 13–15.

(6) Z. Chen, S. Chen, S. Siahrostami, P. Chakthranont, C. Hahn, D. Nordlund, S. Dimosthenis, J. K. Norskov, Z. Bao and T. F. Jaramillo, *React. Chem. Eng.*, 2017, **2**, 239–245.

(7) A. Akram, S. J. Freakley, C. Reece, M. Piccinini, G. Shaw, J. K. Edwards, F. Desmedt, P. Miquel, E. Seuna, D. J. Willock, J. A. Moulijn and G. J. Hutchings, *Chem. Sci.*, 2016, **7**, 5833–5837.

(8) A. Staykov, D. Derekar and K. Yamamura, *International Journal of Quantum Chemistry*, 2016, **116**, 1486–1492.

(9) N. M. Wilson and D. W. Flaherty, *Journal of the American Chemical Society*, 2016, **138**, 574–586.

(10) T. Deguchi and M. Iwamoto, *The Journal of Physical Chemistry C*, 2013, **117**, 18540–18548.

7 | Appendix

```
SYSTEM NEB_run cluster
ISTART = 1      # 0: New job, 1: Continuation job
PREC = Accurate
GGA = PE        # Use the PBE functional 91 is PW91
ENCUT = 500     # Set planewave cutoff by hand
ICHARG = 2      # Initiate charge as superposition of atomic charges

#D3 corrections
IVDW = 11       # Turns on D3
VDW_S6 = 1.0    # S6 parameter
VDW_SR = 1.217 # SR parameter
VDW_S8 = 0.722 # S8 parameter
VDW_RADIUS = 15.0 # Cutoff radius for pair interactions
VDW_CNRADIUS = 10.0 # Cutoff radius for coordination number

#Relaxation parameters
NSW = 100
NELM = 100
ISPIN = 2
IBRION = 2      # Turn off VASP optimisers
#EDIFF = 1E-4   # Electronic relaxation threshold, 1E-4 is default
#EDIFFG = -1.5E-2  # Electronic relaxation threshold, 1E-3 is default
ISIF = 2 # Calculate atom forces and relax but not shape/size cell

# Settings for speed
ALGO =  Fast    # RMM-DIIS algorithm for electrons
LREAL = .FALSE. # evaluate projection operators in real space
NSIM = 4        # blocked algorithm update, four bands at a time
#
# Recommended option for preventing force noise
#
ADDGRID = .TRUE.


#for metal relaxation
ISMEAR=0
ISYM=0
SIGMA=0.01  #default
```

```
NCORE = 8
```

Listing 7.1: INCAR file for optimising structures

```
SYSTEM NEB_run cluster
ISTART = 1      # 0: New job, 1: Continuation job
PREC = Accurate
GGA = PE        # Use the PBE functional 91 is PW91
ENCUT = 500     # Set planewave cutoff by hand
ICHARG = 2      # Initiate charge as superposition of atomic charges

#D3 corrections
IVDW = 11       # Turns on D3
VDW_S6 = 1.0    # S6 parameter
VDW_SR = 1.217 # SR parameter
VDW_S8 = 0.722 # S8 parameter
VDW_RADIUS = 15.0 # Cutoff radius for pair interactions
VDW_CNRADIUS = 10.0 # Cutoff radius for coordination number

#Relaxation parameters
NSW = 100
NELM = 50
ISPIN = 2
IBRION = 3      # Turn off VASP optimisers
#EDIFF = 1E-4   # Electronic relaxation threshold, 1E-4 is default
#EDIFFG = -1.5E-2  # Electronic relaxation threshold, 1E-3 is default
ISIF = 2 # Calculate atom forces and relax but not shape/size cell

# Settings for speed
ALGO =  Fast     # RMM-DIIS algorithm for electrons
LREAL = .FALSE. # evaluate projection operators in real space
NSIM = 4         # blocked algorithm update, four bands at a time
ISYM = 0         # Turns off symmetry

# Recommended option for preventing force noise
ADDGRID = .TRUE.

# Solvation
LSOL = .TRUE.
```

Listing 7.2: INCAR file for performing solvation

```
SYSTEM NEB_run cluster
ISTART = 1      # 0: New job, 1: Continuation job
PREC = Accurate
GGA = PE        # Use the PBE functional 91 is PW91
ENCUT = 500     # Set planewave cutoff by hand
ICHARG = 2      # Initiate charge as superposition of atomic charges
```

```
#D3 corrections
IVDW = 11       # Turns on D3
VDW_S6 = 1.0    # S6 parameter
VDW_SR = 1.217 # SR parameter
VDW_S8 = 0.722 # S8 parameter
VDW_RADIUS = 15.0 # Cutoff radius for pair interactions
VDW_CNRADIUS = 10.0 # Cutoff radius for coordination number

#Relaxation parameters
NSW = 10
NELM = 50
ISPIN = 2
IBRION = 3      # Turn off VASP optimisers
#EDIFF = 1E-4   # Electronic relaxation threshold, 1E-4 is default
#EDIFFG = -1.5E-2  # Electronic relaxation threshold, 1E-3 is default
ISIF = 2 # Calculate atom forces and relax

# Settings for speed
ALGO =  Fast    # RMM-DIIS algorithm for electrons
LREAL = .FALSE. # evaluate projection operators in real space
NSIM = 4        # blocked algorithm update, four bands at a time
ISYM = 0        # Turns off symmetry

# Recommended option for preventing force noise
ADDGRID = .TRUE.

# NEB Calculation
IMAGES=5
ICHAIN=0
SPRINT=-5.0 # Spring constant used for nudging images
LCLIMB=.FALSE.

# Optimiser QM
IOPT=3 # Set to QM optimiser
MAXMOVE=0.2
TIMESTEP=0.1
```

Listing 7.3: INCAR file for performing NEB calculations with QM optimiser

(a) (b)

Figure 7.1: Spin traps used in the Chapter 3 a) DMPO and b) 31-P containing DEPMPO

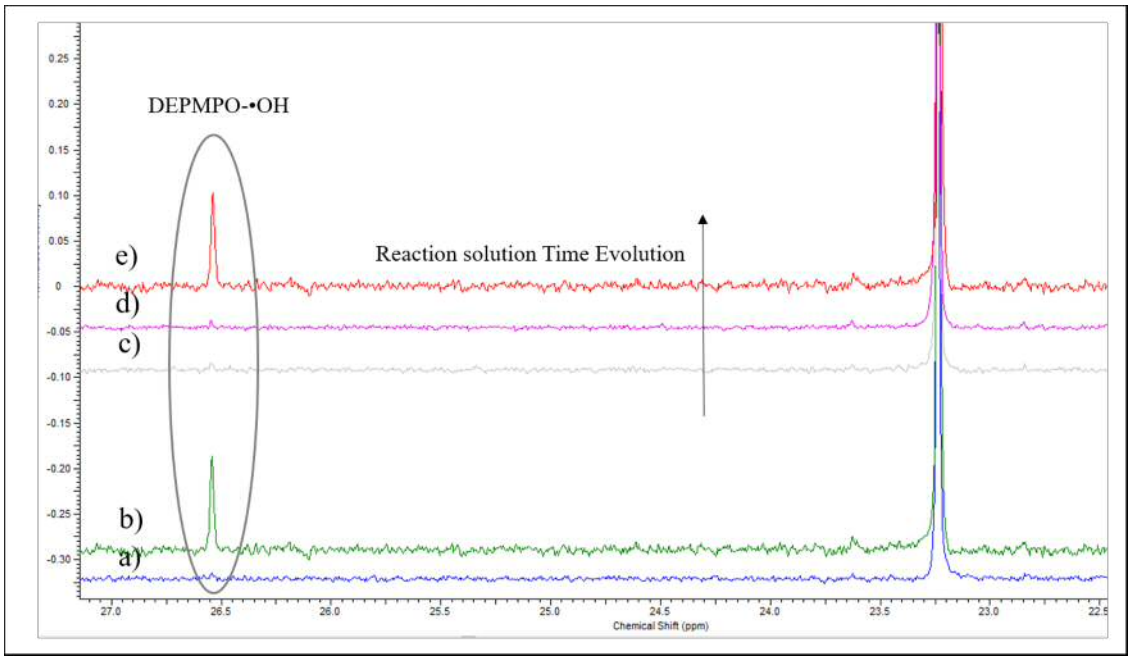

Figure 7.2: NMR analysis of spin trapping experiments with DEPMPO showing evolution of hydroxyl radicals. a) spin trap in Au-Pd colloid, b) spin trap in colloid with hydrogen peroxide after 18 hours showing DEPMPO-·OH at δ = 26.54 ppm (value taken from ref [1]), c) methane oxidation reaction solution containing colloid and H_2O_2, d) reaction solution measured after 2 hours, e) reaction solution measured after 16 hours.

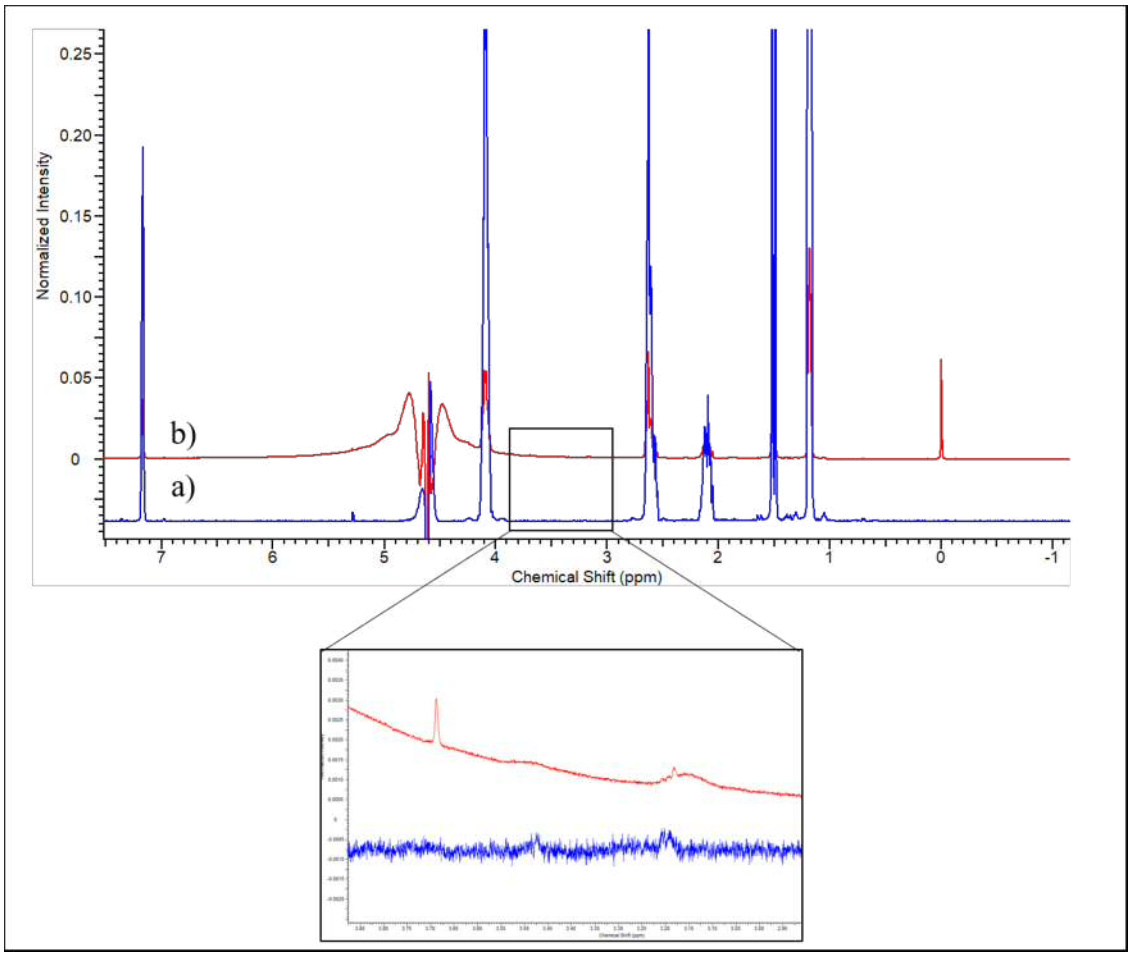

Figure 7.3: NMR analysis of a) reaction solution containing the spin trap showing no products compared to b) reaction solution without the trap.

Bibliography

(1) K. Valery, B. L. J. and C. T. L., *Magnetic Resonance in Medicine*, **42**, 228–234.

Fin.